IntechOpen

Nanocomposites

Recent Evolutions

Edited by Subbarayan Sivasankaran

NANOCOMPOSITES - RECENT EVOLUTIONS

Edited by **Subbarayan Sivasankaran**

Nanocomposites - Recent Evolutions
http://dx.doi.org/10.5772/intechopen.73364
Edited by Subbarayan Sivasankaran

Contributors

Jin Li, Boxue Du, Zhuoran Yang, Gopiraman Mayakrishnan, Kim Ick Soo, Vijay Choyal, Shailesh I. Kundalwal, Ahmed El-Shamy, Nguyen Nang Dinh, Pratima Parashar Pandey, Carlos Ávila-Orta, Pablo Gonzalez-Morones, Víctor Javier Cruz-Delgado, Juan Guillermo Martínez-Colunga, Alain González-Sánchez, Diana Agüero-Valdez, José Manuel Mata-Padilla, Ihab Abdel-Latif, Francesco Picchioni, Ranjita Bose, Henky Muljana, Amanda Oliveira, Cesar Augusto Gonçalves Beatrice, Teresa Golden, Heidi Conrad, Ting Zhou, Ana Piedade

Notice

First published in London, United Kingdom, 2019 by IntechOpen
eBook (PDF) Published by IntechOpen, 2019
IntechOpen is the global imprint of INTECHOPEN LIMITED, registered in England and Wales, registration number: 11086078, The Shard, 25th floor, 32 London Bridge Street
London, SE19SG – United Kingdom
Printed in Croatia

British Library Cataloguing-in-Publication Data
A catalogue record for this book is available from the British Library

Additional hard and PDF copies can be obtained from orders@intechopen.com

Nanocomposites - Recent Evolutions
Edited by Subbarayan Sivasankaran

p. cm.

Print ISBN 978-1-78985-011-6

Online ISBN 978-1-78985-012-3

eBook (PDF) ISBN 978-1-83881-737-4

Meet the editor

Dr. S. Sivasankaran is a faculty member in the Department of Mechanical Engineering, College of Engineering, Qassim University. He completed his PhD degree in Production Engineering (Manufacturing Technology—Nanocomposite Materials) at the National Institute of Technology, Tiruchirappalli, Tamilnadu, India. He passed his Bachelor Degree of Mechanical Engineering, First Class with Distinction, at the University of Madras, India. He did his MTech in Manufacturing Technology, First Class with Distinction, at the Department of Production Engineering, National Institute of Technology, Tiruchirappalli, India. After his doctoral degree, he worked as an associate professor in the KPR Institute of Engineering and Technology (KPRIET), Coimbatore, Tamilnadu, India. He established an advanced materials research laboratory and entrepreneurship development cell in KPRIET. He has received further research and seminar grants from the government of India. Furthermore, he served as an associate professor in Hawassa University, East Africa, from October 2014 to February 2016 where he developed BSc-Industrial Engineering, MSc-Industrial Engineering and Management, and MSc-Manufacturing Technology curricula. He has published more than 50 research articles in refereed international journals of which 20 articles were published by Elsevier, and in national journals and conferences. He is acting as a reviewer for more than 10 refereed international journals (Elsevier). He has organized more than 10 national- and international-level workshops. He has experience in synthesis, characterization, and mechanical behavior of nanocomposites through high-energy ball milling (powder metallurgy process), manufacturing of aluminum-based metal matrix composites through the stir-casting technique, processing of materials via severe plastic deformation techniques, friction stir processing, materials characterization using optical microscopy, XRD, SEM, TEM, microhardness measurement, wear behavior, machining behavior of composite materials, modeling using artificial neural networks, fuzzy logic, adaptive neurofuzzy inference systems, and optimization using Taguchi design of experiments. Finally, his research interests are nanocomposites, mechanical alloying, powder metallurgy, stir-casting, advanced welding, 3D printing, metal matrix composites, polymer matrix composites, mechanical behavior, machining behavior, advanced characterization techniques, optimization, and modeling.

Contents

Preface

Recently, material structures at the nanometric scale have had an influence on functional abilities in all fields of interest, especially in medical, aircraft, spacecraft, and structural properties fields. The adoption of nanocomposite materials by the research community in real-time applications is increasing rapidly in the world. Because of this, this book focuses on a number of recent contributions by several authors, which address the latest developments in nanocomposite material development, various synthesis routes, methods of characterization, several properties correlations, and applications. This book will help all academicians, research scholars, and those working in industries towards the designing of new nanomaterials, by investigating their output, exploring their utilizations, emphasizing their behavior, and making decisions for real-time applications.

Dr. Subbarayan Sivasankaran
College of Engineering
Qassim University, Saudi Arabia

Chapter 1

Nanocomposite for Space Charge Suppression in HVDC Cable Accessory

Boxue Du, Jin Li and Zhuoran Yang

Additional information is available at the end of the chapter

http://dx.doi.org/10.5772/intechopen.80217

Abstract

HVDC cable accessories made of ethylene-vinyl acetate copolymer (EVA) by incorporation of specific fillers have to face the problem of space charge accumulation. The effects of doping contents on the space charge behaviors of EVA/ZnO composite are not completely clear. EVA composites are prepared with the fraction of 0, 1, 5 and 10 wt%, respectively, with which 5 wt% nano-sized plus 5 wt% micro-sized ZnO-doped samples are chosen for comparison. Obtained results show that the particles in EVA composite are in homodisperse. The permittivity is increased by ZnO doping and the dissipation factor of EVA composites with 1 and 5 wt% nanoparticles is lower at the lower frequencies. The homocharge injection occurs in cathode instead of anode when ZnO nanoparticles are introduced and 5 wt% nanoparticle doping performs well in suppressing space charge injection. The electric field in the 5 wt% nanoparticle-doped EVA distributes more uniformly under the high electric stress than that of others. During the depolarization procedure, the total remnant charges of 10 wt% doped samples are the least in the final. The above results are well explained by the DC conduction, apparent mobility and trap distribution characteristics.

Keywords: HVDC, cable accessory, space charge, ZnO nanoparticle, trap distribution, carrier mobility

1. Introduction

The features of the transmission capability and the material are combined by the polymer insulated HVDC cables for high-power, long-distance underwater or underground transmission,

so they have many advantages [1–4]. Space charge can be accumulated under DC electric stress within the insulation matrix through charge injection from impurities' electro-dissociation and electrodes [5]. The electrical field in cable insulation may be changed seriously because of the accumulation of space charge, particularly after polarity reversal which causes probably premature failure and material degradation [6, 7].

Especially being a vital part of the HVDC networks, the performance of cable accessories is critical to the system's reliability considering the mechanical, thermal and electrical characteristics of the models which are combined with great dangers with install faults and environmental pollution [8–10]. Given the complicated geometry, particular fillers' doping and the inferfaces' existence between the accessories insulation and the cable insulation, the accumulation of the space charge as well as its influence has become much harder to make predictions [11].

People use EVA composites very often within the cable accessories because of the manufacture of cable accessory insulation, semi-conductive insulation jackets as well as heat shrinkable insulation and it is able to sustain higher filling contents with no yielding to the mechanical strength loss nor embrittlement and can be cross-linked in an easy way [12, 13]. The use of nonlinear resistive fillers as well as particular conductive additives and so on can create cable accessories which are from EVA composites, for the uniform electric field [14]. At the same time, the cable accessories which are created by EVA also needed to deal with the issue of the accumulation of space charge.

It has been proved that nano-sized particles are a useful strategy of suppressing the accumulation of space charges in dielectrics. A lot of reports have shown that the space charges are suppressed by the interfaces between the polymer matrix and the additives. Fabiani et al. argued that the use of larger TiO_2 nanoparticles to detect conductive processes in EVA nanocomposites has less accumulation of space charges, lower activation energy and lower conductivity [15]. Delpino et al. put forward the outcomes of conduction current measurements and space charges of 5 wt% EVA/montmorillonite nanoplayer composite and discovered big conduction current magnitude and space charge [16]. Montanari et al. did some researches on the electrical properties of layered micron and nano-sized silicate-filled EVA copolymers, and improved the space charge accumulation behavior by changing the nanofillers [17]. However, few studies have helped to know EVA's space charge dynamic actions full of ZnO under the DC electrical stress.

The paper aims at revealing ZnO doping's influence on the actions of space charges, electric field distribution as well as dielectric properties within EVA composites. According to the outcomes, an important influence on the dielectric properties and DC conduction exists in ZnO introduction. Homocharges accumulate near the negative electrode after introducing ZnO nanoparticles and 5 wt% concentration shows better suppression of space charge injection. The distribution of the electric field is more uniform in the 5 wt% doped EVA. The chains can be damaged by the extra micro-sized particles and brand-new disadvantages may be created as well, which may act as carriers.

http://dx.doi.org/10.5772/intechopen.80217

2. Experiments

2.1. Specimens

There is a density of 0.93 g/cm^3 and 14% vinyl acetate content in the EVA 1045. ZnO particles' grain sizes are ~2 μm and ~40 nm. The ZnO had been dried for over 24 h within a desiccator prior to dispersion in the EVA. The mixing was performed at 90°C for 15 min by a two-roll mill set at 30 rpm rotor speed and 2 mm nip gap. All the compounds had been cured for about 5 min at 120°C in a press that was heated electrically under the pressure of 10 MPa and chilled down in a natural way to the room temperature. Specimens that had ~500 μm thickness had been prepared through the incorporation of ZnO nanoparticles to EVA matrix with 10, 5, 1 and 0 wt% fraction respectively, where 5 wt% micro-sized and 5 wt% nano-sized ZnO filled EVA specimen had been set as contrast. ZnO's dispersion in the EVA matrix had been explored through scanning energy dispersive spectrum analysis (EDS) and electron microscopy (SEM) with Hitachi S4800. The mixed doping composites as well as 5 wt% nano ZnO doped EVA's SEM photograph can be seen in **Figure 1**. The white spots are the nano fillers in **Figure 1a**. No important aggregation can be seen in the specimens and the nano fillers are dispersed in a uniform way. The bigger particle stands for the micro-sized ZnO in **Figure 1b**. **Figure 2** is EDS's from **Figure 1** and the zinc factor's higher contents are introduced because of more ZnO doping. The fillers' uniform dispersion may be helpful for analyzing the space charge properties as well as the mechanism for dielectric.

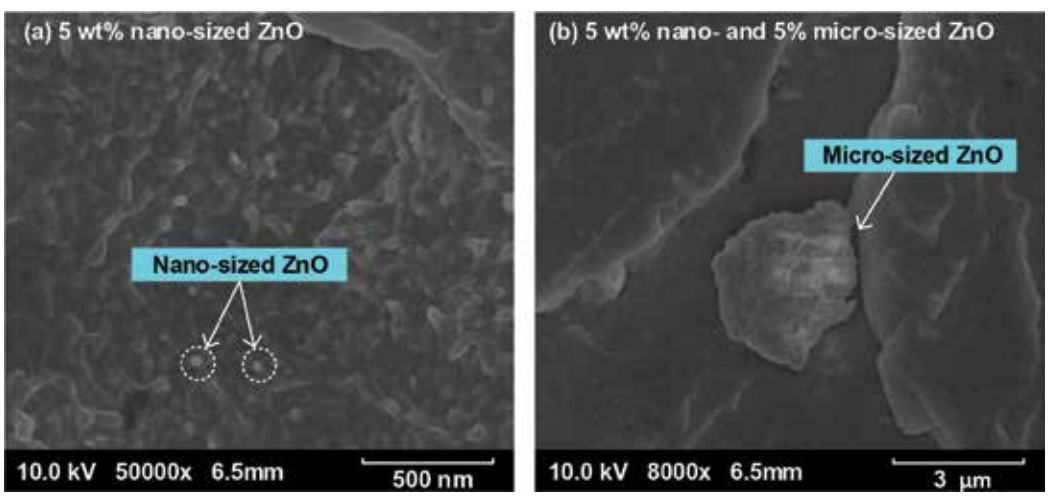

Figure 1. Distribution of ZnO particles in EVA composite.

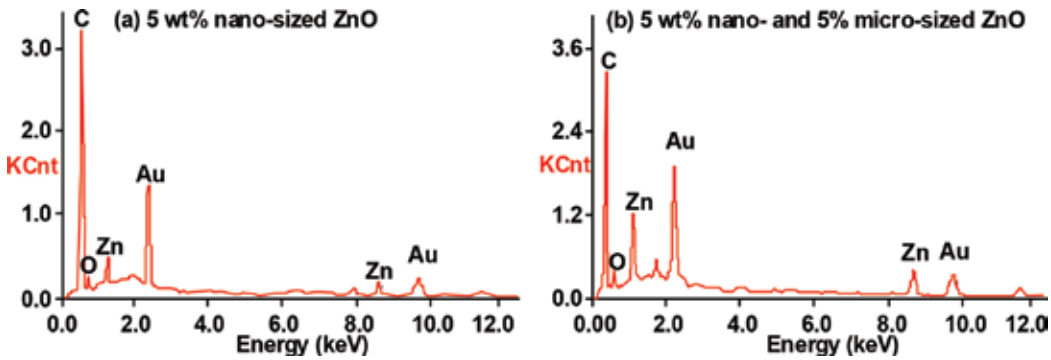

Figure 2. EDS of EVA/ZnO composite fracture surface.

2.2. Test procedure

2.2.1. Space charge measurements

The PEA strategy had been adopted to study the space charge characteristics in ZnO/EVA composites. The width of 10 ns as well as the pulse voltage with 500 V amplitudes had been adopted and silicone oil had been adopted for ensuring great acoustic contact between the electrodes and the specimen. The materials had been dealt with by the Lab VIEW software through the use of a deconvolution technique and a calibration. The specimen has a diameter of about 40 mm and a thickness of 500 μm. The temperature was set as 40°C and the electrical field was set averagely as −25 MV/m. Space charge profiles had been recorded along the depolarization and polarization process every 5 s.

2.2.2. Dielectric properties and DC conduction current measuring

The ZnO/EVA composites' dielectric properties had been measured in the paper through Novocontrol Concept 40. An electrometer (Keithley 6517B) had been used to measure the conduction currents with the space charge measurements under the same condition. Every specimen had been held between electrodes before the measurements for more than 12 h for the purpose of dissipating excess charges. The existing values had been recorded in the stressing process every 2 s.

3. Effects of ZnO contents

3.1. Specimen characteristics

The relation among the frequency, dissipation element and the relative permittivity of the EVA/ZnO composites is presented in **Figures 3** and **4**. As the ZnO concentration varies from 0 to 10wt %, relative permittivity improves from 2.59 to 2.92. While it comes to 3.0 for the hybrid doping. The dissipation factor has been greatly improving over a majority of the frequency range for the doped specimens, but an opposite trend is shown by the undoped specimen. The 5 and 1 wt% filled specimen's loss factor is lower at the lower frequencies compared with that

of the undoped one. The dissipation element is bigger for the higher frequency range or the higher doping proportion.

The relaxation mechanisms and the dielectric polarization determine the dielectric properties in the nanocomposites to a great extent [18]. The polarization which connects with the permittivity happens in the matrix-filler interfaces and the EVA, ZnO particles. In terms of the base EVA, the mobility of the long molecular chain makes contributions to the polarization process. Therefore, the relative permittivity is not high. Because there is relatively higher permittivity in the inorganic ZnO particles, the fillers are helpful to improve the EVA composites' permittivity with higher fillgrade. Nevertheless, the polarization is not improved so much as expected with less content of particles. The possible cause is that the matrix-filler interfaces are introduced by the nanoparticles doping, which may impose restrictions to the polymer polarization and cause the slow improvement of permittivity (**Figures 3** and **4**).

3.2. Space charge accumulation

Figure 5 presents ZnO/EVA composites' space charge polarization under −25 kV/mm on average. The homocharges within the pure EVA comes from the positive electrode with the application of the stress. The charge packages consisting of holes continued to move toward the negative electrode with the increase of time under the electric stress. There was no clear charge injection in EVA near the negative electrode. **Figure 5b** shows that the homocharges injected from negative electrode, which is opposite to the pure specimens. It's noticeable that good performance is demonstrated by the EVA composites doped with 5 wt% nano-sized ZnO to suppress the injection of the space charge within the dielectric matrix. According to **Figure 5d**, space charge distribution's region near the 10 wt% doped specimen's negative

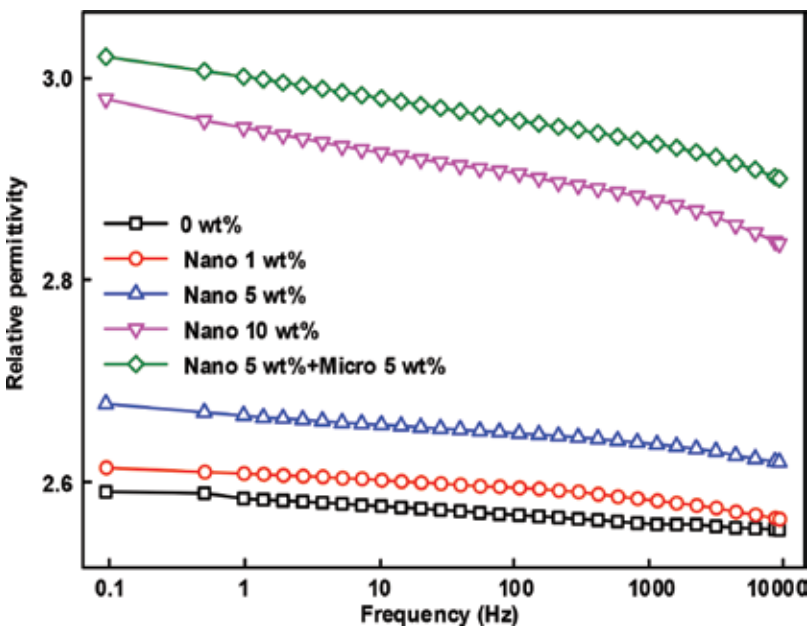

Figure 3. The relative permittivity of EVA/ZnO composites.

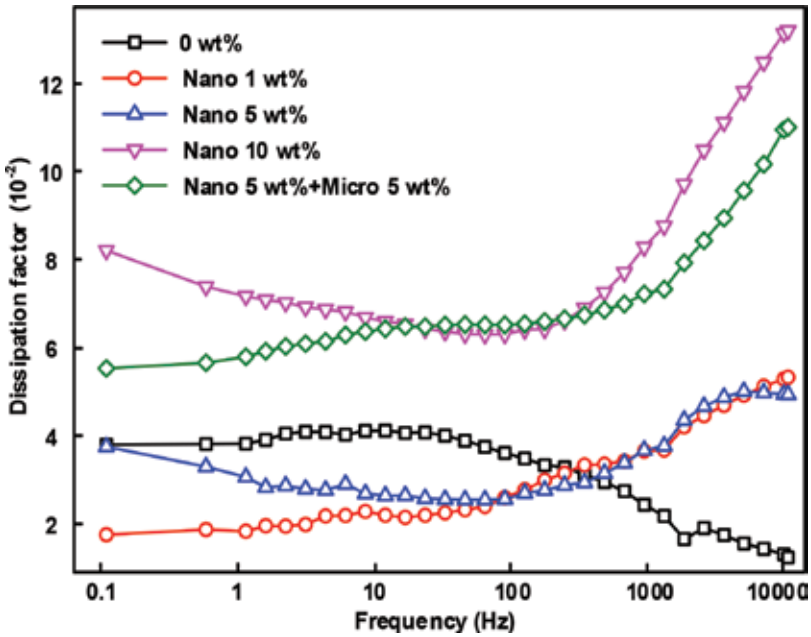

Figure 4. The dissipation factor of EVA/ZnO composites.

electrode is bigger compared with that of the **Figure 5c**. According the space charge pattern analyzed in group e, it is obvious to see a uniform charge close to either electrode. The homocharges migrate gradually toward the specimen matrix.

Since the electric field under the material's DC stress for cable accessories concerns a lot for the practical adoption, the distribution of the electric field $E(x)$ which is presented in **Figure 6** of EVA composites across the specimen had been worked out on the basis of Poisson's Eq. (1):

$$E(x) = -\frac{1}{\varepsilon_0 \cdot \varepsilon_r} \int_0^x \rho(x) dx \tag{1}$$

Where ε_r and ε_0 are the relative and vacuum permittivity; $\rho(x)$ is charge density; x is the specimen's thickness and d is the boundary [19]. The accumulation of the space charge distorted the electric field in undoped EVA more seriously compared with others. The distribution of electric field in 1 wt% filled specimen becomes nicer through the comparison with the undoped one. It seems that the electrical field in 5 wt% filled one is the best result. Additionally, the electrical stress is the highest in hybrid filling.

In general, homocharges usually generate from charges which are injected from metal electrodes. Moreover, they depend on the balance between charge injection and carrier diffusion to the EVA matrix. That is to say, the homocharges remain when people extract negative or positive carriers into the positive electrode/negative electrode electrodes. In terms of the base EVA, the homocharges which are injected from positive electrode move through the polymer

http://dx.doi.org/10.5772/intechopen.80217

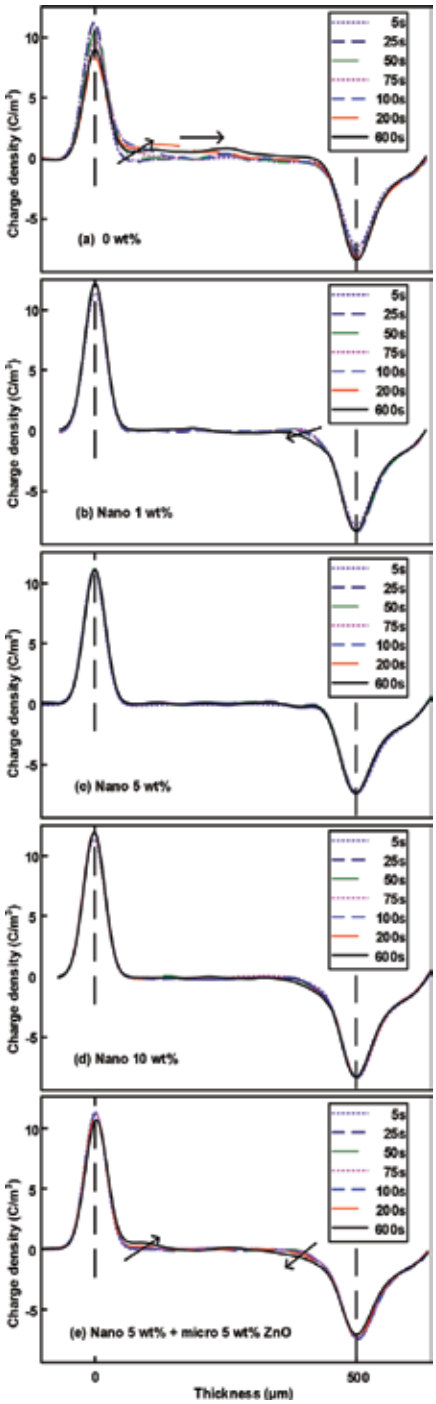

Figure 5. EVA/ZnO composites' space charge profiles during the polarization.

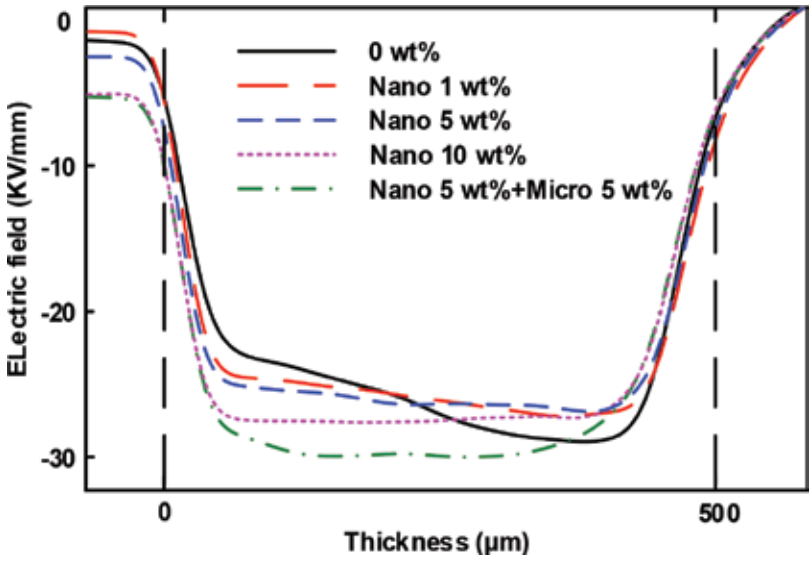

Figure 6. Electric field distribution in EVA/ZnO composites.

matrix. Because there are some similarities between the molecular chains in EVA matrix and the things in PE, which contain electrons that move along the inter chains [20], it's not difficult for the electrons to extract into the positive electrode, which may form positive homocharges and transport into the polymer matrix. Because there are some chemical groups or free chains in the pure EVA within the experiment, acting as space charge or charge carries may be injected very easily. Nevertheless, it's easy to observe the homocharges near the negative electrode when considering the less doping content of ZnO. The electrons are captured by the ZnO nanoparticles and prevented from extracting into the positive electrode.

It's clear that the space charge injection is restrained to a great degree by the sample which contains 5 wt% nanoparticles. Since a lot of traps may be introduced by the ZnO nanoparticles' incorporation into EVA matrix, it is able to capture enough homopolar charges for the purpose of impairing useful electric fields between the specimen's surfaces and the electrodes and devote to the carrier injection's restraint from electrodes. It is possible to form the percolation network with higher fillgrade, which may cause more negative injection close to the negative electrode. Compared with the nanocomposites, the EVA with hybrid doping has done worse. The micro-sized fillers may impair the nanoparticle interface effect and destroy the major polymer chain, which makes the homocharges inject from the electrodes. The space charges' distribution corresponds well with the dielectric properties' outcomes.

3.3. Space charge dissipation

EVA nanocomposites' space charge profiles are displayed in **Figure 7b** and **c** as well as **d**. Both homocharges can be found within the specimen at the initial stage. The beginning stage's

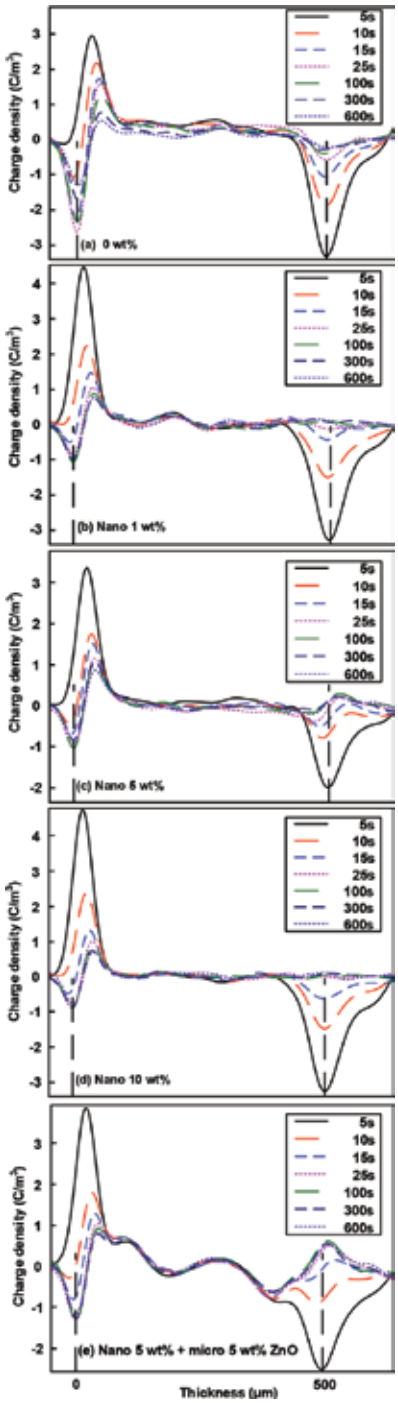

Figure 7. Space charge behaviors of EVA/ZnO composites during depolarization.

decay speed is more quickly compared with the pure EVA. A minute later, the residual charge will reduce in a rather slow rate. More complicated depolarization procedures can be seen in **Figure 7e**. In terms of the EVA doped with micro-sized and nano-ZnO particles, there are some similarities between the nanocomposites and the quick dissipation at the beginning stage. Even so, homocharges have been injected to the matrix's deeper areas instead of being transported into electrodes.

EVA/ZnO composites' space charge profiles are shown in **Figure 7** in the process of the depolarization when removing thirty-minute stressing. It's obvious that the charges dissipate rather quickly at first for the pure sample in **Figure 7a** and positive charges occupy most of the polymer matrix. Later on, both the positive and negative carriers migrate through the electrodes and keep a little totally. The entire charge within the matrix will be worked out by Eq. (2) for further discussion.

$$Q = \int_0^d |\rho(x)| \cdot S \cdot dx \tag{2}$$

Where d is the specimen's thickness, S is the electrode area and $\rho(x)$ is charge density. The entire charge's outcome after being stressed at −25 kV/mm for 30 min is presented within **Figure 8**. It's clear that the 5 samples dissipate fast at the beginning and the base EVA's charge dissipation continues all the time. Nevertheless, the amount of charge remains rather constant nearly a minute later for the doped specimens. It is obvious that the specimens' entire charges in higher fillgrade sample decay more quickly compared with the samples with lower ZnO contents. The decay of the charges with hybrid doping within specimens presents the trend with pure EVA. However, the 10 wt% specimen causes the residual charges in minimum.

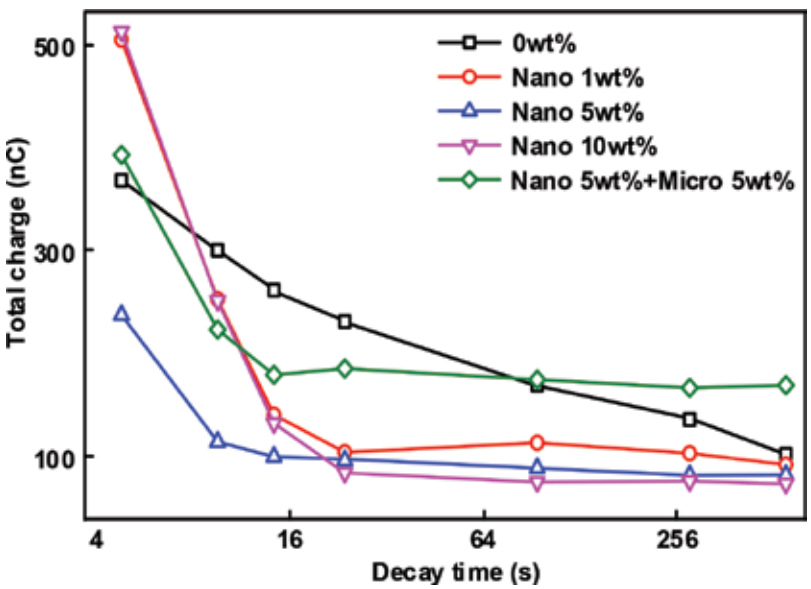

Figure 8. Total space charge decay process of different samples.

After we remove the applied stress from the specimen, the space charges transport with time mostly because of the detrapping process. The differences in the decay rate at various times can depend on the time constants for the trapping of deep and shallow traps. The quick dissipation in the initiative stage corresponds with the detrapping from the shallow traps. In addition, capturing charge carriers are hard in deep traps, which results in a slow rate of charge dissipation in doped specimens. More deep traps and shallow are introduced by nano-sized ZnO particles doping into the polymer. However, deeper traps are produced by the micro-sized ZnO particles through the comparison with the nanocomposites, as the form of brand-new disadvantages, causing more remnant charges. In terms of the base EVA, the traps' energy level is homogeneous to some extent. Therefore, the speed for the base EVA does not have too many changes at the time of dissipation.

A lot of studies have shown that the space charge correlates with the mobility, the conduction as well as the trap features [7]. The model is derived thinking about the trapping-detrapping equilibrium among the trap levels because of the thermal excitation. In accordance with the space charge density's changes and the Poisson's equation with the time of the depolarization, the carriers' obvious mobility as well as the relative trap depth is able to be analyzed as follows:

$$\mu(t) = \frac{2\varepsilon}{q^2(t)} \cdot \frac{\mathrm{d}q(t)}{\mathrm{d}\,t} \tag{3}$$

$$n(t) = kT \cdot \ln\left(\mu(t) \cdot \frac{h}{eR^2}\right) \tag{4}$$

Where R is the mean distance between localized states (5×10^{-7} m), e is the electron's quantity, h is the Planck constant, T is the absolute temperature, ε is the permittivity, k is Boltzmann constant and $q(t)$ is the average charge density [21]. The obvious mobility's outcome which is worked out by equation from the data of **Figure 8** is analyzed in **Figure 9**. it is obvious that undoped EVA's mobility keeps invariant with the time of the depolarization, which is in accordance with EVA copolymer's uniform structure. Nanocomposites' migration rate is high at the original period and the mobility becomes lower with further improvement. 10 and 1 wt% ZnO nanoparticles doped specimens have the highest mobility in accordance with the total space charges' quick dissipation at the initial stage. The specimen's trend with 5 wt% nanoparticles presents a proper central symmetry on the basis of the neat EVA. In terms of the entire mobility expression of the nanocomposite, this value decreases as the time increases, because the doping of nanoparticles leads to deeper traps in the charge release mechanism. It is predicted that the micro-sized particles act as constraint carriers migrating and big disadvantages in the process of the depolarization. According to **Figure 10**, it is clear to see the outcomes of the relative trap depth by Eq. (4). Compared with the change in apparent mobility over time, the results of the depth of the trap show the opposite trend. The base EVA's trap depth on average is nearly 0.81 eV and the deep traps' depth in the EVA composites can be improved by the filler doping. A wide range of trap depth is produced by the 1 wt% nanoparticles doping because of the localization state's changes, where deep traps play an important role in the space charge injection's suppression. A majority of the volume may be covered by the matrix

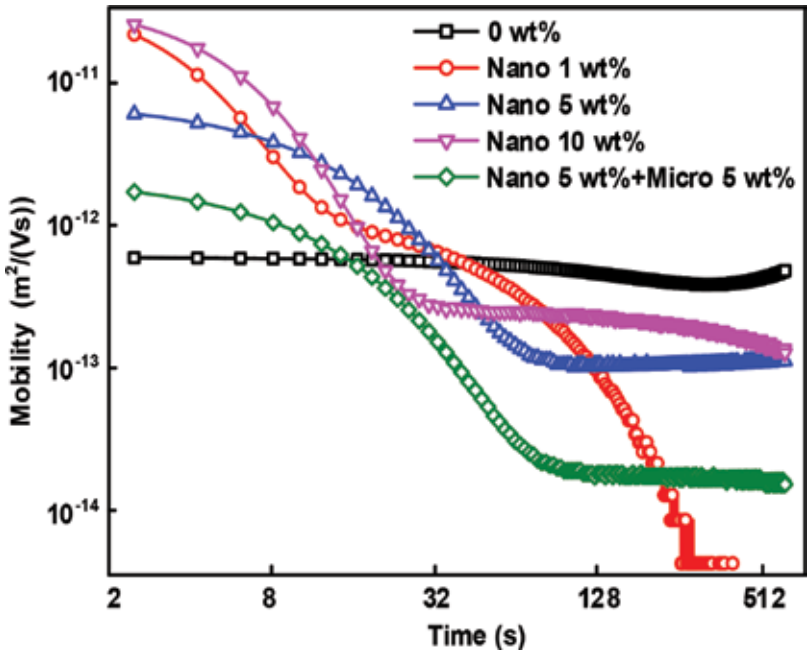

Figure 9. Apparent mobility with depolarization time.

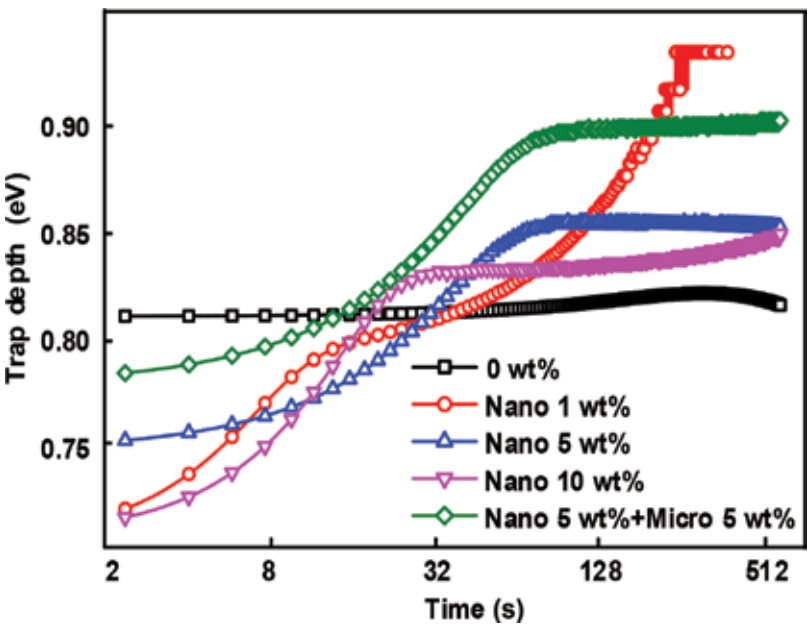

Figure 10. The trap depth with depolarization time.

filler interface region at the time of introducing more filler. Moreover, the deep trap depth can be increased on average, which will prevent the injection of space charge from the electrodes. Nevertheless, the percolation network may be formed or the interface is possible to overlap with the fillgrade reaching 10 wt%, which may reduce the negative homocharge injecting barrier as well as the trap depth. As is mentioned before, the chain may be broken by the extra micro-sized particles and brand-new disadvantages may appear which may act as local deep traps and is not sufficient to construct an injection barrier. In addition, the charge injecting can be accelerated by the weaker interface effect.

In order to confirm these assumptions, the conduction current had been evaluated at −25 kV/mm. It can be seen within **Figure 11**. It's clear that the base EVA conductivity can be greater in general compared with the doped specimen's conductivity. EVA composites' resistance may be increased by both the nanometer and micron-sized ZnO particles at EVA filler ratios. There is a certain relationship between charge mobility and conduction current. A change in conduction can be caused by the interfacial interaction between the polymer body and the filler, or the space charge which is accumulated close to the electrode may limit the conduction current. A charge blocking area can be formed by the trapped charge through the increase of the barrier to the carrier injection. Additionally, the negative and positive charges are localized because of the low charge mobility, which will impair carrier migration. Nevertheless, it seems that the extra micro-ZnO may decrease the mobility of the charge carrier, which in turn increases in the entire conductivity. EVA composites' charge carrier mobility may be reduced by the ZnO particles. The outcomes above can strongly prove the space charge suppression mechanism.

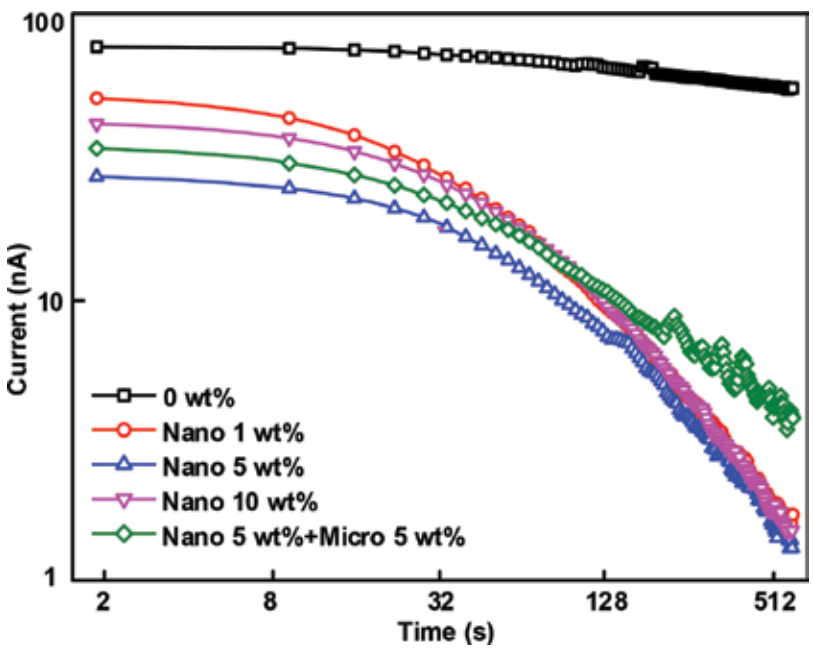

Figure 11. DC conduction currents of EVA/ZnO composite under −25 kV/mm.

4. Conclusions

In the paper, EVA composites which contain 10, 5, 1, and 1 wt% ZnO nanoparticles had been prepared where specimens doped with the comparison of 5 wt% micro-sized and nano-sized ZnO. Micron and nano-ZnO particles on EVA composites' space charge actions and dielectric properties had been researched. Below are the major conclusions.

1. According to the analysis of the SEM, the micro-scaled and nano-particles had been in homodisperse within the EVA composites. The ZnO doping can increase the dielectric constant and the dissipation element of EVA composites with 5 and 1 wt% nanoparticles may be lower at lower frequencies through the formation of the areas which are restricted by polarization and the impediment of the carriers' transport through various kinds of interfaces and chains.
2. When ZnO nanoparticles are introduced, co-directional charge injection takes place at the negative electrode rather than at the positive electrode, thus the change in electron extraction induced by the matrix-filler interface. In 5 wt% nanoparticle-doped EVA, the electric field is uniformly distributed under high electrical stress.
3. During depolarization, the total residual charge of the 10 wt% doped specimen was less than the final remaining charge at last. For dissipating speeds, for micron- and nano-sized particle doping, it is faster at higher filling levels, which has been decided by the obvious mobility and the conductivity.
4. Through correctly doping the nanoparticles, the injection of space charge can be suppressed through the help from the deeper average trap depth. The chain may be damaged by extra micro particles and brand-new disadvantages can be created, which may act as charge carriers.
5. Considering about the outcomes mentioned before, we can conclude that doping with proper ZnO may suppress the injection of space charge, cause to lower loss elements, increase the resistivity of volume and uniform the distribution of electric field. Thus, EVA/ZnO nanocomposites can be hopeful candidates for the applications of HVDC cable attachment insulation. Mechanical properties and breakdown strength should be further studied.

Author details

Boxue Du, Jin Li* and Zhuoran Yang

*Address all correspondence to: lijin@tju.edu.cn

Key Laboratory of Smart Grid of Education Ministry, School of Electrical and Information Engineering, Tianjin University, Tianjin, China

References

[1] Zhou Y, He J, Hu JL, Huang XY, Jiang PK. Evaluation of polypropylene/polyolefin elastomer blends for potential recyclable HVDC cable insulation applications. IEEE Transactions on Dielectrics & Electrical Insulation. 2015;**22**:673-681. DOI: 10.1109/TDEI.2015.7076762

[2] Marzinotto M, Mazzanti G. The statistical enlargement law for HVDC cable lines part 1: Theory and application to the enlargement in length. IEEE Transactions on Dielectrics & Electrical Insulation. 2015;**22**:192-201. DOI: 10.1109/TDEI.2014.004626

[3] Chen G, Hao M, Xu Z, Vaughan A, Cao J, Wang H. Review of high voltage direct current cables. CSEE Journal of Power & Energy Systems. 2015;**1**:9-21. DOI: 10.17775/CSEEJPES.2015.00015

[4] Long W, Nilsson S. HVDC transmission: Yesterday and today. Power & Energy Magazine IEEE. 2007;**5**:22-31. DOI: 10.1109/MPAE.2007.329175

[5] Fu ML, Dissado LA, Chen G, Fothergill JC. Space charge formation and its modified electric field under applied voltage reversal and temperature gradient in XLPE cable. IEEE Transactions on Dielectrics & Electrical Insulation. 2008;**15**:851-860. DOI: 10.1109/TDEI.2008.4543123

[6] Chong YL, Chen G, Ho YFF. Temperature effect on space charge dynamics in XLPE insulation. IEEE Transactions on Dielectrics & Electrical Insulation. 2007;**14**:65-76. DOI: 10.1109/TDEI.2007.302873

[7] Montanari GC. Bringing an insulation to failure: The role of space charge. IEEE Transactions on Dielectrics & Electrical Insulation. 2011;**18**:339-364. DOI: 10.1109/TDEI.2011.5739438

[8] Christen T, Donzel L, Greuter F. Nonlinear resistive electric field grading part 1: Theory and simulation. IEEE Electrical Insulation Magazine. 2010;**26**:47-59. DOI: 10.1109/MEI.2010.5599979

[9] Donzel L, Greuter F, Christen T. Nonlinear resistive electric field grading. Part 2: Materials and applications. IEEE Electrical Insulation Magazine. 2011;**27**:18-29. DOI: 10.1109/MEI.2011.5739419

[10] Cavallini A, Montanari GC, Morshuis P. HVDC insulation and diagnostics. IEEE Transactions on Dielectrics & Electrical Insulation. 2015;**22**:4-6. DOI: 10.1109/TDEI.2014.005122

[11] Delpino S, Fabiani D, Montanari GC. Feature article—Polymeric HVDC cable design and space charge accumulation. Part 2: Insulation interfaces. Electrical Insulation Magazine IEEE. 2008;**24**:14-24. DOI: 10.1109/MEI.2008.4455499

[12] Henderson AM. Ethylene-vinyl acetate (EVA) copolymers: A general review. IEEE Electrical Insulation Magazine. 1993;**9**:30-38. DOI: 10.1109/57.249923

[13] Du BX, Li J. Electrical and mechanical ageing behaviors of used heat-shrinkable insulation tubes. IEEE Transactions on Dielectrics & Electrical Insulation. 2014;**21**:1875-1881. DOI: 10.1109/TDEI.2014.104324

[14] Huang J. Carbon black filled conducting polymers and polymer blends. Advances in Polymer Technology. 2002;**21**:299-313. DOI: 10.1002/adv.10025

[15] Fabiani D, Montanari GC, Palmieri F. Effect of nanoparticle size on space charge behavior of EVA-TiO_2, nanocomposites. In: Proceedings of the IEEE Electrical Insulation and Dielectric Phenomena (CEIDP '11); 16–19 October 2011; Bologna. New York: IEEE; 2011. pp. 322-325

[16] Delpino S, Fabiani D, Montanari GC. High space charge dynamics in EVA-based nanocomposite flat specimens. In: Proceedings of the IEEE Electrical Insulation and Dielectric Phenomena (CEIDP '09); 26–29 October 2009; Quebec City. New York: IEEE; 2009. pp. 137-140

[17] Montanari GC, Cavallini A, Guastavino F. Microscopic and nanoscopic EVA composite investigation: Electrical properties and effect of purification treatment. In: Proceedings of the IEEE Electrical Insulation and Dielectric Phenomena (CEIDP '04); 17–20 October 2004; Boulder. New York: IEEE; 2004. pp. 318-321

[18] Singha S, Thomas MJ. Dielectric properties of epoxy nanocomposites. Dielectrics & Electrical Insulation IEEE Transactions on. 2008;**15**:12-23. DOI: 10.1109/T-DEI.2008.4446732

[19] Zhou T, Chen G, Liao R. Charge trapping and detrapping in polymeric materials: Trapping parameters. Journal of Applied Physics. 2009;**106**:644-637. DOI: 10.1063/1.3273491

[20] Fabiani D, Montanari GC, Dissado LA. Fast and slow charge packets in polymeric materials under DC stress. IEEE Transactions on Dielectrics & Electrical Insulation. 2009;**16**: 241-250. DOI: 10.1109/TDEI.2009.4784573

[21] Mazzanti G, Montanari GC, Alison JM. A space-charge based method for the estimation of apparent mobility and trap depth as markers for insulation degradation-theoretical basis and experimental validation. IEEE Transactions on Dielectrics & Electrical Insulation. 2003;**8**(2):187-197. DOI: 10.1109/TDEI.2003.1194099

Chapter 2

Carbon Nanocomposites: Preparation and Its Application in Catalytic Organic Transformations

Mayakrishnan Gopiraman and Ick Soo Kim

Additional information is available at the end of the chapter

http://dx.doi.org/10.5772/intechopen.81109

Abstract

Carbon nanocomposites have gained huge interest in catalysis due to their small size and shape-dependent physicochemical properties. Particularly, metal nanostructures/carbon materials (mainly graphene and carbon nanotubes) based nanocomposites demonstrated extraordinary catalytic activity in organic reactions. The catalytic products prepared by using carbon nanocomposites are found to be highly valuable in various fields including pharmaceutical, biomedical, agricultural, and material sciences. Hence, the demand of carbon nanocomposites has been increasing rapidly, and the development of novel preparation methods also deserve a special concern. In this chapter, we discuss the main advances in the field over the last few years and explore the novel preparation methods of carbon nanocomposites (metal nanostructures/carbon materials) and their applications in various catalytic organic transformations.

Keywords: carbon nanomaterials, metal nanostructures, nanocomposite, catalysis

1. Introduction

Carbon nanomaterials, including carbon nanotubes [both single-walled (SWCNTs) and multi-walled (MWCNTs)], graphene (G) or graphene oxide (GO), and carbon nanoparticles (CNPs), have attracted increasing attention owing to their unique structural regularity, high surface area, electrical conductivity, chemical inertness, biocompatibility, mechanical, and thermal stability [1, 2]. Graphene is a 2D single-atom-thick sheet of sp^2-hybridized carbon, and it can be stacked to form 3D graphite and rolled to form 1D carbon nanotubes (CNTs). The long-range π-conjugation in graphene possesses astonishing thermal, mechanical, and electrical properties [3, 4]. Because of their outstanding physicochemical properties, researchers turned

straight away into the exploration and modification of graphene and CNTs. To date, the potential applications of graphene and CNTs are diverse, which include catalyst carrier, energy storage, absorbents, biomedical, textiles, and sensors and support in many areas. As a catalyst carrier, the role of graphene and CNTs is just outstanding [5]. Particularly, in heterogeneous catalysts, the carbon materials often employed as a support to disperse the metal nanoparticles [3, 6]. In fact, the metal nanoparticles can easily agglomerate to form big nanoparticles due to their high surface energy, and it can be avoided by using support materials. Generally, the activity of the heterogeneous catalyst is mainly due to the structure of the catalyst, size of the metal nanoparticles, nature of the support, metal-support interaction, and fine dispersion of catalyst in reaction medium [7, 8]. To date, there are several metal nanoparticles supported graphene or CNT catalysts developed and reported for various organic transformations. The catalytic products are highly valuable in various fields including pharmaceutical, biomedical, agricultural, and material sciences [9]. In recent days, the interest on carbon nanocomposites in organic reaction has been increased significantly due to their unexpected positive outcomes. In this chapter, we discuss the main advances in the field over the last few years and explore the novel preparation methods of carbon nanocomposites (metal nanostructures/carbon materials) and their applications in various catalytic organic transformations.

2. Preparation and characterization of carbon nanocomposites

2.1. Noncovalent functionalization

In general, the carbon nanomaterials are chemically inert and highly hydrophobic in nature [10]. Therefore, the dispersion/anchoring of metal nanoparticles on the surface of carbon materials is very challenging task [11]. The noncovalent functionalization is one of the very common methods for the preparation of metal nanoparticles supported carbon nanocomposites. The noncovalent functionalization is mainly referred as a physical absorption, which involves weak interactions (π-interactions) [12]. In general, the noncovalent functionalization method causes no change on the basal plane structure and the electronic properties of carbon materials. However, prior to metal dispersion, in most of the cases, the surface of carbon materials has been modified to improve the hydrophobic nature and better "metal-carbon interactions." There are two main methods for the preparation of metal nanoparticles supported carbon nanocomposites by using the noncovalent functionalization: (1) wet synthesis and (2) dry synthesis.

2.1.1. Wet synthesis

The wet synthesis method has been widely adopted for the preparation of metal nanoparticles supported carbon nanocomposites. The wet synthesis is quite simple and low time-consuming processing steps. Moreover, the uniform nucleation and the high possibility of the control of size and morphology of the metal nanoparticles are the key factors, which can be easily achieved through wet synthesis. So far, the researchers have developed numerous highly unique and efficient carbon nanocomposites. Particularly, in recent years, the numbers have been gradually increased due to the high demand of these useful materials in various fields such as catalysis, energy, sensors, biomedical, and textiles.

Noble metals such as silver (Ag), gold (Au), ruthenium (Ru), and palladium (Pd) nanoparticles have been widely employed as promoters and catalysts in various organic transformations. The carbon-based supports such as CNTs and graphene/graphene oxide (G/GO) are often used as support for the immobilization of Ag, Ru, Pd, and Au nanoparticles. It was found that the preparation method has huge influences on the structure and surface morphology of the carbon nanocomposites. Recently, Salam et al. [13] obtained a highly efficient silver-graphene nanocomposite (Ag-G) through a simple wet chemical route. They used silica-coated Ag nanoparticle solution as Ag sources. In a typical wet synthesis, the silica-coated Ag nanoparticle solution was added with aqueous GO solution under stirring for 15 min followed by the addition of hydrazine solution. The solution was heated at 80°C for 15–20 min, and the resultant precipitate (Ag-G) was filtered and dried. The Ag-G has been characterized by XRD, TEM, and Raman spectroscopy. The results confirmed the uniform dispersion of Ag nanoparticles with good attachment with GO. Well known that the $NaBH_4$ is a strong reducing agent and often used for the preparation of carbon nanocomposites. The Ag/graphene nanocomposites were prepared using $NaBH_4$ as a reducing agent [14]. In a typical procedure, GO was mixed with CH_3COOAg solution and stirred at 100°C, followed by the addition of aqueous $NaBH_4$ solution and stirred at 100°C. Finally, the Ag/G nanocomposites were obtained by centrifugation, washing, and freeze-drying. The SEM and TEM results confirmed that the Ag nanoparticles (ranging from 5 to 25 nm) were orderly decorated and closely attached on the graphene nanosheets.

Bozkurt [15] obtained Ag/graphene nanocomposite by the sonochemical method in situ reducing reaction of silver ions and GO with sodium citrate as a green reducing agent. At first, GO was well dispersed in distilled water, and an aqueous solution of $AgNO_3$ was gradually added to the above suspension under vigorous stirring condition. Finally, sodium citrate was added to the above mixture and sonicated for 1 h. The resultant black solid product (Ag/graphene nanocomposite) was centrifuged and dried in a vacuum. The authors have proposed mechanism for the formation of Ag nanoparticles on GO. Briefly, at first, silver nitrate precursor deposits on the surface of the GO nanosheets. Subsequently, the applied ultrasonic irradiation assists the deposited silver nitrate precursor to homogeneously disperse on the GO surface. The functional groups such as epoxy groups, hydroxyl groups (–OH), carbonyl groups (C = O), and carboxylic acid (–COOH) groups on the surface of GO would also act as the active sites for the metal cations. In general, the oxygen functional groups interact with the metal cations through electrostatic interactions. In the final step, the addition of sodium citrate reduces the GOAg+ to Ag nanoparticles on the GO surface. In comparison with other methods, this ultrasonic irradiation method has advantages such as simplicity and high efficiency. The characterization results confirmed the merit of the ultrasonic irradiation method. TEM results showed the most of Ag nanoparticles deposited on the GO, which are spherical in shape with good attachment over GO surface.

A one-pot strategy was designed for forming the Au-SiO_2-GO composite by Peng and coworkers [16]. To prepare Au-SiO_2-GO composite, tetraethyl orthosilicate (TEOS) and $HAuCl_4$ were dissolved in TX-100 aqueous solution dispersed with GO, followed by the addition of compressed carbon dioxide (CO_2). Here the aim of utilizing compressed CO_2 is to form carbonic acid by reacting CO_2 with water. The carbonic acid can act as a catalyst for TEOS hydrolysis. Certainly, the compressed CO_2 can also promote the deposition of nanoparticles on a solid support. The solution mixture was stirred at room temperature for 7 hours. Finally, the CO_2 was released, and the product Au-SiO_2-GO composite was obtained. The TEM observation confirmed the uniform

dispersion of Au nanoparticles on the GO with a narrow size distribution of 1.4–2.0 nm. The BET surface area and the total pore volume are 429 and 1.01 cm^3 g^1, respectively.

Binary Au-Ag catalyst has been widely demonstrated to be one of the highly efficient catalysts for organic reactions. Babu et al. [17] prepared Au-Ag/SLG nanocatalyst from $HAuCl_4 \times H_2O$, Ag/DNA, and single-layer graphene (SLG). Negatively charged Salmon milt DNA was employed as Ag sources. In a typical wet synthesis, mixture of $HAuCl_4 \times H_2O$ and colloidal Ag/DNA was sonicated for 1 h at room temperature. Then, acid-treated single-layer graphene (*f*-SLG) was added to the above mixture and sonicated. Finally, the mixture was centrifuged to separate the Au-Ag/SLG and calcinated at 700°C for 3 h under inert atmosphere. Similarly, Pt-Ni bimetallic nanoparticles supported on CNTs nanocomposites (xPtNi/CNTs) with different compositions of Pt were synthesized [18]. Chemically modified CNTs were used for the decoration of nanocomposites. The solution phase reduction methods were adopted to prepare the nanocomposites in which ethylene glycol as a reducing agent in the polyol method or using poly (amidoamine) dendrimer as a platform and $NaBH_4$ as a reducing agent were used to deposit the Pt and Ni nanoparticles on the surface of modified CNTs. Recently, Yuan and coworkers [19] found that the bimetallic Pd-Ag nanoparticles supported MWCNTs (Pd-Ag/MWCNTs) are highly active catalyst for the electro-oxidation of ethanol, n-propanol, and *iso*-propanol. The Pd-Ag/MWCNTs was prepared by using the $NaBH_4$ reduction method in a mixed solvent of ethylene glycol and water. In a typical method, MWCNTs were first treated with conc. H_2SO_4 and conc. HNO_3 to create oxygen functional groups on the surface of MWCNTs. Subsequently, the acid-treated MWCNTs were added to a mixture of $PdCl_2$, $AgNO_3$, and ethylene glycol/water, and then the mixture was stirred for 30 min. Finally, $NaBH_4$ dissolved ethylene glycol was slowly added to the above mixture under vigorous stirring for 4 h. The Pd-Ag/MWCNT nanocomposite was characterized and applied for the electro-oxidation of ethanol, n-propanol, and *iso*-propanol.

Ru was found to be an excellent catalyst for organic reactions due to its wide chemical states (II to +VIII) and tunable properties [20]. Particularly, the Ru catalyst has shown an excellent activity in oxidation reactions because of its redox properties. Interconnected RuO_2 nanoparticles anchored GO nanocatalyst (RuO_2/GO) with very good BET surface area (285 m^2/g) were obtained by Yuan and coworkers [21]. Very simple method was adopted for the preparation of RuO_2/GO. Briefly, $Ru(acac)_3$ and GO were dispersed in methanol and sonicated for several hours followed by heating at 65°C to evaporate the methanol. The obtained slurry was grinded well with mortar and pestle until the homogeneous mixture was obtained, and then, it was calcinated in the muffle furnace under N_2 atmosphere at 600°C (heating rate of 5°C/min) for 3 h. The RuO_2/GO was completely characterized by various spectroscopic and microscopic techniques.

Wang et al. [22] obtained Pd nanoparticles immobilized GO nanocomposite by a very simple wet chemical method. $PdCl_2$ and hydrazine hydrate were used as Pd sources and reducing agent, respectively. Initially, an aqueous suspension of GO was prepared, and then, $PdCl_2$ was added under the assistant of mild ultrasound. The hydrazine hydrate was then added to the above mixture and the solution heated at 100°C for 1 h. The black solid of Pd/GO was isolated by filtration and washed copiously with water and methanol. TEM image of the Pd/graphene composite showed that the Pd nanoparticles were supported on the surface of the GO sheets without any agglomeration of the Pd nanoparticles. The Pd nanoparticles are composed of spherical particles. The size of the Pd particles calculated to be 2–6 nm. The metal surface area of Pd/graphene measured to be 161 m^2/g.

Recently, a facile and green method was developed to synthesize a new type of catalyst by coating Pd nanoparticles on reduced graphene oxide (rGO)-CNT nanocomposite [23]. At first, the three-dimensional microstructure of an rGO-CNT nanocomposite was obtained by hydrothermal treatment. The homogeneous mixture of GO and CNTs was prepared under sonication conditions, and the mixture was subsequently sealed in a 50-ml Teflon-lined autoclave and maintained at 180°C for 12 h. A black gel-like 3D cylinder of rGO-CNT composite was obtained. The resultant rGO-CNT composite was dispersed in aqueous solution, and subsequently, K_2PdCl_4 was added. The mixture was vigorously stirred for 30 min in an ice bath. Then, the reaction mixture was washed well with pure water to obtain Pd-rGO-CNT nanocomposite.

Similarly, CuO nanoparticles were decorated on the surface of GO to obtain CuO/GO catalyst [24]. In a typical procedure, GO was dispersed in methanol and sonicated for 1 h. Then, the $Cu(acac)_2$ added to the above mixture was refluxed for 5 h (Step 1), and the MeOH was slowly evaporated. The resultant slurry was mixed well by a mortar and pestle, and obtained homogeneous mixture of GO and $Cu(acac)_2$ was calcinated under inert atmosphere at 350°C for 3 h. **Figure 1(a)** shows a schematic illustration for the preparation of CuO/GNS. The CuO/GNS was completed characterized by TEM, SEM-EDS, XPS, Raman, and XRD (**Figure 1**). The TEM images showed the strong attachment of CuO nanoparticles on the GNS with particle size distribution of 12–35 nm. Raman and XPS results indicated the strong attachment of CuO on GNS through covalent bonding (Cu—C). The Cu 2p XPS spectrum of CuO/GNS showed shakeup satellite peaks of the Cu $2p_{3/2}$ at 942.4 eV and Cu $2p_{1/2}$ at 962.6 eV, which confirmed the presence of Cu(II) species (CuO).

2.1.2. Dry synthesis

The dry synthesis is found to be highly efficient and suitable method for the synthesis of carbon nanocomposite. The main advantages of this method are its simplicity, better adhesion, and advantages of least parameters to be controlled [25]. It was found that the dry synthesis is the method, which is highly suitable for the decoration of metal nanoparticles on carbon

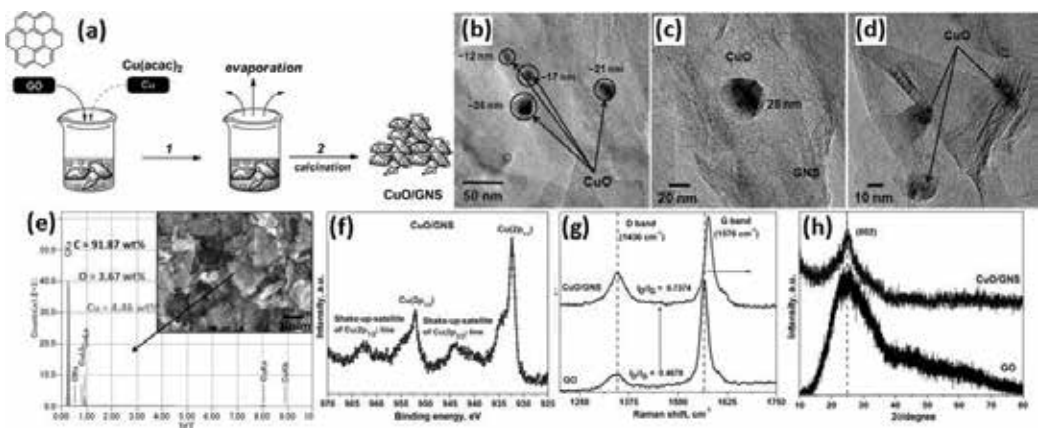

Figure 1. (a) Schematic illustration of the procedure for the preparation of CuO/GNS, (b–d) TEM images, (e) SEM-EDS, (f) XPS, (g) Raman, and (h) XRD patterns of CuO/GNS (from Gopiraman et al. [24]).

nanomaterials when compared with wet synthesis method. In fact, several drawbacks of the wet synthesis method have been resolved by the dry synthesis method. Moreover, the carbon materials are highly hydrophobic, and it needs surface modification (with oxygen functional groups (C—OH, C—O—C, C = O, and COOH or amine groups) prior to the decoration of metal nanoparticles [26]. The oxygen functional groups could play a bridging role between the metal nanoparticles and the carbon materials. However, the creation of the oxygen functional groups is very difficult in case of activated carbon, carbon nanofibers, and carbon black. Interestingly, carbon materials without any surface functional groups could also be utilized successfully for the preparation of carbon nanocomposites. However, the large-scale production of the carbon nanocomposites through dry synthesis is limited.

A rapid and solventless dry synthesis method was described for the preparation of carbon nanocomposites by Lin and coworkers [27]. This straightforward two-step process involves the dry mixing of a precursor metal salt with carbon materials (CNTs or GO) followed by heating in an inert atmosphere. They found that the dry synthesis procedure is scalable and applicable to various other carbon substrates (e.g., CNFs, expanded graphite, CNTs, activated carbon, and carbon black) and many metal salts (e.g., Ag, Au, Co, Ni, and Pd acetates). The Ag nanoparticles decorated CNTs have been reported as a model system, and the composites were prepared under various mixing techniques, metal loading levels, thermal treatment temperatures, and nanotube oxidative acid treatments. The TEM and SEM observation confirmed the uniform and strong attachment of Ag nanoparticles on the surface of the CNTs. However, in a wet synthesis, many factors such as solvent, concentration of metal precursor, reducing agent, deposition time, and temperature need to be controlled very carefully. Similarly, Ag nanoparticles of small average diameter (<5 nm) were decorated on the surface of MWCNTs by a simple mechanochemical process [28]. In a typical preparation, the silver acetate and MWCNTs were placed in a zirconia vial. Then, two zirconia balls were placed in a vial, and the set-up was secured in a SPEX CertiPrep 8000D high energy shaker mill and subjected to mechanical shaking for a desired period of time to yield the Ag/MWCNTs nanocomposite. The mechanochemical process requires no solvent, no additional reducing agents, or no applied electrical current. They demonstrated that the mechanochemical process was found to be readily applicable to not only CNTs, but also other carbon materials that are thermally conductive such as graphene, GO, and activated carbon (**Figure 2**). Moreover, different organic metal salts (e.g., Au and Pd acetates and Pt acetylacetonate) were also successfully applied in

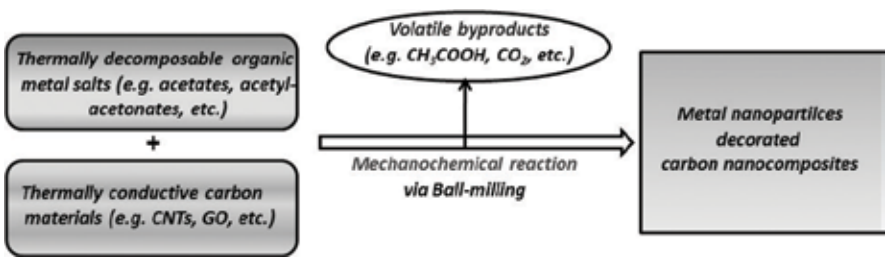

Figure 2. General procedure for preparation of carbon nanocomposites by mechanochemical synthesis (from Lin et al. [28]).

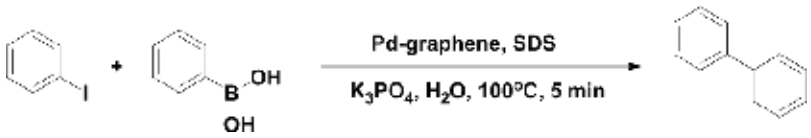

Scheme 1. Suzuki reaction of iodobenzene with phenylboronic acid catalyzed by Pd-graphene nanocomposites (from Li et al. [39]).

similar procedures to obtain the corresponding carbon nanocomposites. The mechanochemical process is found to be rapid, versatile, and potentially scalable, making it useful for further exploitation in various applications. **Scheme 1** shows the general procedure for the preparation of carbon nanocomposites by mechanochemical process.

Later, Kim's group [29–33] developed various carbon nanocomposites by using the dry synthesis method also called "mix-and-heat" method. The prepared carbon nanocomposites were utilized as heterogeneous catalysts in various organic reactions. The metallic Ru nanoparticles were decorated on graphene nanosheets (GNSs) by "mix-and-heat" method [29]. Initially, the bi- and few-layered graphene nanosheets (GNSs) were obtained from graphene nanoplatelets (GNPs) by a solution-phase exfoliation method. The obtained GNSs were chemically treated with concentrated H_2SO_4 and HNO_3 to create oxygen functional groups (—COOH, —C = O, —C—O—C—, and —OH) on the surface of GNSs. The resultant *f*-GNSs were used for the decoration of Ru nanoparticles. In a typical preparation, $Ru(acac)_3$ was added into *f*-GNS and mixed well by a mortar and pestle under ambient conditions. Then, the homogeneous mixture of *f*-GNS and $Ru(acac)_3$ was calcinated at 300°C for 3 h under an argon atmosphere. The morphology of the resultant nanocomposite (GNS-RuNPs) was found to be excellent. Ultrafine Ru nanoparticles were homogeneously dispersed on the surface of GNSs. Interestingly, the size of these attached Ru nanoparticles was found to be below 3.0 nm. Similarly, GNPs-RuO_2NPs was prepared by a simple "mix-and-heat" method. **Figure 3** shows the schematic illustration for the preparation of GNPs-RuO_2NPs, TEM images, RuO_2 particle distribution, XPS,

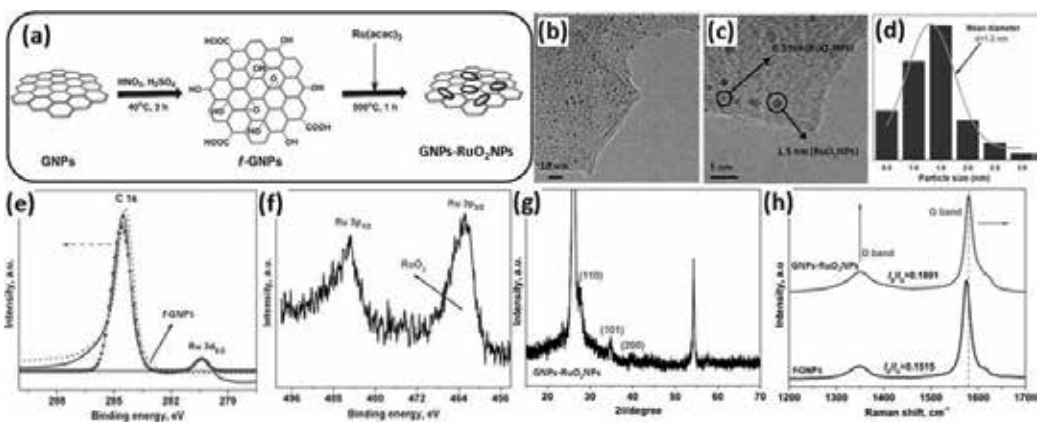

Figure 3. (a) Schematic illustration for the preparation of GNPs-RuO_2NPs, (b and c) TEM images, (d) RuO_2 particle distribution, (e and f) XPS, (g) XRD patterns, and (h) Raman spectra of GNPs-RuO_2NPs (from Gopiraman et al. [32]).

XRD patterns, and Raman of GNPs-RuO_2NPs. Later, CuO/MWCNTs [30], RuO_2/MWCNTs [31], and GNPs-RuO_2NPs [32] were synthesized by the dry synthesis method. It was demonstrated that the SWCNTs were also utilized to successfully decorate the RuO_2 via dry synthesis method [33]. Astonishingly, the mean diameter of the RuO_2 nanoparticles attached to SWCNTs was found to be about 0.9 nm. The BET surface area of RuO_2/SWCNT was found to be 416 m^2 g^{-1}. Moreover, Raman and XPS results confirmed that the RuO_2 nanoparticles were strongly attached on the surface of SWCNTs.

3. Carbon nanocomposites catalyzed organic reactions

Recently, carbon nanocomposites have been widely used as heterogeneous catalysts in various organic transformations. Less than 10% of the chemical processes in chemical industries are still conducted without the addition of catalyst [34]. The catalytic products such as organic building blocks, pharmaceuticals, natural products, and agricultural derivatives are very valuable in chemical industries [35]. Numerous metal catalysts (supported and unsupported) are reported for the industrially important organic transformations. Carbon nanocomposites, particularly structural carbon (graphene and CNTs) based materials, are recently being used as heterogeneous catalysts in organic transformations. In fact, the high surface area, fine dispersion, stability, reusability, and easy recovery are the key factors. Moreover, the immobilization of metal nanoparticles onto the carbon support has revealed more versatility in carrying out the highly selective catalytic processes [36]. In comparison with CNTs, graphene or GO has been preferred due to its low cost, large-scale preparation, and less health risk.

3.1. Noble metals supported carbon catalysts

Pd nanoparticles supported carbon materials have been widely used as heterogeneous or semi-heterogeneous catalysts for C—C coupling reactions, such as Mizoroki-Heck, Suzuki-Miyaura, and Sonogashira reactions [37]. These cross-coupling reactions are the most efficient methods for the construction of C—C bonds. The Pd as a catalyst can assemble C—C bonds between various functionalized substrates allowed researcher to achieve the reactions that were previously impossible (or possible with multiple steps) [38]. Hence, these methodologies have found extensive use in organic synthesis and material science. Moreover, these cross-coupling reactions found to play an important role in pharmaceutical, fine chemical, and agrochemical industries.

Li et al. [39] demonstrated Pd-graphene nanocomposites as an efficient nanocatalyst for Suzuki reaction. The Pd-graphene nanocomposites showed an efficient catalytic activity toward Suzuki reaction in water under aerobic condition for a short time. **Scheme 1** shows the Suzuki reaction of iodobenzene with phenylboronic acid catalyzed by Pd-graphene nanocomposites. The catalyst is not only efficient but also easily recovered and reused several times for the low-cost and environmentally friendly synthesis of biaryls. Using 1.1 mol% of Pd-graphene nanocomposite with sodium dodecyl sulfate (SDS) at 100°C, the catalytic system affords 100% of yield with 95.5% selectivity. Interestingly, the catalyst can be reused at least for 10 times (at 10th cycle, the yield was 78.6%).

http://dx.doi.org/10.5772/intechopen.81109

The complete recovery and excellent reusability are the major advantages of using heterogeneous catalysts [40]. However, in most of the heterogeneous catalytic systems, the isolation of catalysts from the reaction mixture by conventional filtration methods is inefficient and time consuming. Therefore, magnetically recoverable carbon nanocomposites have gained much attention due to it easily and complete recovery of the catalyst from reaction mixture. Fe_3O_4 and Pd nanoparticles were decorated on sulfonated graphene (s-G) by a facile chemical approach [41]. The prepared carbon nanocomposite Pd/Fe_3O_4/s-G was used as an excellent semi-heterogeneous catalyst for the Suzuki-Miyaura cross-coupling reaction in an environmentally friendly solvent (water/ethanol (1:1)) under ligand-free ambient conditions (**Scheme 2**). It was found that even a low amount of catalyst Pd/Fe_3O_4/s-G (0.15 mol% Pd) is also enough to achieve 97% of the product after 30 min of the reaction time. The small size and homogeneous distribution of Pd nanoparticles on the Fe_3O_4/s-G matrix are the main reason for the excellent catalytic activity. The activity of Pd/Fe_3O_4/s-G did not deteriorate even after 10th cycle, which may be due to the easy and efficient magnetic separation of the catalyst and the high dispersion and stability of the catalyst in an aqueous solution. At 10th cycle, the Pd/Fe_3O_4/s-G catalyst gave 84% of the product. Similarly, magnetically recoverable Pd/Fe_3O_4 nanoparticles supported graphene nanosheets (Pd/Fe_3O_4/G) were prepared for Suzuki and Heck coupling reactions (**Figure 4**) [42]. The Pd/Fe_3O_4/G system gave excellent yields over a broad range of highly functionalized substrates in both Suzuki and Heck coupling reactions. With 7.6 wt% of Pd, the Pd/Fe_3O_4/G worked well in Suzuki cross-coupling reaction with a high turnover number (TON) of 9250 and turnover frequency (TOF) of 111,000 h^{-1}. Due to the good magnetic property of the Pd/Fe_3O_4/G, it was easily recovered using a simple magnet and reused for 10 times (**Figure 4**).

Similarly, various Pd nanoparticles supported graphene nanocomposites were prepared and used as an excellent nanocatalyst for the cross-coupling reaction. Pd nanoparticles supported graphitic carbon nitride (Pd/g-C_3N_4) was prepared through a one-step photodeposition strategy, and it was used for Suzuki-Miyaura coupling reactions by Sun and coworkers [43]. They found that the Pd/g-C_3N_4 was worked well at room temperature without any phase transfer agents, toxic solvents, and inert atmosphere. Under the optimized conditions, the Pd/g-C_3N_4 achieved a complete conversion (100%) of the reactant and a high yield of 97% for biphenyl. Unlike other supports, the g-C_3N_4 with plenty of nitrogen-containing anchor sites was a suitable platform for Pd atoms, which could favor fine dispersion and stabilization of the ultrafine Pd nanoparticles on g-C_3N_4. Siamak et al. [44] used single- or multi-walled carbon nanotubes (SWCNTs and MWCNTs) as a support for the decoration of Pd nanoparticles. Both the supported catalysts (Pd/MWCNT)M and (Pd/SWCNT)M) were successfully employed in Suzuki cross-coupling reactions with a wide variety of functionalized substrates. Interestingly, they noticed that the MWCNTs supported Pd nanoparticles catalyst (Pd/MWCNT)M showed slightly better yield

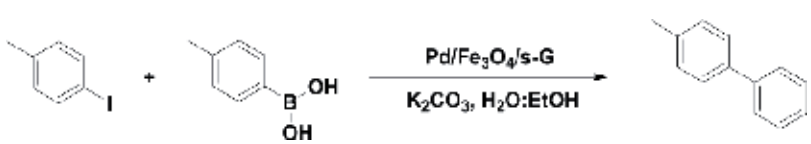

Scheme 2. Suzuki-Miyaura cross-coupling reaction catalyzed by Pd/Fe_3O_4/s-G catalyst (from Elazab et al. [41]).

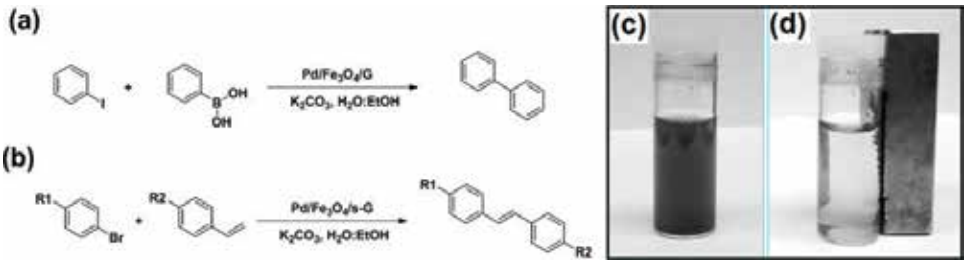

Figure 4. Pd/Fe_3O_4/G catalyzed (a) Suzuki cross coupling, (b) Heck coupling reactions, (c) the reaction mixture with Pd/Fe_3O_4/G, and (d) separation of spent catalyst from reaction mixture using a simple magnet (from Hu et al. [42]).

when compared with SWCNTs supported Pd catalyst (Pd/SWCNT)M). They concluded that the superior catalytic activity and excellent reusability of (Pd/MWCNT)M mainly due to the larger diameter of the MWCNTs (20–150 nm) offer stronger surface interactions and provide large number of anchoring sites for the Pd nanoparticles, thus facilitating the deposition of the greater number of Pd nanoparticles on the surface of MWCNTs with strong attachment.

In organic synthesis, multi-component reactions (MCRs) are very important and essential for the synthesis of diverse complex molecules through a combination of three or more starting materials in a one-pot reaction [45]. For instance, synthesis of propargylamine through coupling reaction of aldehydes, amines, and alkynes (A^3 coupling) is one of the important MCRs. The propargylamines are highly valuable in the synthesis of various biologically active compounds and natural products [46]. To synthesis the propargylamines, graphene-based composite with silver nanoparticles (Ag-G) was prepared *through* a simple chemical route by Salam and coworkers [13]. After being optimized the reaction conditions, the scope of the catalytic was extended. The catalytic system worked well for a wide range of substrates including aromatic and aliphatic aldehydes, including those bearing functional groups such as —OH, —Cl, and —Br additions. The Ag-G is air-stable, heterogeneous, cost-effective, easily recoverable, and reusable without loss in activity and selectivity. **Scheme 3(a)** shows three-component (A^3) coupling reaction catalyzed by the Ag-G. Moreover, the Ag-G catalyst is also suitable for

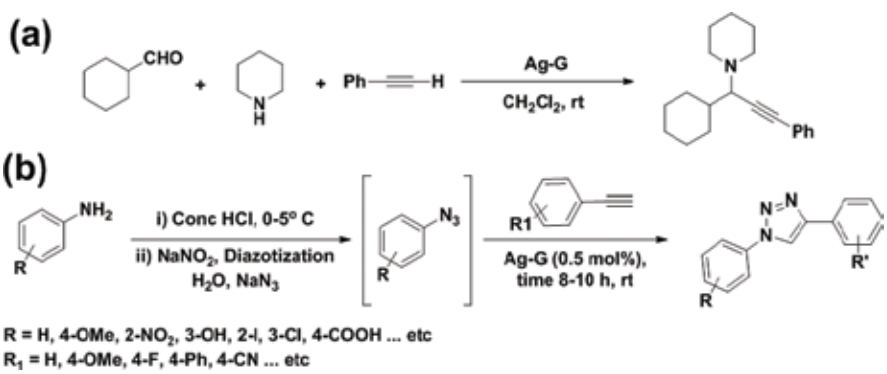

Scheme 3. Ag-G catalyzed (a) three-component (A^3) coupling reaction and (b) synthesis of triazoles from anilines (from Salam et al. [13]).

the synthesis of triazoles from anilines by one-pot two-step click reaction in water medium at room temperature (**Scheme 3(b)**). The excellent catalytic activity is due to the synergistic effect of GO. In fact, GO has high adsorption nature toward reactants through p-p stacking interactions. Hence, the GO could help the reactant to go closer to the Ag nanoparticles on GO, leading to good contact between the reactant and Ag on GO. In addition, electron transfer from the GO to Ag nanoparticles increases the local electron concentration, facilitating the uptake of electrons by reactant molecules [13].

The catalytic conversion of nitrophenols to valuable aminophenols in water by using $NaBH_4$ is one of the important organic conversions [47]. In general, the nitrophenols are the major organic pollutants, which can be found in industrial and agricultural wastewaters. They are highly water soluble and stable in the soil and thus cause harmful effects to human beings, animals, and agricultural plants [48]. Very recently, a simple and efficient method for the reduction of nitrophenols to aminophenols was developed by using carbon nanocomposites as a catalyst. The catalytic products (aminophenols) can be used as anticorrosion-lubricant, corrosion inhibitor, photographic developer, and analgesic and antipyretic drugs [49]. Ag nanoparticles supported carbon nanofiber composites (CNFs/AgNPs) were fabricated for the reduction of 4-nitrophenol with $NaBH_4$ in water [50]. The TEM images confirmed that very fine Ag nanoparticles were homogenously dispersed on the CNFs (**Figure 5**). The results showed an excellent catalytic activity of CNFs/AgNPs in the reduction of 4-nitrophenol. The reason for the superior catalytic activity of CNFs/AgNPs is mainly due to the high surface areas and synergistic effect on delivery of electrons between CNFs and Ag nanoparticles. Notably, the CNFs catalyst could be easily recycled at least for three times without loss in its activity. Possible catalytic mechanism is elucidated schematically in **Figure 5(e)**. Similarly, Wang et al. [51] found that Au nanoparticles supported functionalized CNTs [with cyclotriphosphazene-containing polyphosphazenes (PZS)] (Au@PZS@CNTs nanohybrids) are highly suitable catalyst for the reduction of 4-nitrophenol.

Among noble metals, Ru has shown the ability to catalyze a remarkable range of organic transformations because of its wide range of oxidation states (−2 to +8) and tunable properties [52]. The Ru metal is well known for oxidation-reduction and cross-coupling reactions. The catalytic products are high-functional components in the perfume industry and pharmaceuticals.

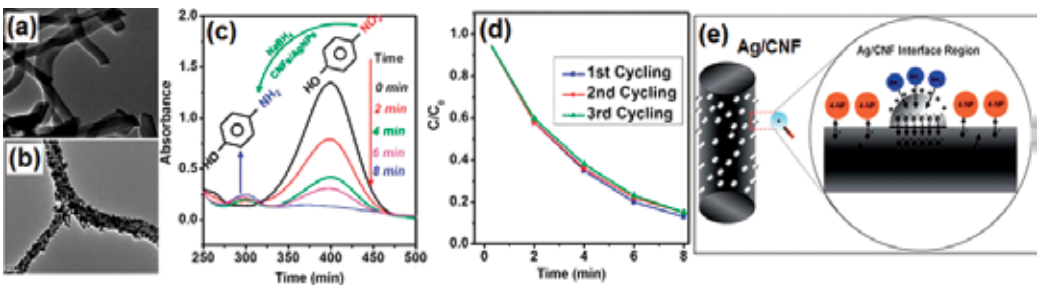

Figure 5. (a and b) TEM images of CNFs/AgNPs, (c) UV-vis absorption spectra during the catalytic reduction of 4-NP over CNFs/AgNPs, (d) reusability test, and (e) postulate mechanism of the catalytic reduction of 4-NP with the CNFs/AgNPs (from Zhang et al. [50]).

So far, several Ru nanoparticles supported CNTs or GO catalyst are developed for the organic transformations [53, 54]. Kim's group prepared various Ru or RuO_2 nanoparticles supported carbon nanocomposites and used as heterogeneous catalysts in organic transformation [29, 31–33]. For example, 0.5–3 nm size of metallic Ru nanoparticles decorated graphene nanosheets (GNSs) was used for the oxidation of alcohols [29]. Results revealed that various alcohols (aliphatic, aromatic, alicyclic, benzylic, allylic, amino, and heterocyclic alcohols) can be oxidized into their corresponding carbonyl compounds in good to excellent yields with high selectivity (**Scheme 4**). Very interestingly, a 0.036 mol% Ru (5 mg) of catalyst (GNS-RuNPs) was more than enough for complete oxidation of alcohols (the lowest amount of catalyst so far reported), which shows the merit of the GNS support. The formation of active Ru-oxo species during the reaction was confirmed. The GNS-RuNPs was found to be highly efficient, chemoselective, heterogeneous, stable, and reusable. The GNS-RuNPs catalyst was reused for four times without significant loss in its catalytic activity. After 4th cycle, the used GNS-RuNPs were calcinated at high temperature and used for transfer hydrogenation of carbonyl compounds. It was concluded that the excellent catalytic activity of GNS-RuNPs is due to the smaller size of the Ru nanoparticles, higher surface area, strong interaction between Ru nanoparticles and GNSs, and an effective dispersion of the catalyst in the reaction medium. Similarly, RuO_2NPs/MWCNTs [31] and RuO_2NRs/GNPs [55] were prepared and used for both aerial oxidation of alcohols and transfer hydrogenation of carbonyl compounds. Aliphatic and aromatic tert-amine oxides (amine N-oxides) are essential and key components in the formulation of several cosmetic products as well as in biomedical applications. The GNPs-RuO_2NPs demonstrated excellent catalytic activity toward oxidation of tertiary amines to their corresponding N-oxides in good to excellent yields [32]. The results showed that the scope of the reaction can be extended to various aliphatic, alicyclic, and aromatic tertiary amines.

Imines are very important moieties for the formation of fine chemicals, biologically active compounds, and their intermediates [56]. Interconnected ruthenium dioxide nanoparticles (RuO_2NPs) anchored graphite oxide nanocatalyst (RuO_2/GO) with good BET surface area (285 m^2/g) were prepared and used as a catalyst for the synthesis of imines (**Scheme 5**) [21]. Generally, the graphene-based nanocomposites are often suffered from the lower BET surface area due to the face-to-face aggregation of graphene sheets. However, in case of RuO_2/GO, the interconnected RuO_2 network strongly prevented the further aggregation of GO, leading to the high-specific surface area of RuO_2/GO. It was noticed that a broad range of

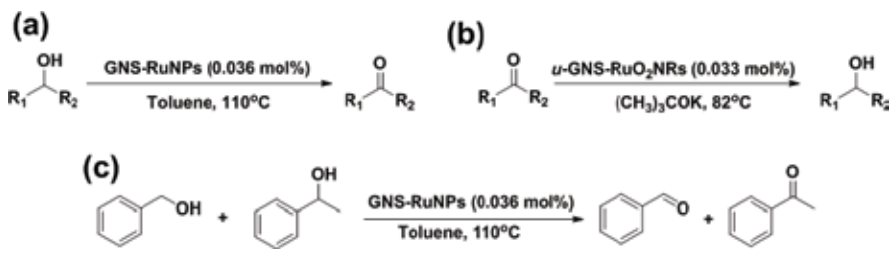

Scheme 4. Ru-graphene catalyzed (a) oxidation of alcohols, (b) transfer hydrogenation of carbonyl compounds, and (c) chemoselectivity oxidation of alcohols (from Gopiraman et al. [29]).

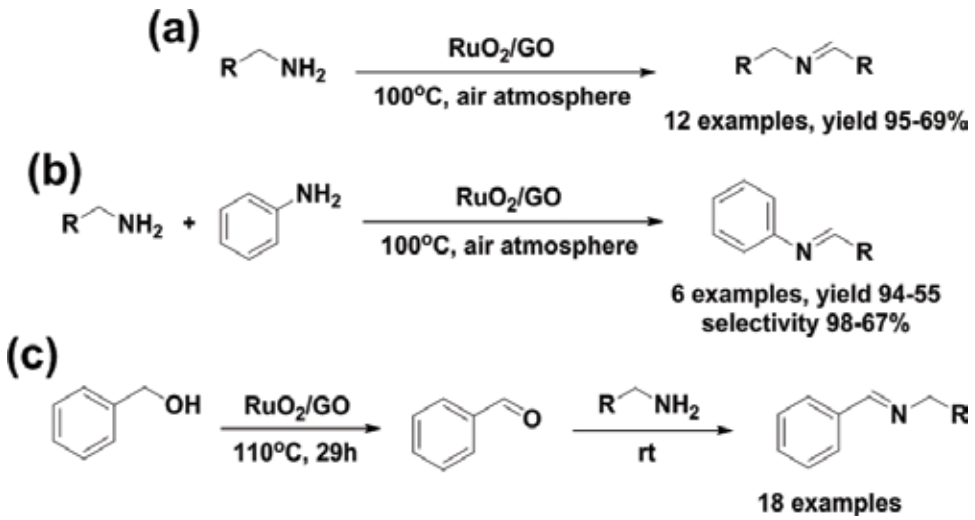

Scheme 5. RuO_2/GO catalyzed (a) self-coupling of amines, (b) cross coupling of aniline with substituted primary amines, and (c) oxidative coupling of benzyl alcohol and substituted primary amines (from Yuan et al. [21]).

amines including less reactive aliphatic amines can be transformed by the RuO_2/GO to obtain the corresponding imines in good yields (98–58%) with an excellent selectivity (100%). In addition, an indirect two-step protocol was adopted for the coupling of alcohols and amines to obtain imines, and the results were found to be excellent. The reusability, stability, and heterogeneity of RuO_2/GO were also investigated. The authors claimed that this is the most efficient RuO_2-based nanocatalyst for the synthesis of imines among those reported to date. Similarly, ultrafine RuO_2 nanoparticles (RuO_2NPs) with 0.9 nm in size were immobilized on SWCNTs by a straightforward "dry synthesis" method and used it for Heck olefination of aryl halides (**Scheme 6**) [33]. Although Ru has showed good catalytic activity toward Heck reaction, the bromo- and chloroarenes are less reactive. Interestingly, the SWCNTs supported RuO_2 catalyst worked well for the olefination of less reactive chloro- and bromoarenes. In case of supported heterogeneous catalysts, the activity is dependent on the nature of the support, metal-support interaction, and the particle size. It was believed that the inert SWCNTs might be transformed to a very active catalyst through the strong interactions between RuO_2 and carbon vacancies.

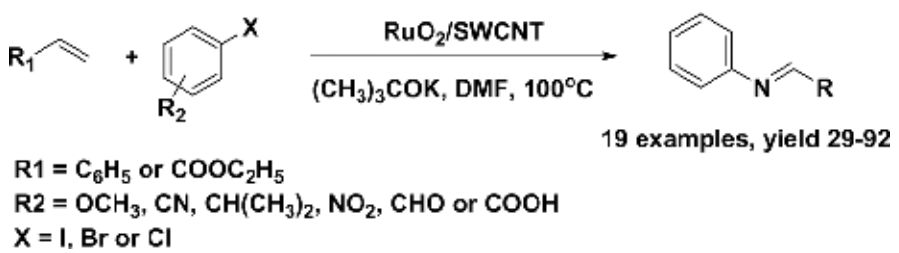

Scheme 6. RuO_2/SWCNT catalyzed Heck type olefination of aryl halides (from Gopiraman et al. [33]).

3.2. Non-noble metal supported carbon nanocomposites

Due to less cost, high activity, and less toxic nature, non-noble (Ni, Cu, Fe, Al, V, Ce, and Mn) nanoparticles are extensively employed studied as efficient catalysts for the organic transformations [57]. Particularly, Ni, Cu, and Fe nanoparticles have been widely studied for the organic conversion. Formamides are valuable intermediates in the synthesis of pharmaceutically important compounds [58]. Fakhri et al. [59] prepared Cu nanoparticles supported GO catalyst (rGO/CuNPs), and it was used for the synthesis of formamides and primary amines (**Scheme 7**). It was demonstrated that the rGO/CuNPs are highly efficient and reusable. Similarly, highly sustainable and versatile carbon nanocomposite CuO/GNS was prepared and used as catalysts for base-free coupling reactions (**Scheme 8**) [24]. Under very mild reaction conditions (CuO/GNS 0.7 mol%, acetonitrile 5 mL, air atmosphere, 3.5–12 h, 82°C), the CuO/GNS demonstrated outstanding catalytic activity in terms of yield (52–98%) and TON/TOF under base-free reaction conditions. A wide range of aromatic aldehydes, amines, and alkynes were employed to extend the scope of the catalytic system. In addition to the heterogeneous, stable, and reusable nature, the versatility of CuO/GNS was realized from the higher yield in aza-Michael reaction (**Scheme 7(b)**). After use, the GNS and CuO NPs (as $CuCl_2$) were successfully recovered from the u-CuO/GNS (**Figure 6**). The recovered GNS and $CuCl_2$ can be used for other applications. Recently, a highly efficient and cost-effective CuO/carbon-nanoparticle catalyst (CuO/CNP) was prepared by a simple "mix-and-heat" method and used for the self-coupling of amines [24]. The CuO/CNP demonstrated excellent catalytic activity toward the synthesis of imines under optimal reaction conditions involving 12 h of reaction time, 25 mg of catalyst, air atmosphere, and 110°C. A wide range of amines (aromatic, aliphatic, alicyclic, and heterocyclic amines) were efficiently catalyzed by CuO/GNS. Heterogeneity, stability, and reusability of CuO/CNP were found to be excellent.

Nitrogen-containing heterocycles including imidazole and its derivatives are prevalent structural motifs in various fields such as biological, pharmaceutical, and material sciences [60]. They are highly efficient antibacterial, antimalarial, antiviral, antimycobacterial, and antifungal compounds. Gopiraman and coworkers [30] have prepared highly efficient and reusable CuO/MWCNT catalyst for N-arylation of imidazole (**Scheme 9**). It was found that a 0.98 mol% (5 mg) of the CuO/MWCNT was sufficient for the efficient N-arylation of imidazole. The results

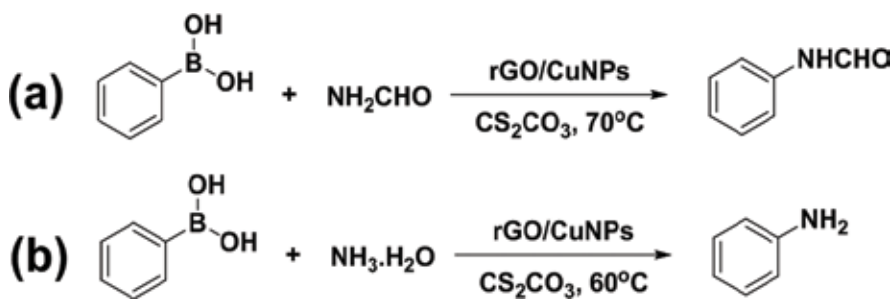

Scheme 7. rGO/Cu NPs catalyzed (a) formylation of different arylboronic acids and (b) amination of different arylboronic acids (from Fakhri et al. [59]).

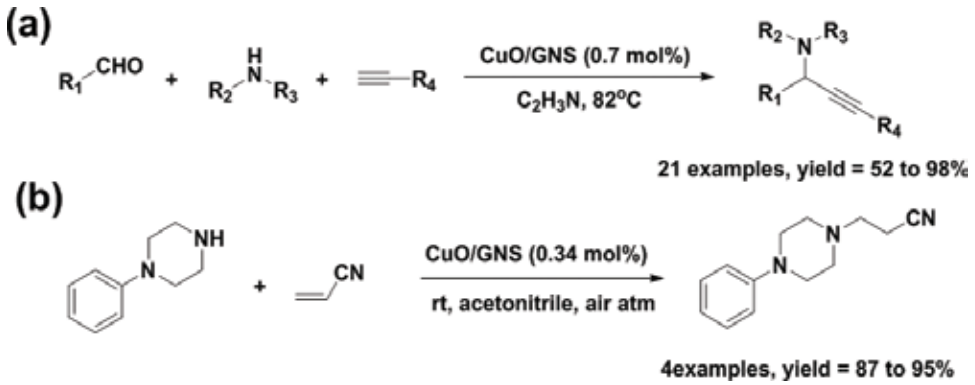

Scheme 8. CuO/GNS catalyzed (a) three-component coupling of aldehyde, amine, and alkynea and (b) aza-Michael reaction of amines with acrylonitrile (from Gopiraman et al. [24]).

showed that this is the smallest amount of catalyst used for N-arylation of imidazole reported to date. Chemical and physical stability, heterogeneity, and reusability of CuO/MWCNT were found to be excellent. After 4th cycle, MWCNTs were successfully separated from the used CuO/MWCNT, and it was confirmed. Based on the results obtained, it was concluded that the good catalytic activity of CuO/MWCNT is due to high surface area and effective dispersion of the CuO/MWCNT in the reaction medium.

Formic acid is often produced from biomass cellulose as well as from fats and oils. This simple acid can be used for storage of hydrogen for different applications [61]. Several metal catalysts including Pt and Cu were employed to decompose formic acid [62]. However, the stability and reusability of the catalysts are limited because the sintering of Cu leads to deactivation in catalytic reactions. Bulushev et al. [63] Cu nanoparticles supported N-doped expanded graphite oxide for the decomposition of formic acid. They showed that the problem of sintering of Cu leaching could be resolved by N-doping of the carbon support. The N-doping leads to a strong interaction of the Cu species with the support by pyridinic nitrogen atoms present in the carbon support. The results showed that the N-doped Cu catalyst has good stability in the formic acid decomposition even at 478 K for at least 7 h on-stream and a significantly higher catalytic activity.

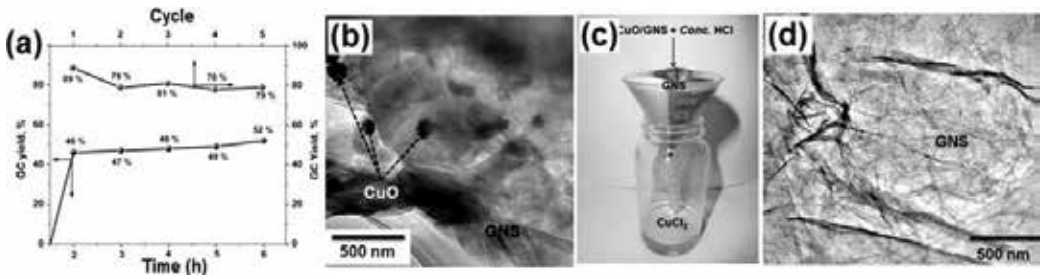

Figure 6. (a) Reusability and heterogeneity tests of CuO/GNS, (b) TEM images of used CuO/GNS, (c) photographic image showing the recovery of GNS and $CuCl_2$ from used CuO/GNS, and (d) TEM images of recovered GNS (from Gopiraman et al. [24]).

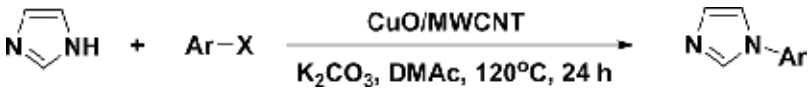

Scheme 9. CuO/MWCNT catalyzed N-arylation of imidazole with various aryl halides (from Gopiraman et al. [30]).

Kamal et al. [64] prepared GO-based nanocomposite (CuO@GO), and it was utilized for ligand-free and solvent-free C—N and C—S cross-coupling reactions with weak bases such as triethylamine (**Scheme 10**). They found that the CuO@GO is a simple and efficient catalyst for solvent- and ligand-free C—S cross-coupling reactions in the presence of weak bases and relatively mild reaction conditions by using the CuO@GO catalytic system. In addition, the CuO@GO was readily separated by centrifugation and could be reused six times under the solvent-free conditions with only a marginal loss of catalytic activity. Catalytic conversion of biomass-derived acids to valuable products is an important process in various chemical industries. Similarly, Ni nanoparticles supported reduced graphene oxide (Ni/RGO) was prepared and used as a heterogeneous catalyst for the C—S cross-coupling reaction between aryl halides and thiols (**Scheme 11**) [65]. They found that the catalytic performance is mainly dependent on the sizes of the Ni nanoparticles. Moreover, the electron-rich planar surface of RGO helps in stabilizing the nanoparticles and prevents agglomeration.

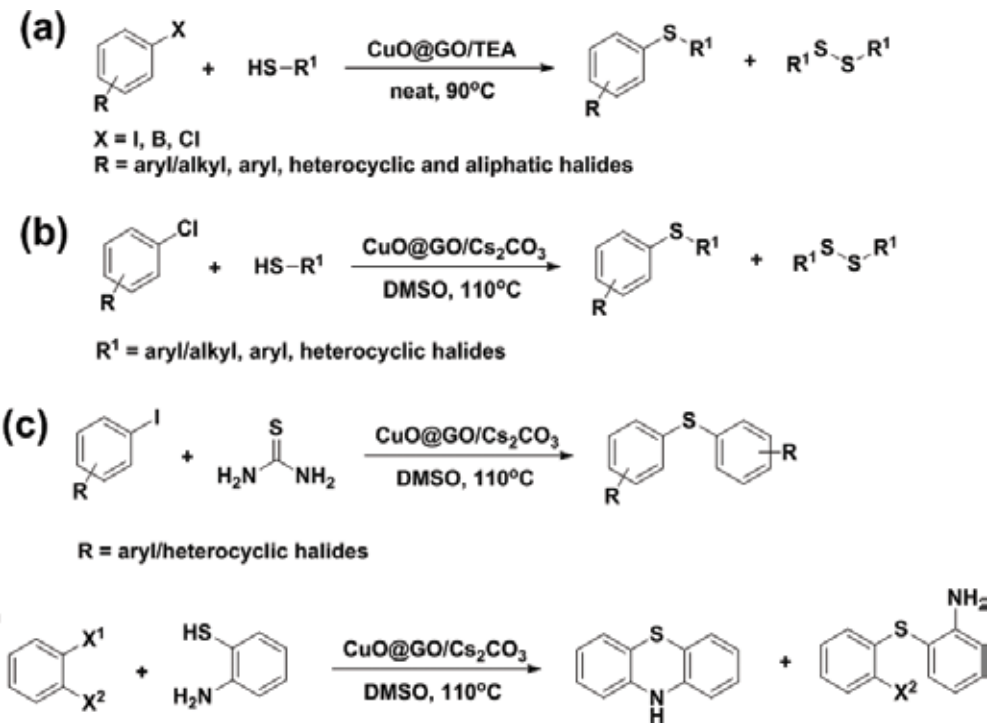

Scheme 10. CuO@GO catalyzed (a) S-arylation of various thiols with different aryl halides, (b) S-arylation of various thiols with different aryl chlorides, (c) reactions of various iodobenzenes with thiourea, and (d) cascade C—S and C—N cross coupling of aryl ortho-dihalides and ortho-aminobenzenethiols (from Kamal et al. [64]).

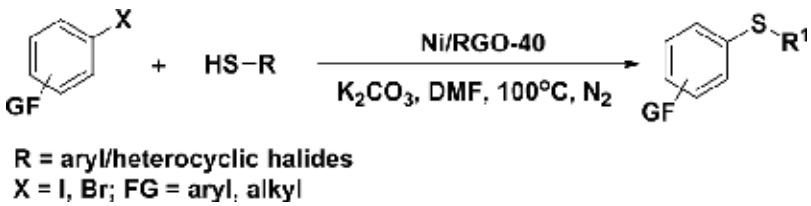

Scheme 11. Ni/RGO-40 catalyzed C—S cross coupling between aryl halide and thiol (from Sengupta et al. [65]).

Very recently, carbon black (CB) supported Ni catalyst (Ni/CB) has been prepared by a facile method using $NiCl_2$ as the nickel source and hydrazine hydrate as the reducing agent [66]. The Ni/CB catalyst showed excellent activity toward hydrogenation of nitrophenols in water at room temperature. Results showed that the synergistic effect of nano-Ni and carbon black, the presence of oxygen functional groups on carbon black for anchoring Ni atoms, strong adsorption ability for organic molecules, and good conductivity for electron transfer from the carbon black to Ni nanoparticles are the main reason of the superior catalytic activity of the Ni/CB. Moreover, the Ni/CB catalyst is not only cheap but also magnetically separable, and therefore, this approach facilitates achieving the cost-effective reduction of nitrophenols to aminophenols. Similarly, Saravanamoorthy et al. [67] prepared highly efficient and cost-effective NiO-based carbon nanocomposite (NiO/CNP) by a simple "mix-and-heat" method. The NiO/CNP exhibited that high-rate constant (k_{app}) values of 4.2×10^{-2} s^{-1} and 3.06×10^{-2} s^{-1} were calculated for the reduction of 4- and 2-nitrophenols. Interestingly, the catalyst worked well for the transfer hydrogenation of carbonyl compounds under mild reaction conditions (5 mg of NiO/CNP, 9 h of reaction time, 2 mmol of NaOH, air atmosphere, and room temperature). It was found that the NiO/CNP composite is chemoselectivity and heterogeneous in nature, stable, and reusable.

Nitrogen-doped carbon materials are found to be highly efficient support for metal nanoparticles [68]. In fact, the N-dopants in the carbon matrix act as efficient anchoring sites or defects for enhancing the nanoparticle nucleation and reducing the nanoparticle size [69]. Interestingly, the N-dopants can modify the electronic structure of the carbon matrix and tune the activity of the sp^2 carbon and metal nanoparticles, thus promoting the higher catalytic activity. In addition, the hydrophilicity and basicity of carbon supports can be improved by N-doping; therefore, the N-doped carbon materials could be effectively used to prepare catalysts in the aqueous phase. However, the recent studies on the N-doped carbon supports are mainly focused on noble metals. Very recently, Nie et al. [70] prepared porous N-doped carbon black supported Ni catalyst (Ni/NCB) by a simple chemical method. The prepared Ni/NCB catalyst showed high performance in the hydrogenation of vanillin (4-hydroxy-3-methoxybenzaldehyde) to 2-methoxy-4-methylphenol under mild conditions at low hydrogen pressure (0.5 MPa) and mild temperature (<150°C), which is significantly superior to other frequently used Ni catalysts. The nanostructure of Ni/NCB, intimate interaction between the Ni nanoparticles and the N species, and lower oxidation state are the main reason for higher catalytic activity of Ni/NCB. Moreover, the Ni/NCB catalyst is cost-effective and easily separable.

The Fe_3O_4 nanoparticles have played a crucial role as a heterogeneous catalyst due to its environmentally benign, high catalytic activity, good magnetic separation performance, and

high chemical stability [71]. Huo et al. [72] prepared graphene-Fe_3O_4 nanocomposite for the A^3 coupling of aldehydes, alkynes, and amines (**Scheme 12**). The catalytic system produced a diverse range of propargylamines in a moderate to high yield under mild conditions. Interestingly, this catalyst could be reused up to eight times with essentially no loss of activity. Moreover, the separation and reuse of graphene-Fe_3O_4 were very simple, effective, and economical. Similarly, Stein and coworkers [58] prepared Fe nanoparticles supported GO for the preparation of hydrogenation of different olefins and alkynes with H_2.

3.3. Bimetallic carbon nanocomposites

Bimetallic alloy nanoparticles show an enhancement in the catalytic properties owing to the synergistic effects between the two or more distinct metals [73]. In particular, carbon materials supported bi- or multi-metallic nanocomposites are often show dramatic change in the catalytic activity when compared with the mono metallic carbon supported catalysts. Babu et al. [17] prepared bimetallic Au-Ag nanoparticles supported single-layer graphene (SLG) nanocomposites (Au-Ag/SLG) for the hydroarylation, C-arylation, and hydrophenoxylation reactions under mild and ligand-free conditions (**Scheme 13**). They found that the catalytic activity of the Au-Ag/SLG found to be better than the mixture of monometallic nanocatalysts (Au/SLG and Ag/SLG). Interestingly, more than twofold synergy was obtained by this bimetallic nanocatalyst (Au-Ag/SLG). Usage of meager amount of precious metals (0.09 mol% of Au and 0.22 mol% of Ag) and very good reusability made this catalytic system economically feasible. Similarly, Lv and coworkers [74] prepared porous Pt-Au nanodendrites supported on reduced graphene oxide nanosheets (Pt-Au pNDs/RGOs) for the reduction of 4-nitrophenol. They found that the Pt-Au pNDs/RGOs exhibited significantly enhanced catalytic performance toward the reduction of 4-nitrophenol, as compared to commercial Pt black and home-made Au nanocrystals. The reason for the enhancement in the catalytic activity of the Pt-Au pNDs/RGOs is due to its unique interconnected nanostructures of Pt-Au pNDs, which provide more available active sites and the improved mass transport by using RGOs as a support, along with the synergistic effects between Pt and Au.

Aryl-substituted alkynes are versatile intermediates in the formation of various agrochemicals, medicines, and functional organic molecules [75]. Sonogashira cross-coupling reaction of terminal alkynes with aryl halides is one of the most efficient routes for the construction of substituted aryl alkynes. Supported Pd-Cu catalyst has been found to be highly efficient for the Sonogashira cross-coupling reaction in good yield. Diyarbakir et al. [76] prepared Cu-Pd alloy nanoparticles immobilized GO catalyst (rGO-CuPd) for the Sonogashira cross-coupling reactions of various aryl halides with phenylacetylene (**Scheme 14**). The rGO-CuPd catalyst worked well for both electron-rich and electron deficient aryl iodides and aryl bromides,

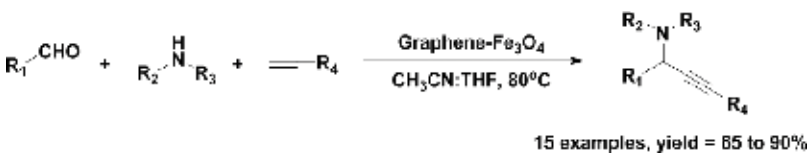

Scheme 12. Graphene-Fe_3O_4 nanocomposite catalyzed A^3 coupling of aldehydes, alkynes, and amines (from Huo et al. [72]).

affording the targeted biaryl products in high yields. They concluded that the rGO-CuPd catalytic system has obvious advantages such as recyclable, easy to operate, and environmentally friendly over the conventional Sonogashira couplings. Goksu et al. [77] developed bimetallic Ni-Pd nanoparticles supported GO catalytic system for the tandem dehydrogenation of ammonia borane and hydrogenation of nitro/nitrile compounds (**Scheme 15**). They found that the G-NiPd catalyst is highly active and reusable. Moreover, the reaction can be performed in an environmentally friendly process with short-reaction times and high yields.

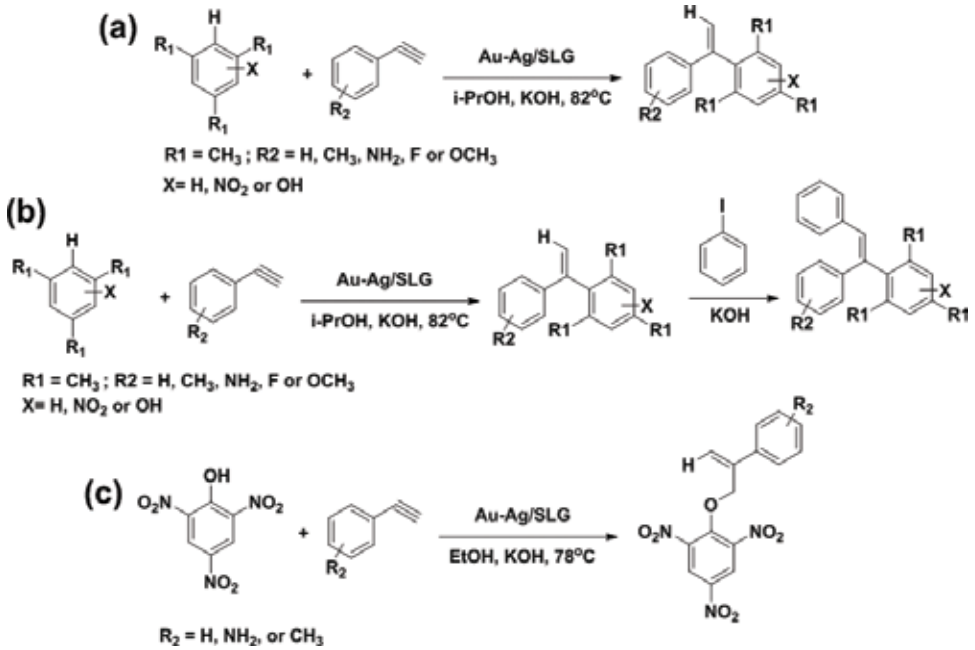

Scheme 13. Au-Ag/SLG catalyzed (a) hydroarylation of alkynes with arenes, (b) direct arylation of 1,1-diphenylethylenes with iodobenzene, and (c) hydrophenoxylation of alkynes with substituted phenols (from Babu et al. [17]).

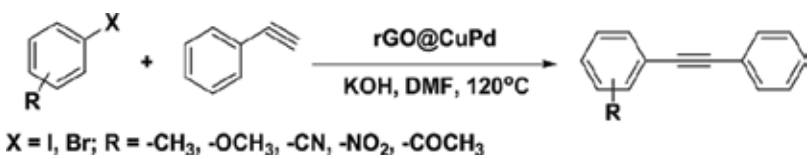

Scheme 14. rGO-CuPd catalyzed Sonogashira couplings of various aryl halides and phenyl acetylene (from Diyarbakir et al. [76]).

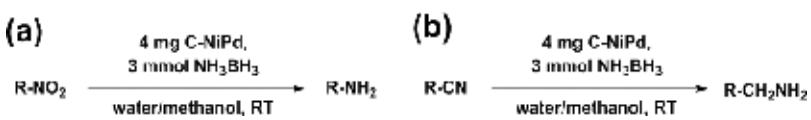

Scheme 15. G-NiPd catalyzed tandem reaction of (a) various R-NO_2 compounds and (b) nitrile and/or nitro compounds (from Goksu et al. [77]).

4. Conclusion

In recent days, the metal nanoparticles supported carbon nanocomposites are found to play a significant role in a wide range of potential applications. Due to unique properties including high surface area, the carbon nanocomposites are often used as an efficient heterogeneous catalyst for industrially important organic reactions. In order to achieve carbon nanocomposites with excellent physicochemical properties, several methods have been developed so far. In this chapter, we have summarized the recent progress in the research on the preparation methods of carbon nanocomposites (mainly, graphene or graphene oxide and CNTs) and its uses in organic reactions.

Author details

Mayakrishnan Gopiraman[1] and Ick Soo Kim[2]*

*Address all correspondence to: kimicksoo@hotmail.com

1 Department of Applied Bioscience, College of Life and Environmental Science, Konkuk University, Seoul, South Korea

2 Nano Fusion Technology Research Group, Division of Frontier Fibers, Institute for Fiber Engineering (IFES), Interdisciplinary Cluster for Cutting Edge Research (ICCER), Shinshu University, Ueda, Nagano Prefecture, Japan

References

[1] Allen MJ, Tung VC, Kaner RB. Honeycomb carbon: A review of graphene. Chemical Reviews. 2010;**110**:132-145. DOI: 10.1021/cr900070d

[2] Vairavapandian D, Vichchulada P, Lay MD. Preparation and modification of carbon nanotubes: Review of recent advances and applications in catalysis and sensing. Analytica Chimica Acta. 2008;**626**:119-129. DOI: 10.1016/j.aca.2008.07.052

[3] Bohua W, Yinjie K, Xiaohua Z, Jinhua C. Noble metal nanoparticles/carbon nanotubes nanohybrids: Synthesis and applications. Nanotoday. 2011;**6**:75-90. DOI: 10.1016/j.nantod.2010.12.008

[4] Zhen-Bo W, Peng-Jian Z, Guang-Jin W, Chun-Yu D, Ge-Ping Y. Effect of Ni on PtRu/C catalyst performance for ethanol electrooxidation in acidic medium. The Journal of Physical Chemistry C. 2008;**112**:6582-6587. DOI: 10.1021/jp800249q

[5] Julkapli NM, Bagheri S. Graphene supported heterogeneous catalysts: An overview. International Journal of Hydrogen Energy. 2015;**40**:948-979

[6] Qin YL, Wang J, Meng FZ, Wang LM, Zhang XB. Efficient PdNi and PdNi@ Pd-catalyzed hydrogen generation via formic acid decomposition at room temperature. Chemical Communications. 2013;**49**:10028-10030. DOI: 10.1039/C3CC46248J

[7] Joo SH, Park JY, Renzas JR, Butcher DR, Huang WY, Somorjai GA. Size effect of ruthenium nanoparticles in catalytic carbon monoxide oxidation. Nano Letters. 2010;**10**:2709-2713. DOI: 10.1021/nl101700j

[8] Krasheninnikov AV, Lehtinen PO, Foster AS, Pyykko P, Nieminen RM. Embedding transition-metal atoms in graphene: Structure, bonding, and magnetism. Physical Review Letters. 2009;**102**:126807. DOI: 10.1103/PhysRevLett.102.126807

[9] Beletskaya IP, Cheprakov AV. The Heck reaction as a sharpening stone of palladium catalysis. Chemical Reviews. 2000;**100**:3009-3066. DOI: 10.1021/cr9903048

[10] Deng D, Xiao L, Chung IM, Kim IS, Gopiraman M. Industrial-quality graphene oxide switched highly efficient metal- and solvent-free synthesis of β-ketoenamines under feasible conditions. ACS Sustainable Chemistry & Engineering. 2017;**5**:1253-1259. DOI: 10.1021/acssuschemeng.6b02766

[11] Sanjib B, Lawrence TD. A novel approach to create a highly ordered monolayer film of graphene nanosheets at the liquid–liquid interface. Nano Letters. 2009;**9**:167-172. DOI: 10.1021/nl802724f

[12] Georgakilas V, Otyepka M, Bourlinos AB, Chandra V, Kim N, Kemp KC, et al. Functionalization of graphene: Covalent and non-covalent approaches, derivatives and applications. Chemical Reviews. 2012;**112**:6156-6214. DOI: 10.1021/cr3000412

[13] Salam N, Sinha A, Roy AS, Mondal P, Jana NR, Manirul Islam SK. Synthesis of silver–graphene nanocomposite and its catalytic application for the one-pot three-component coupling reaction and one-pot synthesis of 1,4-disubstituted 1,2,3-triazoles in water. RSC Adv. 2014;**4**:10001-10012. DOI: 10.1039/C3RA47466F

[14] Meng Y, Yan X, Wang Y. A simple preparation of Ag@graphene nanocomposites for surface-enhanced Raman spectroscopy of fluorescent anticancer drug. Chemical Physics Letters. 2016;**651**:84-87. DOI: 10.1016/j.cplett.2016.03.023

[15] Bozkurt PA. Sonochemical green synthesis of Ag/graphene nanocomposite. Ultrasonics Sonochemistry. 2017;**35**:397-404. DOI: 10.1016/j.ultsonch.2016.10.018

[16] Peng L, Zhang J, Yang S, Han B, Sang X, Liu C, et al. Ultra-small gold nanoparticles immobilized on mesoporous silica/graphene oxide as highly active and stable heterogeneous catalysts. Chemical Communications. 2015;**51**:4398-4401. DOI: 10.1039/C4CC09131K

[17] Babu SG, Gopiraman M, Deng D, Wei K, Karvembu R, Kim IS. Robust Au–Ag/graphene bimetallic nanocatalyst for multifunctional activity with high synergism. Chemical Engineering Journal. 2016;**300**:146-159. DOI: 10.1016/j.cej.2016.04.101

[18] Daoush WM, Imae T. Fabrication of PtNi bimetallic nanoparticles supported on multi-walled carbon nanotubes. Journal of Experimental Nanoscience. 2015;**10**:392-406. DOI: 10.1080/17458080.2013.838703

[19] Zhang YY, QF YI, Chu H, Nie HD. Catalytic activity of Pd-Ag nanoparticles supported on carbon nanotubes for the electro-oxidation of ethanol and propanol. Journal of Fuel Chemistry and Technology. 2017;**45**(17):475, 30026-483, 30029. DOI: 10.1016/S1872-5813

[20] Naota T, Takaya H, Murahashi SI. Ruthenium-catalyzed reactions for organic synthesis. Chemical Reviews. 1998;**98**:2599-2660. DOI: 10.1021/cr9403695

[21] Yuan G, Gopiraman M, Cha HJ, Soo HD, Chung IM, Kim IS. Interconnected ruthenium dioxide nanoparticles anchored on graphite oxide: Highly efficient candidate for solvent-free oxidative synthesis of imines. Journal of Industrial and Engineering Chemistry. 2017;**46**:279-288. DOI: 10.1016/j.jiec.2016.10.040

[22] Wang P, Zhang G, Jiao H, Liu L, Deng X, Chen Y, et al. Pd/graphene nanocomposite as highly active catalyst for the Heck reactions. Applied Catalysis A: General. 2015;**489**: 188-192. DOI: 10.1016/j.apcata.2014.10.044

[23] Sun T, Zhang Z, Xiao J, Chen C, Xiao F, Wang S, et al. Facile and green synthesis of palladium nanoparticles-graphene-carbon nanotube material with high catalytic activity. Scientific Reports. 2013;**3**:2527. DOI: 10.1038/srep02527

[24] Gopiraman M, Deng D, Babu SG, Hayashi T, Karvembu R, Kim IS. Sustainable and versatile CuO/GNS nanocatalyst for highly efficient base free coupling reactions. ACS Sustainable Chemical Engineering. 2015;**3**:2478-2488. DOI: 10.1021/acssuschemeng.5b00542

[25] Tien HW, Huang YL, Yang SY, Wang JY, Ma CCM. The production of graphene nanosheets decorated with silver nanoparticles for use in transparent, conductive films. Carbon. 2011;**49**:1550-1560. DOI: 10.1016/j.carbon.2010.12.022

[26] Akhavan O. The effect of heat treatment on formation of graphene thin films from graphene oxide nanosheets. Carbon. 2010;**48**:509-519. DOI: 10.1016/j.carbon.2009.09.069

[27] Lin Y, Watson KA, Fallbach MJ, Ghose S, Smith JG, Delozier MD, et al. Rapid, solventless, bulk preparation of metal nanoparticle-decorated carbon nanotubes. ACS Nano. 2009;**3**:871-884. DOI: 10.1021/nn8009097

[28] Lin Y, Watson KA, Ghose S, Smith JG, Williams TV, Crooks RE, et al. Direct mechanochemical formation of metal nanoparticles on carbon nanotubes. The Journal of Physical Chemistry C. 2009;**113**:14858-14862. DOI: 10.1021/jp905076u

[29] Gopiraman M, Babu SG, Khatri Z, Kai W, Kim YA, Endo M, et al. Dry synthesis of easily tunable nano ruthenium supported on graphene: Novel nanocatalysts for aerial oxidation of alcohols and transfer hydrogenation of ketones. The Journal of Physical Chemistry C. 2013;**117**:23582-23596. DOI: 10.1021/jp402978q

[30] Gopiraman M, Babu SG, Khatri Z, Kai W, Kim YA, Endo M, et al. An efficient, reusable copper-oxide/carbon-nanotube catalyst for N-arylation of imidazole. Carbon. 2013;**62**: 135-148. DOI: 10.1016/j.carbon.2013.06.005

[31] Gopiraman M, Babu SG, Karvembu R, Kim IS. Nanostructured RuO_2 on MWCNTs: Efficient catalyst for transfer hydrogenation of carbonyl compounds and aerial oxidation of alcohols. Applied Catalysis A: General. 2014;**484**:84-96. DOI: 10.1016/j.apcata.2014.06.032

[32] Gopiraman M, Bang H, Babu SG, Wei K, Karvembu R, Kim IS. Catalytic N-oxidation of tertiary amines on RuO_2 NPs anchored graphene nanoplatelets. Catalytic Science & Technology. 2014;**4**:2099-2106. DOI: 10.1039/C3CY00963G

[33] Gopiraman M, Karvembu R, Kim IS. Highly active, selective, and reusable RuO_2/SWCNT catalyst for Heck olefination of aryl halides. ACS Catalysis. 2014;**4**:2118-2129. DOI: 10.1021/cs500460m

[34] Clark JH. Solid acids for green chemistry. Accounts of Chemical Research. 2002;**35**: 791-797. DOI: 10.1021/ar010072a

[35] Baur JA, Sinclair DA. Therapeutic potential of resveratrol: The in vivo evidence. Nature Reviews Drug Discovery. 2006;**5**:493-506. DOI: 10.1038/nrd2060

[36] Machadoa BF, Serp P. Graphene-based materials for catalysis. Catalysis Science & Technology. 2012;**2**:54-75. DOI: 10.1039/C1CY00361E

[37] Blaser HU, Indolese A, Schnyder A, Steiner H, Studer M. Supported palladium catalysts for fine chemicals synthesis. Journal of Molecular Catalysis A: Chemical. 2001;**173**:3-18. DOI: 10.1016/S1381-1169(01)00143-1

[38] Kantam ML, Roy M, Roy S, Sreedhar B, Madhavendra SS, Choudary BM, et al. Polyaniline supported palladium catalyzed Suzuki–Miyaura cross-coupling of bromo-and chloroarenes in water. Tetrahedron. 2007;**63**:8002-8009. DOI: 10.1016/j.tet.2007.05.064

[39] Li Y, Fan X, Qi J, Ji J, Wang S, Zhang G, et al. Palladium nanoparticle-graphene hybrids as active catalysts for the Suzuki reaction. Nano Research. 2010;**3**:429-437. DOI: 10.1007/s12274-010-0002-z

[40] Deng D, Xiao L, Chung IM, Kim IS, Gopiraman M. Industrial-quality graphene oxide switched highly efficient metal-and solvent-free synthesis of β-ketoenamines under feasible conditions. ACS Sustainable Chemistry & Engineering. 2017;**5**:1253-1259. DOI: 10.1021/acssuschemeng.6b02766

[41] Elazab HA, Siamaki AR, Moussa S, Gupton BF, El-Shall MS. Highly efficient and magnetically recyclable graphene-supported Pd/Fe_3O_4 nanoparticle catalysts for Suzuki and Heck cross-coupling reactions. Applied Catalysis A: General. 2015;**491**:58-69. DOI: 10.1016/j.apcata.2014.11.033

[42] Hu J, Wang Y, Han M, Zhou Y, Jiang X, Sun P. A facile preparation of palladium nanoparticles supported on magnetite/s-graphene and their catalytic application in Suzuki–Miyaura reaction. Catalysis Science & Technology. 2012;**2**:2332-2340. DOI: 10.1039/C2CY20263H

[43] Sun J, Fu Y, He G, Sun X, Wang X. Green Suzuki–Miyaura coupling reaction catalyzed by palladium nanoparticles supported on graphitic carbon nitride. Applied Catalysis B: Environmental. 2015;**165**:661-667. DOI: 10.1016/j.apcatb.2014.10.072

[44] Siamaki AR, Lin Y, Woodberry K, Connell JW, Gupton BF. Palladium nanoparticles supported on carbon nanotubes from solventless preparations: versatile catalysts for ligand-free Suzuki cross coupling reactions. Journal of Materials Chemistry. 2013;**1**:12909-12918. DOI: 10.1039/C3TA12512B

[45] Mandel S, Weinreb O, Amit T, Youdim MBH. Brain Research Reviews. 2005;**48**:379-387. DOI: 10.1016/j.brainresrev.2004.12.027

[46] Binda C, Hubalek F, Li M, Herzig Y, Sterling J, Edmondson DE, et al. Crystal structures of monoamine oxidase B in complex with four inhibitors of the N-propargylaminoindan class. Journal of Medicinal Chemistry. 2004;**47**:1767-1774. DOI: 10.1021/jm031087c

[47] Zhao PX, Feng XW, Huang DS, Yang GY, Astruc D. Basic concepts and recent advances in nitrophenol reduction by gold-and other transition metal nanoparticles. Coordination Chemistry Reviews. 2015;**287**:114-136. DOI: 10.1016/j.ccr.2015.01.002

[48] Narayanan KB, Sakthivel N. Heterogeneous catalytic reduction of anthropogenic pollutant, 4-nitrophenol by silver-bionanocomposite using Cylindrocladium floridanum. Bioresource Technology. 2011;**102**:10737-10740. DOI: 10.1016/j.biortech.2011.08.103

[49] Chang YC, Chen DH. Catalytic reduction of 4-nitrophenol by magnetically recoverable Au nanocatalyst. Journal of Hazardous Materials. 2009;**165**:664-669. DOI: 10.1016/j.jhazmat.2008.10.034

[50] Zhang P, Shao C, Zhang Z, Zhang M, Mu J, Guo Z, et al. In situ assembly of well-dispersed Ag nanoparticles (AgNPs) on electrospun carbon nanofibers (CNFs) for catalytic reduction of 4-nitrophenol. Nanoscale. 2011;**3**:3357-3363. DOI: 10.1039/C1NR10405E

[51] Wang X, Fu J, Wang M, Wang Y, Chen Z, Zhang J, et al. Facile synthesis of Au nanoparticles supported on polyphosphazene functionalized carbon nanotubes for catalytic reduction of 4-nitrophenol. Journal of Materials Science. 2014;**49**:5056-5065. DOI: 10.1007/s10853-014-8212-5

[52] Sarmah PP, Dutta DK. Chemoselective reduction of a nitro group through transfer hydrogenation catalysed by Ru 0-nanoparticles stabilized on modified Montmorillonite clay. Green Chemistry. 2012;**14**:1086-1093. DOI: 10.1039/C2GC16441H

[53] Iqbal S, Kondrat SA, Jones DR, Schoenmakers DC, Edwards JK, Lu L, et al. Ruthenium nanoparticles supported on carbon: An active catalyst for the hydrogenation of lactic acid to 1, 2-propanediol. ACS Catalysis. 2015;**5**:5047-5059. DOI: 10.1021/acscatal.5b00625

[54] Guerrero-Ruiz A, Bachiller-Baeza B, Rodrıiguez-Ramos I. Catalytic properties of carbon-supported ruthenium catalysts for n-hexane conversion. Applied Catalysis A: General. 1998;**173**:231-238. DOI: 10.1016/S0926-860X(98)00181-1

[55] Gopiraman M, Babu SG, Khatri Z, Kai W, Kim YA, Endo M, et al. Facile and homogeneous decoration of RuO_2 nanorods on graphene nanoplatelets for transfer hydrogenation of carbonyl compounds. Catalysis Science & Technology. 2013;**3**:1485-1489. DOI: 10.1039/C3CY20735H

[56] Monopoli A, Cotugno P, Iannone F, Ciminale F, Dell-Anna MM, Mastrorilli P, et al. Ionic-liquid-assisted metal-free oxidative coupling of amines to give imines. European Journal of Organic Chemistry. 2014;**27**. DOI: 5925. DOI: 10.1002/ejoc.201402530

[57] Jiang L, Yao M, Liu B, Li Q, Liu R, Lv H, et al. Controlled synthesis of CeO_2/graphene nanocomposites with highly enhanced optical and catalytic properties. Journal of Physical Chemistry C. 2012;**116**:11741-11745. DOI: 10.1021/jp3015113

[58] Stein M, Wieland J, Steurer P, Tclle F, Mlhaupt R, Breit B. Iron nanoparticles supported on chemically-derived graphene: Catalytic hydrogenation with magnetic catalyst separation. Advanced Synthesis & Catalysis. 2011;**353**:523-527. DOI: 10.1002/adsc.201000877

[59] Fakhri P, Jaleh B, Nasrollahzadeh M. Synthesis and characterization of copper nanoparticles supported on reduced graphene oxide as a highly active and recyclable catalyst for the synthesis of formamides and primary amines. Journal of Molecular Catalysis A: Chemical. 2014;**383-384**:17-22. DOI: 10.1016/j.molcata.2013.10.027

[60] Catarzi D, Colotta V, Varano F, Calabri FR, Filacchioni G, Galli A, et al. Synthesis and Biological evaluation of analogues of 7-Chloro-4,5-dihydro-4- oxo-8-(1,2,4-triazol-4-yl)-1,2,4-triazolo[1,5-a]quinoxaline-2-carboxylic Acid (TQX-173) as novel selective AMPA receptor antagonists. Journal of Medicinal Chemistry. 2004;**47**:262-272. DOI: 10.1021/jm030906q

[61] Zacharska M, Bulusheva LG, Lisitsyn AS, Beloshapkin S, Guo Y, Chuvilin AL, et al. Factors influencing the performance of Pd/C catalysts in the green production of hydrogen from formic acid. ChemSusChem. 2017;**10**:720-730. DOI: 10.1002/cssc.201601637

[62] Grasemann M, Laurenczy G. Formic acid as a hydrogen source – recent developments and future trends. Energy & Environmental Science. 2012;**5**:8171-8181. DOI: 10.1039/C2EE21928J

[63] Bulushev DA, Chuvilin AL, Sobolev VI, Stolyarov SG, Shubin YV, Asanov IP, et al. Copper on carbon materials: Stabilization by nitrogen doping. Journal of Materials Chemistry A. 2017;**5**:10574-10583. DOI: 10.1039/C7TA02282D

[64] Kamal A, Srinivasulu V, Murty JNSRC, Shankaraiah N, Nagesh N, Reddy TS, et al. Copper oxide nanoparticles supported on graphene oxide-catalyzed S-arylation: An efficient and ligand-free synthesis of aryl sulfides. Advanced Synthesis & Catalysis. 2013;**355**:2297-2307. DOI: 10.1002/adsc.201300416

[65] Sengupta D, Bhowmik K, De G, Basu B. Ni nanoparticles on RGO as reusable heterogeneous catalyst: Effect of Ni particle size and intermediate composite structures in C–S cross-coupling reaction. Beilstein Journal of Organic Chemistry. 2017;**13**:1796-1806. DOI: 10.3762/bjoc.13.174

[66] Xia J, He G, Zhang L, Sun X, Wang X. Hydrogenation of nitrophenols catalyzed by carbon black-supported nickel nanoparticles under mild conditions. Applied Catalysis B: Environmental. 2016;**180**:408-415. DOI: 10.1016/j.apcatb.2015.06.043

[67] Saravanamoorthy S, Chung IM, Ramkumar V, Ramaganth B, Gopiraman M. Highly active and reducing agent-free preparation of cost-effective NiO-based carbon nanocomposite and its application in reduction reactions under mild conditions. Journal of Industrial and Engineering Chemistry. 2018;**60**:91-101. DOI: 10.1016/j.jiec.2017.10.006

[68] Deng Y, Xie Y, Zou K, Ji X. Review on recent advances in nitrogen-doped carbons: preparations and applications in supercapacitors. Journal of Materials Chemistry A. 2016;**4**:1144-1173. DOI: 10.1039/C5TA08620E

[69] Wang H, Maiyalagan T, Wang X. Review on recent progress in nitrogen-doped graphene: synthesis, characterization, and its potential applications. ACS Catalysis. 2012;**2**:781-794. DOI: 10.1021/cs200652y

[70] Nie R, Yang H, Zhang H, Yu X, Lu X, Zhou D, et al. Mild-temperature hydrodeoxygenation of vanillin over porous nitrogen-doped carbon black supported nickel nanoparticles. Green Chemistry. 2017;**19**:3126-3134. DOI: 10.1039/C7GC00531H

[71] Cho A, Byun S, Kim BM. AuPd–Fe_3O_4 Nanoparticle catalysts for highly selective, one-pot cascade nitro-reduction and reductive amination. Advanced Synthesis & Catalysis. 2018;**360**:1253-1261. DOI: 10.1002/adsc.201701462

[72] Huo X, Liu J, Wang B, Zhang H, Yang Z, She X, et al. A one-step method to produce graphene–Fe_3O_4 composites and their excellent catalytic activities for three-component coupling of aldehyde, alkyne and amine. Journal of Materials Chemistry A. 2013;**1**: 651-656. DOI: 10.1039/C2TA00485B

[73] Zhang S, Shao Y, Liao HG, Liu J, Aksay IA, Yin G, et al. Graphene decorated with PtAu alloy nanoparticles: facile synthesis and promising application for formic acid oxidation. Chemistry Materials. 2011;**23**:1079-1081. DOI: 10.1021/cm101568z

[74] Lv JJ, Wang AJ, Ma X, Xiang RY, Chen JR, Feng JJ. One-pot synthesis of porous Pt–Au nanodendrites supported on reduced graphene oxide nanosheets toward catalytic reduction of 4-nitrophenol. Journal of Materials Chemistry A. 2015;**3**:290-296. DOI: 10.1039/C4TA05034G

[75] Sonogashira K. Development of Pd–Cu catalyzed cross-coupling of terminal acetylenes with sp^2-carbon halides. Journal of Organometallic Chemistry. 2002;**653**:46-49. DOI: 10.1016/S0022-328X(02)01158-0

[76] Diyarbakir S, Can H, Metin O. Reduced graphene oxide-supported CuPd alloy nanoparticles as efficient catalysts for the sonogashira cross-coupling reactions. ACS Applied Materials & Interfaces. 2015;**7**:3199-3206. DOI: 10.1021/am507764u

[77] Goksu H, Ho SF, Metin O, Korkmaz K, Garcia AM, Gultekin MS, et al. Tandem dehydrogenation of ammonia borane and hydrogenation of nitro/nitrile compounds catalyzed by graphene-supported NiPd alloy nanoparticles. ACS Catalysis. 2014;**4**:1777-1782. DOI: 10.1021/cs500167k

Chapter 3

Polymer/Noble Metal Nanocomposites

Ahmed Gamal Abed El-Azim Khalil El-Shamy

Additional information is available at the end of the chapter

http://dx.doi.org/10.5772/intechopen.79016

Abstract

Recently, the polymeric materials have extensive uses because of their amazing combination of properties, durability, light weight and simplicity of processing. However, these materials face some problems like their weak thermal stability and also poor mechanical stability. Therefore, a large number of additives especially metal nanoparticles were added to polymeric matrix to overcome these problems and designed polymer matrix nanocomposite. A composite is defined as the combination between two individuals or more than one material by physical or mechanical method to get a new material with unique and elegant structure and properties and carrying the feature of the two separated materials and distinguishable interface. Many approaches are used to prepare the polymer nanocomposites such as ex situ, in situ and radiolytic methods. The nanocomposites have important features such as excellent mechanical properties like high stiffness, strength, toughness; good chemical properties like corrosion resistance; and high physical properties like high optical, mechanical, thermal, low density and specific antibacterial properties. The nanocomposite materials with these higher properties have a wonderful and different range of functional applications. The deep view on the synthesis strategies and physical properties of the polymer/noble metal nanocomposites is offered in this book and also their applications in many fields.

Keywords: polymer, noble metals, metal nanoparticles, nanocomposites, mechanical properties, optical properties, antibacteria

1. Introduction

Nanocomposite polymers are the composites where polymer matrix is doped with the particles and the particle size is in the nanoscale in at least one dimension. The main problems facing the nanocomposite are the aggregation and agglomeration. The metals of nanoscopic range doping into dielectric matrices represent a key to manipulation and stabilization

problems. For practical applications of the nanoparticles, they are embedded in the polymers to produce the nanocomposite polymers since these nanocomposite polymers may have optical, electrical and thermal insulators or conductor, mechanical and a variety of properties. The nanocomposites may have mechanically plastic behavior or elastic behavior and may have a water-loving or a water-hating nature. Finally, polymer doping with the metal nanoparticles is the easiest and widely convenient way for stabilization and handling the nanostructured metals [1]. The most interesting metals that were used in the nanocomposite materials are the noble metals. Noble metals lie in group 11 in the periodic tables and called (d-blocks). The most important thing that characterizes the noble metals in nanoscale is the surface plasmon resonance (SPR) and is formed due to the collective oscillations of the electrons that are located on the nanoparticles surface. This electron pulsation is proportionally related to the light electromagnetic field which fall on the electrons, that is, the conduction electrons symmetrically vibrate at its location when exposed to the light, as shown in **Figure 1**.

The simplest and normal shape of the produced composites is the films or powders, and also these are good for exploiting the desired properties. The combination between the metal nanoparticles and the polymer is very wonderful because its composite has good and promising physical and chemical properties. One of the most important things that make this combination to be excellent is the method that combines/connects them together (preparation method).

There are two general and principle approaches for preparation of the polymer/metal nanocomposite: the ex situ and in situ methods [1]. In the ex situ route, at first, the metal nanoparticles are synthesized, and the surface of the created particles is encapsulated and passivated with organic polymer materials. Then, the metal nanoparticle derivatives are dispersed into the liquid monomer of the polymer solution that is then polymerized. Contrarily, the metal ions are located on site with the monomer and the monomer occurred, where the metal ion reduced chemically, thermally, or by UV irradiation during the polymerization process to obtain the nanoparticles; this method is called the in situ methods. Illustration with more information and details of some of these key methods follows.

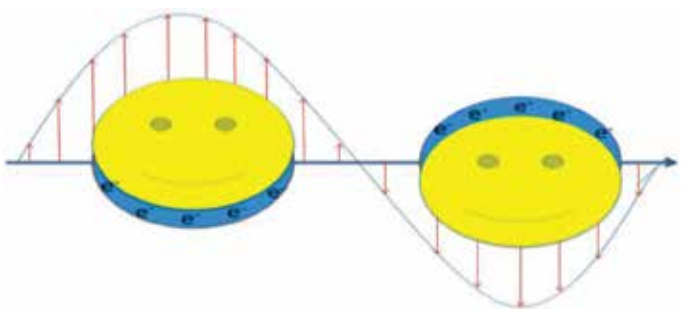

Figure 1. Cartoon showing the happy noble metal possessing the surface plasmon resonance.

http://dx.doi.org/10.5772/intechopen.79016

2. Preparation methods

2.1. Ex situ technique

The metal nanoparticles are created in the ex situ method by any traditional method (chemical reduction, precipitation, laser ablation, etc.) and then the surface of the created particles is stabilized, capsulated and passivated by using stabilizing agent. This can be achieved by the reduction of the metal precursors which was dissolved in the appropriate selected solvent such as water or ethanol, which often contain a polymer as a stabilizing agent [2, 3]. Otherwise, it can be stabilized and be ready by controlling micelle, reverse micelle or micro-emulsion reactions [4–6]. Often, the surface of the obtained particles by the ex situ method is manipulated by covalent bonds, metal-thiol or ligand with other ions to inhibit the agglomeration and aggregation processes [7] or by encapsulating a polymer [8]. Then, the produced metal nanoparticles are inserted into the polymer matrix. This is achieved by combining the obtained nanoparticles with the polymer solution, or by interacting with the monomer, and then followed by the casting techniques, etc. to obtain the nanocomposite films [9, 10], as shown in **Figure 2**.

The ex situ technique was successfully used to prepare many metals in nanoscale such as Ag, Cu, Pt and Au with specific size and shape by using an external reducing agent (sodium borohydride $NaBH_4$, tannic acid and sodium carbonate Na_2CO_3, hydrazine hydrate), then added to the polymer matrix such as (polyvinyl alcohol (PVA), polyvinyl pyrrolidone (PVP), polymethyl methacrylate (PMMA)) to produce the polymer/metal nanocomposites [11–13].

Sharma et al. [14], used the ex situ method to synthesize the polyaniline/copper nanocomposites by using the $NaBH_4$ as a reducing agent to reduce the copper salt to copper nanoparticles. Also, Yao et al. [15] used the trisodium citrate to reduce the gold salt to gold nanoparticles and then embedded in the PVA to produce the PVA/Au nanocomposites. Feng et al. [16] obtained the PVA/Ag nanocomposite films via the ex -situ method. They used the tannic acid and

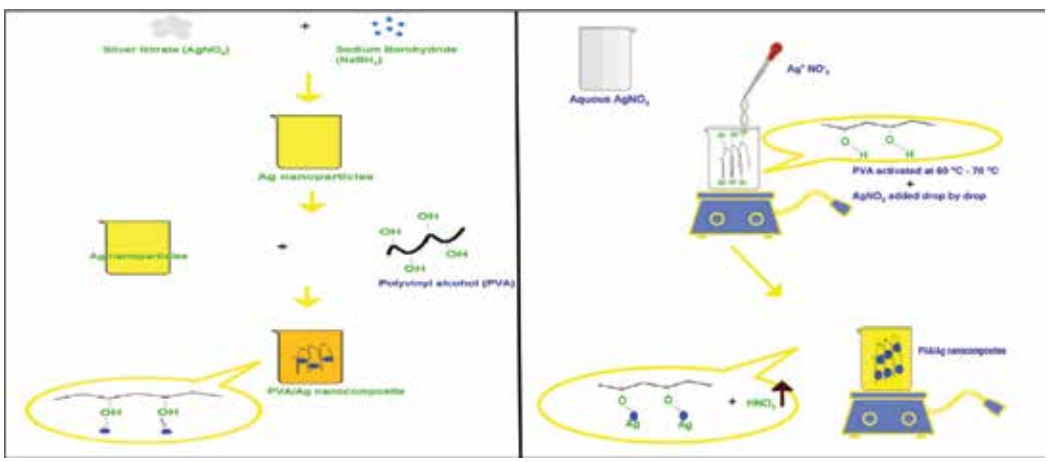

Figure 2. Scenario that depicts the ex situ technique (left side) and the in situ technique (right side).

Na_2CO_3 as a reducing and stabilizing agent to synthesize the silver nanoparticles. Then, the PVA solution was added to produce the nanocomposites. Another work by Campos et al. [17] was reported by the ex situ synthesis of the PVA/Ag nanocomposite films. The Ag nanoparticles powder with an average particle size of 25 nm was obtained and then mixed it with the PVA solution to produce the nanocomposite films.

However, this method has a shortcoming such as the aggregation, agglomeration and dispersion problems. It is necessary to manipulate and passivate the surface of the metal nanoparticles after the reduction process, in order to disperse them in the matrix. This surface manipulation led to changes in the properties of the nanoparticles. However, and after the surface manipulation process, it is very difficult to get well dispersion of nanoparticles in the composite. And also still a certain degree of agglomeration and aggregation is found in the composite. Also, the compatibility is another problem that facing the ex situ method, because of the difficulty of selecting the solvent which facilitates the compatibility between the particle-polymer- solvent systems. So, it was necessary to find a method (the in situ method) to overcome these problems.

2.2. In situ polymerization

The polymeric materials doped with metal nanofillers have been created by the in situ polymerization methods, which are composed of various techniques. The in situ methods have more benefits as compared to the ex situ methods such as its more simple, easy and straight-forward, and producing the class of nanocomposite materials with a higher feature and a higher quality, and more precise controlling. Firstly, the dispersion of metal nanofiller in a polymer monomer is utilized in this in situ method. Also, a technique similar to bulk polymerization is used to polymerize the resulting mixture. **Figure 2** shows a schematic diagram for the in situ technique.

In general, the in situ reduction mechanism in the PVA/Ag nanocomposite films is described as reported as example for the PVA/Ag nanocomposite as the following: the polymer PVA has a linear structure with the principle carbon backbone chains. Polyvinyl alcohol (PVA) molecules are hardly aggregate in dilute solution (water). Nevertheless, **Figure 3** shows the linear chains in a PVA planar structure, which interbridged by the H bonding coming from (or through) the OH groups. **Figure 3(a**, **b)** shows the PVA polymer in model configuration, where the PVA monomer is denoted by the symbol (R) and the PVA in part with an OH group. However, **Figure 3(c)** shows a cross section of the PVA structure. As apparent from the classical structure, especially when the PVA molecules dispersed in a dilute solution (water), the lateral or side growth to the backbone occurs. PVA structure contains weak hydrogen bonds, which extended to a little interbridging chain. In the coplanar PVA molecules structure, the hydrogen H-bond in a warm liquid at 60–70°C showed as floating and handling individually atoms and separately isolated with no much interaction with one another. The dispersion was facilitated by the thermo-mechanical stirring. It is possible that PVA molecular layers transform to a fibril structure or a favored structure, spiral in shape in linear polymer molecules (**Figure 3(d)**). Where the molecular layers of H-bonded monomers were interbridged from the OH groups, this is a compact structure, which takes place preferably in small island and dispersed molecules. At the surfaces, any type of the PVA molecular configurations has plenty of OH groups free from the H-bonding. There are electrons arranged in a definite localized

http://dx.doi.org/10.5772/intechopen.79016

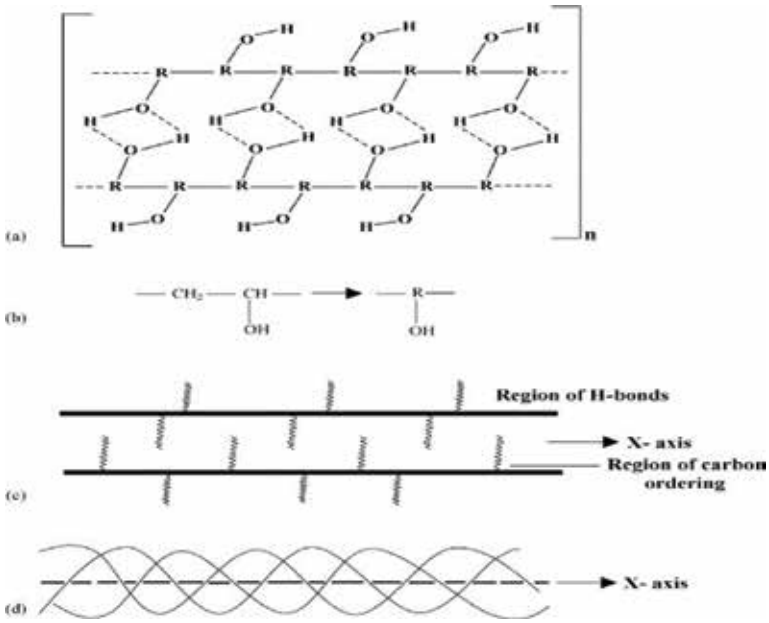

Figure 3. (1) A model coplanar structure of PVA molecules with interchain bridging via H-bonding between (2) the monomers forming (3) a molecular layer of extended surface. Such layers recombine further in different structures such as (4) an arbitrary spiral of three layers. [18]. Copyright 2007. Reused with permission from Elsevier Ltd.

distribution over the surface from the nonbonding hybrid electrons $2p^2(O)$ in such OH groups (the head groups) to interact with the metal ions to create a complex. Thermodynamically, the fugacity of the Ag surface is enhanced by Van der Waals interaction and facilitates a surface reaction of the $Ag+ \rightarrow Ag$, which can be expressed as follows [18]:

$$\begin{array}{l} Ag^{+} + e^{-} \text{ (from a PVA molecule)} \overset{\text{Active}}{\underset{\rightarrow}{}}{}^{PVA} \left[Ag^{+}\text{–PVA}\right]^{-} \text{(complex)} \\ \qquad\qquad\qquad\qquad\qquad\qquad\qquad\qquad\qquad\qquad \downarrow \\ \qquad\qquad\qquad\qquad\qquad\qquad\qquad\qquad\qquad\qquad Ag + PVA^{-} \end{array} \tag{1}$$

The Ag metal, which passes in steps with temporary intermediate Ag oxidation states, creates via an intermediate product of a polymer PVA/Ag^{+} complex in this model reaction, reflecting a rapid transform in the mixture color. Where the Ag metal creates through a polymer PVA/Ag^{+} complex of an intermediate state Agq^{+} ($q < 1$), the PVA oxidation during this reaction interrupts the PVA/Ag^{+} complex structure. The Ag clusters formed from the Ag^{q+} species convert to Ag atoms followed by coalescence, and then the Ag cluster forms and grows to achieve Ag particles. The Ag nanoparticles capsulated by the PVA molecules are stabilized from oxidative reactions. Where and simply, the PVA^{-} represents a partially oxidized state of PVA as follows:

$$[-R-OH-]_{n} \rightarrow \Omega 1\,[-R-OH]_{n'} - CH_{2} - CH - O + 12\,H_{2} \tag{2}$$

that is, one hydroxyl group "OH" is substituted by oxygen 'O' group, with the number of monomers ($n = \Omega_{1n'}$) in the native polymer molecule. Where the produced hydrogen atoms drives the $Ag^{+} \rightarrow Ag$ reduction,

$$Ag^{+} + 12\,H_2 \rightarrow Ag + H^{+}\,(\text{here, nitric acid}) \tag{3}$$

The byproduct nitric acid (HNO_3) evaporates during the heating process, and the PVA polymer molecules capping the Ag metal results in small size particles (nanoparticles). To obtain the Ag metal of neat dispersed particles in the PVA matrix, the external heating is very important and a crucial process. Otherwise, the residual of (HNO_3) acid interacts with Ag metal back to $AgNO_3$. The PVA has two functions in the reaction, first encapsulating the Ag particles and separating the $Ag^{+} \rightarrow Ag$ reactions in small isolated groups. Second, the structure of the isolated Ag particles can be controlled by the PVA. Under a hot condition of 60–70°C and mechanical stirring, the PVA molecules dissolved in the water are difficult to agglomerate and aggregate. From the models shown in **Figure 3**, the surface energy of the planar structure is high because of the molecular stretching of the bonds. Also, the PVA molecules interacted with OH groups via the hydrogen bonds, which work as follows:

1. A matrix to $Ag^{+} \rightarrow Ag$ reaction occurs over such surfaces;
2. A weak reducing agent, at moderate rate, to give $Ag^{+} \rightarrow Ag$ reaction;
3. A surface stabilizer to maintain the Ag nanoparticles in the sample;
4. A protecting surface coating to inhibit the growth of the Ag nanoparticles and obtain a stable PVA/Ag surface-interface.

The nucleation and growth processes of the Ag particles start and depend on their morphology, the Ag size, and also on its template stability. A spiral structure stimulates a fibril of the PVA, whereas the different shapes (platelet or spheroids) grow by a PVA crystalline lamellar regions. The small spherical templates participate to evolve the spherical or near special shapes of the nanoparticles according to the reaction species interactions through the interface layer.

The reported mechanism of this reaction based on 'polyol route,' the PVA monomer, involves the secondary alcohol groups, R_2CHOH, on the polymer.

$$R_2CHOH + AgNO_3 \rightarrow R_2CO + H_2O + NO_2 + Ag \tag{4}$$

Here, R denotes a PVA monomer.

Recently, Deb and Sarkar [19] used the in situ method to prepare the PVA/Ag nanocomposite films and then followed the films by thermal annealing to obtain the PVA/Ag nanorods. In the same context, Llorens et al. [20] synthesized the cellulose/copper nanocomposite fibers by using in situ thermal treatment. Bogdanovic et al. [21] prepared the polyaniline/copper nanocomposites via the in situ method, wherein the Cu nanoparticles and polyaniline are created at the same instant. In this case, the reaction takes place at room temperature to obtain the nanocomposite. This route can be counted as a simple and inexpensive method of preparation. Also, Becerra et al. [22] prepared the poly(vinyl chloride)/copper nanocomposite films by the in situ method for antibacterial applications. Also, El-Shamy et al. [23] recently used the in situ method to produce the PVA/Ag nanocomposites, where they used the PVA polymer as a reducing agent by activation of the OH group in the PVA at 60°C to reduce the $AgNO_3$ to

Ag nanoparticles and obtained the nanocomposites. Ananth et al. [11] prepared the PVA/Ag nanocomposites by using the in situ method for the SPR-based protein sensors. Karthikeyan et al. [24] synthesized free-standing PVA/Pt nanocomposite films via in situ method for ultrafast optical power-limiting applications.

2.3. Radiolytic method

The radiolytic process means that the molecules separate to smaller atoms, radicals or ions by ionizing radiation like γ rays, UV irradiation. In fact, the gamma irradiation method is one of the most interested methods for preparing the polymer/metal nanocomposites. The desired highly reducing radicals generated free from any by-product are the main feature of gamma irradiation method for the creation of noble metallic nanoparticles. The primary and first radicals and upon gamma irradiation, the molecules produced in water are [25].

$$H_2O \rightarrow e_{aq}^{-}(2.7), OH^{*}(2.7)\ H^{*}(0.6), H_2(0.45), H_2O_2(0.7) \tag{5}$$

The numbers in parentheses represents the G values. The G value for a given irradiated system is the absolute chemical yield expressed as the number of individual chemical events occurring per 100 eV of absorbed energy. Thus the G (e_{aq}-), G (OH•), etc. are the number of solvated electrons, hydroxyl radicals, etc., formed per 100 eV of absorbed energy. The alcohol radical is produced when the radicals (OH* and H*) are able to capture hydrogen from the alcohol group. This way, oxidizing OH* radicals are transformed into reducing alcohol radicals. The scavenger material was used to make the reaction free from the OH* radicals. The e_{aq}^{-} and OH* radicals possess the electron transfer reaction between the PVA and Ag+, and then the reduction of Ag^{+} ions to Ag particles takes place. The color of the composite solution is converted from colorless to pale yellow color as a result of the Ag^{+} ions reduction in PVA solution by the radiolytic method.

It is well known that the OH* radicals induce the cross-linking of PVA molecules in aqueous medium by/through the gamma radiation (with the G value of the intermolecular cross-linking induced via the gamma irradiation is 0.48).

$$2PVA(H) + 2OH^{*} \rightarrow PVA\text{——}PVA(\text{cross}-\text{linked polymer}) + 2H_2O \tag{6}$$

The Ag^{+} ions are reduced, under the given conditions of the experiment, with highly reducing hydrated electrons, reducing agent and the PVA radicals created by the H atom, which is abstracted from the (OH*) radicals in the PVA chains.

$$nAg^{+} + n\, e_{aq}^{-}/PVA^{*} \rightarrow (Ag)_n \tag{7}$$

The hydroxyl radicals formed by the hydrated electrons during the gamma irradiation of N_2O-saturated aqueous solution are as follows:

$$N_2O + 2\, e_{aq}^{-} \rightarrow N_2 + 2OH^{*} \tag{8}$$

According to the reaction in Eq. (6), the PVA interacts with the hydroxyl (OH*) radicals and is lost in the reaction to obtain the polymeric PVA* radicals. After the gamma irradiation of the (PVA/Ag^+ ions) hydrogel, the color of the hydrogel is changed to pale yellow color due to the electron transfer interaction between the PVA and Ag+. Reduction of the silver ions in PVA/Ag^+ hydrogel induced the creation of Ag nanoparticles with a characteristic fingerprint surface plasmon resonance (SPR) band.

The advantage of the gamma irradiation method comes from the gamma rays and is as follows: (1) hydrated electron resulted from the gamma radiolysis can reduce metal ions to metal nanoparticles. (2) Escaping from the use of external reducing agent and the resultant side reactions like oxidation reactions in UV irradiations and other byproducts produced in the reducing agent methods. (3) The gamma rays used to control the reduction reaction by controlling the doses of the irradiation and also the amount of the reduced nanoparticles nuclei by controlling the amount of radicals. (4) The gamma radiation used to reduce the $AgNO_3$ to Ag seeds point which serves as nuclei or nucleation sites for Ag atoms formation, to start the Ag nanoparticles growing directly on the PVA backbone. Also, this method has the ability to produce the metal nanoparticles in different shape and size.

Recently, El-Shamy and his group [26] reported a promising route for the creation of the PVA/Ag and the (PVA/Ag nanorods) nanocomposites by using the gamma rays. After producing the PVA/Ag nanocomposite films via the chemical reduction in situ route, the films were directed to gamma rays with different irradiation doses from 25 to 100 KGy with steps 25 KGy, and at special case, the Ag nano-rods were produced at 125 KGy, and the Ag nanoparticles appeared on the back surface (the surface not facing the gamma source) as nanorods, as shown in **Figure 4**.

In the real reaction, two processes may occur simultaneously. At first, Ag nanoparticles are created through homogeneous nucleation process and then grow along the direction of the lowest energy {111} plane. The Ag nanoparticles were firstly created by the homogeneous nucleation process, through the silver nitrate reduction by gamma rays. The nucleation process was done by the Ag seeds which was a source of the formation of Ag atoms. The rod-like PVA micelles were created through the gamma irradiation, and this is strongly related to the PVA: Ag + molar ratio. The backbone chain of PVA contains oxygen atoms from the (-OH) groups in the PVA. This oxygen atoms coordinate with the Ag to form complexes (PVA/Ag+) as an intermediate state in the reaction via the covalent bonds. The second step includes merging and fusing of the Ag nanoparticles to create Ag nanorods in the matrix via the photothermal effect of gamma irradiation.

Here, the PVA polymer has two functions in the reaction: (1) the first function is the PVA forming a complex (PVA/Ag+) with Ag + through the coordination reaction and (2) the second function is the PVA used to adsorb on the Ag nanoparticles facets. From the PVA structure, the binding capacity of PVA to the Ag surface increases, because of the PVA containing the ═C=O groups. So, the adsorption of the PVA on the Ag nanoparticles surface increases. From this fact, the Ag crystals interact with the PVA groups (═C=O), leading to a decrease in the crystal growth of the {100} plane as compared to the {111} plane. The plane {100} has energy lower than the plane {111}, so there is a high energy difference between the two surfaces. According

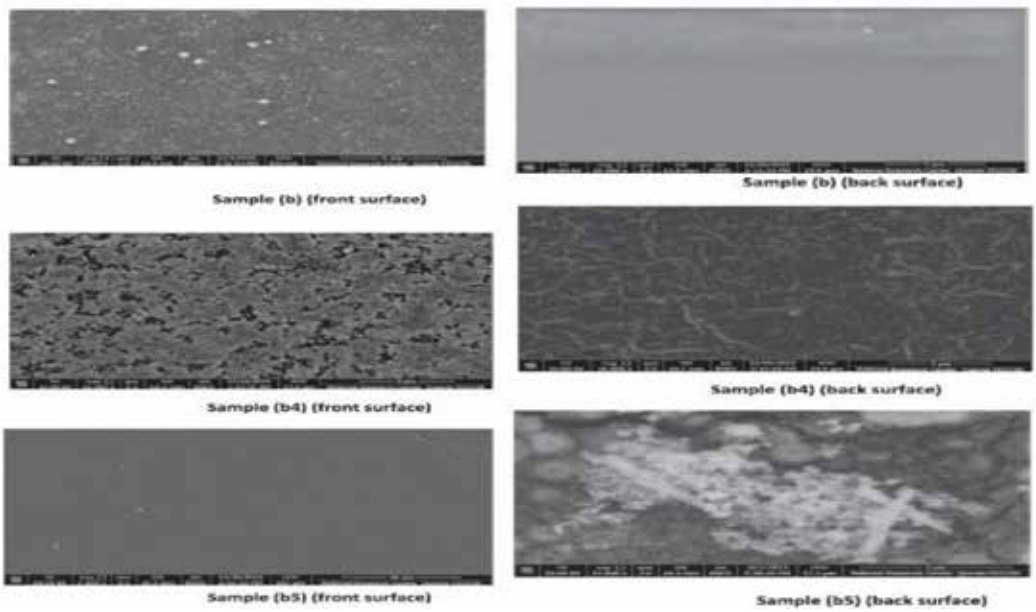

Figure 4. SEM images of front and back surfaces for samples 0 (b1), 100 (b4) and 125 KGy (b5) [26]. Copyright 2018. Reused with permission from Elsevier Ltd.

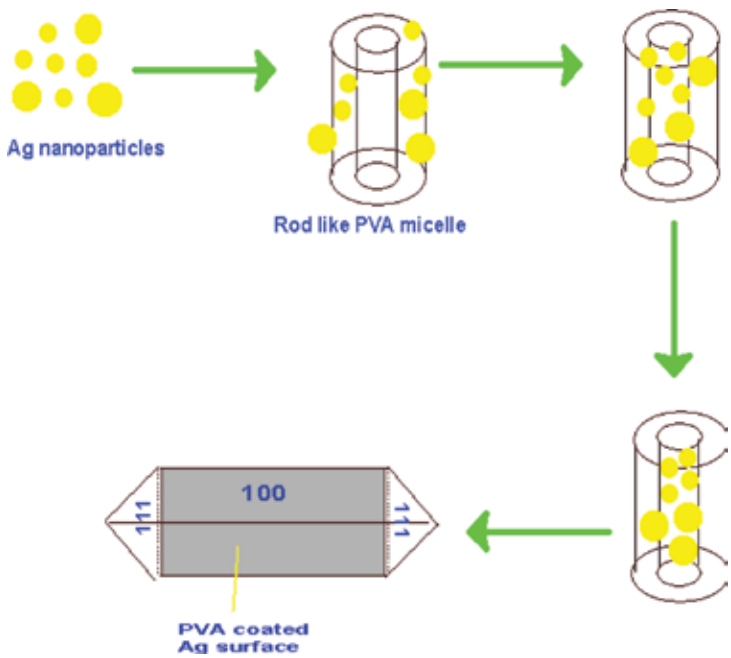

Figure 5. Schematic illustration of the formation of the Ag nanorods in the PVA matrix.

to this fact, the reactivity of the plane {100} to interact with PVA is larger than the reactivity of the plane {111} with PVA. So, there is a large difference in reactivity between the two surfaces of Ag nanorods. Consequently, the PVA coated the plane {100} of the Ag nanorods and completely blocked Ag nanorods from growing. On the other hand, the PVA partially coated the plane {111} of the Ag and also PVA partially blocked the Ag nanorods from growing along this direction as shown in **Figure 5**. This investigation confirms that the PVA macromolecule interacts with the Ag plane {100}, which is stronger than the Ag plane {111}.

Yonghong et al. [27] successfully prepared the polyacrylamide/gold (PAM/Au) nanocomposites by γ (gamma)-irradiation in an ethanol system. In a similar way, Krkljes et al. [28] prepared the PVA/gold nanocomposites via the gamma irradiation, in situ method. Also, Ali et al. [29] recently used the gamma irradiation to prepare the PVA/copper nanocomposites, with the obtained copper size ranging from 13.9 to around 19 nm. Graeser et al. [30] used gamma irradiation to reduce Ag + ions in the presence of polyvinylpyrrolidone (PVP) to produce the PVP/Ag nanocomposites.

3. Properties of PVA/Ag nanocomposites

3.1. Mechanical properties

From the experimental and theoretical approaches that deal and explain the behavior of the nanocomposites, the insertion of the nanoparticles into polymer matrices is the direct reason to obtain nanocomposite materials with higher mechanical properties. There are many techniques to determine the mechanical parameters of the polymer/metal nanocomposites such as tensile, compression and shear stress techniques. From the stress-strain curve, the mechanical parameters including Young's modulus, elongation at break, stress yield, tensile strength and compressive strength were determined. The interfaces between the nanoparticles surface and polymer matrix (called the interfacial or boundary region) exhibit the nanocomposites local properties different than that of the bulk or traditional composites.

One of the most important and major factors that affect the mechanical behavior of the polymer/metal nanocomposite is the concentration of the metal nanoparticles and the preparation method. Experiments showed that the mechanical parameters of the polymer/metal nanocomposites are strongly altered by these two parameters. Given facts showed that Young's modulus was found to be 2.2 [31] and 4.6 GPa [23] at approximately the same concentration of Ag nanoparticles 1 wt.% for the PVA/Ag nanocomposites, but with different experimental procedures. Also, it increased with raising the Ag nanoparticles content by using the same experimental procedures for the same nanocomposite. We believed that this increment in Young's modulus and the reduction in the elongation at break is assigned to the growth in the intra- and intermolecular hydrogen bonding due to the increase in the content of the Ag nanoparticles and then higher the cross-linking level in the nanocomposite. So, the increasing Young's modulus behavior and the decrease in the behavior of the elongation at break take place.

Figure 6 explains as follows: the true stress-strain curve is changed after the addition of Ag nanoparticles in the PVA that show a transformation from a rubber-like of the PVA polymer

http://dx.doi.org/10.5772/intechopen.79016

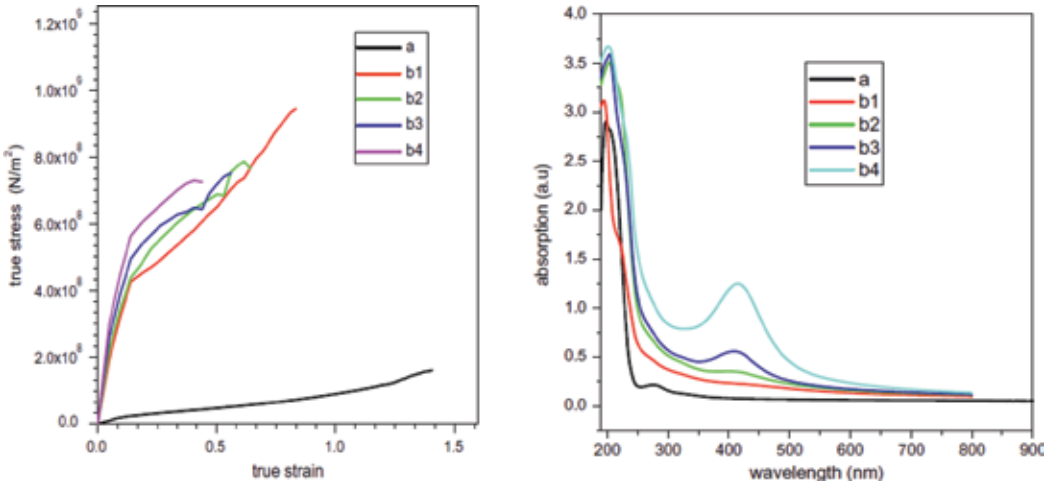

Figure 6. (left side) the stress-strain behaviors, (right side) the optical absorption spectra for prepared samples (pure PVA (a) and 0.2, 0.4, 0.8 and 1.5 wt.% of Ag nanoparticles take a label (b1–b4)) [23]. Copyright 2014. Reused with permission from Elsevier Ltd.

to a semi-crystalline state. The behavior of true stress-strain curve can be divided into three distinct lines. The first stage is the linear part and called the elastic strain following Hooke's law. The increase in the slope of this stage is attributed to the increase in the density of Ag nanoparticles. The second stage shows the starting of the neck formation. The length of this stage decreases with raising the content of Ag nanoparticles. Accordingly, the crystals of the isotropic PVA begin to be oriented in this deformation stage under the tensile stress. Also, it is clear that Young's modulus raises as the amount of Ag nanoparticles increases. This may be illustrated on the assumption that the introduction of metals in the polymer chain increases the density of the materials which leads to a decrease in lattice strain under external mechanical stress (where the introduction of silver nanoparticles in the PVA leads to the increase in the intra-molecular forces, creating a charge transfer complex which inhibits the molecules of PVA from sliding over each other. This may describe the raise of Young's modulus). The increase in the concentration of Ag nanoparticles causes shifts in the neck region to low strain side and the neck formation appears by increasing the concentration of Ag nanoparticles. These results can be explained by the fact that the increase of silver nanoparticles concentration causes an increase in the intra-intermolecular forces inside the polymer. This increase demonstrates itself by the shift of the formed neck to low strain appearance on its gradual side.

Chatterjee et al. [32] doped the PMMA/block copolymer with the Ag (from 0.16 to 0.65 wt.%) and then studied the storage moduli for this nanocomposite film. They documented the increment in both the storage and loss moduli of nanocomposite as the Ag concentration raise. This behavior was explained on the basis of the attraction forces (van der Waals forces) between the PVA and the Ag nanoparticles, and huge surface area to volume ratio of the Ag nanoparticles. Also, Deka et al. [33] recorded enhancement in the mechanical parameters such as Young's modulus, tensile strength, elongation at break, impact resistance and Shore A hardness of the

polyurethane PU/Ag nanocomposites with the Ag nanoparticles concentration from 2.5 to 5 wt.%. Moreover, Young's and storage moduli of PVP/PU blend were enhanced by introducing the Ag nanowires in the matrix. However, the elongation at break decreased from 536% for neat PVP/PU to 304% for 1.5 vol.% of Ag-doped PVA/PU in the PVA/PU blend, and also the ultimate strength decreased from 12.7 for PVA/PU to 9.8 MPa for 1.5 vol.% of Ag [34]. Also, Papageorgiou et al. [35] determined the tensile mechanical parameters (Young's modulus, strain) and impact strength of the same polymer polystyrene (PS) doping with 3 wt.% of different nanofillers such as PS/Ag nanoparticles, PS/Cu nanofiber, PS/nano-diamond and PS/MWCNT nanocomposites (**Table 1**). By comparing the obtained data, it is shown that Young's modulus, elongation and impact strength in PS matrix containing the metal nanoparticles are better than the other nanocomposites containing the multiwall carbon nanotube MWCNT, and nanodiamond. The improvement and enhancement of the mechanical parameters by embedding metal nanoparticles was also reported in chitosan/Ag [36] and PVA/Ag [37] nanocomposites. As a result, the mechanical behavior of polymer matrices can be improved by dispersing the metal nanoparticles through the polymer and giving many benefits.

3.2. Optical properties

For centuries, the polymer/metal nanocomposite is one of the most important classes of functional materials due to its useful optical properties, including light absorption, photoluminescence spectra and refractive index, and its applications. The size of metal particles and their allocation inside the polymer matrix are the two strongest parameters that the optical properties of these polymer/metal nanocomposites depend on them. Polymer/metal nanocomposites that consist of inorganic UV-absorbers and polymer have been of interest in many fields. The fingerprint behavior for all the noble metal nanoparticles is the unique absorption peak in the visible spectrum (**Figure 6**). This band called surface plasmon resonance (SPR) band is attributed to the excitation of the collective modes of motion of the electron cloud (plasmon excitation) at the boundary of the particle under the effect of the light electrical field. When the light falls with a definite frequency, the resonance takes place and results in an optical absorption, surface plasmon, plasma resonance absorption, plasmons or localized surface. Some factors exerted on this band position, width and intensity, are as follows:

Polymer/metal nanocomposites	Young's modulus (Gpa)	Elongation (%)	Impact strength (J/m)
Ps	2.59	1.93	11.1
Ps/Ag	2.81	2.65	12.5
PS/Cu nanofibers	2.79	1.8	14.6
Ps/MWCNT	2.92	2.06	13.9
Ps/nanodiamond	3.1	2.34	11.7

Table 1. Mechanical properties of PS nanocomposites, data were collected from [35]. Copyright 2014. Elsevier Ltd. Reused with permission from Elsevier Ltd.

1. The dielectric constants for both the metal and its surrounding matrix;
2. Size, dimensions and shape of the particle;
3. The interface area, crossing point or the boundary between the particle and the surrounding matrix;
4. The particles distribution in the surrounding matrix.

Metals in the nanoscale range allow to control the refractive index (RI) and the dispersion behavior of polymeric nanocomposites when inserted into the polymer matrix. The higher refractive index of nanocomposite materials obey these materials to a functional application in many fields such as optical and optoelectronic lab (lenses, optical filters, optical waveguides), and advanced technology such as solar cells, photodiodes, optical adhesives or antireflection films [38]. A large number of the metal nanoparticles can be inserted into the polymer matrix for boosting the refractive index of polymer nanocomposites. The refractive index of polymer/metal nanocomposites has a linear function with the density of the metal nanoparticles and the absorption coefficient. Either the increase in the refractive index or a decrease makes the polymer/metal nanocomposites very useful in many applications such as chemical and biosensors. Another important parameter, which very much influences the refractive index of the nanocomposites, is the isotropy or anisotropy of the metal nanoparticles in the polymer matrix. The anisotropy of the metal nanoparticles in the polymer matrix produces birefringence behavior; this means that the nanocomposites have two refractive indexes [39].

3.3. Antibacterial properties

In recent years, the race to develop polymer/metal nanocomposite materials with microorganisms' resistance properties had been of a very significant value and considered an important key factor for inhibiting foodborne diseases and preventing or controlling bacteria and infections originating in a hospital (nosocomial infections) from growth. Marketing, the polymer/metal nanocomposite product with the antibacterial properties is extremely used. The mechanism of the interaction between the polymer/metal nanocomposite and the bacteria is subsequently summarized and is shown in **Figure 7**.

3.4. Antibacterial mechanism of metal/polymer nanocomposites

The antimicrobial effects showed in polymer/metal nanocomposites depend on three phenomena:

1. Metal ions that can release from the nanocomposites,
2. Nanocomposites can release metal nanoparticles from it.
3. The inhibition was done by biofilms.

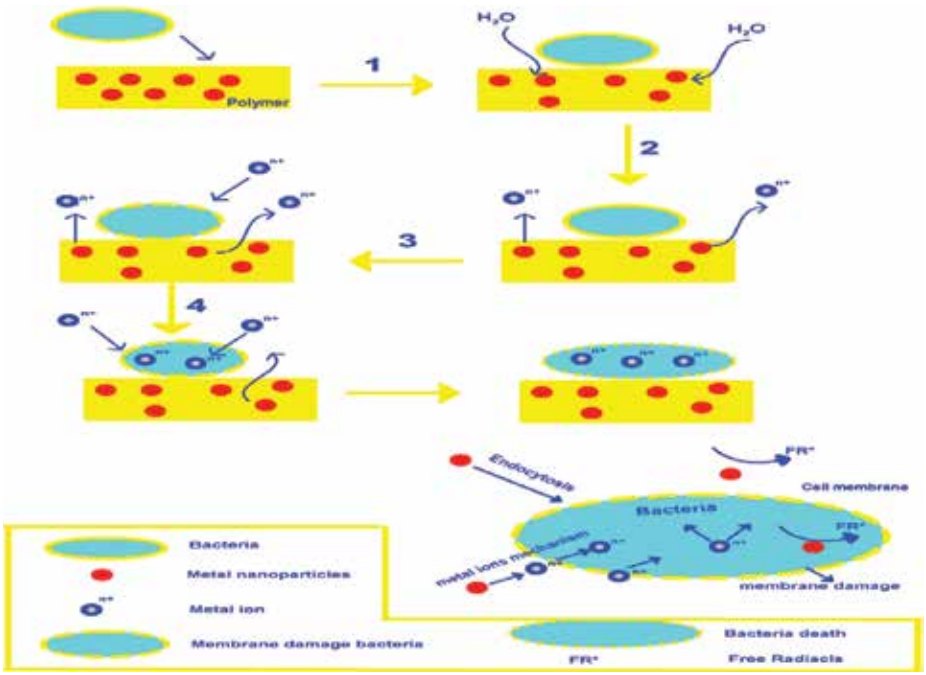

Figure 7. Mechanisms for the antibacterial behavior of polymer/metal nanocomposites: (1) adsorption of bacteria on the polymer surface triggering the diffusion of water through the polymer matrix due to the medium surrounding the bacteria; (2) water with dissolved oxygen reaches the surface of embedded metal nanoparticles allowing dissolution or corrosion processes, and this way metal ions are realized; (3) metal ions reach the nanocomposite surface damaging the bacteria membrane; (4) afterward, metal ions can diffuse into the bacteria.

3.4.1. Release of metal ions

1. The metal ions are released from the polymer/metal nanocomposites and reach the bacteria cell wall (the outer membrane) and denaturation of proteins in the bacterial membrane by their interaction with the sulfhydryl groups and amines and carboxyl groups in the peptidoglycan layer that found in N-acetylglucosamine and N-acetylmuramic acid.
2. The cell wall and membrane of the bacteria are destabilized or broken and subsequently disintegrated by these interactions, which is known as the bacteriolytic effect.
3. The released ions bind to DNA in the bacteria resulting in disorganized helical structures involved in cross-linking within and between nucleic acid strands; this leads to the cell not capable of reproducing. Also, the reactive oxygen species, lipid peroxidation and protein oxidation are generated by the metal ions.

3.4.2. Release of metal nanoparticles

1. The metal nanoparticles via molecular interactions adhere to the bacteria surface and with the electrostatic forces.

2. By one of two ways (endocytosis or direct diffusion), the bacteria cell wall penetrates by the metal nanoparticles.
3. There are three steps for the metal nanoparticles within (10 and 100 nm to penetrate the bacteria cell wall by endocytosis: sticking to the membrane, the metal nanoparticles warped by the membrane and finally the particle-lipid complex separates from the membrane.
4. The hydrophobic or hydrophilic nature of the metal nanoparticles at 10 nm plays an important role. The metal nanoparticle penetrates the membrane of the bacteria cell wall, if the interaction is strong, driven by its preference for the lipid head group or tail.
5. Side by side and at the same time with these above mechanisms, the ions were freed and released from the nanoparticles and also concurrently excite the effects linked with the ions release.

3.4.3. Biofilm inhibition

1. The metal nanoparticles move through the nanocomposite matrix toward the surface, so the outer layer of the nanocomposite becomes much more active.
2. The attachment of bacteria is altered, by reducing the cell surface hydrophobicity (CSH) via the surface of the metal nanoparticles. Also, the extracellular polymeric substances (EPSs) are reduced by the surface of the metal nanoparticles, which also take a role in biofilm creation and growth.

Recently, Fatema et al. [40] prepared the PVA/Ag nanocomposites by two methods: first, by water in oil (w/o) microemulsion and the second by the in situ method. The antibacterial efficiency was done against G- bacteria '*E. coli*' and G+ bacteria '*S. aureus*,' respectively, for the above nanocomposites. They observed that the (w/o) microemulsion films have antibacterial activity higher than the in situ films under the same test condition. Also, Espana-Sanchez et al. reported the treatment of polypropylene PP/Ag and PP/Cu nanocomposites surface by using the argon plasma [41]. They showed that the nanocomposites have a higher quality in the antibacterial efficiency versus, pathogenic, the human disease bacteria, because of the larger surface area of the metal nanoparticles and the raising of the hydrophilicity and the roughness of film surface. Also, the in situ route was used to prepare the polyethylene PE/Ag nanocomposites for antibacterial applications [42]. They recorded that the Ag ions were released from the PE/Ag nanocomposites with larger Ag concentration higher than the neat PE.

4. Applications of polymer-metal nanocomposites

The embedding of noble metal nanoparticles as filler into organic polymer matrices gives superior thermal, electronic, optical and mechanical properties for the resulting polymer/metal nanocomposite materials. The improvements and enhancement of the physical properties go with these materials to be used in different technical applications in many various

Metal/polymer nanocomposite	Microorganism	Application	Refs.
Hydroxypropyl Methylcellulose/ Cu	*S. epidermis*, *B. cereus*, *E. faecalis*, *Salmonella*, *P. aeruginosa*, *Staphylococcus aureus*	Food packaging	[43]
Polymers based on acrylic/ Cu	Chlamydomonas CD1 Red, Synechocystis PCC 6803, *Phaeodactylum tricornutum* CCMP 1327	Marine antifouling coatings	[44]
Cellulose acetate/Ag nanofibers	G- bacteria (*E. coli* and *Pseudomonas aeruginosa*); G+ bacteria such as (*S. aureus* and *Bacillus subtilis*)	wound dressing	[33]
Polyurethane/Ag nanocomposites	G- bacteria (*E. coli* and *Pseudomonas aeruginosa*); G+ bacteria such as (*S. aureus* and *Bacillus subtilis*)	Marine antifouling coatings	[45]

Table 2. Main application of polymer/metal nanocomposites in antibacteria.

Polymer/metal nanocomposites	Application/Refs.
Polyaniline/gold	Sensor [46]
Natural rubber/Ag	Latex gloves [47]
Polysulfone/Pt	Sensor [48]
Polypyrrole/Pt	Fuel cell [49]

Table 3. Application of polymer/metal nanocomposites.

fields, such as energy, environment, mechanics, optics, electronics, optical transformation technology, engineering, biology and medicine. Many applications like catalysts, membranes military equipment and separation devices, and solar cells, aerospace, fuel sensors, automobiles, antimicrobial, have been reported for the polymer/noble metal nanocompostes. Nanocomposite materials are used for this purpose, as shown in **Table 2**: tissue engineering, textiles and functional smart coatings, paints and drug carriers. Furthermore, the superior and high-quality mechanical and thermal properties of these nanocomposites allow them to be used in many various industrial applications, such as filters for irradiation protection, life power equipment, electronic devices, conductors and insulators in daily electrical tools, and pagers for the manufacturing of pressure molds in the ceramic industry. More details about the application of polymer/metal nanocomposites are shown in **Table 3**.

5. Conclusions

From the previous discussion and clear different examples and principal strategies of the polymer/noble nanocomposites preparation mentioned in this chapter, it can be concluded that the radiolytic route for the synthesis of the nanocomposites is a smart way and a very easy method with a large possibility to solve the problems of the nanocomposite synthesis in the future. For polymer/metal nanocomposite synthesis, one main problem is the nanoparticles agglomeration and it must be solved: once obtained, and how to inhibit this

problem. The synthesis methods have to be tuned in such a way that gamma irradiation is used that avoids the agglomeration of nanoparticles. The mechanical parameters, Young's modulus, of the polymer/metal nanocomposites are highly dependent on the cross-linking density of the polymer, the morphology of the nanoparticles and the molecular interaction (intra- and intertype) between the metal nanoparticles and the polymer matrix. The optical properties of polymer/metal nanocomposites, such as the SPR intensity and position and the refractive index, are strongly dependent on the dimensions and shape of the metal nanoparticles, the dielectric functions of the metal and the surrounding material, the boundary between the particle and the surrounding, and the particle distribution in the surrounding matrix. The polymer/metal nanocomposites have a strong resistance toward the bacteria or antibacterial activity. The polymer capping metal nanocomposite materials have many various and important functional potential applications. Finally, it can be concluded that the main advantage of polymer/metal nanocomposites is the possibility to obtain the needed desired properties with higher quality than that from the conventional microcomposites by using very small volume of filler that can be low in magnitude by one or even two orders.

Author details

Ahmed Gamal Abed El-Azim Khalil El-Shamy

Address all correspondence to: agabedelazim@yahoo.com

Physics Department, Faculty of Science, Suez Canal University, Ismailia, Egypt

References

[1] Nicolais L, Carotenuto G. Metal-Polymer Nanocomposites. Hoboken: Wiley; 2005

[2] Goia DV. Preparation and formation mechanisms of uniform metallic particles in homogeneous solutions. Journal of Materials Chemistry. 2004;**14**:451-458

[3] Schmid G. Cluster and Colloids: From Theory to Applications. Weinham: VCH; 1994

[4] Volpe MV, Longo A, Pasquini L, Casuscelli V, Carotenuto G. Synthesis and characterization of gold-based quantum dots. Journal of Materials Science Letters. 2003:**22**:1697-1699

[5] Serebryakova NV, Uryupina, Roldughin VI. Formation of the bimodal ensemble of silver nanoparticles in polymer solutions. Colloid Journal. 2005;**67**:79-84

[6] Hutter E, Fendler JH. Exploitation of Localized Surface Plasmon Resonance. Advanced Materials. 2004:**16**:1685-1706. https://doi.org/10.1002/adma.200400271

[7] Ahmadi TS, Wang ZL, Henglein A, El Sayed MA. "Cubic" Colloidal Platinum Nanoparticles. Chemistry of Material Materials. 1996;**8**:1161

[8] Pileni MP. Reverse micelles as microreactors. Journal of Physical Chemistry. 1993;**97**: 6961-6973

[9] Carotenuto G, Nicolais L. Size-controlled synthesis of thiol-derivatized gold clusters. Journal of Materials Chemistry. 2003;**13**:1038-1041

[10] El-Shamy AG, Attia W, Abd El-Kader KM. Enhancement of the conductivity and dielectric properties of PVA/Ag nanocomposite films using γ irradiation. Materials Chemistry and Physics. 2017;**191**:225-229

[11] Ananth AN, Umapathy S, Sophia J, Mathavan T, Mangalaraj D. On the optical and thermal properties of in situ/ex situ reduced Ag NP's/PVA composites and its role as a simple SPR-based protein sensor. Applied Nanoscience. 2011;**1**:87-96. DOI: 10.1007/s13204-011-0010-7

[12] Solomon SD, Bahadory M, Jeyarasingam AV, Ruthkowsky SA, Boritz C, Mulfinger L. Synthesis and Study of Silver Nanoparticles. Journal of Chemical Education. 2007;**84**:322-325

[13] Mahendia S, Tomar AK, Kumar S. Electrical conductivity and dielectric spectroscopic studies of PVA–Ag nanocomposite films. Journal of Alloys and Compounds. 2010;**508**:406-411. DOI: 10.1016/j.jallcom.2010.08.075

[14] Sharma S, Nirkhe C, Pethkar S, Athawale AA. Chloroform vapour sensor based on copper/polyaniline nanocomposite. Sensors and Actuators B. 2002;**85**:131-136

[15] Yao W, Chen X, Zhang J. A capacitive humidity sensor based on gold–PVA core–shell nanocomposites. Sensors and Actuators B. 2010;**145**:327-333

[16] Feng Q, Dang Z, Li N, Cao X. Preparation and dielectric property of Ag/PVA nanocomposite. Materials Science and Engineering B. 2003;**99**:325-328

[17] Campos JBG, Prokhorov E, Sanchez IC, Barcenas JGL, Ramirez AM, Herniandez JG, Castro YL, del Rio RE. Molecular dynamics analysis of PVA-Ag NP composites by dielectric spectroscopy. Journal of Nanomaterials. 2012;**2012**:1-11. https://doi.org/10.1155/2012/925750

[18] Gautam A, Singh GP, Ram S. A simple polyol synthesis of silver metal nanopowder of uniform particles. Synthetic Metals. 2007;**157**:5-10

[19] Deb S, Sarkar D. Effect of annealing temperature on optical properties of silver-PVA nanocomposite. Optik. 2018;**157**:1115-1121

[20] Llorens A, Lloret E, Picouet P, Fernandez A. Study of the antifungical potential of novel cellulose/copper composites as absorbent materials for fruit juices. International Journal of Food Microbiology. 2012;**158**:113-119

[21] Bogdanovic U, Vodnik V, Mitric M, Dimitrijevic S, Skapin SD, Zunic V, Budimir M, Stoiljkovic M. Nanomaterial with high antimicrobial efficacy-copper/ polyaniline nanocomposite. Applied Materials & Interfaces. 2015;**7**:1955-1966

[22] Becerra A, Rodríguez-Llamazares S, Carrasco C, Díaz-Visurraga J, Riffo C, Mondaca MA. Preparation of poly(vinyl chloride)/copper nanocomposite films with reduced bacterial adhesion. High Performance Polymers. 2012;**25**:51-60

[23] El-Shamy AG, Attia W, Abd El-Kader KM. The optical and mechanical properties of PVA-Ag nanocomposite films. Journal of Alloys and Compounds. 2014;**590**:309-312. DOI: 10.1016/j.jallcom.2013.11.203

[24] Karthikeyan B, Anija M, Venkatesan P, Suchand Sandeep CS, Philip R. Ultrafast optical power limiting in free-standing Pt–polyvinyl alcohol nanocomposite films synthesized in situ. Optics Communications. 2007;**280**:482-486

[25] Krklješ A, Nedeljković JM, Kačarević-Popović ZM. Fabrication of Ag-PVA hydrogel nanocomposite by γ-irradiation. Polymer Bulletin. 2007;**58**:271-279

[26] El-Shamy AG, Maati AA, Attia W, Abd El-Kader KM. Promising method for preparation the PVA/Ag nanocomposite and Ag nano-rods. Journal of Alloys and Compounds. 2018;**744**:701-711. DOI: 10.1016/j.jallcom.2018.02.026

[27] Ni Y, Ge X, Zhang Z, Ye Q. In situ single-step synthesis of gold/polyacrylamide nanocomposites in an ethanol system. Materials Letters. 2002;**55**:171

[28] Krkljes A, Bozanic DK, Bibić N, Nedeljković JM. Characterization of poly(vinyl alcohol)/gold nanocomposites obtained by in situ gamma irradiation method. Journal of Applied Polymer Science. 2012;**125**(2):1244-1251

[29] Ali ZI, Ghazy OA, Meligi G, Saleh HH, Bekhit M. Radiation-induced synthesis of copper/poly(vinyl alcohol) nanocomposites and their catalytic activity. Advances in Polymer Technology. 2016. DOI: 10.1002/adv.21675

[30] Graeser M, Pippel E, Greiner A, Wendorff J. Polymer Core–Shell Fibers with Metal Nanoparticles as Nanoreactor for Catalysis. Macromolecules. 2007;**40**:6032

[31] Sedlarik V, Galya T, Sedlarikova J, Valasek P, Saha P. The effect of preparation temperature on the mechanical and antibacterial properties of poly(vinyl alcohol)/silver nitrate films. Polymer Degradation and Stability. 2010;**95**:399-404

[32] Chatterjee U, Jewrajka SK, Guha S. Dispersion of functionalized silver nanoparticles in polymer matrices: Stability, characterization, and physical properties. Polymer Composites. 2009;**30**:827-834

[33] Deka H, Karak N, Kalita RD, Buragohain AK. Bio-based thermostable, biodegradable and biocompatible hyperbranched polyurethane/Ag nanocomposites with antimicrobial activity. Polymer Degradation and Stability. 2010;**95**:1509-1517

[34] Mi HY, Li Z, Turng LS, Sun Y, Gong S. Silver nanowire/thermoplastic polyurethane elastomer nanocomposites: Thermal, mechanical, and dielectric properties. Materials and Design. 2014;**56**:398-404

[35] Papageorgiou G, Achilias D, Nianias N, Trikalitis P, Bikiaris D. Effect of the type of nano-filler on the crystallization and mechanical properties of syndiotactic polystyrene based nanocomposites. Thermochimica Acta. 2013;**565**:82-94

[36] Vimala K, Mohan YM, Sivudu KS, Varaprasad K, Ravindra S, Reddy NN, Padma Y, Sreedhar B, MohanaRaju K. Fabrication of porous chitosan films impregnated with silver nanoparticles: A facile approach for superior antibacterial application. Colloids and Surfaces B: Biointerfaces. 2010;**76**:248-258

[37] Gautam A, Ram S. Preparation and thermomechanical properties of Ag–PVA nanocomposite films. Materials Chemistry and Physics. 2010;**119**:266-271

[38] Tamayo LA, Zapata PA, Rabagliati FM, Azócar MI, Muñoz LA, Zhou X, Thompson GE, Páez MA. Antibacterial and non-cytotoxic effect of nanocomposites based in polyethylene and copper nanoparticles. Journal of Materials Science. Materials in Medicine. 2015;**26**(129)

[39] Chandola M, Tiwari S, Babar R, Chikte P, Mundhe G, Hivrale V, Marathe S. Controllable refractive index of PVA-Ag films. International Journal of Innovative and Emerging Research in Engineering. 2016;**3**(4):43-45

[40] Fatema UK, Rahman MM, Islam MR, Mollah MYA, Md ABHS. Silver/poly(vinyl alcohol) nanocomposite film prepared using water in oil microemulsion for antibacterial applications. Journal of Colloid and Interface Science. 2018;**514**:648-655

[41] Espana-Sanchez España-Sanchez BL, Avila-Orta CA, Padilla-Vaca F, Neira-Velazquez MG, Gonzalez-Morones P, Rodriguez-Gonzalez JA, Hernandez-Hernandez E, Rangel-Serrano A, Barriga-c ED, Yate L, Ziolo RF. Enhanced antibacterial activity of melt processed polypropylene Ag and Cu nanocomposites by argon plasma treatment. Plasma Processes and Polymers. 2014;**11**:353-365. https://doi.org/10.1002/ppap.201300152

[42] Zapata PA, Tamayo L, Páez M, Cerda E, Azócar I, Rabagliati FM. Nanocomposites based on polyethylene and nanosilver particles produced by metallocenic "in situ" polymerization: Synthesis, characterization, and antimicrobial behavior. European Polymer Journal. 2011;**47**:1541-1549

[43] Anyaogu KC, Fedorov AV, Neckers DC. Synthesis characterization, and antifouling potential of funtionalized copper nanoparticles. Langmuir. 2008;**24**:4340-4346

[44] Longano D, Ditaranto N, Cioffi N, Di Niso F, Sibillano T, Ancona A, Conte A, Del Nobile MA, Sabattini L, Torsi L. Analytical characterization of laser-generated copper nanoparticles for antibacterial composite food packaging. Analytical and Bioanalytical Chemistry. 2012;**403**:1179-1186

[45] Owens DE III, Eby JK, Jian Y, Peppas NA. Temperature responsive polymer-gold nanocomposites as intelligent therapeutic systems. Journal of Biomedical Materials Research Part A. 2007:692-695

[46] Paul DR, Robeson LM. Polymer nanotechnology: Nanocomposites. Polymer. 2008;**49**: 3187-3204

[47] Muraviev DN, Macanas J, Farre M, Munoz M, Alegret S. Novel routes for inter-matrix synthesis and characterization of polymer stabilized metal nanoparticles for molecular recognition devices. Sensors and Actuators B: Chemical. 2006;**118**:408-417

[48] Malinauska A, Malinauskiene J, Ramanavicius A. Conducting polymer-based nanostructurized materials: Electrochemical aspects. Nanotechnology. 2005;**16**:R51-R62

[49] Folarin OM, Sadiku ER, Maity A. Polymer-noble metal nanocomposites: Review, International Journal of the Physical Sciences. 2011;**6**(21):4869-4882

Chapter 4

Hybrid Nanocomposites Produced by Sputtering: Interaction with Eukaryotic and Prokaryotic Cells

Ana Paula Piedade

Additional information is available at the end of the chapter

http://dx.doi.org/10.5772/intechopen.79048

Abstract

The use of composite materials for different and diverse technological applications is a growing field. The development of this class of materials arises when it is required from a material a combination of properties that are impossible to co-exist, such as, for example, high hardness and good tenacity. However, in some applications the main focus of this combination of characteristics/properties is only required at the material surface; in this cases, the composite will be deposited onto the surface as a coating. Moreover, the introduction of reinforcements of nanometric size, where one of the dimensions is lower than 100 nm, may induce, in the deposited composite, particularly appealing properties due to the nanometric scale. This chapter presents the use of a particular deposition technique—sputtering—for the production of nanocomposites made of dissimilar materials such as ceramic/metal, ceramic/polymer and ceramic/polymer/metal. The application of these surfaces in interaction with both eukaryotic and prokaryotic cells will be given as an example of the broad range of applications of the developed surfaces.

Keywords: hybrid nanocomposites, sputtering, dissimilar materials, thin films, prokaryotic and eukaryotic cells

1. Introduction

In this introduction, a brief overview of the sputtering process is given based on a working class manuscript [1], but excellent reviews on the process have been published (see, e.g., Ref. [2]).

Sputtering is one of the techniques of coating a material by physical vapor deposition (PVD). Sputtering consists in the ejection of particles, atoms or clusters, by the bombardment of a solid or target by energetic particles, mostly ions. It results from collisions between the

incident energetic particles, and/or resultant recoil atoms, with surface atoms. A measure of the removal rate of surface atoms is the sputter yield Y, defined as the ratio between the number of sputter ejected species and the number of incident particles. Sputtering only occurs if the incident particles have enough energy to overcome the binding energy of the elements that constitute the material. In a deposition chamber under reduced pressure, a discharge is established between the cathode (target material from where the particles are ejected) and the anode (substrate onto which the coating will be formed). Usually there are three distinct phases in the sputtering process: (i) ejection of the target material; (ii) transport of the ejected material and (iii) nucleation and growth of the film. The control of several deposition parameters in each one of these three phases allow to a perfect control over the deposited thin film and obtaining tailor made materials, which are not predicted by conventional thermodynamics.

The ejection of the target material is achieved by simply momentum transfer between the ionic rare gas positive ions with the constituent material of the target. Argon is one of the most commonly used rare gases. It is an inert gas and therefore has the advantage of not change the chemistry of the target material by reacting with the ejected species. It has an atomic weight that guarantees the adequate sputtering of most of the chemical elements, has a low cost and high availability in the market, and can be purchased with high purity. In the course of the ionization inside the chamber, a plasma is formed which needs to be stable, in order for the process to proceed. In order to induce the plasma positive ions collision with the target, they must be accelerated by a negative potential. For this reason, the applied deposition power must be high, so that the ions can acquire sufficient energy to promote the ejection of secondary electrons from the target, contributing to the maintenance of plasma. The pressure in the deposition chamber needs to be well-controlled in order to promote a high number of collisions between the secondary electrons and the gas atoms, allowing ionization to proceed and ensure the maintenance of the plasma. However, it must not be too high, as in this case, argon ions will suffer too many collisions in their path, diminishing the free mean path, leading to loss of energy and arriving at the target with lower energy that the one needed to promote sputtering.

If they have enough energy, the ejected particles from the target are transported through the plasma to the substrate, where they eventually deposit and form the coating. The trajectory of the ejected particles is random, in their direction, following a cosine law. The process of the formation of the coating can also be considered in three phases (**Figure 1**). In the first phase, the atoms ejected from the target transfer their kinetic energy to the substrate, becoming "adatoms," that is, nonbonded atoms. In the second phase, the adatoms diffuse superficially over the substrate where they either suffer desorption or are accommodated in a low surface energy location onto the substrate. Finally, the third phase takes place when the atoms readjust their position in the network by bulk diffusion processes.

The properties of the films deposited by this technique depend on the material of the target, the gas used for the discharge and deposition parameters such as pressure, target-distance, polarization of the substrate and the chemical composition of the discharge gas. In fact, in addition to the nonreactive noble gas, the discharge gas, others can be added such as oxygen, nitrogen or methane. In these cases, the sputtering is said to occur in a reactive mode. The use of a magnetron associated with the cathode creates a magnetic field that imposes compulsory trajectories to the electrons ejected by the target, increasing the bombardment density.

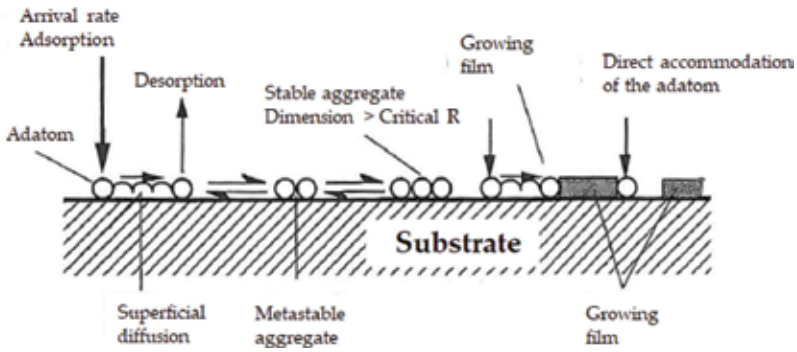

Figure 1. Schematic representation of the nucleation and grow of a film deposited by sputtering.

2. Production of nanocomposites

The use of composites is usually required when the materials or its surface must present a combination of properties/characteristics that are not possible to obtain from a single material. The materials for the matrix can be either organic, polymeric materials, or inorganic, such as ceramics and metals or metal alloys. In addition, the fillers can belong to these two classes of materials. When one of the dimensions of the filler is of nanometric scale, lower than 100 nm, it is called nanofiller and the resulting material a nanocomposite. The most commonly used inorganic nanofillers are carbides, nitrides, borides, oxides, metallic particles, clay, carbon nanotubes, nanodiamond and, more recently, graphene. Regarding the organic nanofillers, the most common, depending on the application, are polytetrafluoroethylene, nanocellulose fibers or cellulose nanocrystals. Nevertheless, some combinations of matrix and reinforcement are not able to be produced by conventional methods. In fact, the reinforcement of a metallic matrix with an organic nanofiller is forbidden, as the processing temperature of the metal material occurs at a temperature that completely degrades the organic filler. There are an extensive number of excellent reviews on the production of nanocomposites (see Refs. [3, 4] as examples) and some brief examples, based in these two references, are given.

The sol–gel method is suitable for obtaining nanocomposites coatings with a thickness up to 1 μm. However, the method presents several drawbacks, namely its application onto metallic substrates, crackability and not appropriate if a thermal treatment is required. This method can be used in combination with sputtering or electrodeposition.

Chemical vapor deposition (CVD) method is usually used for the fabrication of inorganic/inorganic nanocomposites coatings and, sometimes, in order to improve the quality of the coatings, the aerosol-assisted CVD can be used. Some organic (matrix)/inorganic nanocomposites have also been produced by this method.

Physical vapor deposition (PVD) technology includes evaporation and sputtering, among other less used technologies. It can be used for the production of hybrid nanocomposites and, especially sputtering, as described in the next point of this chapter, is one of the most versatile for the production of a great combination of inorganic/organic nanocomposites.

The thermal spray method is often used for making nanocomposites with a metallic matrix. The spray material is a nanosized metallic or alloyed powder that is dispersed into a solution in order to conduct plasma thermal spraying.

Electroless deposition method is often used for producing nanocomposite coatings with polymeric matrix where the nanofillers are carbides, nitrides, borides or other polymers. In order to improve the mechanical and degradation properties of the coatings, a thermal treatment is made.

Electrodeposition method is used for the production of nanocomposites which contain organic nanofillers dispersed in organic or inorganic matrix. By changing the duty cycle and frequency during pulsed electrodeposition can also produce nanocomposite coatings.

Spray coating and spin coating methods are widely used for the preparation of polymeric-based nanocomposites. However, the latter can only be used for coating flat substrates and, therefore, is mostly used for the preparation of thin-film nanocomposite coatings.

Dip coating is a method widely used in the industry. It consists of soaking the substrate in a solution with the nanocomposite and pulled up at a constant and controlled speed. Some of the advantages of this method are that the solution can be reused until evaporation or depletion. The disadvantages are mainly related with the poor adhesion between the substrate and the coating, which makes this method unsuitable for a number of applications.

3. Application of sputtered hybrid nanocomposites

3.1. Interaction with eukaryotic cells

With the advance of technology and medical research, the replacement of hard tissues is essential for improving the quality of life of an aging population. Implants placed in contact with biological tissues should promote a positive response; they must be bioactive and biocompatible. For orthopedic and orthodontic applications, hydroxyapatite (HA) is the gold standard due to its chemical mimicking of the inorganic constitution of human hard tissue [5]. The use of HA as a coating is justified when the economic factor imposes and cheaper bulk materials, such as 316L stainless steel, are used to replace the much more expensive commercial pure titanium (Ti cp) or titanium alloys.

The use of HA-based nanocomposites has been described in the literature. One of the elements used to dope HA coatings is yttrium (Y) which is a transition metal with hydrophilic characteristics [6], used to improve the mechanical properties of ceramic materials [7] and, when bonded to hydroxyapatite, lowers its electrical resistance. When yttrium reinforced hydroxyapatite was used as a coating, it was found to possess a greater ability to form apatite when in contact with biological fluids than the HA coating [8].

Magnesium (Mg) is an element that is involved in the early mineralization process and is necessary to ensure adequate function of osteoblasts and osteoclasts. For this reason, studies are also reported in the literature in which HA coatings are doped with this element. The effect of the incorporation of magnesium in HA on the adhesion of osteoblasts showed that cell adhesion

was higher in the co-deposited samples compared to the control samples without Mg [9]. Another element that is known to cause the increase of the number of osteoblasts and reduce the activity of osteoclasts is strontium (Sr). This is the reason why it is recommended in several countries as treatment of osteoporosis [10]. Its integration into hydroxyapatite coatings demonstrated a 46% increase in the area of contact between bone and implant when compared to the HA monolithic coatings [11]. This study also demonstrated that the osteoconductivity of doped coatings was not only faster but also provided a better quality of bone-implant integration.

Moreover, other metallic elements such as cobalt (Co), chromium (Cr) and nickel (Ni) were used in hydroxyapatite composites [12] to study their effect on the *in vitro* growth of an apatite layer. This study demonstrated that metal ions can be incorporated during the mineralization process affecting its structure and size and, consequently, the quality of the mineral coating.

Also, all ceramic composites, such as those obtained from the incorporation of ZrO_2 into HA, decreased the porosity and surface area of the coating and inhibited the proliferation of microorganisms, implying their possible use as biomaterials that may reduce the inflammatory process, according to a published study [13]. The same type of nanocomposites was also obtained by adding TiO_2 (10 wt%) to HA to determine the potential of the composite in the development, adhesion and growth of mesenchymal cells, as well as their ability to differentiate into osteoblasts. The results indicated that TiO_2-HA coatings were structurally nanocomposites with highly osteoinductive capacity, allowing their possible use as coatings for implants that support high loads. Moreover, also doping HA films with magnesium oxide (MgO) allowed to obtain better corrosion resistance and lower porosity of the coatings both when in contact with simulated human fluids and under conditions of osteoclastic resorption *in vivo* [14].

Silicon (Si) is a chemical element that is found in active zones of calcification. Its absence is associated with a poor production of collagen that reduces bone proliferation leading to the appearance of deformations and lesions. For this reason, it is a very important chemical element in the early stages of bone mineralization and soft tissue development [15]. Some of the invoked benefits are related to the release of small amounts of silicon ions, which stimulate the activity of seven families of genes, increasing osteoblasts proliferation and differentiation. In addition, silicon increases the solubility of the coatings by generating a more electronegative surface resulting in a surface biologically equivalent to apatite [16]. The development, in our laboratory, of hybrid sputtered nanocomposite HA/Si coatings confirmed these claims and the results presented here have never been published before.

The coatings were deposited, onto 316L stainless steel, by sputtering r.f. magnetron from HA target doped with silicon foils. The choice of steel is related to economic factors (especially in the context of economic crisis) given the price of the materials used in this type of implant—titanium and its alloys. The use of 2 and 4 10 × 10 mm Si foils gave rise to coatings with atomic percentages of Si of 2 (HA/Si2) and 4 (HA/Si4), respectively.

The thin films, with thickness of approximately 700 nm, demonstrated a nanocomposite structure (**Figure 2**) with an average surface roughness (Sa) of 15 , 63 and 29 nm for HA, HA/Si2 and HA/Si4, respectively. All the surfaces presented moderate overall hydrophilic characteristics, although the surfaces of HA doped with elemental Si reveal a heterogeneous distribution of

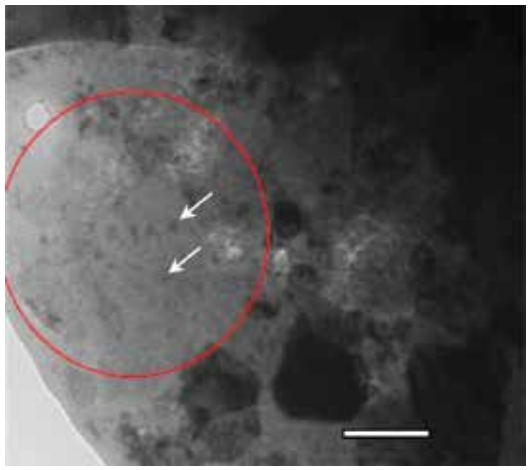

Figure 2. TEM bright field image of HA4 sample, highlighting the heterogeneous distribution (circle) of the nanosized Si (arrows); bar = 100 nm.

hydrophobic domains, as determined by dynamic contact angles studies (**Figure 3**). This can be related with the heterogeneous distribution of Si onto the HA matrix as reveled by the bright field TEM micrograph. In fact, the addition of Si changes the behavior of the monolithic HA coating. For surface HA2, it is apparent that the forward angle is not constant revealing the existence of heterogeneously hydrophobic domains distributed on the surface, which also influence the value of the contact angle during the retraction step. When the content of the reinforcement element increases, HA4, this behavior is more evident since the presence of the hydrophobic domains prevents the free spreading of the water causing the contact angle to increase from 40° to about 140°. When the volume of water is high enough to overcome this barrier, the liquid spreads freely reaching a value that remains constant during the step of decreasing the volume of liquid.

For biomedical applications, a surface charge value, given by the zeta potential (ζ), between −30 and 30 mV is considered unstable. Therefore, it is required that the potential value of the surfaces stays outside this range. Also, the pH value is a factor that influences the value of the zeta potential. In fact, the physiological pH comprises the minimum values of 6.8 (denominated acidosis) to a maximum limit of 8.0 (denominated alkalosis), being its normal value 7.4. The evaluation of zeta potential, in a KCl 1 mM solution, between pH values of 3 and 10 showed that the produced monolithic and nanocomposites thin films present stable zeta potential values, for the range of biological pH values. Moreover, for the physiological pH value all the sputtered surfaces have lower zeta potential values than the 316L substrate (−35.8 mV), determined with the same electrolyte. Published studies [17] show that a more negative zeta potential value implies a better adsorption of the extracellular matrix and increases binding of fibroblasts. It should be highlighted the higher standard deviation observed in the determination of the zeta potential values of sample HA 4 (−80 ± 30 mV), which indicates that the surface is reacting with the electrolyte. This observation is valuable for the envisaged application, where the dissolution of the coating with the consequent deposition of an apatite like layer is mandatory for a good osteoinductive coating.

http://dx.doi.org/10.5772/intechopen.79048

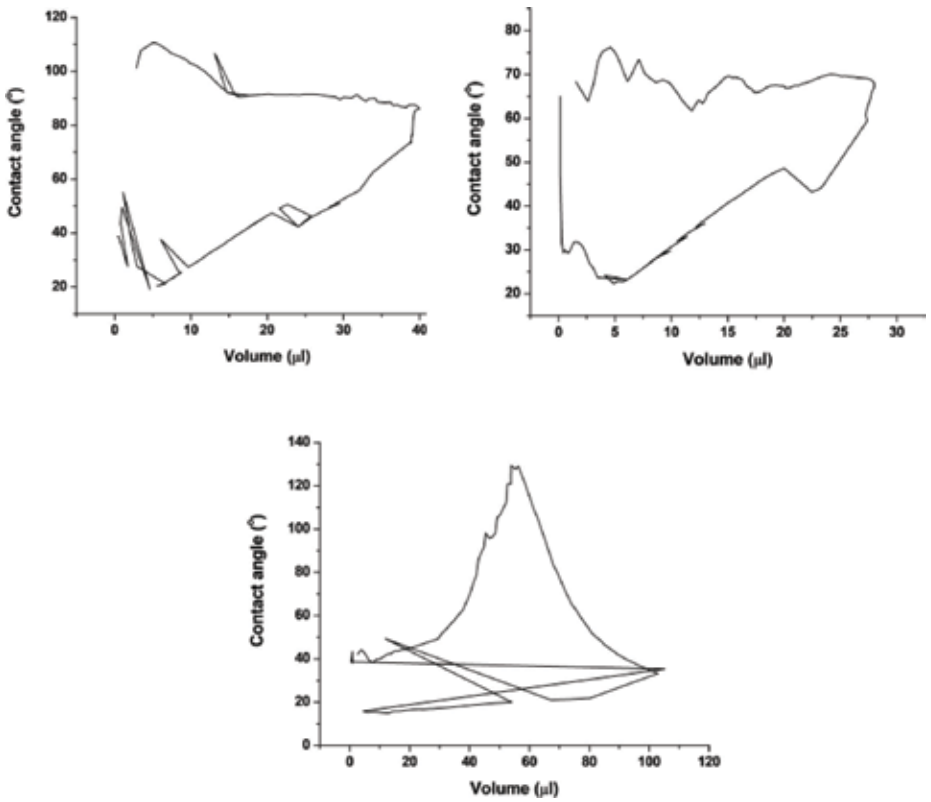

Figure 3. Dynamic contact angle characterization of surfaces (a) HA, (b) HA2 and (c) HA4.

When preliminary *in vitro* tests were made, by 14 days immersion in Hanks balanced salt solution (HBSS), at 37°C, under shaking conditions (100 rpm), the formation of an apatite like layer was more exuberant in the HA4 coating due to the more rapid dissolution of the Si ions as expected from the previous results (**Figure 4**).

All the previous characterization indicated that the hybrid nanocomposite HA4 could induce a better interface for the adhesion and proliferation of osteoblastic cells. For this reason, all the films were tested with MG63 osteoblastic cells line. This biological system allows a homogenous and proliferative population that contains phenotypic characteristics of normal osteoblastic cells, including hormonal response and genetic expression, and is frequently used as an osteoblast model for *in vitro* studies. The confocal laser microscopy images (**Figure 5**) show that MG63 cells adhere to all surfaces, as can be seen in the images corresponding to day 1.

The HA film shows cells with rounded morphology and also with elongated morphology. Comparatively, cell adhesion and cytoplasmic growth are more pronounced in the films HA2 and HA4, where the cells have a typical elongated morphology, expected for 24 h cultures and greater cytoplasmic expansion. After 5 days, the MG63 cells proliferated on the surfaces which are partially covered by an organized cell layer. The images suggest that the proliferation is more abundant in the HA2 and HA4 surfaces when compared to the HA surface. In the latter

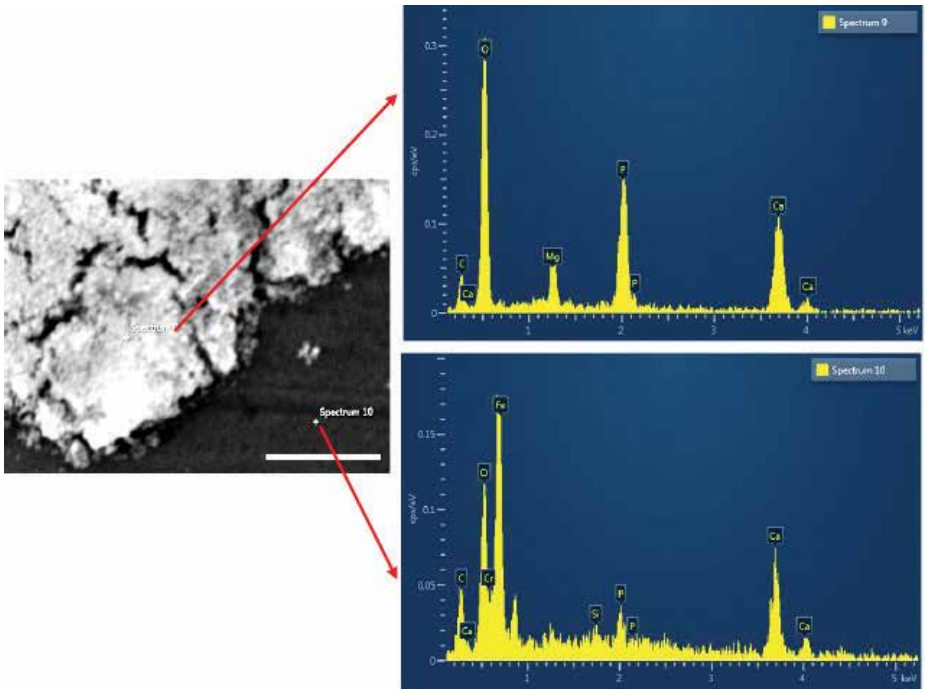

Figure 4. Scanning electron microscopy micrograph of the HA4 after 14 days in Hanks solution. The energy disperse spectra show that the formed layer is composed of the same chemical elements as apatite.

occurred an abnormal proliferation of cellular clusters in which cell division occurred, but not a normal cytoplasmic expansion, presenting an altered F-actin cytoskeleton. In comparison, HA2 and HA4 nanocomposite surfaces exhibit an organized cell layer with elongated/polygonal morphology, normal organization of the cytoskeleton F-actin (with greater staining intensity at the cell boundaries) and perfect contact between cells.

In summary, the addition of silicon to hydroxyapatite, in the form of hybrid nanocomposite thin films, induces a set of properties/characteristics that are ideal for promoting cell adhesion and proliferation: controlled structural order, good wettability, concordant surface charge, nanometer scale size and surface nanotopography.

3.2. Interaction with prokaryotic cells

In order to give a different perspective of the same problem, the prevention of bacterial infection in orthopedic implants will be presented. Especial relevance will be given to hydroxyapatite (HA) coatings doped with two known antibacterial elements: silver (Ag) and fluorine (F).

Over the past decades, several studies have been made concerning the antibacterial effect of HA-Ag coatings in order to evaluate their efficiency [18–21]. Despite some contradictory results, it is generally accepted that silver can contribute for the antibacterial effect although the mechanisms responsible for this action is far from being completely understood [22]. It also known that the nanometric size of the silver particles in the composite is responsible

http://dx.doi.org/10.5772/intechopen.79048

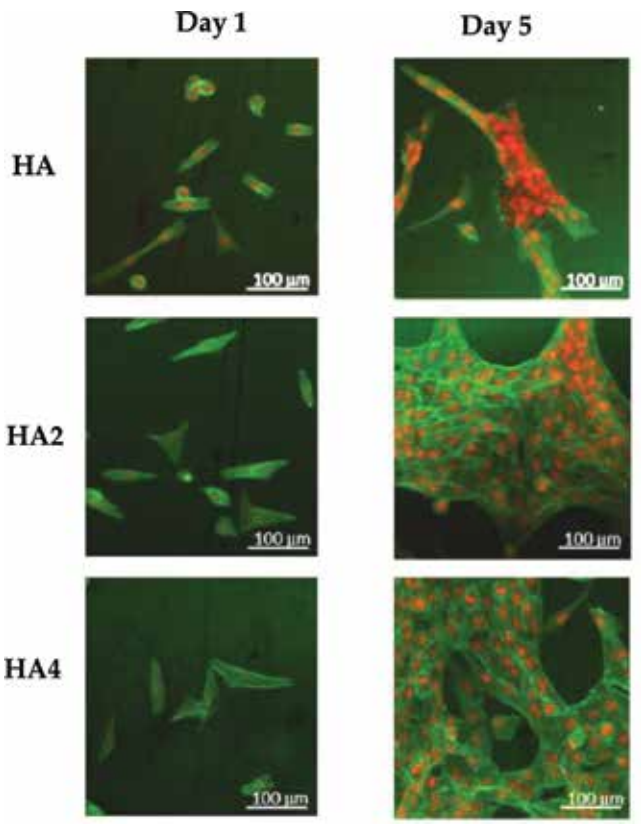

Figure 5. Confocal laser microscopy images of the nanocomposites after 1 and 5 days of culture with MG63 cells (red = nucleus; green = F actin from cytoskeleton).

for a more efficient effect [23] due to the more rapid kinetic of silver ions production, when compared with micrometric size silver.

Concerning the effects of fluorine, some of the studies done on HA coatings have focused on the incorporation of this element into the hydroxyapatite structure, $Ca_{10}(PO_4)_2F_x(OH)_{2-x}$, where the F^- ions replace the OH^- groups. The results show that by incorporating fluorine it is possible to improve the characteristics of hydroxyapatite [17]. HA with hydroxyl groups partially replaced by F has been the subject of some investigation due to the considerable presence of partially fluoridated HA in bones and teeth. Fluoride promotes the mineralization and crystallization of calcium phosphate in the dental and bone development process, also enhances the differentiation of osteoblasts in cell culture. Additionally, HA coatings with F can provide low enough levels of this element to improve bone formation by enhancing cell attachment [24]. Several studies with HA/F coatings have been published, were the effect of fluorine is assessed as an antimicrobial agent [25, 26].

Results from sputtered HA, HA/F, HA/Ag and HA/F/Ag coatings developed in our laboratory, and never published before, will be presented. Moreover, the incorporation of F is achieved by the co-sputtering from HA and polytetrafluoroethylene (PTFE) targets, while

the introduction of Ag in the nanocomposite is achieved by doping the HA target with one Ag foils (10 × 10 mm), which induces a 8 at.% of silver in the coating. The use of PTFE as fluorine source in hybrid nanocomposites HA-based coatings has never been described in the consulted literature. The deposition parameters were chosen in order to obtain 1 at.% of F in the nanocomposite coatings. This ensures that the amount of released fluorine ions is not toxic for the eukaryotic cells. The coatings were deposited onto 316L stainless steel and Ti cp.

The thickness of all thin films was around 200 nm except for the HA/F/Ag system with 300 nm. The mean surface roughness (Sa), evaluated in the coatings deposited onto polished 316L stainless steel, was around 10 nm for all the coatings, except for the HA/F nanocomposite with a value of 25 nm. Also, the nanocomposite structure of the films was observed by transmission electron microscopy (TEM) (**Figure 6**), where is possible to see, for the HA/F/Ag coating, nanosized silver dispersed onto the amorphous HA and PTFE matrix.

The wettability of the surfaces was evaluated by static contact angle, using water and formamide. The use of two liquids, with distinct surface tensions, allowed to calculate the surface energy (γs) as the sum of its dispersive (γs^d) and polar (γs^p) components [27]. The results in **Table 1** show that regarding the contact angles with water the HA monolithic coating is the more hydrophilic and that both F and Ag addition decrease slightly that characteristic. In what concerns the surface energy of the surfaces, more important than the total value of surface tension is the ratio between its polar and dispersive components. In fact, the polar component gives an idea of the amount of polar groups, with hydrophilic characteristics, which are present.

Of the studied surfaces, the one with the largest polar component is HA. The addition of F, from PTFE target, decreases this value due to known hydrophobic behavior of this polymer. However, its small concentration does not allow for a great decrease in the polar component. The slight decrease of the polar component in the HA/Ag thin film is due to the presence of the metal element having markedly hydrophobic characteristics. However, given that its content

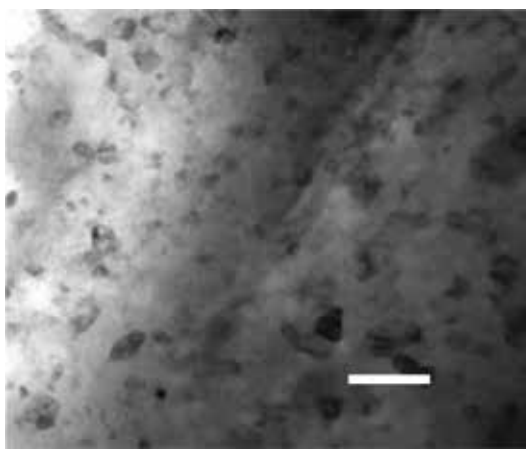

Figure 6. TEM bright field image of HA/F/Ag coating showing the nanocomposite structure of the hybrid sputtered thin film (bar = 100 nm).

http://dx.doi.org/10.5772/intechopen.79048

Surfaces	Contact angle (°)		Surface energy (mJ.m^{-2})		
	Water	Formamide	γs^d	γs^p	γs
HA	35	15	55.9	8.7	63.6
HA/F	40	41	44.3	8.3	52.6
HA/Ag	50	57	32.3	7.5	39.8
HA/F/Ag	53	29	41.7	7.2	48.9

Table 1. Contact angle and surface energy of the monolithic and HA-based nanocomposites thin films.

in the film is only 8% at, its contribution to the reduction of γs^p cannot be very marked. The HA/F/Ag coating is the one with the greatest decrease in the polar component, since both silver and PTFE contribute to the hydrophobicity.

The surface hydrophilicity and surface charge strongly influences the biological response of a biomaterial, since hydrophilic surfaces do not favor the adsorption of proteins because it is an energetically unfavorable process. The hydrophilicity allows the surfaces to become more efficient in cell attachment, which in this study is important factor since the coatings are designed to induce better osseointegration of implant/bone cells. It is also intended that the coating has a good antibacterial activity, and the free energy of the surface has a significant influence on bacterial adhesion. However, Vogler [28] claims that it is not possible to control the bacterial binding solely by the handling of surface energy. Thus, there is no concrete data to support the claim that a hydrophilic surface is detrimental to good antibacterial activity.

The zeta potential values of the surfaces determined in KCl 1 mM pH 7.4 electrolyte presented very similar values between −81 and −87 mV. These values are more negative than those obtained, for the same electrolyte, with 316L and Ti cp surfaces: −35.8 and −60 mV, respectively. This fact, as explained in the previous section, is very positive as a more negative surface charge implies a better adhesion and proliferation of osteoblastic cells [17].

In order to assess the amount of fluorine release by the HA/F and HA/F/Ag nanocomposites coatings, these samples were immersed, during 30 days in simulated body fluid (SBF) at 37°C with shaking (100 rpm). The fluorine content was measured with a fluorine electrode. The results (**Figure 7**) show, with the help of the trend line, that the amount of fluoride in the solution increase during the first 5 days and after the 10th day the quantity of fluorine in the solution tends to stabilize. The release of F ions is low enough to aid bone formation and at the same time noncytotoxic for the cells.

The antibacterial activity of the coatings were tested by the inhibition growth halo test, which consist of plaiting the selected bacterial strain into solid agar plates with the appropriate culture medium. The surfaces are then placed in contact with the plated microorganism and, after incubation, the plates are observed to see the existence, or absence, of a halo around the tested sample. Its presence indicates that the bacteria did not grow due to the antibacterial effect of the tested sample. In this study, the deposited monolithic and nanocomposite surfaces were tested against *Staphylococcus epidermidis*, a known Gram-positive bacteria.

The results revealed that, after 24 h of incubation, only the surfaces with Ag gave rise to the appearance of an inhibition growth halo, which was bigger in HA/Ag than for HA/F/Ag, 2.6 and 1.4 mm, respectively. The absence of inhibition halo around the samples with fluorine (HA/F) was surprising as this element is cited as an antibacterial agent. The surfaces were then observed by scanning electron microscopy (SEM) (**Figure 8**).

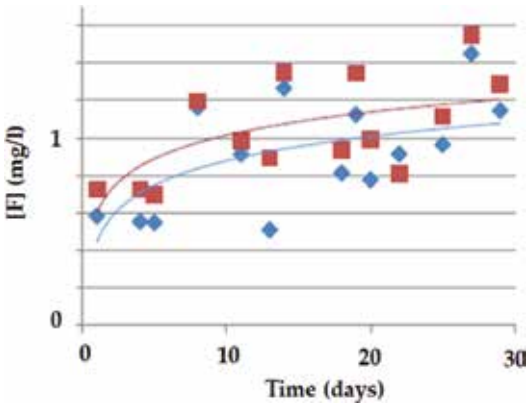

Figure 7. Release of fluorine from HA/F (blue) and HA/F/Ag (red).

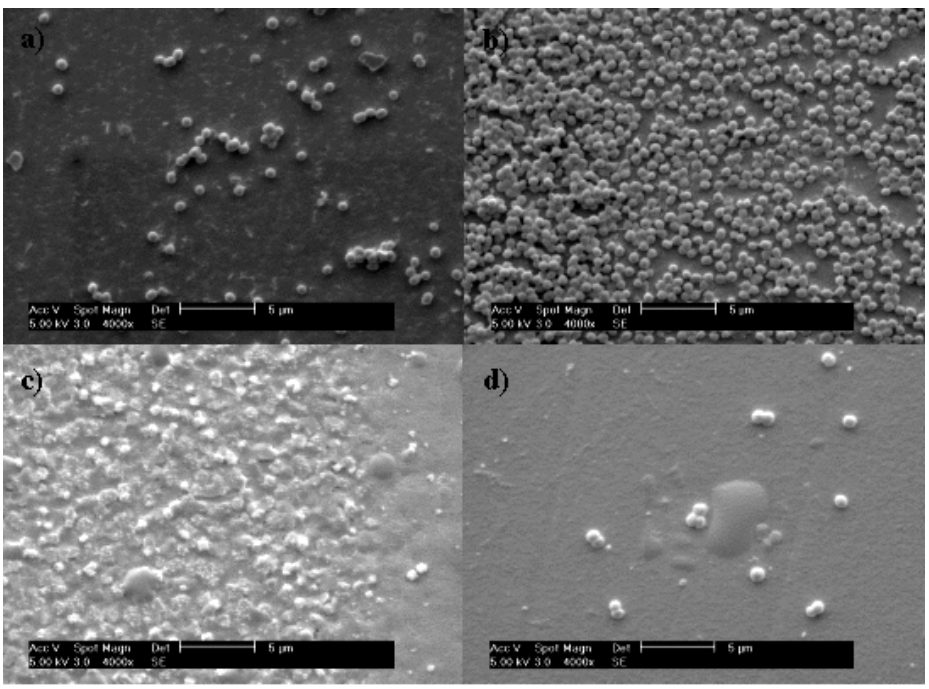

Figure 8. SEM micrographs of the surface of the produced coatings after 24 h of contact with *Staphylococcus epidermidis.*

Through this characterization, it was possible to better understand the way bacteria interacted with the different surfaces. It is possible to note that the HA/F surface is the surface with the greater bacteria colonization, which leads to the conclusion that the presence of fluorine in the coating does not induce any inhibition. This observation is in contradiction with some published results [25] where fluoride HA coating presented a higher antibacterial rate than a monolithic HA coating. However, the observations are in accordance with other published research [29] that concluded that the increase of fluoride ions leads to an increase of bacterial adhesion. As expected, the monolithic HA coating did not present any antibacterial activity. For all surfaces, the bacteria retain their morphology, except in the HA/Ag coating, where it is visible cellular matrix, which is a consequence of the loss of cell wall integrity. Thus, the few cells that colonize the surface do not survive.

In summary, in what concerns the antibacterial activity of hybrid nanocomposite sputtered thin films, each system must be designed and thoroughly characterized in order to understand their real ability has an antimicrobial surface. As explained, the literature is contradictory in some of the real effect of the so-called antibacterial chemical elements that are used to develop nanocomposite coatings.

4. Conclusions

Sputtering is a very versatile technology for the production of hybrid nanocomposite thin films. The ability to develop materials that are not predicted by conventional thermodynamics inheres this technology as one of the best for the development of tailor-made surfaces. In this chapter, it has been highlighted this capacity by describing HA-based hybrid nanocomposites that can be designed to increase the osseointegration of metallic materials usually used for implants with contact with biological hard tissue. The HA-based nanocomposites hybrid coatings were also chosen to demonstrate the capacity of developing hybrid ceramic/polymer/metal nanocomposites with good antibacterial activity. The combination of these three types of materials in one surface is almost impossible to obtain, except by the use of the sputtering technique.

Acknowledgements

This work was partially supported by the Foundation of Science and Technology of Portugal through the project UID/EMS/00285/2013. The author also acknowledges C. Fernandes, S. Neves, R. Branco and P. Morais for their contribution in some of the presented results.

Conflict of interest

The author declares no conflict of interest.

Author details

Ana Paula Piedade

Address all correspondence to: ana.piedade@dem.uc.pt

CEMMPRE-Department of Mechanical Engineering, University of Coimbra, Coimbra, Portugal

References

[1] Cavaleiro A, Vieira MT. Textos de apoio às disciplinas de engenharia de superfícies e degradação de superfícies. Department of Mechanical Engineering, University of Coimbra; 1993

[2] Nastasi M, Mayer J, Hirvonen JK. Ion-solid interactions: Fundamentals and applications. Cambridge Solid State Science Series. Cambridge: Cambridge University Press; 2010. p. 540. DOI: 10.1017/CBO9780511565007

[3] Nguyen-Tri P, Nguyen TA, Carriere P, Xuan CN. Nanocomposite coatings: Preparation, characterization, properties, and applications. International Journal of Corrosion. 2018;article ID 4749501:19. DOI: 10.1155/2018/4749501

[4] Mehram QM, Fazal MA, Bushroa AR, Rubaiee S. A critical review on physical vapor deposition coatings applied on different engine components. Critical Reviews in Solid State and Materials Sciences. 2018;**43**:158-179. DOI: 10.1080/10408436.2017.1320648

[5] Zhou H, Lee J. Nanoscale hydroxyapatite particles for bone tissue engineering. Acta Biomaterialia. 2011;**7**:2769-2781. DOI: 10.1016/j.actbio.2011.03.019

[6] Newham RE. Composite electroceramics. Ferroelectrics. 1986;**68**:1-32. DOI: 10.1080/00150198608238734

[7] Gulgun MA, Voytovych R, Maclaren I, Ruhle M. Cation segregation in an oxide ceramic with low solubility: Yttrium doped α-alumina interface. Science. 2002;**10**:99-110. DOI: 10.1023/A:1015268232315

[8] Sato M, Sambito MA, Aslani A, Kalkhoran NM, Slamovich EB, Webster TJ. Increased osteoblast functions on undoped and yttrium-doped nanocrystalline hydroxyapatite coatings on titanium. Biomaterials. 2006;**27**:2358-2369. DOI: 10.1016/j.biomaterials.2005.10.041

[9] Mroz W, Bombalska A, Burdynska S, Jedynski M, Prokopiuk A, Budner B, Scislosarczyk AS, Zima A, Menaszek E, Ścisłowska-Czarnecka A, Niedzielski K. Structural studies of magnesium doped hydroxyapatite coatings after osteoblast culture. Journal of Molecular Structure. 2010;**977**:145-152. DOI: 10.1016/j.molstruc.2010.05.025

[10] Roy M, Banyopadhyay A, Bose S. Induction plasma sprayed Sr and Mg doped nano hydroxyapatite coatings on Ti for bone implant. Journal of Biomedical Materials Research Part B. 2011;**99**:258-265. DOI: 10.1002/jbm.b.31893

[11] Yan J, Sun JF, Chu PK, Han Y, Zhang YM. Bone integration capability of a series of strontium-containing hydroxyapatite coatings formed by micro-arc oxidation. Journal of Biomedical Materials Research Part A. 2013;**101**:2465-2480. DOI: 10.1002/jbm.a.34548

[12] Mabilleau G, Filmon R, Petrov PK, Baslé MF, Sabokbar A, Chappard D. Cobalt, chromium and nickel affect hydroxyapatite crystal growth in vitro. Acta Biomaterialia. 2010;**6**:1555-1560. DOI: 10.1016/j.actbio.2009.10.035

[13] Bermúdez-Reyes B, Espinoza-Bertrán FJ, Espitia-Cabrera I, Contreras-García ME. Characterization of HA/ZrO_2-base bilayer on 316L stainless steel substrates for orthopedic prosthesis applications. AZojomo. 2008;**4**:1-12. DOI: 10.2240/azojomo0264

[14] Sreekanth D, Rameshbabu N. Development and characterization of MgO/hydroxyapatite composite coating on AZ31 magnesium alloy by plasma electrolytic oxidation coupled with electrophoretic deposition. Materials Letters. 2012;**68**:439-442. DOI: 10.1016/j.matlet.2011.11.025

[15] Carlisle EM. Silicon: A possible factor in bone calcification. Science. 1970;**167**:279-280. DOI: 10.1126/science.167.3916.279

[16] Pietak AM, Reid JW, Stott MJ, Sayer M. Silicon substitution in the calcium phosphate bioceramics. Biomaterials. 2007;**28**:4023-4032. DOI: 10.1016/j.biomaterials.2007.05.003

[17] Xe G, Yang L, Fuzeng R, Xu L. Integrity and zeta potential of fluoridated hydroxyapatite nanothick coatings for biomedical applications. Journal of the Mechanical Behavior of Biomedical Materials. 2011;**4**:1046-1056. DOI: 10.1016/j.jmbbm.2011.03.013

[18] Sandukas S, Yamamoto A, Rabiei A. Osteoblast adhesion to functionally graded hydroxyapatite coatings doped with silver. Journal of Biomedical Materials Research Part A. 2011;**97**:490-497. DOI: 10.1002/jbm.a.33081

[19] Ando Y, Miyamoto H, Noda I, Sakurai N, Akiyama T, Yonekura Y, Shimazaki T, Miyazaki M, Mawatari M, Hotokebuchi T. Calcium phosphate coating containing silver shows high antibacterial activity and low cytotoxicity and inhibits bacterial adhesion. Materials Science and Engineering C-Materials for Biological Applications. 2010;**30**:175-180. DOI: 10.1016/j.msec.2009.09.015

[20] Qu J, Lu X, Li D, Ding Y, Leng Y, Weng J, Qu S, Feng B, Watari F. Silver/hydroxyapatite composite coatings on porous titanium surfaces by sol-gel method. Journal of Biomedical Materials Part B. 2011;**79**:40-48. DOI: 10.1002/jbm.b.31784

[21] Stanić V, Janaćković D, Dimitrijević S, Tanasković SB, Mitrić M, Pavlović MS, Krstić A, Jovanović D, Raičević S. Synthesis of antimicrobial monophase silver-doped hydroxyapatite nanopowders for bone tissue engineering. Applied Surface Science. 2011;**257**:4510-4518. DOI: 10.1016/j.apsusc.2010.12.113

[22] Sygnatowicz M. Antimicrobial properties of silver-doped hydroxyapatite nano-powders and thin films. Biological and Biomedical Materials. 2010;**62**:65-70. DOI: 10.1007/s11837-010-0111-x

[23] Jelínek M, Kocourek T, Jurek K, Remsa J, Mikšovský J, Weiserová M, Strnad J, Luxbacher T. Antibacterial properties of Ag-doped hydroxyapatite layers prepared by PLD method. Applied Physics A—Materials Science & Processing. 2010;**101**:615-620. DOI: 10.1007/s00339-010-5911-x

[24] Fathi MH, Zahrani EM. Mechanical alloying synthesis and bioactivity evaluation of nanocrystalline fluoridated hydroxyapatite. Journal of Crystal Growth. 2009;**311**:1392-1403. DOI: 10.1016/j.jcrysgro.2008.11.100

[25] Ge X, Leng Y, Bao C, Xu SL, Wang R, Ren F. Antibacterial coatings of fluoridated hydroxyapatite for percutaneous implants. Journal of Biomedical Materials Research Part A. 2010;**95**:588-599. DOI: 10.1002/jbm.a.32862

[26] Cheng K, Weng W, Wang H, Zhang S. In vitro behavior of osteoblast-like cells on fluoridated hydroxyapatite coatings. Biomaterials. 2005;**26**:6288-6295. DOI: 10.1016/j.biomaterials.2005.03.041

[27] Jie-Rong C, Wakida T. Studies on the surface free energy and surface structure of PTFE film treated with low temperature plasma. Journal of Applied Polymer Science. 1997;**63**:1733-1739. DOI: 10.1002/(SICI)1097-4628

[28] Vogler EA. Structure and reactivity of water at biomaterial surfaces. Advances in Colloid and Interface Science. 1998;**74**:69-117. DOI: 10.1016/S0001-8686(97)00040-7

[29] Puckett SD, Taylor E, Raimondo T, Webster TJ. The relationship between the nanostructure of titanium surfaces and bacterial attachment. Biomaterials. 2010;**31**:706-713. DOI: 10.1016/j.biomaterials.2009.09.081

Chapter 5

Conducting Polymers Incorporated with Related Graphene Compound Films for Use for Humidity and NH_3 Gas Sensing

Nguyen Nang Dinh

Additional information is available at the end of the chapter

http://dx.doi.org/10.5772/intechopen.79060

Abstract

Using spin-coating technique, PEDOT:PSS+GQD+CNT (GPC), PEDOT:PSS+GQD+AgNW (GPA) films used for humidity sensors and P3HT + rGO + CNT (P3GC) films used for NH_3 gas sensors were prepared. At room temperature and atmospheric pressure, all the sensing devices have extremely simple structure and they respond well to the humidity change (for GPC and GPA) and NH_3 gas (for P3GC). The sensitivity of both the GPC and GPA humidity sensing devices was found to be dependent on the additives of CNT or AgNW. For the GPA sensors, the best sensitivity attained a value as large as 15.2% with a response time of 30 s. For the NH_3 gas sensors made from P3GC films with a content of 20 wt.% of rGO and 10% of CNTs, the best performance parameters were obtained, such as responding time of ca. 30 s, sensing response of 0.8% at ammonia gas concentration of 10 ppm and a relative sensitivity of 0.05%/ppm. The fact that the P3HT + rGO + CNT sensors do not respond to humidity suggests useful applications in gas thin-film sensors for selectively sensing ammonia gas in a humid environment.

Keywords: graphene quantum dots (GQDs), polymeric nanocomposite, surface morphology, humidity and NH_3 sensing, sensing response and sensitivity

1. Introduction

Nanocomposites are known as materials mixing two or more different materials, where at least one of these having a nanodimensional phase, for example, conjugate polymers embedded with metallic, semiconducting, and dielectric nanoparticles. In comparison with devices made from standard materials, the nanocomposites based devices usually possess enhanced

efficiency and service life [1–4]. This is because inorganic nanoparticles embedded in conducting polymers can improve the mechanical, electrical, and optical properties such as nonlinear optical behavior, photoluminescence, electroluminescence, and photoconductivity [5–7]. Nanostructured composites or nanohybrid layers containing numerous heterojunctions can be utilized for optoelectronics, organic light emitting diodes (OLEDs), organic solar flexible cells (OSC) [8, 9], etc. Among conducting polymers, polyethylenedioxythiophene:poly(4-styrenesulfonate) (abbreviated to PEDOT:PSS) as a p-type organic semiconductor is well used for the hole transport layer in OLED [10] and OSC [4] as well as for the matrix materials in various sensors [11]. Various nanocomposite films consisting of conducting polymers mixed with carbon nanotubes (CNT) as an active material have been prepared for application in gas thin-film sensors. Recently, Olenych et al. [12] used hybrid composites based on PEDOT:PSS-porous silicon-CNT for preparation and characterization of humidity sensors. The value of the resistance of the hybrid films was as large as 10 MΩ that may have caused a reduced accuracy in monitoring the resistance change versus humidity.

It is known that graphene possesses many excellent electrical properties, since it is an allotrope of carbon with a structure of a single two-dimensional (2D) layer of sp^2 hybridized carbon atoms. Graphene quantum dots (GQDs), as seen in [13, 14], are a kind of 0D material made from small pieces of graphene. GQDs exhibit new phenomena due to quantum confinement and edge effects, which are similar to semiconducting QDs [15]. Graphene and related materials like graphene oxide (GO) or reduced graphene oxide (rGO) as materials used for chemical sensing have significant application potential. This is due to the two-dimensional structure that results in a high sensing area per unit volume and a low noise compared to other solid-state sensors. There were many works reporting on the use of graphene or graphene-related materials for monitoring gases and vapors [16, 17]. Especially, some of the works attempted to connect the advantages of nanoscale metals with that of graphene for the improvement of gas sensor applications [18, 19]. GQDs were mainly used in a single-electron transistor (SET). Besides detecting charge in SETs, GQDs have also been recruited to build electronic sensors for the detection of humidity and pressure [20].

Ammonia is a compound of nitrogen and hydrogen with the formula NH_3; it contributes significantly to the nutritional needs of terrestrial organisms by serving as a precursor to food and fertilizer. With the development of the chemical industry, more and more generation of ammonia gas is brought into the environment. It is known that ammonia gas is a toxic compound; consequently, it is harmful to human health when a large enough concentration of this compound is attained [21]. Thus, production of devices (or sensors) to detect ammonia gas with a large sensitivity and selective property is very important. Many scientific groups have researched and developed gas ammonia sensors for applications. Sensors based on nanostructured inorganic structures like SnO_2, WO_3, TiO_2, etc., have large sensitivity and response time, but the technology for producing both the materials and devices for gas sensors usually requests vacuum and high temperature that results in considerably large expenses [22]. With the aim to reduce these costs, many scientific groups have developed gas sensors based on conducting polymers [23–25]. The advantage of the polymer-based sensors consists of easy fabrication, low power consumption, room temperature operation, etc. [26]. Among the conducting polymers, polyethylenedioxythiophene + poly(4-styrenesulfonate)

(PEDOT:PSS) is the most utilized in organic light-emitting diode (OLED) and in organic solar cells (OSCs). PEDOT:PSS is also used for producing gas like CO [27], NH_3 [17], and vapors of organic solvents or water [18, 19]. We recently reported that PEDOT:PSS-based sensors can detect both ammonia gas [28] and humidity [29]. We have in particular observed that PEDOT:PSS + rGO + AgNWs-based sensors are sensitive to relative humidity (RH%) at a value as low as 30% [29]. This ability for detecting humidity is however a disadvantage when monitoring ammonia or other gases in a humid environment is considered. For practical applications, we need a sensor that is not only sensitive to the gas to be measured, but also selectively detecting toward the gas. During our study of OSCs using poly(3-hexylthiophene) (P3HT) as a photoactive layer [4], we recognized that P3HT films synthetized in air with a humidity larger than RH%60 exhibited a quality as good as when it was synthetized in a dried nitrogen glove-box. This would show that the P3HT structure was not affected by the absorption of water vapor. This observation prompted us to investigate the preparation and characterization of potential P3HT-based sensors for selectively detecting ammonia gas, even in a humid environment.

In this work, we report results of our investigation on the fabrication of graphene-quantum dots and nanocomposites of PEDOT:PSS + GQDs+CNT and P3HT + rGO + CNT. The humidity- and NH_3-sensing properties, respectively, of the first and the second composite films are also presented. Comparison of gas-sensing properties between P3HT- and PEDOT:PSS-based composite films is also made.

2. Experimental

2.1. Samples preparation

2.1.1. Preparation of PEDOT-PSS + GQD + CNT (GPC) and PEDOT-PSS + GQD + AgNW (GPA) humidity sensors

Firstly, GQDs were prepared; for this, a solution of graphite flake (GF), $KMnO_4$, and HNO_3 with a weight ratio of 0.2 g:0.2 g:0.4 ml was prepared and put in a Pt crucible. This solution was then put in a microwave heaven for heating in 1 min to separate GF into laminar form (EG). The second solution was made from 0.2 g $NaNO_3$ + 9.6 ml H_2SO_4 (98%) + 1.2 g $KMnO_4$ (called as NKH). EG was mixed with NKH solution and carefully stirred by use of a magnetic device for 2 h to have a GO solution. Adding to the GO solution 30 ml distilled water, and then 10 ml H_2O_2 allowed us to get a dark-yellow solution. By spinning with a rate of 7000 rpm for 5 min, a GO powder was obtained and it was diluted in deionized water. In the next step, NH_3 was added in the solution and stirred at 100°C for 5 h until a solution with a uniform dispersion of GQDs was reached. Finally, the GQDs dispersed solution was filtrated by using the "Dialysis" funnel to collect GQD powder with a volume of 0.2 g. This powder then was dissolved in 20 ml of twice-distilled water to get GQD-dispersion solution of 10 wt.% GQDs (abbreviated to GQD10).

Next, GQD + PEDOT:PSS + CNT composite solutions were prepared. Firstly, a powder of multiple wall carbonate tubes (shortly abbreviated to CNT) with an average size of 30 nm in diameter

and 2 μm in length was embedded in 10 ml of the GQD10 solution without CNT and with three contents of CNT, respectively, 0.5, 1.0, and 1.5 mg. All of the solutions obtained are called GQC solutions. These solutions were treated by plasma in a microwave oven. Then, 2 ml of polyethylene-dioxythiophene + PEDOT:PSS (1.25 wt.% in H_2O) was poured into each GQC solution. The solutions of GQDs-PEDOT:PSS without and with CNT of the three abovementioned volumes of CNT were stirred by ultrasonic wave for 1 h. From all the volumes of chemicals such as GQDs, PEDOT:PSS, and CNT used for the film preparation, the CNT weight contents (wt.%) in the GQDs-PEDOT:PSS matrix have been calculated. It is seen that the samples embedded with the CNT volume of 0.5, 1.0, and 1.5 mg consist of 0.4, 0.8, and 1.2 wt.%, respectively.

Synthesis of Ag nanowires (AgNW) was carried out as follows. Firstly, 20 ml of ethylene glycol was heated within stirring in a 250ml Corning-0215 glass at 70°C for 15 min; then, 17 mg of NaCl was added. Raising temperature up to 100°C, 20 mg of $AgNO_3$ was filled into the glass. The reaction between NaCl and $AgNO_3$ occurred, resulting in formation of opaque AgCl solution. Ethylene glycol was decomposed in aldehyde that played a role of a catalyst for creating Ag nuclei. The next step, 5 mg of KBr was added to the glass and heated up to 140°C for 10 min, following 300 mg of PVP was filled and raising temperature to 160°C. The solution temperature was maintained for 15 min. Finally, 250mg of $AgNO_3$ was added into the solution. The last solution was kept at 160°C for 30 min for growing silver nanowires. In the duration of this time, one can observe the change of the solution color from opaque to bright-gray, proving the formation of AgNWs in the solution. After the solution was cooled automatically to room temperature (in ~90 min), the solution was diluted by 80 ml of ethanol and kept for 10 h to deposit an AgNWs paste. This paste was put into a glass with 350 ml of distilled water for spinning with 6000 rpm for 30 min to get silver nanowires adhering to the glass walls. This AgNWs paste was removed from the glass and put into other glass with 200 ml of ethanol. By ultrasonic stirring, the AgNWs paste was dispersed completely in 2 h. Finally, 100 ml of distilled water was added into the AgNWs + ethanol solution; totally, 300 ml of the AgNWs solution was prepared for further studies.

Next, to prepare PEDOT-PSS + GQD + AgNW solutions, we used GQDs+PEDOT:PSS mixture with a volume ratio 2/1 of 10 wt.% GQDs solution/PEDOT:PSS, further this solution is called as GPA. Next step, to the GPA solution, a small amount of the AgNWs paste was added. The AgNWs pastes were dispersed in the GPA solutions by ultrasonic wave for at 65°C 1 h.

Using spin coating, GQC and GPA solutions were deposited onto glass substrates which were coated by two silver planar electrode arrays with a length (L) of 10 mm and separated each one from the other by a distance (l) of 5 mm, as shown in **Figure 1**. In the spin-coating technique used for preparing composite films, the following parameters were chosen: a delay time of 100 s, a rest time of 45 s, a spin speed of 1500–1800 rpm, an acceleration of 500 rpm, and finally, a drying time of 3 min. To dry the composite films, a flow of dried gaseous nitrogen was used for 10 h. For a solidification avoiding the use of solvents, the film samples were annealed at 120°C for 8 h in a "SPT-200" vacuum drier.

For simplicity in further analysis, the GPC sensor samples without and with CNT of 0.4, 0.8, and 1.2 wt.% were abbreviated to GPC-0, GPC-1, GPC-2, and GPC-3, respectively, whereas GPA sensors with AgNW of 0.2, 0.4, and 0.6 wt.% are called GPA1, GPA2, and GPA3, respectively.

http://dx.doi.org/10.5772/intechopen.79060

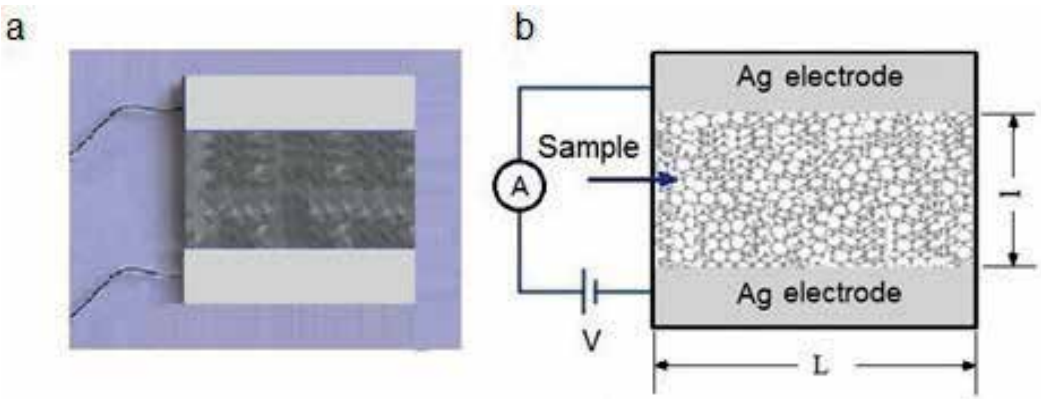

Figure 1. Image of a humidity sensor made from a single layer of composite films (a) and the schematic drawing of the device with the two planar electrodes (b). Humidity change is detected by the change in the current with a constant Dc-bias applied to the two electrodes.

2.1.2. Preparation of P3HT + rGO + CNT film sensors

All chemicals like PEDOT:PSS, P3HT, and multiple wall CNTs, with purity of ≥ 99.9% were purchased from Sigma-Aldrich Corporation. To prepare reduced graphene oxide (rGO), graphite flakes (GF) were taken off from graphite pieces with fewer layers by microwave heating solution of graphite filled in $KMnO_4$ and HNO_3. Mixtures of 0.2 g GF, 0.2 g $NaNO_3$, and 9.6 ml H_2SO_4 were put in a 200 mL volume Corning-247 glass beaker, then 1.2 g $KMnO_4$ and 28 ml of distilled water were poured into the glass beaker to get a liquid solution. Next, 10 ml H_2O_2 was added to this solution and ultrasonically stirred at room temperature for 8 h to separate MnO_4^- and MnO_2 into Mn^+ ions, yielding a solution with a bright-yellow color. The obtained solution was unmoved for 24 h, and at the glass beaker bottom, a paste-like layer with dark-yellow color was deposited, constituting the rGO paste. By slowly sucking, the solution above the rGO paste was completely taken from the glass beaker. Finally, 0.2 g of rGO paste was diluted in 40 ml of N,N-dimethylformamide (DMF) solvent in 50 ml-volume glass beaker and ultrasonically stirred for 900 s to get completely dispersive rGO in DMF (rGO-DMF). After 24 h waiting for the solution stabilization, 30 ml of rGO-DMF solution from the glass beaker top was taken and kept in another glass beaker for further use.

P3HT powder with a volume of 6 mg was mixed in 0.6 ml of rGO-DMF solution. This solution was ultrasonically stirred for 2 h at room temperature. At the same time, 1 mg of multiwalled carbon nanotubes (shortly called CNTs) was embedded in 0.5 ml of DMF (CNT-DMF) and also stirred by ultrasonic machine for 1 h. Finally, mixtures of the rGO-DMF and CNT-DMF solutions were put in a small glass beaker and carefully stirred for 5 h at 80°C by using a magnetic stirrer. For all the volumes of chemicals of P3HT, rGO, and CNTs used for further solid film preparation, the weight ratio of P3HT:rGO:CNTs was 100:20:10 (namely, the volume content of rGO and CNTs embedded in P3HT matrix was chosen to be, respectively, 20 and 10 wt.%. For simplicity in further analysis, the composite samples with such contents of P3HT, rGO, and CNTs were abbreviated to P3GC.

Using spin coating, P3GC solutions were deposited onto glass substrates which were coated by two silver planar electrode arrays with a length of 4 mm and separated from each other by a distance of 2 mm, which is similar to the image in **Figure 1**. The following parameters were used for spin coating: a delay time of 100 s, a rest time of 45 s, a spin speed of 1500–1800 rpm, an acceleration of 500 rpm, and finally a drying time of 300 s. To dry the composite films, a flow of dried gaseous nitrogen was used for 10 h. For a solidification avoiding the use of solvents, the film samples were annealed at 120°C for 2 h in a "SPT-200" vacuum drier. To compare the performance efficiency of P3HT + rGO + CNT with the one for PEDOT:PSS + rGO + CNT-based sensors, PEDOT:PSS + rGO + CNT composites (shortly called PEGC) were prepared by the abovementioned procedure with replacement of P3HT by PEDOT:PSS polymer.

2.2. Characterization techniques

The thickness of the films was measured on a "Veeco Dektak 6M" stylus profilometer. The size of GQDs and the surface morphology of the films were characterized by using "Hitachi" Transmission Electron Microscopy (TEM), Emission Scanning Electron Microscopy (FE-SEM), and NT-MDT atomic force microscope operating in a tunnel current mode. Crystalline structures were investigated by X-ray diffraction (XRD) with a Philips D-5005 diffractometer using filtered Cu-K_{α} radiation ($\lambda = 0.15406$ nm). The ultraviolet–visible absorption spectra were carried out on a Jasco UV–VIS–NIR V570.

For humidity sensing measurements, the samples were put in a 10 dm^3-volume chamber; a humidity value could be fixed in a range from 20 to 80% by the use of an "EPA-2TH" moisture profilometer (USA). The adsorption process is controlled by insertion of water vapor, while desorption process was done by extraction of the vapor followed by insertion of dry gaseous Ar. The measurement system that was described in [30] consisting of an Ar gas tank, gas/vapor hoses and solenoids system, two flow meters, a bubbler with vapor solution, and an airtight test chamber connected with collect-store data DAQ component. The Ar gas played a role as carrier gas, dilution gas, and purge gas.

For each sample, the number of measuring cycles was chosen to be at least 10 cycles. The humidity flow taken for measurements was of ~60 sccm ml/min. The sheet resistance of the samples were measured on a "KEITHLEY 2602" system source meter. To characterize humidity sensitivity of the composite samples, the devices were placed in a test chamber and device electrodes were connected to electrical feedthroughs.

For monitoring gases, the prepared sensing samples were put in a testing chamber of 10 dm^3 in volume. The gases value can be fixed in a rage from 10 to 1000 ppm by use of an "EPA-2TH" profilometer (USA). To characterize the gas sensitivity of the samples, the devices were placed in a test chamber at the room temperature (namely 300 K) and the Ar gas pressure of 101.325 kPa (or 1 Atm); the device electrodes were connected to electrical feedthroughs. The measurements that were carried out included two processes: adsorption and desorption. In the adsorption process, the gas (or vapor) flow consisting of Ar carrier and measuring vapor from a bubbler was introduced into the test chamber for an interval of time, following which the change in resistance of the sensors was recorded. In the desorption process, a dried Ar gas flow was inserted in the chamber in order to recover the initial resistance of the sensors. Through the recovering time dependence of the resistance, one can obtain information on the desorption ability of the sensor in the desorption process.

The P3GC film sensors were exposed to NH_3 gas with concentration (C_{gas}) that was controlled with step decreases from 50 to 40, 30, 20, and 10 ppm. The repeatability in the resistance change of P3GC sensor was studied by measuring the resistance of sensor as a function of both the insertion/extraction of ammonia gas in/out chamber and measurement time. Each measurement cycle consists of the following time durations: 20 s for NH_3 gas detecting to saturation state, 50 s for maintaining exposed ammonia gas in chamber with abovementioned concentrations (namely C_{gas} = 50, 40, 30, 20, and 10 ppm), 30 s for extraction of Ar and ammonia gas out from chamber; then, 20 s for heating samples at 70°C for completing extraction of NH_3 and finishing the prior cycle. The next cycle was repeated by the same steps.

3. Results and discussion

3.1. PEDOT-PSS + GQD + CNT and PEDOT-PSS + GQD + AgNW

3.1.1. Electrical property and morphology of PEDOT-PSS + GQD + CNT and PEDOT-PSS + GQD + AgNW composite films

From a TEM micrograph of a GQDs sample (**Figure 2a**), it is seen that the size distribution of the dots is considerably homogenous, as evaluated in this micrograph, the dots size ranged from 10 to 15 nm. **Figure 2b** is an FE-SEM micrograph of the GPC-3 sample where the CNT and GQDs clearly appeared while the conjugate polymer PEDOT:PSS exhibited a transparent matrix. This SEM micrograph also shows that in the GPC composite film, there are mainly heterojunctions of the GQD/PEDOT-PSS and CNT/PEDOT:PSS, whereas CNT/GQD junctions are rarely formed.

From the thickness measurements, it can be seen that embedding CNT made the GPC samples considerably thicker. However, for the CNT-embedded GPC films, the CNT concentration was not much affected by the film thickness, so that the change in the thickness versus CNT

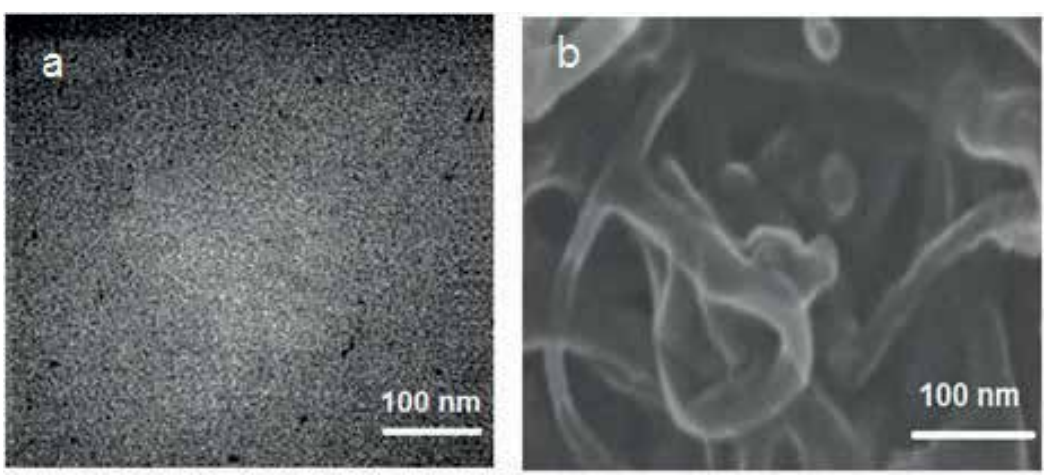

Figure 2. A TEM micrograph of GQDs sample (a) and FE-SEM of GPC-3 composite film (b) [29].

Samples	CNT content (wt.%)	Thickness, d (nm)	R_s (kΩ)	Conductivity, σ (S/cm)
GPC-0	0	460	2.180	4.98
GPC-1	0.4	485	2.160	4.76
GPC-2	0.8	487	0.814	7.93
GPC-3	1.2	490	0.356	27.52

Table 1. Thickness and resistance at room temperature of graphene quantum dots/CNT composite films [29].

concentration could be neglected. Indeed, for GPC-0 samples (i.e., the samples without CNT) the value of the film thickness was found to be ~5% smaller than that of the GPC + CNT samples (**Table 1**). This can be explained by the lower viscosity of GPC solution in comparison with the viscosity of GPC composite solutions. The results of measurements of the sheet resistance (R) of the samples are listed in **Table 1**.

The conductivity of the GPC-3 film is the largest and can be compatible to the conductivity of a pure PEDOT-PSS film as reported in [31]. Embedding GQDs and CNT into PEDOT-PSS has made the conductivity of PEDOT-PSS to decrease, leading to the expectation that the sensitivity of the GPC composite films would be enhanced. The temperature dependence of the conductivity of GPC samples is shown in **Figure 3**. For GPC-1 sample, σ versus T curves exhibit a typical property of the inorganic semiconductors: with increase in temperature, the conductivity increases. With increases in the CNT content, the composite exhibited a clearer semiconductor behavior; and when it reached a value as large as 1.2 wt.% (namely in GPC-3 sample), the conductivity of the films maintained an almost unchanged value of 37.2 S/cm

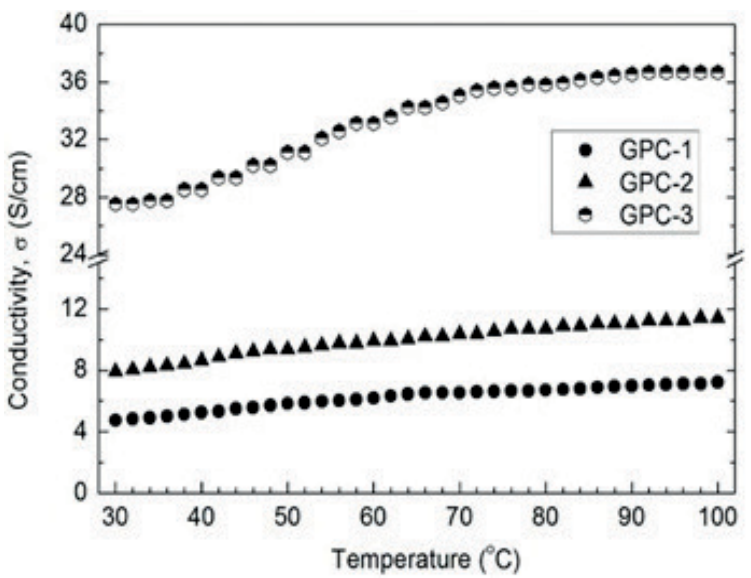

Figure 3. Temperature dependence of the conductivity of GPC-1, GPC-2 and GPC-3 films [29].

Samples abbreviation	AgNW content (wt.%)	Film thickness, d (nm)	Resistance at 50°C (MΩ)	Conductivity (S/m)
GPA1	0.2	450	4.56	0.024
GPA2	0.4	460	4.24	0.026
GPA3	0.6	480	3.88	0.027

Table 2. The data of the AgNWs-doped GQDs+PEDOT:PSS composite films used for humidity sensors [28].

under elevated operating temperatures. This thermal stability property is a desired factor for materials that are used in sensing applications.

The data of the samples including the AgNWs content, thickness, initial resistance, and conductivity are listed in **Table 2**. The value of the conductivity of the pure PEDOT:PSS film is ~80 S/cm as reported in [17] that is much larger than the one of the GPA composite films. This proves that the composite films possess a poor concentration of charge carriers. However, for materials used in gas sensing monitoring, this fact is an advantage in detecting a small amount of charge carries generated from adsorbed molecules, for instance, H_2O vapor.

FE-SEM image of AgNWs solution (**Figure 4a**) shows clearly the shape and dimension of the stick-like Ag wires, as evaluated in this image, the wire size is of 70 nm. **Figure 4b** is an FE-SEM image of the GPA3 film where the AgNWs and GQDs clearly appeared while the conjugate polymer PEDOT:PSS exhibited a transparent matrix. This SEM micrograph also shows that in the composite film, there are mainly heterojunctions of the GQD/PEDOT-PSS and AgNW/PEDOT:PSS, whereas AgNW/GQD junctions are rarely formed.

From our experiments, the temperature dependences of the resistance of AgNWs-doped GQDs+PEDOT:PSS composite films were found to be similar to those reported for CNTs-doped GQDs+PEDOT:PSS films [14]. With the increase of temperature, the AgNWs-doped composite exhibited the behavior of a heavily doped semiconductor: the resistance decreased

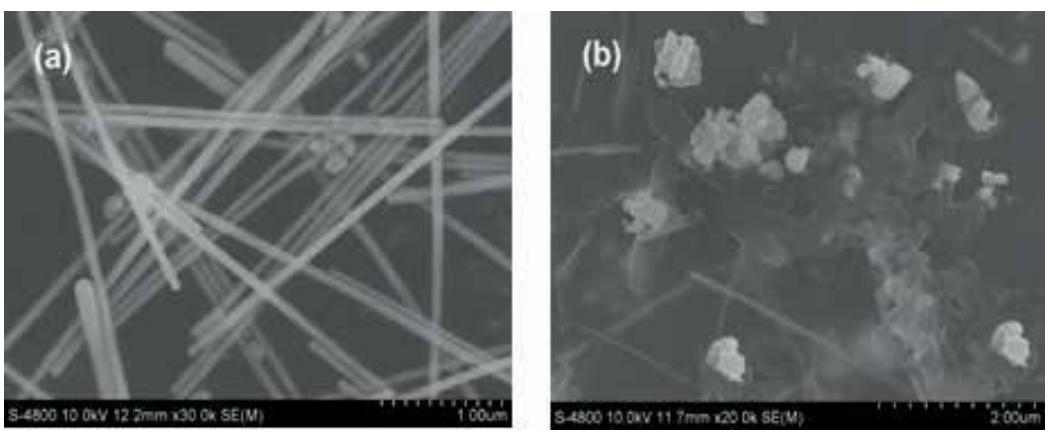

Figure 4. FE-SEM micrograph of an AgNWs containing solution (a) and surface of GPA3 film [28].

one order in magnitude from the initial values. Indeed, with the AgNWs content of 0.6 wt.% (GPA3), the resistance of the sensor lowered from 3.88 to 400 kΩ with increase of temperature from room temperature to 80°C and maintained a unchanged value of 350 kΩ under elevated (100–140°C) operating temperatures. This thermal stability is a desired factor for materials used in sensing applications.

3.1.2. Humidity sensing

3.1.2.1. For GPC

Figure 5 demonstrates the adsorption and desorption processes of the GQDs-PEDOT:PSS and CNT-PEDOT:PSS sensors. **Figure 5** shows that in the first 60 s, Ar gaseous flow eliminated the contamination agents from the GQDs-PEDOT:PSS surface, consequently the surface resistance increased. After the cleaning of the sensor surface during 30 s, the introduced humidity vapor was adsorbed onto the sensor surface, resulting in the decrease of the resistance. In the subsequent cycles, the humidity desorption/adsorption process led respectively to increase and decrease of the resistance of sensors, with results similar to those reported in [11]. However, through each cycle, the resistance of the GQDs-PEDOT:PSS film did not recover/restore to its initial value, but increased in 1–2 kΩ, to a final value of 235 kΩ after 1000 s from 220 kΩ. The increase in the initial resistance of the GQDs-PEDOT:PSS mainly related to the decrease of the major charge carriers in PEDOT:PSS. This is due to the elimination of holes (as the major carriers in PEDOT:PSS) by electrons that were generated from the H_2O adsorption. The

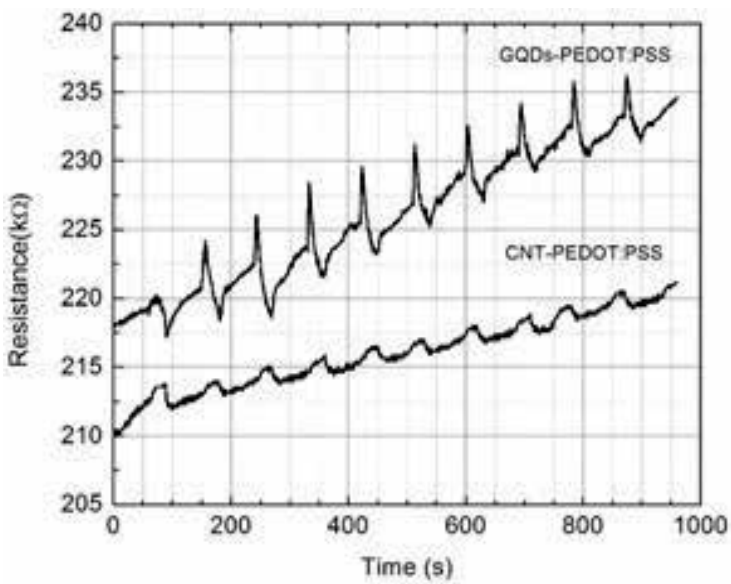

Figure 5. Sheet resistance change vs. humidity of GQDs-PEDOT:PSS and CNT-PEDOT:PSS composite films during adsorption/desorption processes [29].

more desorption/adsorption cycles, the more holes were eliminated in the deeper distances in the composite films. The similar feature in the sheet resistance change versus humidity was observed for the CNT-PEDOT:PSS, but the sensitivity of the last was much less than the one of the GQDs-PEDOT:PSS sensor. This proves the advantage of GQDs embedded in PEDOT:PSS polymer for the humidity sensing.

To evaluate sensing performance, a sensitivity (η) of the devices was introduced. It is determined by following equation:

$$\eta = \frac{R - R_o}{R_0}(\%) \tag{1}$$

The absolute magnitude of the sensitivity of the GPC-0 calculated by formula (3) is of ca. 2.5%.

Plots of time dependence of the sensitivity of the CNT-doped GPC composite films are shown in **Figure 6**. From **Figure 6**, one can see that for the GPC samples, vice versa to the GQDs-PEDOT:PSS, the humidity (i.e., H_2O vapor) adsorption process led to increase in the resistance of the films. Moreover, the resistance increased at a much faster rate than when it decreased.

Looking at the humidity sensing curves in **Figure 6**, one can distinguish two phenomena: the "rapid" (steep slope) and "slow" (shallow slope) response. The rapid response arises from H_2O molecular adsorption onto low-energy binding sites, such as sp^2-bonded carbon, and the slow response arises from molecular interactions with higher energy binding sites, such as vacancies, structural defects, and other functional groups [32, 33]. For the next step, the sensitivity ability of GPC composite was studied and the whole experiment process as described above was repeated. The data in **Figure 6** show that the presence of CNT can improve the sensing properties of GPC sheets. With increase in the CNT content, the resistivity increased, from 4.5% (for GPC-1) to 9.0% (for GPC-2) and 11.0% (for GPC-3).

The response time (i.e., the duration for R_o raising up to R_{max} in the adsorption process) for all three GPC sheets is almost the same value of 20 s, whereas the recovery time (the

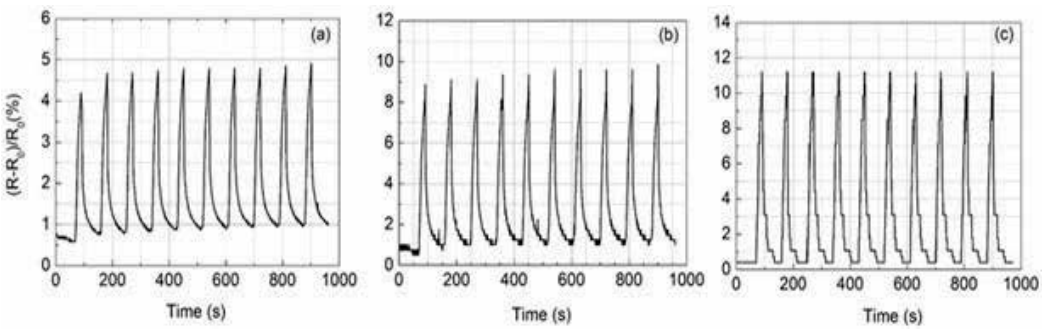

Figure 6. Comparison of the humidity sensing of the GPC composite-based sensors vs. CNT content; (a) GPC-1 (0.4 wt%), (b) GPC-2 (0.8 wt %) and (c) GPC-3 (1.2 wt.%) [29].

duration for R_o lowering to R_{max} in the desorption process) decreased from 70 s (GPC-1, **Figure 6a**) to 60 s (GPC-2, **Figure 6b**) and 40 s (GPC-3, **Figure 6c**). In addition, the complete H_2O molecular desorption on the surface of GPC composites took place at room temperature and atmospheric pressure. One can guess that connecting together, individual GPC sheets by CNTs caused the increase of the mobility of carriers in GPC composite films, consequently leading to higher H_2O vapor sensing ability of the CNT-doped GQDs-PEDOT:PSS composites. Indeed, due to the appearance of CNTs bridges, the number of the sites with high binding energies in GPC sheets decreases, while the number of those with low binding energies increases. Since the H_2O molecules was mainly adsorbed at the sites with low binding energies, the appearance of CNTs bridges led to the complete desorption ability of GPC composites.

3.1.2.2. For GPA

From experimental measurements, we have found that the electrical characteristics of our thin-film sensor elements are strongly dependent on the surrounding atmosphere, on humidity in particular. The increase in relative humidity results in significant decrease of the electrical resistance of the GPA composite films, namely GPA1, GPA2, and GPA3 (see **Figure 7**). At the RH lower 30%, the resistance of the sensors intensively decreased and reached an almost the same value of 400 kΩ from RH larger 50%. This demonstrates that AgNWs-doped GQDs+PEDOT:PSS composite films can be used well for humidity sensing in a range from RH10% to RH40%. Moreover, in this RH range, GRA3 sensor is the most sensitive to humidity, comparing to GRA1 and GRA2.

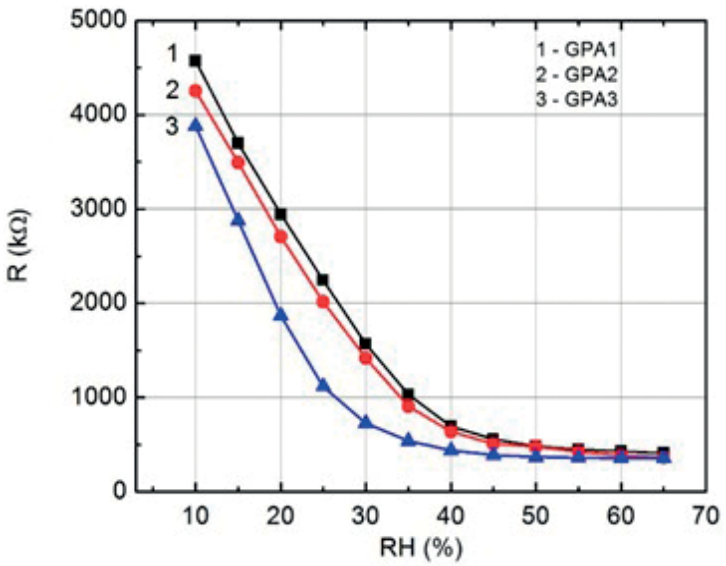

Figure 7. RH% dependence of the surface resistance of AgNWs-doped GQDs+PEDOT:PSS for three composite films with 0.2 wt.% (curve "1"), 0.4 wt.% (curve "2") and 0.6 wt.% of AgNWs (curve "3") [28].

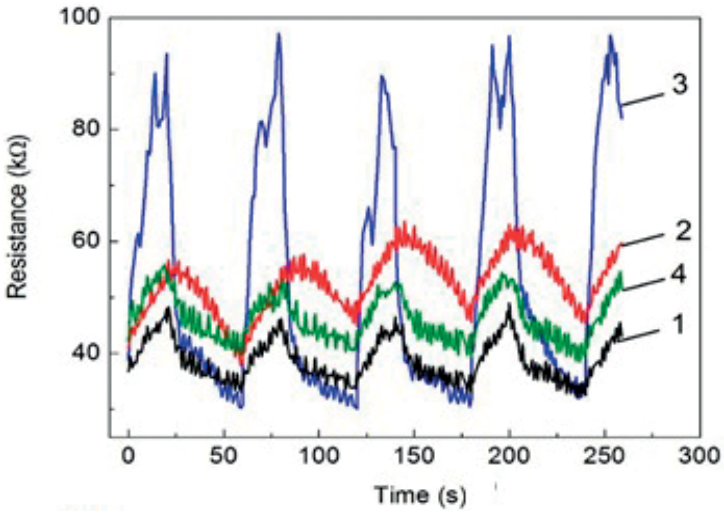

Figure 8. Responses of resistance of the sensors based on AgNWs-doped GQD/PEDOT:PSS films to the pulse of relative humidity (RH 30%) at room temperature for samples GPA1 (curve "1"), GPA2 (curve "2"), GPA3 (curve "3") and GPA1 (curve "4") [28].

The humidity dependence of the resistance of the hybrid (or composite) films can be explained by the interaction of water molecules with the surface of the composite, which leads to changing electric parameters of the GQDs. On the other hand, water impurities might induce additional or so called "secondary" doping of the conjugated polymer PEDOT:PSS. This manifests itself in change of the chain shape to an "unfolded spiral" and, therefore, stimulates increase in the conductivity [8].

More detailed measurements of the time response of the sensors were carried out in the conditions of H_2O vapor insertion and extraction, respectively, to the adsorption and desorption processes. **Figure 8** demonstrates the results of the measurements for AgNWs-doped GQDs+PEDOT:PSS sensors, i.e., for GPA1, GPA2, and GPA3. From **Figure 4**, one can see that the best humidity sensitivity was obtained in the sensor made from GPA3 film where the AgNWs content is of 0.6 wt.%. The samples with larger AgNWs contents (namely 0.8–1.2 wt.%) in the composites were also made; however, the sensing to humidity of these composite decreased rapidly. Indeed, in **Figure 8**, the adsorption and desorption processes of the 0.8 wt.% AgNWs-doped GQDs+PEDOT:PSS sensor (called as GPA4) were revealed worse than that of the GPA3 sensor (0.6 wt.% AgNWs). **Figure 8** shows that the humidity desorption/adsorption process led, respectively, to increase/decrease of the resistance of sensors, with results similar to those reported in [18].

Figure 9 shows the sensitivity determined by Formula (1) for the GPA3 sensor during 5 cycles of the adsorption and desorption of H_2O vapor. The absolute magnitude of the sensitivity of the GPA3 calculated by formula (3) reached a value as large as 15.2%. The plots for GPA1 and GPA2 sensors have a shape similar to the one of GPA3 (here they are not presented); however, the sensitivity was smaller, namely 5.5 and 6.5%, respectively, for

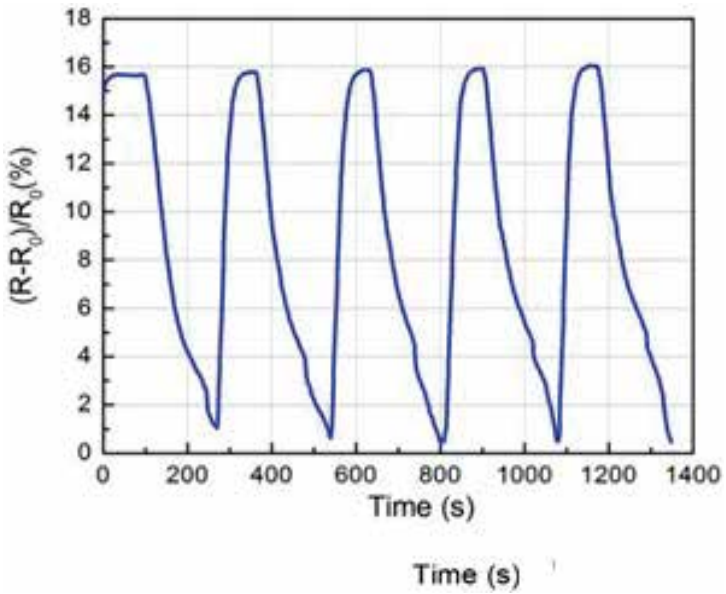

Figure 9. Responses of the sensitivity of the GPA3 sensor to the pulse of relative air humidity (RH30%) at room temperature [28].

GPA1 and GPA2. Comparing with the CNT-doped GQDs+PEDOT:PSS film sensor (η ~11%) as reported in [14], the humidity sensing of 0.6 wt.% AgNWs-doped composite is much larger.

In addition, the complete H_2O molecular desorption on the surface of GPA composites took place at room temperature and atmospheric pressure. One can guess that connecting together individual GPA sheets by AgNWs caused the increase of the mobility of carriers in composite films, consequently leading to higher H_2O vapor sensing ability of the AgNWs-doped GQDs+PEDOT:PSS composites. Similar to CNT-doped GQDs+PEDOT:PSS composites, due to the appearance of AgNWs bridges, the number of the sites with high binding energies in GPA sheets decreases, while the number of those with low binding energies increases. Since the H_2O molecules were mainly adsorbed at the sites with low binding energies, the appearance of AgNWs bridges led to the complete desorption ability of GPA composites.

3.2. NH_3 gas sensing

3.2.1. Film morphology and structures

Figure 10 shows AFM images of a pure P3HT and annealed P3GC composite films. The thickness of the film is 550 nm, the annealing temperature is 120°C and the annealing time is 2 h. **Figure 10a** shows that the pure P3HT film exhibited a smooth surface, whereas the roughness of the P3GC film surface was estimated as about 1.50 nm (**Figure 10b**). Thus, the roughness of the P3GC film can be attributed to the presence of both rGO and CNTs nanoparticles. The roughness and porosity of the composite sample were also observed by FE-SEM micrograph

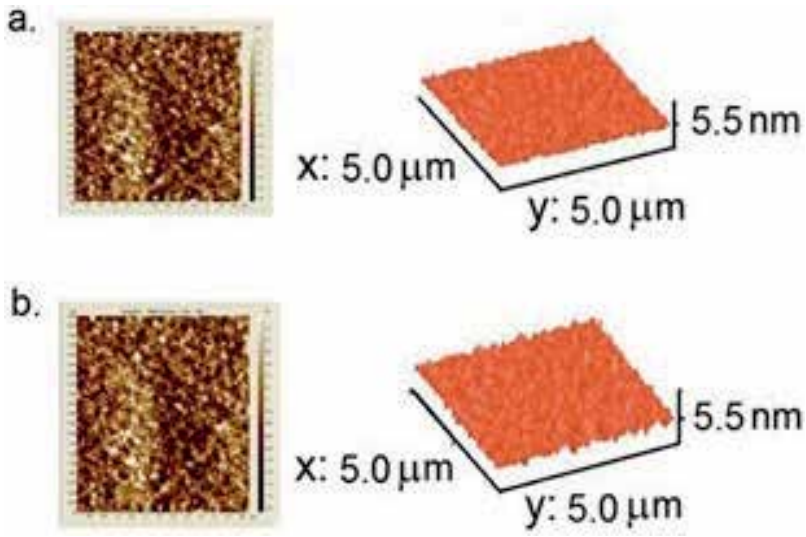

Figure 10. AFMs of a pure P3HT (a) and P3GC (b) film annealed at 120°C for 2 h.

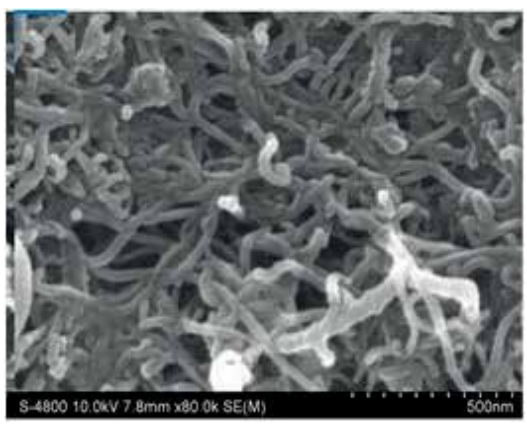

Figure 11. FE-SEM of a P3GC composite film.

(**Figure 11**) where P3HT polymer matrix is not revealed in the FE-SEM. **Figure 11** clearly shows the presence of the multiwalled carbon nanotubes in the P3GC sample.

3.2.2. Ammonia gas sensing

The results for the measurements of 5 cycles according to the ammonia concentration from 50, 40, 30, 20, and 10 ppm are shown in **Figure 12**. The cyclic behavior of the sensor performance shows that the P3GC sensors exhibited a good reversible sensing property toward ammonia gas. With exposition of ammonia gas in chamber, the sensor resistance increased rapidly, reaching the saturation value in about 20 s; and recovering its initial value in about 30 s after

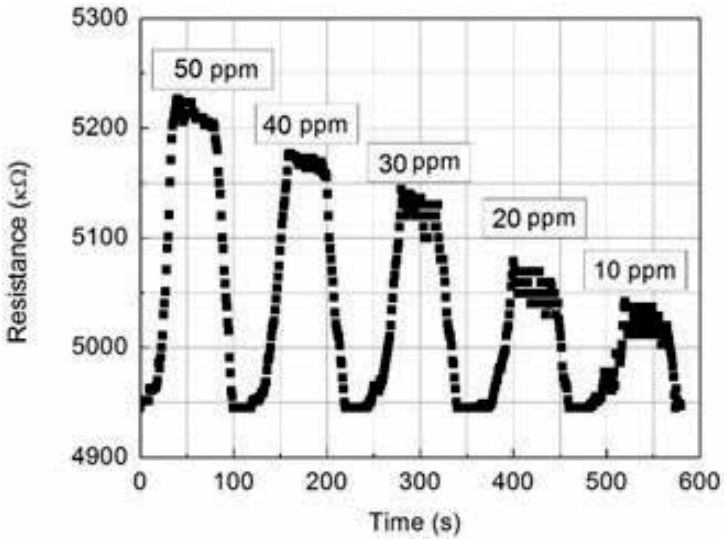

Figure 12. Time dependence of resistance of P3GC film on repeated exposure and removal of NH_3 gas.

the extraction of ammonia gas from the chamber. The increase in resistance of the P3GC sensor is closely related to a lowering of major charge carriers (namely holes) in P3HT polymer that is considered as a p-type organic semiconductor [34]. Whereas NH_3 is a highly active and electron-donating free radical [24], electrons generated by the absorption of ammonia gas on the surface of P3GC film eliminated a part of holes by coupling with each other, resulting in an increase of the P3HT resistance. When the P3GC film was slightly heated, NH_3 molecules in P3HT rapidly evaporated from the film surface, leaving holes along the backbone of the polymer. In such fashion, the concentration of major charge carriers rapidly increases while the resistance of the sensor decreases.

Embedding rGO in P3HT has enabled to enhance sensing properties of the P3GC films. This is similar to the results reported in [35] for polypyrrole (Py)-rGO-based sensors. Wang et al. explained the excellent sensing properties of Py-rGO-based sensors due to the parts of oxygen-based moieties and structure defects after chemical reduction process, resulting to the p-type semiconducting behavior of the resultant rGO. NH_3, as a reducing agent, has a lone electron pair that can be easily donated to the p-type rGO sheets, leading to the increase of the resistance of the rGO devices, whereas multiwalled CNTs have contributed to improve the adsorption efficiency of gas molecules (included NH_3) due to larger effective surface areas with many sites, as suggested by Varghese et al. [36]. Moreover, the addition of rGO and CNTs together in P3GC composite films created not only numerous nanoheterojunctions of P3HT/rGO and P3HT/CNT, but also nanotube "bridges" for electron transferring. These "bridges" are clearly revealed by the SEM micrograph, as shown in **Figure 11**.

In [4], we also demonstrated that inorganic nanoparticles embedded in polymers filled up most of the cracked spots in polymers that were often created during postannealing. By this way, the cracked spots served as charge traps were eliminated in nanocomposite films. With

the presence of nanoheterojunctions of P3HT/rGO and P3HT/CNT that together reduced the charge traps, one can enhance the performance of the sensors made from P3GC films.

From the sensitivity (η) of the P3GC sensor determined by Formula (1), the $\eta - C_{gas}$ dependence was plotted in **Figure 13**. The responding time of the sensor was about 30 s and the resistance of the P3GC composite films fast recovered to baseline when exposed to air. In the same period of time (namely 30 s), the sensing response to NH_3 with C_{gas} lowering from 50 to 40, 30, 20, and 10 ppm decreased from 2.9 to 2.4, 1.8, 1.3, and 0.8%, respectively.

Figures 12 and **13** show that the detection limit for NH_3 gas can attain a value is lower than 10 ppm. However, using the EPA-2TH gas profilometer, we could not introduce NH_3 gas with an accurate concentration in the range from 0 to 10 ppm. From **Figure 13**, one can see that the response of the sensor linearly decreases with decreases in ammonia gas concentration; and the slope of the linear plot reflects the relative sensitivity of the sensor. Thus, for the P3GC composite film sensor, the relative sensitivity was found to be of 0.05%/ppm. This value is still rather low, but it is about two times larger than the sensitivity of the ammonia gas sensor made from PEDOT: PSS [37].

Concerning the capacity for detecting ammonia gas in an environment that often has a relatively large humidity, we found that the P3HT-based sensor does not respond to humidity, whereas the PEDOT: PSS-based sensor is highly sensitive to this factor [29]. Indeed, this was confirmed by our results of the investigation on humidity (RH%) sensing of the two types of sensors, as a function of both the measurement time (**Figure 14**) and the relative humidity in the range from RH%20 to RH%65 (**Figure 15**).

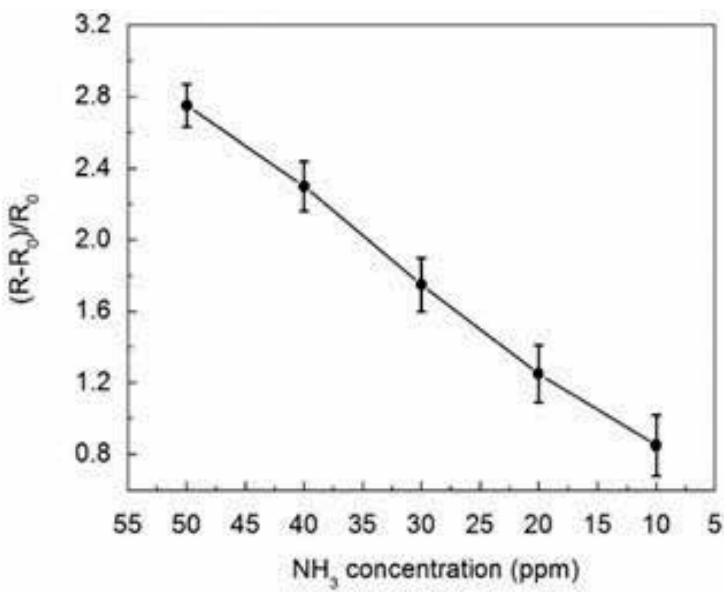

Figure 13. Sensitivity of P3GC sensor vs. ammonia concentration.

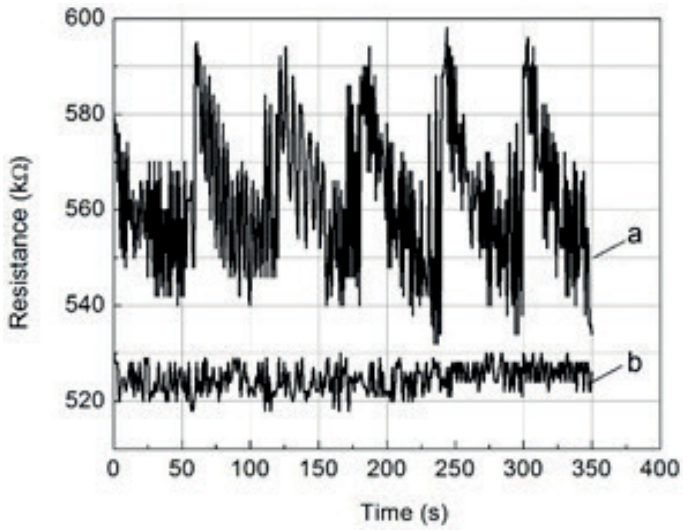

Figure 14. Comparison of the RH% sensitivity of PEGC (a) and P3GC sensors (b).

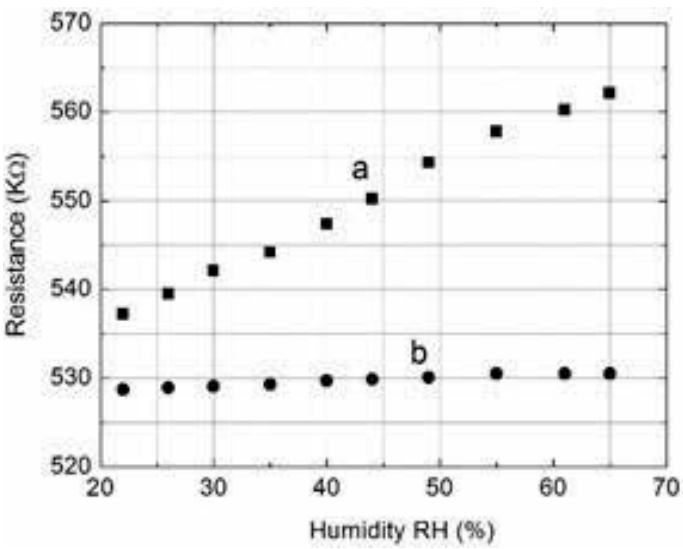

Figure 15. Humidity dependence of resistance of the PEGC (a) and P3GC films (b).

Although the ammonia gas response of P3GC sensors at 50 ppm (η = 2.9%) is lower compared to PEDOT: PSS-based sensors (η = 4.0% [28]), when one needs to monitor ammonia gas in a humid environment, P3HT/rGO/CNT (namely P3GC) sensors would be preferred. This is because signals obtained from measurements on PEDOT: PSS-based sensors would be undistinguishable between ammonia gas and water vapor.

http://dx.doi.org/10.5772/intechopen.79060

4. Conclusion

- Using spin-coating technique, PEDOT: PSS + GQD + CNT (GPC), PEDOT: PSS + GQD + AgNW (GPA) films used for humidity sensors and P3HT + rGO + CNT (P3GC) films used for NH_3 gas sensors were prepared at room temperature and atmospheric pressure, all the sensing devices have extremely simple structure and they respond well to the humidity change (for GPC and GPA) and NH_3 gas (for P3GC).
- With the CNT content increase, from 0% (GPC-0) to 0.4 wt.% (GPC-1), 0.8 wt.% (GPC-2), and 1.2 wt.% (GPC-3), the sensitivity of the humidity sensing devices based on CNT-doped graphene quantum dot-PEDOT: PSS composites improved from 2.5% (GPC-0) to 4.5% (GPC-1), 9.0% (GPC-1), and 11.0% (GPC-2), respectively The response time of the GPC sensors was as fast as 20 s; and the recovery time of the sensors lowered from 70 s (0.4 wt.% CNT) to 60 s (0.8 wt.% CNT) and 40 s (1.2 wt.% CNT). With the AgNWs content increase, from 0.2 wt.% (GPA1) to 0.4 wt.% (GPA2) and 0.6 wt.% (GPA3), the sensitivity of the humidity sensing devices based on AgNWs-doped graphene quantum dot-PEDOT: PSS composites improved from 5.5% (GPA1), 6.5% (GPA2) and 15.2% (GPA3), respectively The best response time (~30 s) was obtained for sensors made from 0.6 wt.% AgNWs-doped GQDs+PEDOT: PSS composite films.
- P3GC (namely P3HT embedded with a content of 20 wt.% of rGO and 10% of CNTs) film sensors possessed a responding time of ca. 30 s, a sensing response of 0.8% at ammonia gas concentration of 10 ppm and a relative sensitivity of 0.05%/ppm. Investigation of humidity sensing of both the PEDOT: PSS + rGO + CNT and P3HT + rGO + CNT film sensors has demonstrated that P3HT + rGO + CNT film does not respond to humidity as it is the case for PEDOT: PSS + rGO + CNT. Useful applications in gas thin-film sensors for selectively sensing ammonia gas in a humid environment can thus be envisaged.

Acknowledgements

This research was funded by the Vietnam National Foundation for Science and Technology (NAFOSTED). The authors express sincere thanks to Prof. Dr. Vo-Van Truong (Concordia University, Canada) for useful discussions.

Author details

Nguyen Nang Dinh

Address all correspondence to: dinhnn@vnu.edu.vn

University of Engineering and Technology, Vietnam National University Hanoi, Hanoi, Vietnam

References

[1] Thomas PS, Kuruvilla J, Sabu T. Mechanical properties of titanium dioxide-filled polystyrene microcomposites. Materials Letters. 2004;**58**:281-289

[2] Móczó J, Pukánszky B. Polymer micro and nanocomposites: Structure, interactions, properties. Journal of Industrial and Engineering Chemistry. 2008;**14**:535-563

[3] Choulis SA, Mathai MK, Choong V-E. Influence of metallic nanoparticles on the performance of organic electrophosphorescence devices. Applied Physics Letters. 2006;**88**: 213503-213505

[4] Thao TT, Trung TQ, Truong V-V, Dinh NN. Enhancement of power efficiency and stability of P3HT-based organic solar cells under elevated operating-temperatures by using a nanocomposite photoactive layer. Journal of Nanomaterials. 2015;**2015**:7. Article ID 463565

[5] Huynh WU, Dittmer JJ, Alivisatos AP. Hybrid nanorod, polymer solar cells. Science. 2002;**295**:2425-2427

[6] Petrella A, Tamborra M, Cozzoli PD, Curri ML, Striccoli M, Cosma P, et al. TiO_2 nanocrystals – MEH-PPV composite thin films as photoactive material. Thin Solid Films. 2004;**451/452**:64-68

[7] Burlakov VM, Kawata K, Assender HE, Briggs GAD, Ruseckas A, Samuel IDW. Discrete hopping model of exciton transport in disordered media. Physical Review B. 2005; **72**:075206-1-075206-5

[8] Quyang J, Xu Q, Chu C-W, Yang Y, Li G, Shinar J. On the mechanism of conductivity enhancement in poly(3,4, ethylenedioxythiophene): Poly(styrene sufonate) film through solvent treament. Polymer. 2004;**45**:8443-8450

[9] Tehrani P, Kanciurzewska A, Crispin X, Robinson ND, Fahlman M, Berggren M. The effect of pH on the electrochemical over, oxidation in PEDOT:PSS films. Solid State Ionics. 2007;**177**:3521-3529

[10] Ummartyotin S, Juntaro J, Wu C, Sain M, Manuspiya H. Deposition of PEDOT: PSS nanoparticles as a conductive microlayer anode in OLEDs device by desktop inkjet printer. Journal of Nanomaterials. 2011;**2011**:7; Article ID 606714

[11] Gavgani JN, Dehsari HS, Hasani A, Mahyari M, Shalamzari EK, Salehi A, Taromi FA. A room temperature volatile organic compound sensor with enhanced performance, fast response and recovery based on N-doped graphene quantum dots and poly(3,4-ethylenedioxythiophene)–poly(styrenesulfonate) nanocomposite. Royal Society Of Chemistry. 2015;**5**:57559-57567

[12] Olenych IB, Aksimentyeva OI, Monastyrskii LS, Horbenko YY, Yarytska LI. Sensory properties of hybrid composites based on poly(3,4-ethylenedioxythiophene)-porous silicon-carbon nanotubes. Nanoscale Research Letters. 2015;**10**:187 (6p)

[13] Shen JH, Zhu YH, Yang XL, Li CZ. Graphene quantum dots: Emergent nanolights for bioimaging, sensors, catalysis and photovoltaic devices. Chemical Communications. 2012;**48**:3686-3699

[14] Zhang ZP, Zhang J, Chen N, Qu LT. Graphene quantum dots: An emerging material for energy-related applications and beyond. Energy & Environmental Science. 2012;**5**(10):8869-8890

[15] Li L, Wu G, Yang G, Peng J, Zhao J, Zhu J-J. Focusing on luminescent graphene quantum dots: Current status and future perspectives. Nanoscale. 2013;**5**:4015-4039

[16] Basu S, Bhattacharyya P. Recent developments on graphene and graphene oxide based solid state gas sensors. Sensors and Actuators B. 2012;**173**:1-21

[17] Yin PT, Kim TH, Choi JW, Lee KB. Prospects for graphene-nanoparticle-based hybrid sensors. Physical Chemistry Chemical Physics. 2013;**15**:12785-12799

[18] Chu BH, Nicolosi J, Lo CF, Strupinski W, Pearton SJ, Ren F. Effect of coated platinum thickness on hydrogen detection sensitivity of graphene-based sensors. Electrochemical and Solid-State Letters. 2011;**14**:K43-K44

[19] Zhang M, Wang Z. Nanostructured silver nanowires-graphene hybrids for enhanced electrochemical detection of hydrogen peroxide. Applied Physics Letters. 2013;**102**: 213104-213106

[20] Sreeprasad TS, Rodriguez AA, Colston J, Graham A, Shishkin E, Pallem V, Berry V. Electron-tunneling modulation in percolating network of graphene quantum dots: Fabrication, phenomenological understanding, and humidity/pressure sensing applications. Nano Letters. 2013;**13**:1757-1763

[21] Hibbard T, Crowley K, Killard AJ. Direct measurement of ammonia in simulated human breath using an inkjet-printed polyaniline nanoparticle sensor. Analytica Chimica Acta. 2013;**779**:6-63

[22] Gardon M, Guilemany JM. A review on fabrication, sensing mechanisms and performance of metal oxide gas sensors. Journal of Materials Science. 2013;**24**:1410-1421

[23] Janata J, Josowicz M. Conducting polymers in electronic chemical sensors. Nature Materials. 2003;**2**(1):19-24

[24] Bai H, Shi G. Gas sensors based on conducting polymers. Sensors. 2007;**7**(3):267-307

[25] Patois T, Sanchez J-B, Bergeretal F. Elaboration of ammonia gas sensors based on electrodeposited polypyrrole-cobalt phthalocyanine hybrid films. Talanta. 2013;**17**:45-54

[26] Lee Y-S, Joo B-S, Choi N-J, Lim J-O, Huh J-S, Lee D-D. Visible optical sensing of ammonia based on polyaniline film. Sensors and Actuators B. 2003;**93**(1-3):148-152

[27] Basu S, Bhattacharyya P. Recent development on graphene and graphene oxide based solid state gas sensors. Sensors and Actuators B. 2012;**173**:1-21

[28] Long LM, Dinh NN, Thu HT, Phong HT, Trung TQ. Characterization of humidity sensing of polymeric graphene-quantum-dots composites incorporated with silver nanowires. VNU Journal of Science: Mathematics-Physics. 2017;**33**(3):52-60

[29] Long LM, Dinh NN, Trung TQ. Synthesis and characterization of polymeric graphene-quantum-dots based nanocomposites for humidity sensing. Journal of Nanomaterials. 2016;**2016**(2016):6; Article ID 5849018

[30] Trung TQ, Huynh TMH, Tong DT, Van Tam T, Dinh NN. Synthesis and application of graphene–silver nanowires composite for ammonia gas sensing. Advances in Natural Sciences: Nanoscience and Nanotechnology. 2013;**4**:045012-1-045012-4

[31] Quyang J, Chu C-W, Chen F-C, Xu Q, Yang Y. High-conductivity poly(3,4-ethylenedioxythiophene): Poly(styrene sulfonate) film and its application in polymer optoelectronic devices. Advanced Functional Materials. 2005;**15**:203-208

[32] Lu G, Park S, Yu K, Ruoff RS, Ocola LE, Rosenmann D, Chen J. Toward practical gas sensing using highly reduced graphene oxide: A new signal processing method to circumvent run-to-run and device-to-device variations. ACS Nano. 2011;**5**:1154-1164

[33] Robinson JT, Perkins FK, Snow ES, Wei Z, Sheehan PE. Reduced graphene oxide molecular sensors. Nano Letters. 2008;**8**:3137-3140

[34] Omer BM. Optical properties of poly (3-hexylthiophene-2,5-diyl) and poly (3-hexylthiophene-2,5-diyl)/[6,6]-phenyl C61-butyric acid 3-ethylthiophene ester thin films. Journal of Nano and Electronic Physics. 2013;**5**(3):03010-1-03010-4

[35] Wang Y, Zhang L, Hu N, Wang Y, Zhang Y, Zhou Z, Liu Y, Shen S, Peng C. Ammonia gas sensors based on chemically reduced graphene oxide sheets self-assembled on au electrodes. Nanoscale Research Letters. 2014;**9**:12; Article 251

[36] Varghese OK, Kichambre PD, Gong D, Ong KG, Dickey EC, Grimes CA. Gas sensing characteristics of multi-wall carbon nanotubes. Sensors and Actuators B. 2001;**81**(1):32-41

[37] Aba L, Yusuf Y, Mitrayana, Triyana K. Selectivity improvement of gas sensor based on poly(3,4-ethylenedioxythiophene): Poly(styrenesulfonate) thin film by using imprinting method. Journal of Modern Physics. 2012;**3**:529-533

Chapter 6

Polymer Nanocomposites with Different Types of Nanofiller

Amanda Dantas de Oliveira and
Cesar Augusto Gonçalves Beatrice

Additional information is available at the end of the chapter

http://dx.doi.org/10.5772/intechopen.81329

Abstract

The development of polymer nanocomposites has been an area of high scientific and industrial interest in the recent years, due to several improvements achieved in these materials, as a result of the combination of a polymeric matrix and, usually, an inorganic nanomaterial. The improved performance of those materials can include mechanical strength, toughness and stiffness, electrical and thermal conductivity, superior flame retardancy and higher barrier to moisture and gases. Nanocomposites can also show unique design possibilities, which offer excellent advantages in creating functional materials with desired properties for specific applications. The possibility of using natural resources and the fact of being environmentally friendly have also offered new opportunities for applications. This chapter aims to review the main topics and recent progresses related to polymer nanocomposites, such as techniques of characterization, methods of production, structures, compatibilization and applications. First, the most important concepts about nanocomposites will be presented. Additionally, an approach on the different types of filler that can be used as reinforcement in polymeric matrices will be made. After that, sections about methods of production and structures of nanocomposites will be detailed. Finally, some properties and potential applications that have been achieved in polymer nanocomposites will be highlighted.

Keywords: nanocomposites, polymers, nanofillers, processing, compatibilization, morphology, structures, characterizations, properties, applications

1. Introduction

Polymer nanocomposites (PNCs) may be defined as a mixture of two or more materials, where the matrix is a polymer and the dispersed phase has at least one dimension smaller than 100 nm [1]. In

the last decades, it has been observed that the addition of low contents of these nanofillers into the polymer can lead to improvements in their mechanical, thermal, barrier and flammability properties, without affecting their processability [1, 2]. The ideal design of a nanocomposite involves individual nanoparticles homogeneously dispersed in a matrix polymer. The dispersion state of nanoparticles is the key challenge in order to obtain the full potential of properties enhancement [1, 2]. This uniform dispersion of nanofillers can lead to a large interfacial area between the constituents of the nanocomposites [2]. The reinforcing effect of filler is attributed to several factors, such as properties of the polymer matrix, nature and type of nanofiller, concentration of polymer and filler, particle aspect ratio, particle size, particle orientation and particle distribution [3]. Various types of nanoparticles, such as clays [3, 4], carbon nanotubes [5], graphene [6, 7], nanocellulose [8] and halloysite [9], have been used to obtain nanocomposites with different polymers.

The evaluation of the nanofiller dispersion in the polymer matrix is very important, since the mechanical and thermal properties are strongly related to the morphologies obtained. Depending on the degree of separation of the nanoparticles, three types of nanocomposite morphologies are possible (**Figure 1**) [10]: conventional composites (or microcomposites), intercalated nanocomposites and exfoliated nanocomposites. When the polymer is unable to intercalate between the silicate layers, a composite of separate phases is obtained (**Figure 1(a)**), whose properties are in the same range as those observed in traditional composites [1]. An intercalated structure, in which a single (and sometimes more than one) extended polymer chain is intercalated between the layers of the silicate, results in a well-ordered multilayer morphology with intercalated layers of polymer and clay (**Figure 1(b)**). When the silicate layers are completely and uniformly dispersed in a continuous polymer matrix, an exfoliated structure is obtained (**Figure 1(c)**) [10].

Exfoliated nanocomposites have maximum reinforcement due to the large surface area of contact between the matrix and nanoparticles. This would be one of the main differences between nanocomposites and the conventional composites [11].

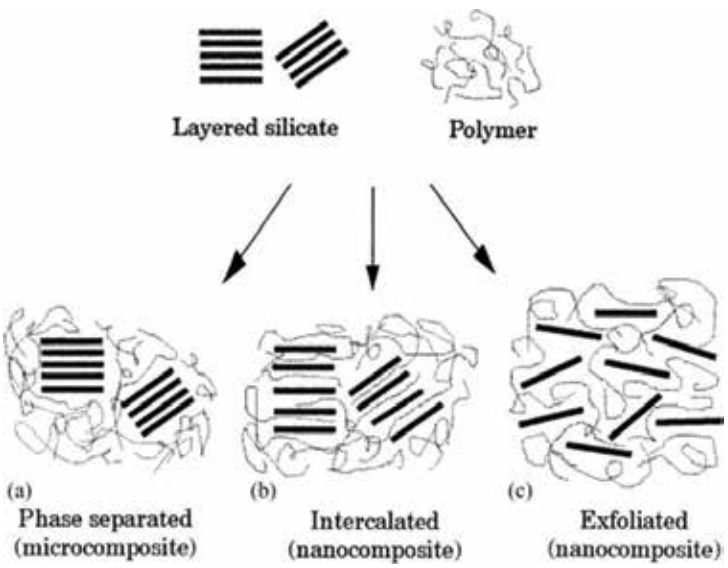

Figure 1. Possible structures of polymer nanocomposites using layered nanoclays: (a) microcomposite, (b) intercalated nanocomposite and (c) exfoliated nanocomposite [10].

The aim of this chapter is to review the common types of fillers used in nanocomposites, to provide an understanding of how nanocomposites are currently produced and characterized and, finally, to present some examples of applications of these materials.

2. Nanofillers and compatibilization of nanocomposites

2.1. Carbon-based nanofillers

2.1.1. Carbon nanotubes

Carbon nanotubes (CNTs) are ultrathin carbon fibers with nanometer-size diameter and micrometer-size length. CNTs were discovered in 1991 by Sumio Iijima, and since then, these nanomaterials have been used in various applications [12]. The structure of CNT consists of enrolled graphitic sheet, which is a planar-hexagonal arrangement of carbon atoms distributed in a honeycomb lattice [12, 13]. The nanotubes can be classified into either multi-walled (MWCNT) or single-walled (SWCNT) depending on its preparation method [12, 14], as can be seen in **Figure 2**. MWCNTs consist of two or more concentric cylindrical shells of graphene sheets coaxially arranged around a central hollow core. On the other hand, SWCNT consists of a single graphene layer rolled up into a seamless cylinder [15, 16]. In addition to the exceptional electrical and conductive properties, the CNTs also present excellent mechanical properties, with an elastic modulus in the order of 1 TPa and maximum tensile strength can reach 300 GPa (for CNTs free of defects) [13, 17]. These properties are related to a strong covalent bond between carbons and its arrangement in cylindrical nanostructures [5].

Due to their excellent properties, considerable interest has been drawn on polymer nanocomposites with CNTs [18]. The incorporation of carbon nanotubes in polymer matrices has been explored as a strategy to obtain composite materials with electrical properties and with superior mechanical and thermal properties. However, these fillers are materials of difficult dispersion in polymeric matrices. Problems arising from agglomeration during processing are commonly observed due to the low polymer/CNT interaction (see **Figure 3**) [19]. The processing conditions may influence the dispersion state of these nanofillers in the resulting material. In addition, carbon nanotubes can be chemically modified to improve the interfacial interaction [19, 20].

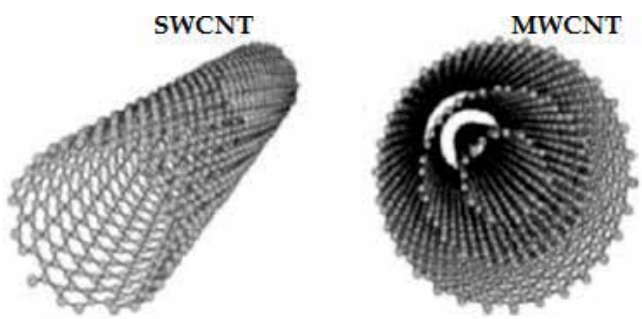

Figure 2. Representation of SWCNT and MWCNT [14].

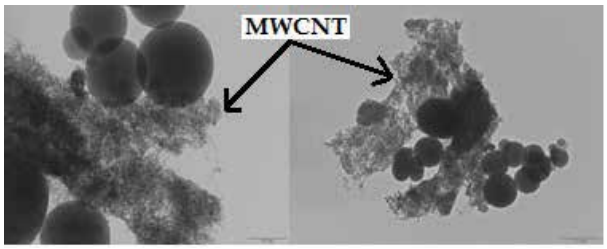

Figure 3. Micrographs obtained by transmission electron microscopy of nanocomposites with polyetherimide (PEI) and MWCNT [19].

The presence of functional groups on the side walls of CNTs increases the chemical reactivity between the filler and matrix, inducing to a better interface and consequently a better load transfer from the matrix to the reinforcement [5]. One route that has been considered for modification of carbon nanotubes is the surface treatment of these materials with a mixture of nitric and sulfuric acids (HNO_3/H_2SO_4), which results in the formation of carboxylic acid groups (-COOH) on the surface [5]. This treatment was developed by Goyanes et al [21] and can alter the nature of the CNTs surface making them more compatible with the polymer matrix. Besides the acid treatment, secondary particles, such as clay, have been used to improve the dispersion of carbon nanotubes and increase the electrical properties of composites containing these fillers [20]. In addition to obtaining nanocomposites using a single polymer matrix, the use of polymer/polymer blends as matrix has attracted the attention of researchers. It has been observed that polymer/polymer blends with carbon nanotubes have better electrical and thermal properties when compared to unfilled blends [18].

The electrical conductivity after the incorporation of CNTs in polymers occurs due to the formation of a three-dimensional network of CNTs inside the polymer matrix, which strength dependents on the distribution and dispersion of the CNTs. When the concentration of the nanofiller reaches a critical value, known as the limit of electrical percolation, the electrical conductivity of the nanocomposite increases unexpectedly. After this abrupt increase in electrical conductivity, it will show modest increases as the conductive additive increases inside the polymer matrix [18, 22]. In nanocomposites based on polymer blends, the amount of CNTs required to achieve electrical percolation may be even lower than in nanocomposites with a single polymer matrix, provided that a selective location of the CNTs occurs in the matrix phase or at the interface of the blend [18, 23]. In addition, it is especially desired the formation of blends with co-continuous morphology, where a double phenomenon of electric percolation can be found. Thus, the limit of electric percolation in polymer blends is strongly influenced by the concentration of nanotubes and also by the final morphology of the blends, which in turn is a function of the composition of the blend, the compatibilizer and the processing conditions [18].

2.1.2. Graphene

Graphene was discovered in 2004 by Andre. K. Geim and Konstantin S. Novoselov and has revolutionized the scientific frontiers in nanoscience and condensed matter physics due to its exceptional electrical, physical and chemical properties. Graphene has sparked enormous

interest in many research groups around the world and has resulted in an abrupt increase in publications on the subject. This material consists of one atomic thick sheet of covalently sp^2-bonded carbon atoms in a hexagonal arrangement [24, 25], as illustrated in **Figure 4**.

The primitive cell of graphene is composed of two non-equivalent atoms, A and B, and these two sub-lattices are translated from each other by a carbon-carbon distance $a_{c\text{-}c}$ = 1.44 Å [25]. Graphene can be produced from graphite by different methods, such as thermal expansion of chemically intercalated graphite, micromechanical exfoliation of graphite, chemical vapor deposition and chemical reduction method of graphene oxide [27]. Graphene has Young´s modulus of 1 TPa, fracture strength of 125 GPa, thermal conductivity of 5000 W/m.fK and electrical conductivity up to 6000 S/cm [28]. These properties in addition to extremely high surface area (theoretical limit: 2630 m^2/g) and gas impermeability indicate graphene's great potential for improving mechanical, electrical, thermal and gas barrier properties of polymer nanocomposites [28, 29].

The successful use of graphene depends on the exfoliation of bulk graphite into individual sheets. Several chemical-mechanical routes have been developed to produce individual exfoliated graphene sheets, for example, mechanical exfoliation, chemical exfoliation and chemical vapor deposition [30, 31]. Each method has its own advantages and drawbacks related to the purity and the presence of defects (oxygen and functional groups on the surface). The most common route to produce graphene involves the production of graphite oxide (GO) by oxidation chemistry followed by a reduction and mechanical exfoliation [6]. This is the basis of Hummers and Offeman's process [32]. GO is nonconductive, hydrophilic and can readily swell and disperse in water. Recently, several new methods of graphene functionalization were reported. Functionalized graphene sheets (FGS) demonstrate improved dispersibility in organic solvents and polymers [28, 30].

2.2. Layered nanoclays

Nanoclays belong to a class of materials generally made of layered silicates or clay minerals with traces of metal oxides and organic matter. Clay minerals are hydrous aluminum phyllosilicates, sometimes with variable amounts of iron, magnesium, alkali metals, alkaline earths and others cations [33]. In the last decades, several published works have shown that the dispersion of exfoliated clays in polymer leads to a remarkable increase in stiffness, fire retardancy and barrier properties, beginning at a very low nanoparticle volume fraction [3]. Clays have been found to be effective reinforcing fillers for polymer due to lamellar structure and high specific surface area (750 m^2/g) [2]. Smectite clays are layered silicates, and they are a

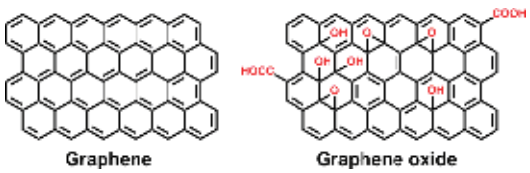

Figure 4. Honeycomb lattice of graphene [26].

required choice for the preparation of polymer nanocomposites due to their low cost, swelling properties and high cation exchange capacities. Some examples of these clays are montmorillonite, saponite, laponite, hectorite, sepiolite and vermiculite [16, 33]. Among these clays, montmorillonite is the most widely used clay in polymer nanocomposites, because of its large availability, well-known intercalation/exfoliation chemistry, high surface area and reactivity [33]. Montmorillonite (MMT) is composed of two tetrahedral silica sheets with an alumina octahedral sheet in the middle (2:1 layered structure), and the hydrated exchangeable cations occupy the spaces between lattices, as shown in **Figure 5**.

The sheets have dimensions of 1 nm thickness and are 100–500 nm in diameter, resulting in platelets with high aspect ratio [35]. Stacking of the clay layers leads to a regular van der Waals gap between the layers called interlayer or gallery. Isomorphic substitution within the layers generates negative charges that are counterbalanced by alkali and alkaline earth cations (Li^+, Na^+ or Ca^{2+}) situated inside the galleries. The extent of the negative charge of the clay is characterized by the cation exchange capacity (CEC) [36]. Natural montmorillonite is hydrophilic and most polymers tend to be hydrophobic, so the clay surface must be modified to yield organophilic clay in these cases. This is often done by exchanging the cations in the gallery with alkylammonium or alkylphosphonium salts (for example, dioctadecyl dimethyl ammonium bromide), typically with chain lengths longer than eight carbon atoms (C_8). The clay that was previously hydrophilic becomes organophilic after modification [35]. The replacement of inorganic exchange cations with organic ions on the gallery surfaces of smectite clays is useful to expand the clay galleries. This facilitates the penetration into the gallery space (intercalation) by either the polymer chains. Other type of modification that has been used in nanoclays is the process known as silanization. The modification of the clay with organosilanes promoted covalent bonds between polymer and clay by reactive extrusion favoring strong interactions between clay and matrix. Examples of those silanes that have been used to modify nanofiller are 3-aminopropyltriethoxysilane (APTES) and vinyltrimethoxysilane (VTMS) [37].

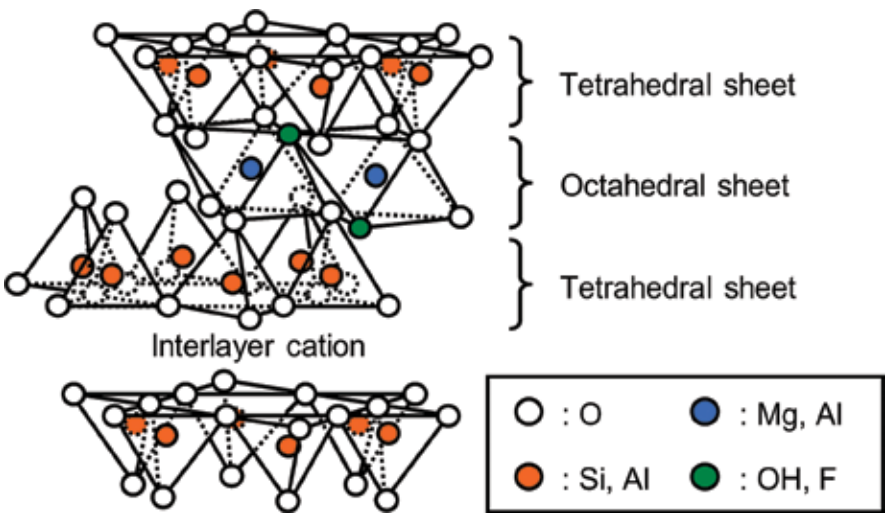

Figure 5. Structure of 2:1 layered silicates [34].

2.3. Porous and hollow nanoparticles

2.3.1. Halloysite

Halloysite nanotube (HNT) is an aluminosilicate with hollow micro- and nanotubular structure [38]. HNT is structurally much to kaolinite [39] and may intercalate a monolayer of water molecules, which is weakly held. It consists of sheets of SiO_4 tetrahedra with sheets of edge sharing AlO_6 octahedral [40], as shown in **Figure 6**. Consequently, the chemical composition of HNT is similar to nanoclays, while nanotubular geometry is similar to CNTs. Uniqueness of HNT exists in its tubular form with length up to few microns and diameter in nm range. It offers innovative possibilities for nanocomposite preparation [41]. Optimizing polymer properties by filler addition of low content has been the focus of industrial and academic research. HNT as nanofiller in polymeric materials has been found to significantly increase the mechanical, thermal, non-flammability and other physical properties of the nanocomposite [42]. Due to variety of characteristics, such as nanoscale size, shape, surface area and high length to diameter ratio, HNT has been discovered for numerous applications.

2.3.2. Zeolite

Zeolites are widely used as catalysts or catalyst supports in a variety of applications in refining and (petro)chemical industries [44]. Particularly, the faujasite-type framework is an aluminosilicate with cavities of 1.3 nm of diameter interconnected by pores of 0.74 nm, as illustrated in **Figure 7**. The cubic unit cell of these aluminosilicates contains around 192 $(Si,Al)O_4$ tetrahedrons [45]. The development of zeolite synthesis methods to reduce the size of the particles has received special interest [46]. Micrometer-sized zeolites have a negligible external surface area compared with the large surface area in their internal microporous [47]. Zeolite nanoparticles lead to substantial changes in the material properties, increasing the intercrystalline space, the external and internal surface area and volume and pore mouths exposed. Therefore, the application of nanozeolites in some catalytic reactions can reduce diffusion path lengths and increase catalytic activity and selectivity, as well as improve reaction medium stability [48].

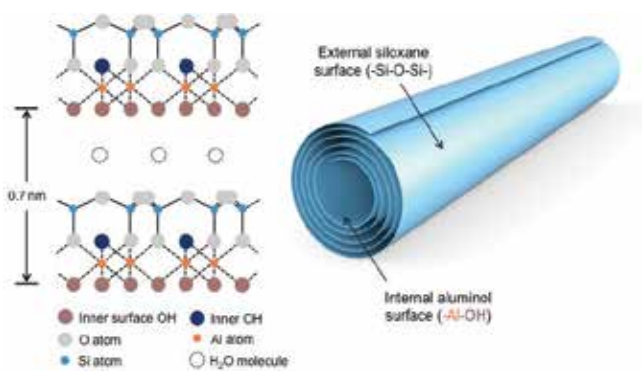

Figure 6. Structure of halloysite nanotube [43].

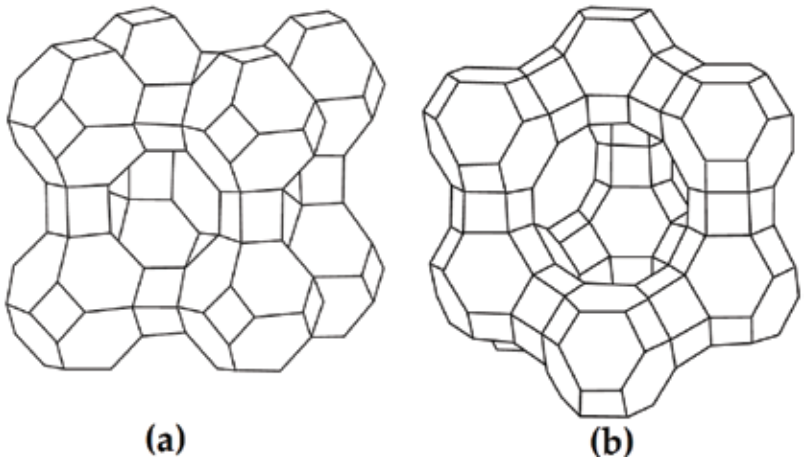

Figure 7. (a) Zeolite A and (b) faujasite-type zeolites X and Y [45].

2.4. Nanocellulose

There is an interest in the use of biomass as a source of renewable energy and materials. A promising source of biomass is cellulose. By suitable chemical and mechanical treatments, it is possible to produce fibrous materials with one or two dimensions in the nanometer range from any naturally occurring sources of cellulose [49]. The term "nanocellulose" is used to cover the range of materials derived from cellulose with at least one dimension in the nanometer range. This material has been described as a new bionanomaterial [50]. Isolation of crystalline cellulosic regions, in the form of monocrystals, is done by an acid hydrolysis process [51]. The first report on the mechanical destructuration of cellulose fibers was published in 1983 in two companion papers [52]. Nanocellulose-based materials have a low carbon footprint and are sustainable, renewable, recyclable and nontoxic; they thus have the potential to be truly green nanomaterials with many useful and unexpected properties. **Figure 8** shows the illustration of the crystalline structure of cellulose.

2.4.1. Cellulose nanofibrils

The mechanically induced destructuration strategy consists of applying severe multiple mechanical shearing actions to a cellulosic fiber slurry to release more or less individually

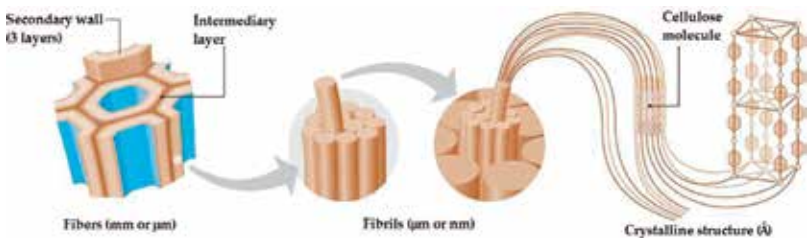

Figure 8. Crystalline structure of cellulose [53].

the constitutive microfibrils. Different shearing types of equipment, such as a homogenizer, microfluidizer or ultra-fine friction grinder, are generally used. This material is usually called nanofibrillated cellulose (NFC) or cellulose nanofibrils (CNF) and is obtained as an aqueous suspension [49]. The width is 3–100 nm depending on the source of cellulose, defibrillation process and pretreatment, and the length is usually higher than 1 μm [53].

2.4.2. Cellulose nanocrystals

The chemically induced destructuration strategy consists of applying a controlled strong acid hydrolysis treatment to cellulosic fibers, allowing dissolution of amorphous domains and therefore longitudinal cutting of the microfibrils. The ensuing nanoparticles are called cellulose nanocrystals (CNCs) and are obtained as an aqueous suspension [51]. These nanoparticles have high aspect ratio rod-like nanocrystals (whiskers). Their geometrical dimensions depend on the origin of the cellulose and hydrolysis conditions. Sulfuric acid is used for the preparation of CNC, and this process induces the formation of negatively charged sulfate groups at the surface. The average length is of the order of a few hundred nanometers and the width is of the order of a few nanometers [53]. An important parameter for CNCs is the aspect ratio, which is defined as the ratio of the length to the width [49].

2.5. Nanoparticles of metallic alloys

The possibility of using metal hydrides (MH) alloys in hydrogen technology has being attracting interest [54]. These types of material react with hydrogen reversibly, thus being successfully utilized in the solid state storage of the gas. However, MH alloys under repeated hydriding/dehydriding cycling suffer from a pulverization phenomenon due to a large volume mismatch between the hydride and the metal compound [55]. As a consequence, repeated hydrogen loading/unloading cycles produce free metal powder particles in nanoscale size. Particle fragmentation results in a considerable increasing of the metal surface area with a consequent enhancement of some properties. Among these, the hydriding kinetics is expected to improve even if a parallel increasing of undesired degradative phenomena (such as oxidation) can result in a detriment of the overall storage capacity of the material. Furthermore, from a technological point of view, the presence of unconfined nanoparticles inside the device can constitute an obstacle to the gas flow through the material [55]. Anyway, storing hydrogen in MH beds as a chemical compound appears to be a promising, cost-effective and safe method of hydrogen storage in the near future [56]. An example of polymer nanocomposite with MH alloy is shown in **Figure 9**.

2.6. Compatibilization in polymer nanocomposites

To obtain a polymer blend or nanocomposite with the desired properties, compatibilization is an important issue. Actually, the differences in chemical nature between the polymers or the polymer matrix and the nanoparticles give rise to systems with poor properties [58]. Compatibilization gains importance in order to improve the properties. The degradation, which must be minimized, involves the decomposition of the organomodifier and the interactions among the degradation products and the polymers. These, together with the processing conditions, influence the morphology and the properties of the material [59, 60] (**Figure 10**).

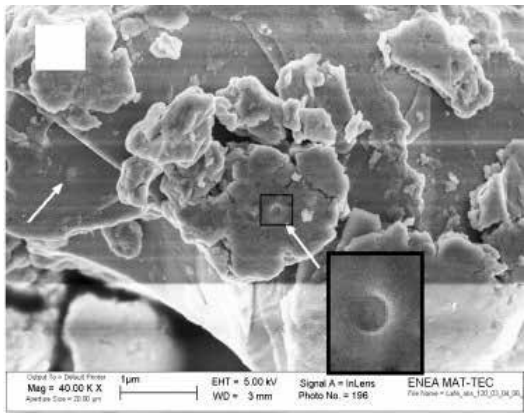

Figure 9. $LaNi_5$/ABS after a mechanical-dry particle coating process in a tumbling mill [57].

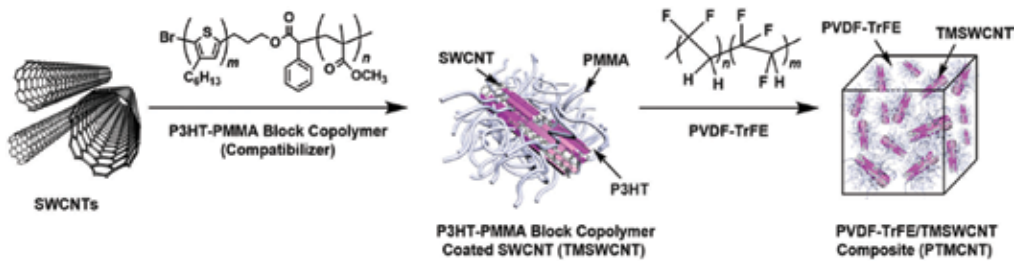

Figure 10. Scheme of production of compatibilized nanocomposite of PVDF/SWCNT [60].

3. Processing of polymer nanocomposites

Polymer nanocomposites can be produced by three methods: in situ polymerization, solution and melt blending. An appropriate method is selected according to the type of polymeric matrix, nanofiller and desired properties for the final products [61].

3.1. In situ polymerization

During the in situ polymerization, the nanofiller must be properly dispersed in the monomer solution before the polymerization process starts, ensuring the polymer will be formed between the nanoparticles. Polymerization can be started using several techniques (heat, use of an appropriate initiator, etc.) [62]. Using this technique, a polymer grafted nanoparticle and high loading of nanofillers without aggregation can be carried out [63]. Organic modifiers may be used to help the dispersion of the nanoparticles and take part in the polymerization [64]. It can be an alternative way for the production of nanocomposites using polymers that are non-soluble or thermally unstable [65]. In some cases, this technique can be applied in solvent-free form [66]. It is also a technique which can result to higher performance products [67]. Mini-emulsion polymerization is based on the creation of monomer droplets that are dispersed in a solution in a nanoscale [68]. The procedure for the production of polymer nanocomposites by this technique is shown in **Figure 11**.

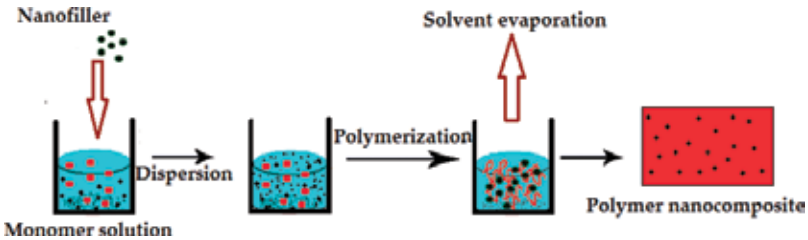

Figure 11. Schematic illustration for the in situ polymerization method.

Some of the benefits are controllable particle morphology [69], good interfacial adhesion of the nanofillers [70] and high transparency [71, 72]. When using this method, it is possible to [61] apply higher contents of nanofillers without agglomeration, have better performance of the final products, expand to the solvent-free form, have covalent bond among the nanoparticle functional groups and polymer chains and use both thermoset and thermoplastic polymers. One main limitation is the ease of agglomeration [63, 65].

3.2. Blending

This method is widely used for the production of polymer nanocomposites due to its simplicity. However, reaching a proper dispersion of the nanofiller in the polymer matrix can be more difficult when compared to other methods [61, 62].

3.2.1. Solution blending

Solution blending is actually a system including the polymer and nanofiller, which are easily dispersed in an appropriate solvent [62]. Ultrasonic irradiation, magnetic stirring or even shear mixing can be used to disperse the nanofiller within the polymer [63]. In this method, when the solvent evaporates, the nanoparticle remains dispersed into the polymer chains, as shown in **Figure 12**. The produced nanocomposite can also be obtained as a thin film [61].

There are some problems for the solution blending from the economic and environmental point of view. A proper decision must be taken to choose a correct method according to the situation and the desired product [73]. Some of the benefits of using solution blending are [61]

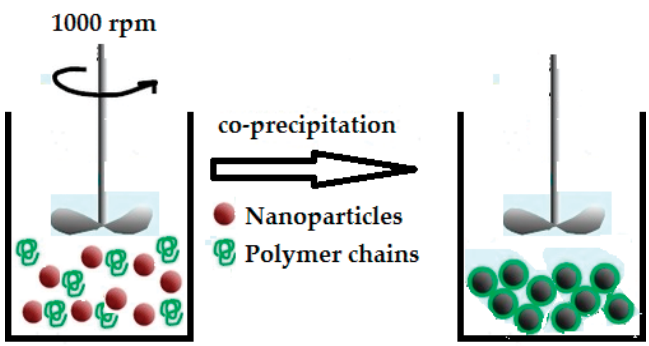

Figure 12. Schematic illustration for the solution blending method.

reduction in the permeability of gases [74], easy operation, and general technique for all types of nanofillers and to both thermoset and thermoplastic polymers [75]. The main limitations are aggregation and environmental constraints [73, 76]. This technique will likely be limited to polymers that are soluble in water [77].

3.2.2. Melt blending

In the melt blending method, the nanofillers are directly dispersed into the molten polymer. During mixing in the melt state, the strain that the polymer applies on the particles depends on its molecular weight and weight distribution. High levels of shear stress reduce the size of the agglomerates [61]. The mechanism for the action of shear flow during the dispersion and distribution of nanoparticles is shown in **Figure 13**. Initially, large agglomerates break down and form smaller ones dispersed through the polymer matrix. The transfer of strain from the polymer to these new agglomerates leads to stronger shearing, which breaks them into individual particles; this step depends fundamentally on time and on the chemical affinity between the polymer and the surface of the nanoparticles [59, 78].

Both single and twin-screw extruders are usually applied for melt blending [79], although it must be noted that in some cases high temperatures can have unfavorable effects on the modified surface of the nanofiller and an optimization must be employed [80]. Intermeshing co-rotating twin-screw extruders are quite popular for this purpose. This method has some drawbacks that involve parameters that are not easy to control, such as the interaction between the polymer and the nanoparticles and the processing conditions (temperature and residence time) [81]. Therefore, in some cases, it can be difficult to obtain well-dispersed nanoparticles. An example of a medium dispersive screw profile for a twin-screw extruder is shown in **Figure 14**. It was designed with transport and kneading block elements and one turbine element at the end of the melting zone [82].

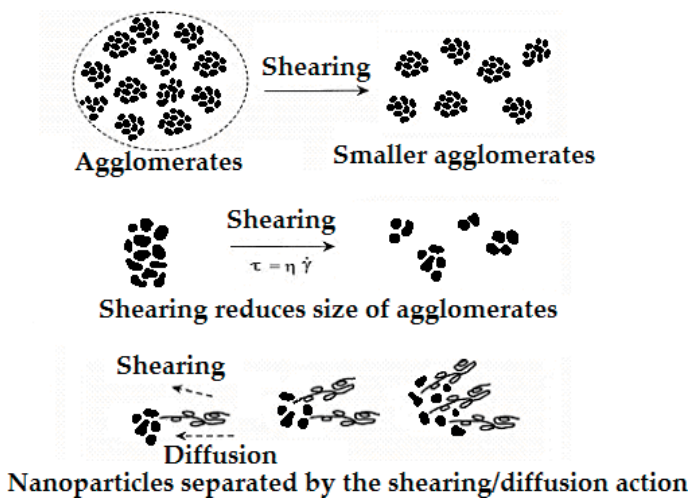

Figure 13. Effect of shearing on the dispersion of the nanoparticles during melt blending.

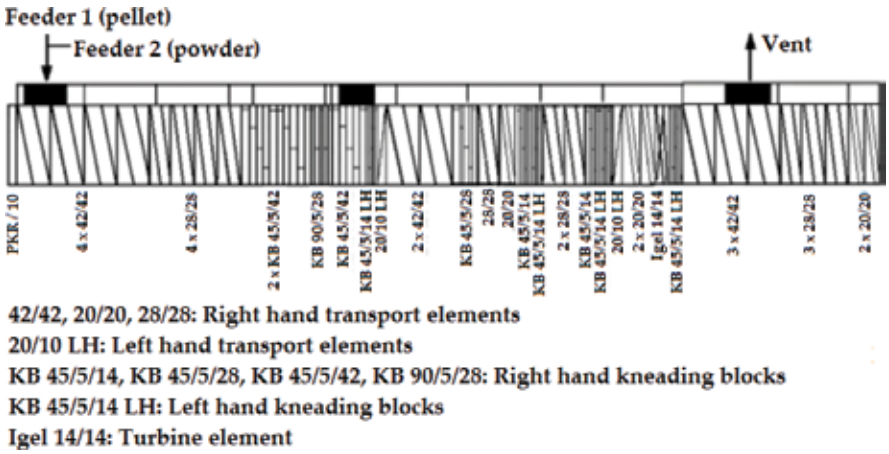

Figure 14. Schematic illustration of a screw profile of a twin-screw extruder [82].

Melt blending has been used for the production of polymer nanocomposites with different types of matrices: polypropylene [83–85], poly(methyl methacrylate) [86], poly(lactic acid) [75], poly(vinyl chloride) [87], polycarbonate [88, 89], polyamide 6 [4, 90, 91], etc.

The melt blending is well matched with several industrial operations, such as extrusion and injection molding, and consequently, it can be commercialized [61]. Some of the benefits of this technique are good dispersion of the nanoparticles [92], enhancement of the heat stability [93], improvement of mechanical properties [83–86] and low cost-effectiveness and eco-friendly (do not use solvent). A considerable limitation is the use of high temperatures, which can damage the modified surface of the nanofillers [94].

By and large, each technique has some advantages over the others and can be selected as the best method according to the conditions and applying materials [61].

4. Techniques of characterization

The knowledge and use of techniques of characterization is determinative to understand the basic physical and chemical properties of polymer nanocomposites. For several applications, it facilitates the study of emerging materials by giving information on intrinsic properties [95]. Various techniques have been used extensively in polymer nanocomposite research.

4.1. Structural and morphological characterization

The commonly used techniques are wide-angle X-ray diffraction (WAXD), small-angle X-ray scattering (SAXS), scanning electron microscopy (SEM) and transmission electron microscopy (TEM) [10, 96, 97]. The SEM provides images of surface features associated with a sample. The atomic force microscope (AFM) uses a sharp tip to scan across the sample. Raman spectroscopy has proved a useful probe of carbon-based material properties [95, 98].

Due to the easiness and availability, WAXD is most commonly used to probe the nanocomposite structure [99, 100] and to study the kinetics of the polymer melt intercalation, when using layered silicates [100]. In these systems, a fully exfoliated system is characterized by the absence of intensity peaks in WAXD pattern [101]. Therefore, a WAXD pattern concerning the mechanism of nanocomposite formation and their structure are tentative issues for making any conclusion. On the other hand, TEM allows a qualitative understanding of the internal structure, spatial distribution of the various phases and views of the defective structure through direct visualization. Thus, TEM complements WAXD data [102]. **Figure 15** illustrates some results obtained from both analyses.

SAXS is used to observe structures on the order of 10 Å or larger, in the range of 0–5°. The TEM, AFM and SEM are also required to characterize the dispersion and distribution of nanoparticles. WAXD has found relatively limited success in CNT research [95]. In the Raman spectra of graphite and SWNTs, there are many features that can be identified with specific phonon modes that contribute to each feature. The Raman spectra of both materials can provide much information about the exceptional 1D properties of carbon materials, such as their phonon structure and their electronic structure, as well as information about sample imperfections. Since mechanical, elastic and thermal properties are also strongly influenced by phonons, Raman spectra provide general information about the structure and properties of SWNTs [98].

4.2. Thermal, mechanical, rheological and other techniques of characterization

For further characterization of polymer nanocomposites, the commonly used techniques are Fourier-transform infrared (FTIR), rheometry [82], differential scanning calorimeter (DSC), thermogravimetric (TGA), thermomechanical (TMA) and dynamic modulus analysis (DMA) [96].

Because viscoelastic measurements are highly sensitive to the nano- and mesoscale structure of polymers, when combined with WAXD, TEM, DSC, TGA and DMA, they will provide fundamental understanding of the state and mechanism of dispersion of the nanoparticles in the

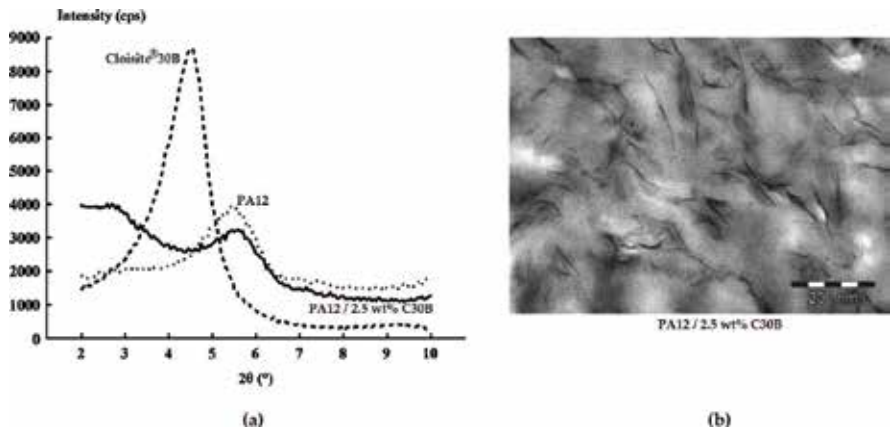

Figure 15. (a) WAXD diffractograms and (b) TEM micrograph of a 2.5 wt% MMT-PA12 nanocomposite [103].

http://dx.doi.org/10.5772/intechopen.81329

matrix [104]. In addition, understanding rheological properties of nanocomposites is crucial for application development and understanding polymer processability. The nanocomposites usually demonstrate a change of pattern in dynamic mechanical spectrum, as a function of the degree of exfoliation/dispersion, from typical polymer response [$G' \sim \omega^2$, $G'' \sim \omega^1$] to a terminal response [$G' \sim \omega^1$, $G'' \sim \omega^1$], then to a pattern with double crossover frequencies, and

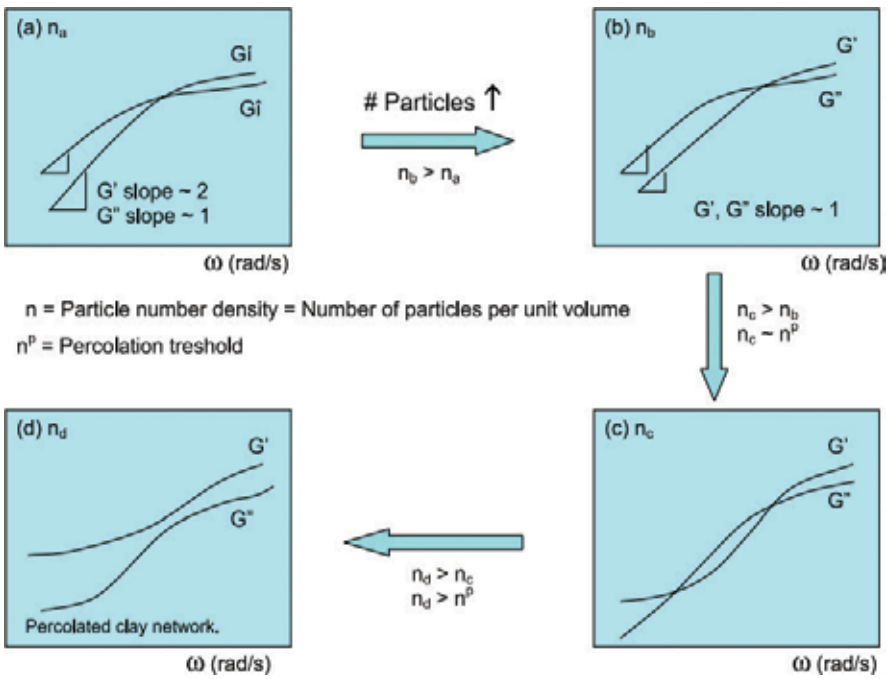

Figure 16. Schematic representation of the rheological response to the increase in the number of particles per unit volume [104].

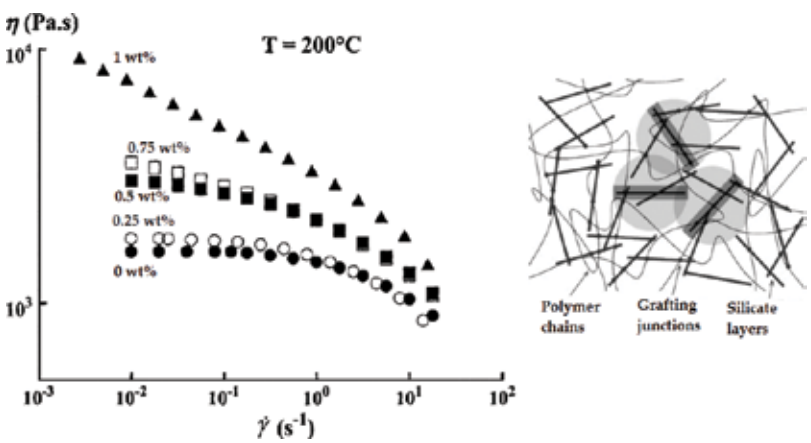

Figure 17. Steady shear viscosities as a function of shear rate at different montmorillonite concentrations in PA12 and a scheme of a percolated network in a nanocomposite [103, 105].

finally to a solid-like response with G′ > G″ in all frequency ranges, as seen in **Figure 16**. The number of particles per unit volume is a key factor determining the characteristic response of nanocomposites [82, 104].

The presence of nanofillers caused these nanocomposites to have solid-like behaviors and slower relaxation. This behavior can be explained in terms of the development of a grafting-percolated nanoparticle network structure [105]. Its formation is a consequence of physical interactions between dispersed nanoparticles, polymeric chains and surfactants, which promote a considerable resistance to flow [103]. This behavior is shown in **Figure 17**.

The next section will briefly discuss the main properties and characteristics of some polymer nanocomposites, which have been used in relevant applications.

5. Properties and potential applications

Polymer nanocomposites have advantages: (1) they are lighter than conventional composites because high degrees of stiffness and strength are realized with far less high-density material, (2) their barrier properties are improved compared with the neat polymer, (3) their mechanical and thermal properties are potentially superior and (4) exhibit excellent flammability properties and increased biodegradability of biodegradable polymers [106].

There are many applications of polymer/clay nanocomposites and an increasing number of commercial products available on the market. Notable examples are automotive parts [16, 20], packaging [2, 8, 107], construction materials [36], biotechnology [108], medical devices, etc. [3, 36, 108]. One important property observed due to the incorporation of clay particles in polymers is a significant level of flame retardancy. This property also provides avenues for applications in many other areas, such as building materials, computer housings and car interiors [36]. Moreover, balanced mechanical properties, functionalities and biocompatibility of bionanocomposites provide an exciting platform for the design and fabrication of new materials for biomedical applications [36]. Another area of interest for nanocomposites is the packaging industry. The impermeable clay layers mandate a tortuous pathway, which difficult the diffusion of molecules throughout the matrix [109]. Improving food quality and shelf life, while reducing plastic waste, has stimulated the development of biodegradable polymer-based PCNs as advanced and smart packaging materials [109].

There are also several applications with carbon nanotubes and graphene. An area of notable application of these materials is in the optoelectronic industry [110, 111]. There is a wide range of applications which include fiber lasers, supercapacitor, field emission devices and photovoltaics, where the combination of tunable optoelectronic properties as well as structural and chemical stability, high surface area and low mass density of nanofillers with the processability of polymers offers a new class of materials [110, 111].

Nanocomposites of an organic-modified MMT and PA6 with a residual monomer were once produced by melt blending in a torque rheometer [112]. By WAXD, intercalated structures were observed in the nanocomposites with 3 and 5 wt% of MMT; on the other hand,

when 7 wt% of MMT was added, an exfoliated structure was obtained due to the predominant linking reactions between the residual monomer and the polar organic surfactant. Solutions of these nanocomposites in formic acid were prepared, and the 3 and 5 wt% nanocomposites were successfully electrospun; however, electrospinning of the 7 wt% nanocomposite was not possible. WAXD, SEM and TEM results showed that the 3 and 5 wt% nanofibers with average diameter between 80 and 250 nm had exfoliated structures. These results indicate that the high elongational forces developed during the electrospinning process changed the initial intercalated/exfoliated structure of the nanocomposites to an exfoliated one [112].

The use of an aqueous dispersion of polyethylene copolymer with a relatively high content of acrylic acid as a compatibilizer and as an alternative medium to obtain polyethylene NFC nanocomposites was a matter of recent study [113]. The NFC content was varied from 1 to 90 wt%, and the appearance, optical, thermal, mechanical and rheological properties, as well the morphology of the films, were evaluated. The PE/NFC films were transparent up to 20 wt% of NFC indicating a good dispersion of NFC, with PE-rich and NFC-rich regions observed by SEM. Improved mechanical properties were achieved with an increase in the Young's modulus. The rheological behavior indicated good melt processability [113].

Water suspensions of NFC with xylan, xyloglucan and pectin were studied for foaming and structural properties as a new means for food structuring [114]. They were analyzed by rheometry, microscopy and optical coherence tomography (OCT). A combination of xylan with TEMPO-oxidized NFC produced a mixture with well-dispersed air bubbles, while the addition of pectin improved the elastic modulus, hardness and toughness of the structures. Shear flow caused NFC to form plate-like flocs in the suspension that accumulated near bubble interfaces. This tendency could be affected by adding laccase to the dispersion. Xyloglucan interacted strongly with TEMPO-oxidized NFC (high storage modulus) [114].

6. Conclusions

Polymer nanocomposites offer excellent opportunities to explore new functionalities beyond those of conventional materials. The field of nanocomposites has been one of the most promising and emerging research areas. They find special attention due to the unique properties such as light weight, ease of production and flexibility. A defining feature of polymer nanocomposites is that the small size of the fillers leads to an enormous increase in interfacial area as compared to traditional composites. The interfacial area creates a significant volume fraction of interfacial polymer with properties different from the bulk polymer even at low loadings of the nanofiller. Interfacial structure is known to be different from bulk structure, and in polymers with nanoparticles possessing high surface areas, most parts of the polymers are present near the interfaces, in spite of the small weight fraction of the filler. This is one of the reasons why the nature of reinforcement is different in nanocomposites. The crucial parameters which determine the effects of fillers on the properties of composites are filler size, shape and aspect ratio and filler-matrix interactions.

Acknowledgements

The authors would like to thank the Coordination for the Improvement of Higher Education Personnel (CAPES, process PNPD20131474-33001014004P9) for the financial aid.

Author details

Amanda Dantas de Oliveira[1]* and Cesar Augusto Gonçalves Beatrice[2]
*Address all correspondence to: amandaoliveira82@gmail.com

1 Technology Development Center, Federal University of Pelotas, Pelotas, RS, Brazil

2 Department of Materials Engineering, Federal University of São Carlos, São Carlos, SP, Brazil

References

[1] Müller K, Bugnicourt E, Latorre M, Jorda M, Echegoyen Sanz Y, Lagaron J, et al. Review on the processing and properties of polymer nanocomposites and nanocoatings and their applications in the packaging, automotive and solar energy fields. Nanomaterials. 2017;**7**:74-121

[2] Bitinis N, Hernandez M, Verdejo R, Kenny JM, Lopez-Manchado MA. Recent advances in clay/polymer nanocomposites. Advanced Materials. 2011;**23**:5229-5236

[3] Zaïri F, Gloaguen JM, Naït-Abdelaziz M, Mesbah A, Lefebvre JM. Study of the effect of size and clay structural parameters on the yield and post-yield response of polymer/clay nanocomposites via a multiscale micromechanical modelling. Acta Materialia. 2011;**59**:3851-3863

[4] Oliveira AD, Larocca NM, Paul DR, Pessan LA. Effects of mixing protocol on the performance of nanocomposites based on polyamide 6/acrylonitrile-butadiene-styrene blends. Polymer Engineering and Science. 2012;**52**:1909-1919

[5] Maron GK, Noremberg BS, Alano JH, Pereira FR, Deon VG, Santos RCR, et al. Carbon fiber/epoxy composites: Effect of zinc sulphide coated carbon nanotube on thermal and mechanical properties. Polymer Bulletin. 2017;**75**:1619-1633

[6] de Melo CCN, Beatrice CAG, Pessan LA, de Oliveira AD, Machado FM. Analysis of nonisothermal crystallization kinetics of graphene oxide-reinforced polyamide 6 nanocomposites. Thermochimica Acta. 2018;**667**:111-121

[7] Gómez H, Ram MK, Alvi F, Villalba P, Stefanakos E, Kumar A. Graphene-conducting polymer nanocomposite as novel electrode for supercapacitors. Journal of Power Sources. 2011;**196**:4102-4108

[8] Sonia A, Priya Dasan K. Celluloses microfibers (CMF)/poly (ethylene-co-vinyl acetate) (EVA) composites for food packaging applications: A study based on barrier and biodegradation behavior. Journal of Food Engineering. 2013;**118**:78-89

[9] Marini J, Pollet E, Averous L, Bretas RES. Elaboration and properties of novel biobased nanocomposites with halloysite nanotubes and thermoplastic polyurethane from dimerized fatty acids. Polymer (Guildf). 2014;**55**:5226-5234

[10] Alexandre M, Dubois P. Polymer-layered silicate nanocomposites: Preparation, properties and uses of a new class of materials. Materials Science & Engineering R: Reports. 2000;**28**:1-63

[11] Bhattacharya SN, Kamal MR, Gupta RK. Polymeric Nanocomposites Theory and Practice. Munich/Cincinnati: Carl Hanser Publishers/Hanser Gardner Publications. 2007. pp. 5-10

[12] Tanaka K, Yamabe T, Fukui K. The Science and Technology of Carbon Nanotubes. Elsevier; 1999. p. 750. https://doi.org/10.1016/B978-0-08-042696-9.X5000-9

[13] Guldi DM, Martín N. Carbon Nanotubes and Related Structures: Synthesis, Characterization, Functionalization, and Applications. Wiley-VCH; 2010. p. 539. https://doi.org/10.1002/9783527629930

[14] Machado IRL, Mendes HMF, Alves GES, Faleiros RR. Nanotubos de carbono: Potencial de uso em medicina veterinária. Ciência Rural. 2014;**44**:1823-1829

[15] Ma PC, Siddiqui NA, Marom G, Kim JK. Dispersion and functionalization of carbon nanotubes for polymer-based nanocomposites: A review. Composites. Part A, Applied Science and Manufacturing. 2010;**41**:1345-1367

[16] Schadler LS. Polymer-based and polymer-filled nanocomposites. In: Nanocomposite Science and Technology. Wiley-VCH; 2003. pp. 77-153. https://doi.org/10.1002/3527602127.ch2

[17] Sui Y, Cui B, Guardián R, Acosta D, Martínez L, Perez R. Growth of carbon nanotubes and nanofibres in porous anodic alumina film. Carbon N. Y. 2002;**40**:1011-1016

[18] Monemian S, Jafari SH, Khonakdar HA, Goodarzi V, Reuter U, Pötschke P. MWNT-filled PC/ABS blends: Correlation of morphology with rheological and electrical response. Journal of Applied Polymer Science. 2013;**130**:739-748

[19] Oliveira AD, Beatrice CAG, Passador FR, Pessan LA. Polyetherimide-based nanocomposites materials for hydrogen storage. AIP Conference Proceedings. 2016;**1779**:1-6

[20] Liu L, Grunlan JC. Clay assisted dispersion of carbon nanotubes in conductive epoxy nanocomposites. Advanced Functional Materials. 2007;**17**:2343-2348

[21] Goyanes S, Rubiolo GR, Salazar A, Jimeno A, Corcuera MA, Mondragon I. Carboxylation treatment of multiwalled carbon nanotubes monitored by infrared and ultraviolet spectroscopies and scanning probe microscopy. Diamond and Related Materials. 2007;**16**:412-417

[22] Ribeiro B, Cocchieri E, Leali M. Estudo das propriedades elétricas e térmicas de compósitos nanoestruturados de poli (sulfeto de fenileno) reforçados com nanotubos de carbono

[Electrical and thermal study of carbon nanotubes reinforced poly (phenylene sulfide) nanostructured composite]. 2015;**25**:94-100

[23] Wegrzyn M, Galindo B, Benedito A, Giménez E. Effect of processing method on mechanical properties of PC/ABS-MWCNT nanocomposites. Macromolecular Symposia. 2012; **321-322**:161-165

[24] Lee S, Lee KK, Lim E. Synthesis of Aqueous Dispersion of Graphenes via Reduction of Graphite Oxide in the Solution of Conductive Polymer. In: Graphene – Synthesis, Characterization, Properties and Applications. IntechOpen; 2011. pp. 37-44. https://doi.org/10.5772/1742

[25] Choi W, Lee J. Graphene: Synthesis and applications. In: Handbook of Nanomaterials and their Applications. 1st ed. CRC Press; 2011. p. 394. ISBN 9781439861875

[26] Graphenes, Graphene Oxides (GOs) [Internet]. Tokyo Chemical Industry. Available from: https://www.tcichemicals.com/eshop/en/kr/category_index/12962;jsessionid=FFE5981474BE18FA56275B7CA60D0D93 [Accessed: 2018/07/23]

[27] Mittal V, Chaudhry AU. Polymer-graphene nanocomposites: Effect of polymer matrix and filler amount on properties. Macromolecular Materials and Engineering. 2015;**300**: 510-521

[28] Wan C, Chen B. Reinforcement and interphase of polymer/graphene oxide nanocomposites. Journal of Materials Chemistry. 2012;**22**:3637-3646

[29] Tan B, Thomas NL. A review of the water barrier properties of polymer/clay and polymer/graphene nanocomposites. Journal of Membrane Science. 2016;**514**:595-612

[30] Mukhopadhyay P, Gupta RK. Graphite, Graphene and their Polymer Nanocomposites. 1st ed. CRC Press; 2013. p. 589. ISBN 9781439827796

[31] Sengupta R, Bhattacharya M, Bandyopadhyay S, Bhowmick AK. A review on the mechanical and electrical properties of graphite and modified graphite reinforced polymer composites. Progress in Polymer Science. 2011;**36**:638-670

[32] Hummers WS, Offeman RE. Preparation of graphitic oxide. Journal of American Chemical Society. 1958;**80**:1339-1339

[33] Kotal M, Bhowmick AK. Polymer nanocomposites from modified clays: Recent advances and challenges. Progress in Polymer Science. 2015;**51**:127-187

[34] Ino K, Udagawa I, Iwabata K, Takakusagi Y, Kubota M, Arai K, et al. Heterogeneous nucleation of protein crystals on fluorinated layered silicate. 2011;**6**:1-9

[35] Chen B. Polymer–clay nanocomposites: An overview with emphasis on interaction mechanisms. British Ceramic Transactions. 2004;**103**:241-249

[36] Ray SS. Recent trends and future outlooks in the field of clay-containing polymer nanocomposites. Macromolecular Chemistry and Physics. 2014;**215**:1162-1179

[37] Raji M, Mekhzoum MEM, Rodrigue D, El Kacem QA, Bouhfid R. Effect of silane functionalization on properties of polypropylene/clay nanocomposites. Composites. Part B, Engineering. 2018;**146**:106-115

[38] Kausar A. Review on polymer/halloysite nanotube nanocomposite. Polymer-Plastics Technology and Engineering. 2018;**57**:548-564

[39] Pal P, Kundu MK, Maitra A, Malas A, Das CK. Synergistic effect of halloysite nanotubes and MA-*g*-PE on thermo-mechanical properties of polycarbonate-cyclic olefin copolymer based nanocomposite. Polymer-Plastics Technology and Engineering. 2016;**55**:1481-1488

[40] Teo ZX, Chow WS. Impact, thermal, and morphological properties of poly(lactic acid)/poly(methyl methacrylate)/halloysite nanotube nanocomposites. Polymer-Plastics Technology and Engineering. 2016;**55**:1474-1480

[41] Vahedi V, Pasbakhsh P. Polymer nanocomposites reinforced by halloysite nanotubes: A review. 2015. pp. 141-172

[42] Pasbakhsh P, Churchman GJ, Keeling JL. Characterisation of properties of various halloysites relevant to their use as nanotubes and microfibre fillers. Applied Clay Science. 2013;**74**:47-57

[43] Halloysite Clay Nanotubes [Internet]. Available from: http://phantomplastics.com/functional-fillers/halloysite/ [Accessed: 2018/07/23]

[44] Vermeiren W, Gilson J-P. Impact of zeolites on the petroleum and petrochemical industry. Topics in Catalysis. 2009;**52**:1131-1161

[45] Lutz W. Zeolite Y: Synthesis, modification, and properties—A case revisited. Advances in Materials Science and Engineering. 2014;**2014**:1-20

[46] Reinoso D, Adrover M, Pedernera M. Green synthesis of nanocrystalline faujasite zeolite. Ultrasonics Sonochemistry. 2018;**42**:303-309

[47] Mintova S, Gilson J-P, Valtchev V. Advances in nanosized zeolites. Nanoscale. 2013;**5**:6693-6703

[48] Song W, Li G, Grassian VH, Larsen SC. Development of improved materials for environmental applications: Nanocrystalline NaY zeolites. Environmental Science and Technology. 2005;**39**:1214-1220

[49] Dufresne A. Cellulose nanomaterial reinforced polymer nanocomposites. Current Opinion in Colloid & Interface Science. 2017;**29**:1-8

[50] Dufresne A. Nanocellulose: A new ageless bionanomaterial. Materials Today. 2013;**16**:220-227

[51] Nickerson RF, Habrle JA. Cellulose intercrystalline structure. Industrial and Engineering Chemistry. 1947;**39**:1507-1512

[52] Lin N, Huang J, Dufresne A. Preparation, properties and applications of polysaccharide nanocrystals in advanced functional nanomaterials: A review. Nanoscale. 2012;**4**:3274-3294

[53] Ben Azouz K, Ramires EC, Van den Fonteyne W, El Kissi N, Dufresne A. Simple method for the melt extrusion of a cellulose nanocrystal reinforced hydrophobic polymer. ACS Macro Letters. 2012;**1**:236-240

[54] Sakintuna B, Lamari-Darkrim F, Hirscher M. Metal hydride materials for solid hydrogen storage: A review. International Journal of Hydrogen Energy. 2007;**32**:1121-1140

[55] Goodell PD. Stability of rechargeable hydriding alloys during extended cycling. Journal of the Less Common Metals. 1984;**99**:1-14

[56] Kikkinides ES, Georgiadis MC, Stubos AK. On the optimization of hydrogen storage in metal hydride beds. International Journal of Hydrogen Energy. 2006;**31**:737-751

[57] Pentimalli M, Padella F, Pilloni L, Imperi E, Matricardi P. AB5/ABS composite material for hydrogen storage. International Journal of Hydrogen Energy. 2009;**34**:4592-4596

[58] Mistretta MC, Ceraulo M, La Mantia FP, Morreale M. Compatibilization of polyethylene/polyamide 6 blend nanocomposite films. Polymer Composites. 2015;**36**:992-998

[59] Mistretta MC, Morreale M, La Mantia FP. Thermomechanical degradation of polyethylene/polyamide 6 blend-clay nanocomposites. Polymer Degradation and Stability. 2014;**99**:61-67

[60] Cho KY, Park H, Kim H-J, Do XH, Koo CM, Hwang SS, et al. Highly enhanced electromechanical properties of PVDF-TrFE/SWCNT nanocomposites using an efficient polymer compatibilizer. Composites Science and Technology. 2018;**157**:21-29

[61] Mallakpour S, Naghdi M. Polymer/SiO_2 nanocomposites: Production and applications. Progress in Materials Science. 2018

[62] Passador FR, Ruvolo-Filho A, Pessan LA. Nanocomposites of polymer matrices and lamellar clays. In: Nanostructures. 1st ed. Elsevier. 2017. pp. 187-207. https://doi.org/10.1016/C2015-0-00785-7

[63] Naz A, Kausar A, Siddiq M, Choudhary MA. Comparative review on structure, properties, fabrication techniques, and relevance of polymer nanocomposites reinforced with carbon nanotube and graphite fillers. Polymer-Plastics Technology and Engineering. 2016; **55**:171-198

[64] Shin S-YA, Simon LC, Soares JB, Scholz G. Polyethylene–clay hybrid nanocomposites: in situ polymerization using bifunctional organic modifiers. Polymer (Guildf). 2003;**44**:5317-5321

[65] Lawal GI, Balogun SA, Akpan EI. Review of green polymer nanocomposites. Journal of Minerals & Materials Characterization & Engineering. 2012;**11**:385-416

[66] Mallakpour S, Khadem E. Recent development in the synthesis of polymer nanocomposites based on nano-alumina. Progress in Polymer Science. 2015;**51**:74-93

[67] Modi VK, Shrives Y, Sharma C, Sen PK. Review on green polymer nanocomposite and their applications. International Journal of Innovative Research in Science, Engineering and Technology. 2014;**3**:17651-17656

[68] Yao J, Cao Z, Chen Q, Zhao S, Zhang Y, Qi D. Efficient preparation and formation mechanism of polymer/SiO_2 nanocomposite particles in miniemulsions. Colloid & Polymer Science. 2017;**295**:1223-1232

[69] Qi D, Liu C, Chen Z, Dong G, Cao Z. In situ emulsion copolymerization of methyl methacrylate and butyl acrylate in the presence of SiO_2 with various surface coupling densities. Colloid & Polymer Science. 2015;**293**:463-471

[70] Wang X, Wang L, Su Q, Zheng J. Use of unmodified SiO_2 as nanofiller to improve mechanical properties of polymer-based nanocomposites. Composites Science and Technology. 2013;**89**:52-60

[71] Yang F, Yang W, Zhu L, Chen Y, Ye Z. Preparation and investigation of waterborne fluorinated polyacrylate/silica nanocomposite coatings. Progress in Organic Coatings. 2016;**95**:1-7

[72] Il JC, Ko J, Yin Z, Kim Y-J, Kim YS. Solvent-free and highly transparent SiO_2 nanoparticle–polymer composite with an enhanced moisture barrier property. Industrial and Engineering Chemistry Research. 2016;**55**:9433-9439

[73] Kango S, Kalia S, Celli A, Njuguna J, Habibi Y, Kumar R. Surface modification of inorganic nanoparticles for development of organic–inorganic nanocomposites—A review. Progress in Polymer Science. 2013;**38**:1232-1261

[74] Torabi Z, Mohammadi Nafchi A. The effects of SiO_2 nanoparticles on mechanical and physicochemical properties of potato starch films. Journal of Chemical Health Risks. 2013;**3**:33-42

[75] Zhu A, Diao H, Rong Q, Cai A. Preparation and properties of polylactide-silica nanocomposites. Journal of Applied Polymer Science. 2010;**116**:2866-2873

[76] Cong H, Radosz M, Towler BF, Shen Y. Polymer–inorganic nanocomposite membranes for gas separation. Separation and Purification Technology. 2007;**55**:281-291

[77] Bhattacharya M. Polymer nanocomposites—A comparison between carbon nanotubes, graphene, and clay as nanofillers. Materials (Basel). 2016;**9**:262-297

[78] Fornes TD, Yoon PJ, Keskkula H, Paul DR. Nylon 6 nanocomposites: The effect of matrix molecular weight. Polymer. 2001;**42**:09929-09940

[79] Isobe H, Kaneko K. Porous silica particles prepared from silicon tetrachloride using ultrasonic spray method. Journal of Colloid and Interface Science. 1999;**212**:234-241

[80] Fawaz J, Mittal V. Synthesis of polymer nanocomposites: Review of various techniques. In: Synthesis Techniques for Polymer Nanocomposites. Weinheim, Germany: Wiley-VCH Verlag GmbH & Co. KGaA; 2014. pp. 1-30

[81] Fischer H. Polymer nanocomposites: From fundamental research to specific applications. Materials Science and Engineering: C. 2003;**23**:763-772

[82] Beatrice CAG, Branciforti MC, Alves RMV, Bretas RES. Rheological, mechanical, optical, and transport properties of blown films of polyamide 6/residual monomer/montmorillonite nanocomposites. Journal of Applied Polymer Science. 2010;**116**:3581-3592

[83] Garcia M, van Vliet G, Jain S, Schrauwen BA, Sarkissov A, van Zyl W, et al. Polypropylene/SiO_2 nanocomposites with improved mechanical properties. Reviews on Advanced Materials Science. 2005;**6**:169-175

[84] Lin OH, Akil HM, Mohd Ishak ZA. Surface-activated nanosilica treated with silane coupling agents/polypropylene composites: Mechanical, morphological, and thermal studies. Polymer Composites. 2011;**32**:1568-1583

[85] Grala M, Bartczak Z, Różański A. Morphology, thermal and mechanical properties of polypropylene/SiO_2 nanocomposites obtained by reactive blending. Journal of Polymer Research. 2016;**23**:25

[86] Etienne S, Becker C, Ruch D, Grignard B, Cartigny G, Detrembleur C, et al. Effects of incorporation of modified silica nanoparticles on the mechanical and thermal properties of PMMA. Journal of Thermal Analysis and Calorimetry. 2007;**87**:101-104

[87] Sun S, Li C, Zhang L, Du HL, Burnell-Gray JS. Effects of surface modification of fumed silica on interfacial structures and mechanical properties of poly(vinyl chloride) composites. European Polymer Journal. 2006;**42**:1643-1652

[88] Chau JLH, Hsu SL-C, Chen Y-M, Yang C-C, Hsu PCF. A simple route towards polycarbonate–silica nanocomposite. Advanced Powder Technology. 2010;**21**:341-343

[89] Grande R, Pessan LA. Effects of nanoclay addition on phase morphology and stability of polycarbonate/styrene-acrylonitrile blends. Applied Clay Science. 2017;**140**:112-118

[90] Castro LDC, Oliveira AD, Kersch M, Altstädt V, Pessan LA. Effect of organoclay incorporation and blending protocol on performance of PA6/ABS nanocomposites compatibilized with SANMA. Polymer Engineering and Science. 2017;**57**:1147-1154

[91] Castro LDC, Oliveira AD, Kersch M, Altstädt V, Pessan LA. Effects of mixing protocol on morphology and properties of PA6/ABS blends compatibilized with MMA-MA. Journal of Applied Polymer Science. 2016;**133**:1-8

[92] Mallakpour S, Marefatpour F. Novel chiral poly(amide-imide)/surface modified SiO_2 nanocomposites based on N-trimellitylimido-l-methionine: Synthesis and a morphological study. Progress in Organic Coatings. 2014;**77**:1271-1276

[93] Dong Q, Ding Y, Wen B, Wang F, Dong H, Zhang S, et al. Improvement of thermal stability of polypropylene using DOPO-immobilized silica nanoparticles. Colloid & Polymer Science. 2012;**290**:1371-1380

[94] Tanahashi M, Mitsuru. Development of fabrication methods of filler/polymer nanocomposites: With focus on simple melt-compounding-based approach without surface modification of nanofillers. Materials (Basel). 2010;**3**:1593-1619

[95] Meyyappan M. Carbon Nanotubes: Science and Applications. 1st ed. CRC Press; 2004. 310 p. ISBN 9780849321115

[96] Sinha Ray S, Okamoto M. Polymer/layered silicate nanocomposites: A review from preparation to processing. Progress in Polymer Science. 2003;**28**:1539-1641

[97] Giannelis EP. Polymer layered silicate nanocomposites. Advanced Materials. 1996;**8**: 29-35

[98] Dresselhaus MS, Dresselhaus G, Saito R, Jorio A. Raman spectroscopy of carbon nanotubes. Physics Reports. 2005;**409**:47-99

[99] Reichert P, Kressler J, Thomann R, Müllhaupt R, Stöppelmann G. Nanocomposites based on a synthetic layer silicate and polyamide-12. Acta Polymerica. 1998;**49**:116-123

[100] Yano K, Usuki A, Okada A, Kurauchi T, Kamigaito O. Synthesis and properties of polyimide–clay hybrid. Journal of Polymer Science, Part A: Polymer Chemistry. 1993;**31**:2493-2498

[101] Park JH, Jana SC. Mechanism of exfoliation of nanoclay particles in epoxy−clay nanocomposites. Macromolecules. 2003;**36**:2758-2768

[102] Chen TK, Tien YI, Wei KH. Synthesis and characterization of novel segmented polyurethane clay nanocomposite via poly(epsilon-caprolactone)/clay. Journal of Polymer Science, Part A: Polymer Chemistry. 1999;**37**:2225-2233

[103] Aubry T, Razafinimaro T, Médéric P. Rheological investigation of the melt state elastic and yield properties of a polyamide-12 layered silicate nanocomposite. Journal of Rheology (N. Y. N. Y). 2005;**49**:425-440

[104] Zhao J, Morgan AB, Harris JD. Rheological characterization of polystyrene–clay nanocomposites to compare the degree of exfoliation and dispersion. Polymer (Guildf). 2005; **46**:8641-8660

[105] Shen L, Lin Y, Du Q, Zhong W, Yang Y. Preparation and rheology of polyamide-6/attapulgite nanocomposites and studies on their percolated structure. Polymer (Guildf). 2005; **46**:5758-5766

[106] Giannelis EP. Polymer-layered silicate nanocomposites: Synthesis, properties and applications. Applied Organometallic Chemistry. 1998;**680**:675-680

[107] Henrique P, Camargo C, Satyanarayana KG, Wypych F. Nanocomposites: Synthesis, structureproperties and new application opportunities. Materials Research. 2009;**12**:1-39

[108] Suter JL, Groen D, Coveney PV. Chemically specific multiscale modeling of clay-polymer nanocomposites reveals intercalation dynamics, tactoid self-assembly and emergent materials properties. Advanced Materials. 2015;**27**:966-984

[109] LeBaron PC, Wang Z, Pinnavaia TJ. Polymer layered silicate nanocomposites: An overview. Applied Clay Science. 1999;**15**:11-29

[110] Alvi F, Ram MK, Basnayaka PA, Stefanakos E, Goswami Y, Kumar A. Graphene-polyethylenedioxythiophene conducting polymer nanocomposite based supercapacitor. Electrochimica Acta. 2011;**56**:9406-9412

[111] Radmilović VV, Carraro C, Uskoković PS, Radmilović VR. Structure and properties of polymer nanocomposite films with carbon nanotubes and graphene. Polymer Composites. 2017;**38**:E490-E497

[112] Beatrice CAG, dos SCR, Branciforti MC, Bretas RES. Nanocomposites of polyamide 6/residual monomer with organic-modified montmorillonite and their nanofibers produced by electrospinning. Materials Research. 2012;**15**:611-621

[113] Maia THS, Larocca NM, Beatrice CAG, de Menezes AJ, de Freitas Siqueira G, Pessan LA, et al. Polyethylene cellulose nanofibrils nanocomposites. Carbohydrate Polymers. 2017;**173**:50-56

[114] Beatrice CAG, Rosa-Sibakov N, Lille M, Sözer N, Poutanen K, Ketoja JA. Structural properties and foaming of plant cell wall polysaccharide dispersions. Carbohydrate Polymers. 2017;**173**:508-518

Chapter 7

Perovskite Strontium Doped Rare Earth Manganites Nanocomposites and Their Photocatalytic Performances

Ihab A. Abdel-Latif

Additional information is available at the end of the chapter

http://dx.doi.org/10.5772/intechopen.79479

Abstract

Studying catalysts *in situ* is an important topic that helps us to understand their surface structure and electronic states in operation. Three types of materials are used in the degradation of organic matter, which has applications in the environmental remediation and self -cleaning surfaces. The technique is widely known but still hampered by one significant limitation. The materials generally absorb ultra violet UV light but we need to develop active materials for visible light. Utilizing the sunlight efficiently for solar energy conversion is an important demand in the present time. The research on visible-light active photocatalysts attracted a lot of interest. The perovskite-like compounds are found to be active catalysts for the oxidation of carbon monoxide. In the present chapter, we will focus on the application of the nano-sized strontium doped neodymium manganites within perovskite like structure as photocatalysis and studying their photocatalytic performance.

Keywords: photocatalytic, perovskite, manganites, nanocomposites, visible light

1. Introduction

Photocatalysis is the acceleration of a photoreaction in the presence of a catalyst. The ability to generate electron–hole pairs and free radicals is very important parameters to understand the photocatalytic activity (PCA) in photogenerated catalysis [1]. On other words we can describe the photocatalysis process as two parts, "photo" and "catalysis". Let us define the catalysis as the process in which a material participates in modifying the rate of a chemical transformation of the reactants without altering or consuming in the end. This material is so called catalyst,

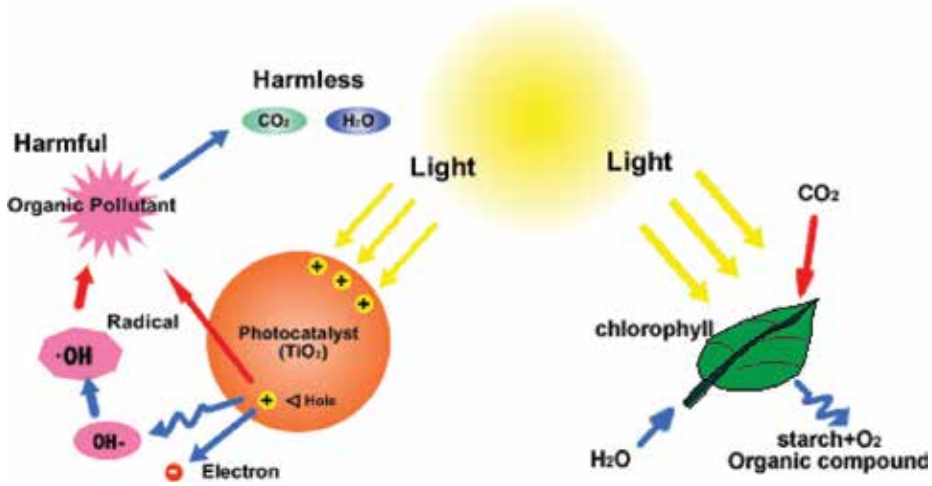

Figure 1. Nano TiO_2 photocatalyst and chlorophyll of plants is a typical natural photocatalyst [2].

which the activation energy is reduced that may lead to acceleration of the reaction. In general, light is used to activate a substance, which modifies the rate of a chemical reaction without being involved itself, and the photocatalyst is the substance, which can modify the rate of chemical reaction using light irradiation [1]. Chlorophyll of plants is good example for the natural photocatalyst. The difference between chlorophyll photocatalyst and nano TiO_2 photocatalyst (see **Figure 1**) [2] is, usually chlorophyll captures sunlight to turn water and carbon dioxide into oxygen and glucose, while photocatalyst creates strong oxidation agent and electronic holes to breakdown the organic matter to carbon dioxide and water in the presence of photocatalyst, light and water [2]. So many materials are developed daily to be applied as photocatalysis and nanocompsites that have perovskites-like structure are promising materials for these applications.

2. Mechanism of photocatalysis

When photocatalyst such as titanium dioxide (TiO_2) absorbs Ultraviolet (UV)* radiation comes from sun or any other illuminated light source (e.g., fluorescent lamps), pairs of electrons and holes are produced, see **Figure 2**. As a result of the light illumination, the electron of the valence band of titanium dioxide becomes excited. Excited electron transits to the conduction band of titanium dioxide with excess energy to create pair of charges; the negative-electron (e-) and positive-hole (h+). This behaviour is well known as the semiconductor's photo-excitation' state. The 'Band Gap' is defined as a result of the difference in energy between the valence band and the conduction band. The necessary wavelength of the light required for the photo-excitation is given according to 1240 (Planck's constant, h)/3.2 eV (band gap energy) and equal to 388 nm [3]. The hole with positive charge in titanium dioxide may split the water molecule into both of the hydrogen gas and hydroxyl radical. On the other side, the electron with negative charge reacts with oxygen molecule forming the super oxide anion. The continuity of this cycle depends on the availability of the light [3].

http://dx.doi.org/10.5772/intechopen.79479

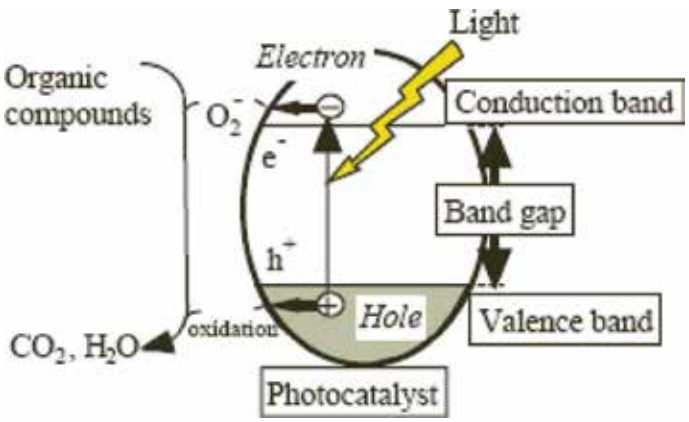

Figure 2. Schematic diagram showing the photocatalysis mechanism by producing both holes and electrons as a result of illumination [3].

Solar energy is clean and till now its utilization is limited. A strong need to develop a sustainable and cost-effective manner for harvesting solar energy to satisfy the growing energy demand of the world with a minimal environmental impact [4]. Photo-catalysis plays an important role for the conversion of solar energy into chemical fuel, electricity, the decomposition of organic pollutants etc.

The degradation behaviors were studied by Sher Bahadar Khan et al. [5] and the degradation pattern of AO by Langmuir–Hinshelwood (L–H) model was defined and given from the relationship between the rate of degradation and the initial concentration of AO in photo-catalytic reaction [6].

The rate of photo-degradation was calculated according to the following equation; Eq. (1)

$$r = -dC/dt = KrKC = KappC \quad (1)$$

where r in this equation is defined as the degradation rate of organic pollutant, *K*r is describing the reaction rate constant, *K* is constant equal to the equilibrium constant, C is the concentration of the reactant. From Eq. 1, we can neglect KC when C becomes very small so this equation could describe the first order kinetic. Applying the following initial conditions, ($t = 0$, $C = C_0$) in Eq. (1), that may lead to a new equation; Eq. (2).

$$-\ln C/C_0 = kt \quad (2)$$

Half-life, $t_{1/2}$ (in min) is

$$t_{1/2} = 0.693/k \quad (3)$$

The photo degradation of AO in the presence of CeO_2 **1** nano-particles is shown in **Figure 3**.

Different materials are used as photocatalysis and research is going on to apply a new material for this applications. The rare earth manganite is one of the promising materials for

photocatalysis and so in the present proposal we develop the strontium doped neodymium manganites nanocomposites within perovskite like structure as photocatalysis and studying its performance and so the main goals are; –synthesis new perovskite materials enhanced the photocatalysis performance applying the obtained results for solar energy utilizations.

Metal oxide photocatalysis is based on metal oxide like titanium dioxide as light-activated catalysts [7]. Three types of materials are used in the degradation of organic matter which has

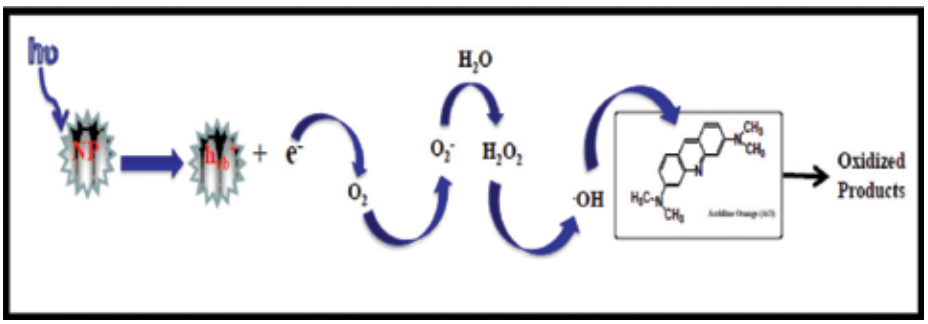

Figure 3. Photo-degradation of AO in the presence of CeO_2 **1** nanoparticles [5].

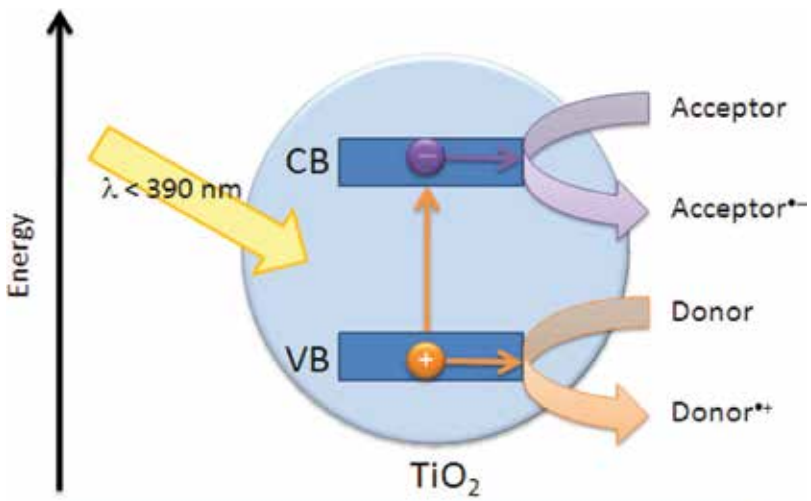

Process	Name
$TiO_2 + h\upsilon \rightarrow h_{VB}^+ + e_{CB}^-$	Charge Separation
$h_{VB}^+ + H_2O \rightarrow OH^\bullet$	$OH^\bullet$ Generation (VB)
$e_{CB}^- + O_2 \rightarrow O_2^{\bullet-} + H_2O \rightarrow OH^\bullet$	$OH^\bullet$ Generation (CB)

Figure 4. Schematic representation; top light with energy higher than band gap leads to charge separation, with electron reducing a donor (usually oxygen) and hole oxidizing a donor (usually water); summary of processes occurring. Image based on Bahnemann (2004) [7].

applications in the environmental remediation and self -cleaning surfaces. The technique is widely known but still hampered by one significant limitation. The materials generally absorb ultra violet UV light but we need to develop active materials for visible light, see **Figure 4**.

3. Perovskites as photocatalytic

ABO_3 perovskites are very essential family of oxide materials because they possess very interesting physical and chemical properties. These unusual properties may lead to use these materials in potential applications. The corner-shared octahedral BO_6 lattice site in these materials play very important role in transfer of oxygen and electrons easily and may lead to nonstoichiometry of oxygen [8–23]. Moreover, the mixed valence states of the transition metal at B-site are also important term in such perovskite-type oxides, which affect their activity. Nevertheless a lot of applications depend on the A and B cations in the ABO_3 perovskites, such as electrocatalysts for O_2 evolution [8–10], catalysts [11, 12], photo/electro- catalysts for hydrogen production and pollutants degradation [13–19] and electrode material used in fuel cells [13]. The synthesis of perovskite materials could be done using different methods such as solid state reaction [24–28], chemical co-precipitation [29–33], sol–gel [34–38]. In each method there are parameters to play with in order to improve the properties of the required materials. A lot of perovskite oxides have been synthesized such as tantalate [39–43], titanate [14, 44–50], ferrite, [51, 52] vanadium-and niobium-based perovskites [53–56], and manganites [57, 58] and they have shown visible light photocatalytic activity as a result of their unique electronic properties and crystal structures [59]. The reduced band-gap energy values in the doped alkaline rare-earth transition metal perovskite-like structure oxides focus more attention because this property enhances the separation of charge carriers (photogenerated electrons and holes) [60]. Intensive studies have been done on these materials because of the capability of tuning their electrical and optical properties, indicating a control of their rational design structure by substitutions of cationic in ABO_3 pervoskite [61, 62]. Therefore, we can say that the perovskite compounds are one of the promising structure that are adapting the bandgap values to harvest visible-light absorption and the potentials of band edge to tailor the needs of particular photocatalysis.

Furthermore, the lattice distortion existed in the rare earth transition metal perovskite compounds strongly affects the separation of photogenerated charge carriers [59, 63, 64]. The distortion in the bond angles resulted from both; metal-ligand or the metal-ligand-metal into perovskite framework are significantly related to their charge carriers and band gap values [65–67]. The crystallinity, phase structure, size, and surface area affect the efficiency of photocatalysts. Consequently, control of the shape of perovskites and the size and crystal phase is essential and significant parameter for assessing their phase-dependent photoactivity and promoting perovskites-based driven visible light photocatalysts. According to Abdel-Latif et al. [66], $Nd_{0.6}Sr_{0.4}MnO_3$ was studied as superior photocatalyst under visible light, different modifications of perovskite $Nd_{0.6}Sr_{0.4}MnO_3$ to get high harvesting of photons and enhancing the migration and separation of the photogenerated charge carriers through the photocatalytic reaction [61–65]. For the first time, the impact on phase structures and photocatalytic efficiencies under visible light of the annealed $Nd_{0.6}Sr_{0.4}MnO_3$ perovskite which prepared by sol–gel

method in the presence of polyethylene glycol and citric acid was studied by Abdel-Latif et al. [66], and the $Nd_{0.6}Sr_{0.4}MnO_3$ perovskite annealed at 500°C was found to be a superior photocatalyst than that annealed at 800, 1000 and 1150°C. $Nd_{0.6}Sr_{0.4}MnO_3$ semiconductor has a narrow band gap energy values ranged from 2 to 2.98 eV, which we can control its value by changing its annealing temperatures. Charge carriers created by absorbing visible light (photogenerated electrons and holes) depend on the excitation by this visible light. The hole, which photogenerated in the valence band reacts either with the adsorbed −OH ions or H_2O onto the surface of NSMO producing $OH^{\bullet}$. On the other side, the electron, which photogenerated in the conduction band reduces O_2 to get $O_2^{\bullet-}$ give rising to other oxidative O_2 species (i.e., $OH^{\bullet}$ and H_2O_2). The photocatalytic efficiencies of the $Nd_{0.6}Sr_{0.4}MnO_3$ nanocomposites were evaluated in Ref. [66] for the MB photodegradation, where they calculated the MB photodecomposition under visible light illumination by recording absorption spectra. They found that MB is negligible at the photolysis and it is stable after visible light illumination for 3 h. Furthermore, there is a slight decrease in MB concentration as a result of adsorption onto $Nd_{0.6}Sr_{0.4}MnO_3$ surface when it is suspended with MB solution in dark as shown in **Figure 5**. The observed MB absorption bands at $\lambda = 663$ and 291 nm gradually decreased upon boosting illumination times.

As it is clear from the photocatalytic performance of the $Nd_{0.6}Sr_{0.4}MnO_3$ perovskite, the crystalline size (55 nm), which depends on the annealed temperature (500°C). The mixed perovskite structure $Nd_{0.6}Sr_{0.4}MnO_3$ (26.18% orthorhombic "Orth" and 73.82% monoclinic "Mon") obtained at annealing temperature 500°C is a superior photocatalyst candidate than that of $Nd_{0.6}Sr_{0.4}MnO_3$ perovskite obtained at annealing temperature 1150°C and with mixed structure (82.22% cubic "Cub" and 17.78% orthorhombic "Orth" phases). The observed photo degradation was 100% by the annealing temperate 500°C of the $Nd_{0.6}Sr_{0.4}MnO_3$ perovskite [66]. However, as a result of the increase in the annealing temperature to 1150°C, reduction in the photocatalytic efficiency was observed to be 60%. Looking at the effect of the annealing temperature in $Nd_{0.6}Sr_{0.4}MnO_3$ perovskite according to Abdel-Latif et al., [66], the overall photodegradation rate of the sample annealed at 500°C is significantly 3-times higher than that of the other sample, which annealed at 1150°C. The superiority of the neodymium strontium doped manganite, which annealed at 500°C is attributed to the mixed crystallographic structure with double phases (Mon/Orth) framework, high crystallinity, and the Mn-O polyhedron distortion. From this work on can say that key factors for the high photocatalytic activity of the obtained neodymium strontium doped manganite with annealing temperature 500°C are the high visible-light absorption, lattice distortion and narrow band gap.

Another example of the rare earth manganites is the non-stoichiometric perovskites; $La_{1-x}Sr_xMnO_{3-\delta}$ ($x = 0.35, 0.50, 0.65, 0.80$) series, which was examined by Antoine Demont and Stéphane Abanades [67] in the context of solar-driven two-step thermo-chemical dissociation of CO_2. All the performance characterization measurements such as X-ray diffraction and thermochemical characterizations were carried out in order to the evaluation of the redox activity of these materials toward the thermal reduction under inert atmosphere followed by the re-oxidation process and carbon oxide generation from CO_2. They found that, the control of introducing strontium into lantanium manganite allowed tuning the redox thermodynamics within the series. The high activity observed toward both thermal reduction and CO_2 dissociation occurred. As a result of analysis of experimental measurements they found that the $La_{0.50}Sr_{0.50}MnO_{3-\delta}$ composition is a promising candidate for thermochemical CO_2 splitting **Figures 6** and **7**.

http://dx.doi.org/10.5772/intechopen.79479

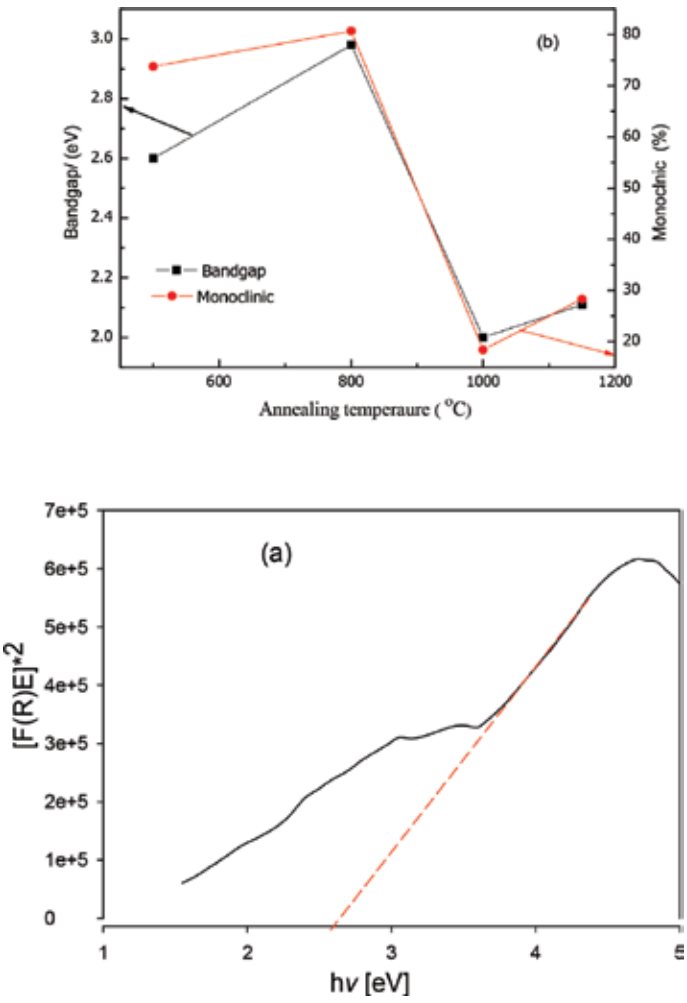

Figure 5. Optical bandgap energy E_g for nano $Nd_{0.6}Sr_{0.4}MnO_3$ perovskite annealed at 500°C (a), relation between the bandgap energy E_g values and the percentage of the monoclinic phase (b) [66].

Maximum production of carbon oxide is reached in the range of 270 μmol g^{-1} during the carbon dioxide splitting step with an optimal temperature of re-oxidation 1050°C (thermal reduction performed under Argon gas at 1400°C), in spite of the re-oxidation yield limitation "50%". The evolution of the manganese oxidation state reveal partial re-oxidation of Mn^{3+} into Mn^{4+}, thus the activation of Mn^{4+}/Mn^{3+} redox pair in the perovskites was confirmed. They concluded that the mixed valence perovskites have clear potential for displaying redox properties suitable for efficient solar-driven thermochemical CO_2 dissociation [67].

Oxygen diffusion and desorption in oxides have been developed for slightly defective and well crystallized bulky materials in Ref. [68]. The relation between nanostructure and the change of the mechanism of oxygen mobility has been studied in this work. Temperature programmed oxygen desorption and thermogravimetric analysis applied to study some nanostructured perovskite-like structure $La_{1-x}A_xMnO_{3\pm\delta}$ samples (A = Sr. and Ce, 20–60 nm

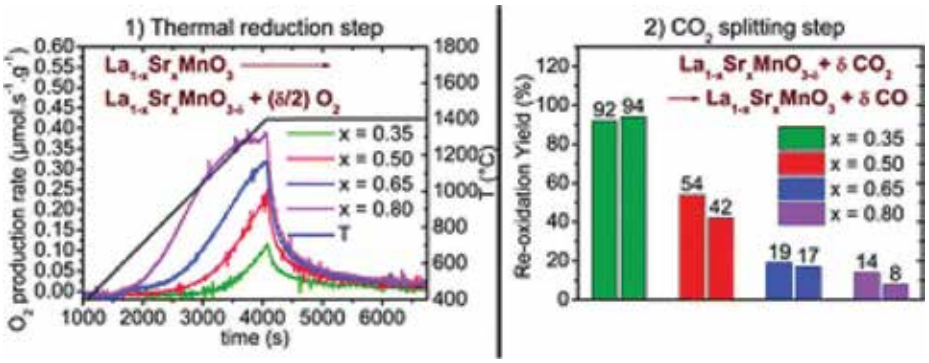

Figure 6. Solar-driven two-step thermochemical dissociation of CO_2 in $La_{1-x}Sr_xMnO_{3-\delta}$ [67].

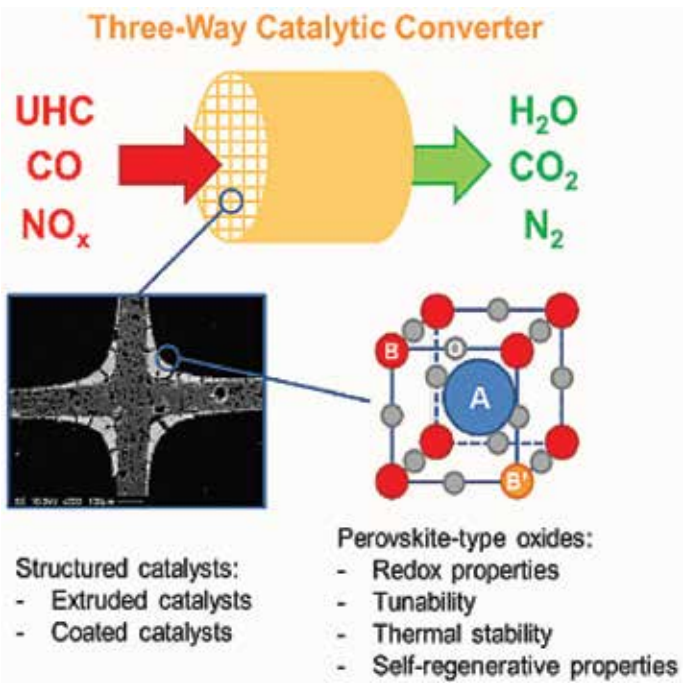

Figure 7. Three-way catalytic converter TWC [71].

particle size) [53]. Depending on the temperature range and oxygen depletion of the material different rate-determining steps have been identified. Particularly, oxygen diffusion was demonstrated at low temperature and defect concentration, whereas the oxygen recombination at the surface seems is controlled at high temperature. However, the lower activation energy is responsible for the oxygen recombination step.

Utilizing the sunlight efficiently for solar energy conversion, the research on visible-light active photocatalysts attracted a lot of interest [4]. The photosensitization of transition metal oxides is a promising approach for achieving effective visible light photocatalysis. The world

of nanostructured photosensitizers, for example, plasmonic metal nanostructures, quantum dots, and carbon nanostructures engaged with the wide-bandgap in transition metal oxides that allow us to design a new visible-light active photocatalysts [4]. The implied mechanisms of the nanocomposite photocatalysts, for example, the charge separation inducing light and the visible-light photocatalytic reaction procedure in environmental treatment besides solar fuel generation fields, are also presented [10].

The rare earth manganites as well as the rare earth cobalt with perovskite-like structure (the rare earth like; lanthanum, praseodymium, or neodymium) are studied in Ref. [69], where they found that these materials are active catalysts for the oxidation of carbon monoxide. Comparing initial activity and lifetime in crushed single crystals of these composites and the commercial platinum catalysts showed its good performance. Therefore, one can say that these materials are considered as a promising alternate for platinum in devices for the catalytic treatment of auto exhaust.

The phonon-mode assignment of dysprosium chromate ($DyCrO_3$) nanoplatelets by Raman spectroscopy was reported recently [70]. They reported the effect of temperature on Raman spectra and they showed the shift in the phonon frequency of most intense modes in dysprosium chromate ($DyCrO_3$). The change in Raman line-width is observed, which is an indication to its correlation with the spin–phonon coupling. The impedance spectroscopy described in this work implied the anomalies in the dielectric constant *dependent on* temperature near the magnetic transitions point that may lead to postulate possible weak magnetoelectric coupling in $DyCrO_3$ nanoplatelets. Furthermore, UV–Vis absorption spectroscopy has been measured beside the photocatalytic activity measurement for $DyCrO_3$ nanoplatelets. The band gap deduced from the optical absorption spectrum was ~2.8 eV for $DyCrO_3$ nanoplatelets and this energy is considered as a good enough for the photocatalytic activity application. The efficient photocatalytic activity of $DyCrO_3$ nanoplatelets are described in this work, where degrading value was 65% for 8 h irradiation [70].

Three-way catalysts (TWC) were introduced more than 40 years ago and the development of a sustainable TWC still remains an important subject owing to the increasingly stringent emission regulations together with the price and scarcity of precious metals [71]. Perovskite-type oxides are alternatives to the conventionally used TWC compositions and it is suitable for a wide range of automotive applications, ranging from TWC to diesel oxidation catalysts (DOC). The interest in these catalysts has been renewed because of the catalyst regenerability of perovskite-based TWC concept. Principally, it is applicable to other catalytic processes and there is possibility to reduce the amounts of critical elements, such as valuable metals without industriously lowering the catalytic performance.

Studying catalysts *in situ* is of high interest for understanding their surface structure and electronic states in operation [72]. The epitaxial manganite perovskite thin films ($Pr_{1-x}Ca_xMnO_3$) were found to be active for the oxygen evolution reaction (OER) from water splitting as a result of electro-catalytic water splitting. X-ray absorption near-edge spectroscopy (XANES), at the Mn L- and O K-edges, was measured and analyzed in Ref. [72], besides measuring the X-ray photoemission spectroscopy (XPS) of the O 1s and Ca 2p states. Both measurements were carried out under the following conditions; in water vapor under positive applied bias, in ultra-high vacuum and at room temperature [72]. According to the research in Ref. [72] under the oxidizing conditions of the OER a reduced Mn^{2+} species is generated at the catalyst surface and the Mn valence shift is accompanied by the formation of surface oxygen vacancies.

According to Madhavan and Ashok [73], perovskite materials exhibiting proton and oxide ion conductivities have been used for various energy-related applications such as solid oxide fuel cells (SOFCs), hydrogen production, gas sensors, etc. Nowadays, nanoperovskites were synthesized and were studied for catalytic activity and energy-related applications. The mechanism of proton and oxide ion conduction, and some specific properties and behaviors of few nanoperovskites as oxide ion and proton conductors and applications have been reported and discussed in this work [73].

4. Conclusions

As it is clear from the photocatalytic performance of the $Nd_{0.6}Sr_{0.4}MnO_3$ perovskite, the crystalline size (55 nm), which depends on the annealed temperature (500°C). The mixed phases (26.18% Orth and 73.82% Mono) in the $Nd_{0.6}Sr_{0.4}MnO_3$ perovskite as a result of annealing at 500°C is a superior photocatalyst than those of $Nd_{0.6}Sr_{0.4}MnO_3$ perovskite annealed at different temperatures. The maximum photodegradation of MB for the strontium doped neodymium manganites perovskite was achieved for those annealed at 500°C. As a result of the increase in the annealing temperature (annealing at 1150°C), the reduction to 60% in the photocatalytic efficiency was achieved. Comparing the overall photodegradation rates of the strontium doped neodymium manganites perovskite as a function of the annealing temperature we found 500°C annealing temperature is significantly 3-times higher than that of other temperatures. This superiority of the low annealing temperature in the case of $Nd_{0.6}Sr_{0.4}MnO_3$ perovskite is attributed to the forming these materials in mixed phases (double phases, Mono – Ortho phases) and its high crystallinity. Besides, the high Mn-O polyhedron distortion excited in these materials. So one can conclude that the annealing temperature plays very important role to improving the photocatalytic performance. The following factors; visible-light absorption, narrow band gap and lattice distortion are the key factors that determine the high photocatalytic activity of the obtained in such materials and good example for that the $Nd_{0.6}Sr_{0.4}MnO_3$ perovskite annealed at 500°C.

Acknowledgements

The author is thankful to the Deanship of Scientific Research in Najran University for their support NU/ESCI/15/011.

Author details

Ihab A. Abdel-Latif[1,2]*

*Address all correspondence to: ihab_abdellatif@yahoo.co.uk

1 Physics Department, Najran University, Najran, Saudi Arabia

2 Reactor Physics Department, NRC, Cairo, Egypt

References

[1] https://en.wikipedia.org/wiki/Photocatalysis

[2] http://www.greenearthnanoscience.com/what-is-photocatalyst.php

[3] http://www.mchnanosolutions.com/mechanism.html

[4] Chen H, Wang L. Nanostructure sensitization of transition metal oxides for visible-light photocatalysis. Beilstein Journal of Nanotechnology. 2014;**5**:696-710

[5] Bahadar KS, Faisal M, Rahman Mohammed M, Kalsoom A, Asiri Abdullah M, Anish K, Alamry Khalid A. Effect of particle size on the photocatalytic activity and sensing properties of CeO_2 nanoparticles. International Journal of Electrochemical Science. 2013;**8**:7284-7297

[6] Faisal M, Khan SB, Rahman MM, Jamal A, Asiri AM, Abdullah MM. Smart chemical sensor and active photo-catalyst for environmental pollutants. Chemical Engineering Journal. 2011;**173**:178-184

[7] Bahnemann D. Photocatalytic water treatment: Solar energy applications. Solar Energy. 2004;**77**:445-459. https://photochemistry.wordpress.com/2009/09/30/metal-oxide-photocatalysis/

[8] Soares CO, Silva RA, Carvalho MD, Melo Jorge ME, Gomes A, Rangel CM, da Silva Pereira MI. Oxide loading effect on the electrochemical performance of $LaNiO_3$ coatings in alkaline media. Electrochimica Acta. 2013;**89**:106-113

[9] Costa AB, Melo Jorge ME, Carvalho MD, Gomes A. $LaNi_{1-x}Cu_xO_3$ (x = 0.05, 0.10, 0.30) coated electrodes for oxygen evolution in alkaline medium. Journal of Solid State Electrochemistry. 2013;**17**:2311-2318

[10] Soares CO, Carvalho MD, Melo Jorge ME, Gomes A, Silva RA, Rangel CM, da Silva Pereira MI. High surface area $LaNiO_3$ electrodes for oxygen electrocatalysis in alkaline media. Journal of Applied Electrochemistry. 2012;**42**:325-332

[11] Machida M, Ochiai K, Ito K, Ikeue K. Catalytic properties of novel La–Sr–Cu–O–S perovskites for automotive C_3H_6/CO oxidation in the presence of SO_x. Catalysis Today. 2006;**117**:584-587

[12] Wang C-H, Chen CL, Weng HS. Surface properties and catalytic performance of $La_{1-x}Sr_xFeO_3$ perovskite-type oxides for methane combustion. Chemosphere. 2004;**57**:1131-1138

[13] Pacheco MJ, Regalado F, Santos D, Ciríaco L, Lopes A. Synthesis and environmental applications of $BaPb_{1-x}Sb_xO_3$ solid solutions. Journal of The Electrochemical Society. 2014;**161**:H474-H480

[14] Gao F, Chen X, Yin K, Dong S, Ren Z, Yuan F, Yu T, Zou Z, Liu JM. Visible-light photocatalytic properties of weak magnetic $BiFeO_3$ nanoparticles. Advanced Materials. 2007;**19**:2889-2892

[15] Li FT, Liu Y, Liu RH, Sun ZM, Zhao DS, Kou CG. Preparation of Ca-doped $LaFeO_3$ nanopowders in a reverse microemulsion and their visible light photocatalytic activity. Materials Letters. 2010;**64**:223-225

[16] Parida KM, Reddy KH, Martha S, Das DP, Biswal N. Pt modified TiO_2 nanotubes electrode: Preparation and electrocatalytic application for methanol oxidation. International Journal of Hydrogen Energy. 2010;**35**:12161-12168

[17] Pareek VK, Adesina AA. Handbook of photochemistry and photobiology. Stevenson Ranch, CA: American Scientific Publishers; 2003

[18] Cui BJ, Dunn S. Effect of ferroelectricity on solar-light-driven photocatalytic activity of $BaTiO_3$—Influence on the carrier separation and stern layer formation. Chemistry of Materials. 2013;**25**:4215-4223

[19] Barrocas B, Sério S, Rovisco A, Melo Jorge ME. Visible-light photocatalysis in $Ca_{0.6}Ho_{0.4}MnO_3$ films deposited by RF-magnetron sputtering using nanosized powder compacted target. Journal of Physical Chemistry C. 2014;**118**:590-597

[20] Zhou W, Ran R, Shao Z. Progress in understanding and development of $Ba_{0.5}Sr_{0.5}Co_{0.8}Fe_{0.2}O_3$–δ-based cathodes for intermediate-temperature solid-oxide fuel cells: A review. Journal of Power Sources. 2009;**192**:231-246

[21] Ni L, Tanabe M, Irie H. A visible-light-induced overall water-splitting photocatalyst: conduction-band-controlled silver tantalate. Chemical Communications. 2013;**49**:10094-10096

[22] Li M, Zhang J, Dang W, Cushing SK, Guo D, Wu N, Yin P. Photocatalytic hydrogen generation enhanced by band gap narrowing and improved charge carrier mobility in $AgTaO_3$ by compensated co-doping. Physical Chemistry Chemical Physics. 2013;**15**:16220-16226

[23] Kanhere P, Shenai P, Chakraborty S, Ahuja R, Zheng J, Chen Z. Mono- and co-doped $NaTaO_3$ for visible light photocatalysis. Physical Chemistry Chemical Physics. 2014;**16**:16085-16094

[24] Abdel-Latif IA, Hassen A, Zybill C, Abdel-Hafiez M, Allam S, El-Sherbini T. The influence of tilt angle on the CMR in $Sm_{0.6}Sr_{0.4}MnO_3$. Journal of Alloys and Compounds. 2008;**452**(2):245-248

[25] Bouziane K, Yousif A, Abdel-Latif IA, Hricovini K, Richter C. Electronic and magnetic properties of $SmFe_{1-x}Mn_xO_3$ orthoferrites (x = 0.1, 0.2 and 0.3). Journal of Applied Physics. 2005;**97**(10A):504

[26] Bashkirov S, Parfenov VV, Abdel-Latif IA, Zaripova LD. Mössbauer effect and electrical conductivity studies of $SmFe_xMn_{1-x}O_3$ (x = 0.7, 0.8 and 0.9). Journal of Alloys and Compounds. 2005;**387**:70

[27] Yousif AA, Abdel-Latif IA, Bouziane K, Sellai A, Gismelseed A, Al-Omari I, Widatallah H, Al-Rawas AD, Elzain M. Study on mössbauer and magnetic properties of strontium doped neodymium ferrimanganites perovskite-like structure. AIP Conference Proceedings. 2011;**1370**:103-107

[28] Bashkirov S, Parfenov VV, Valiullin AA, Khramov AS, Trounov VA, Smirnov AP, Abdel-Latif IA. Crystal structure, electric and magnetic properties of ferrimanganite $NdFe_xMn_{1-x}O_3$. Izv. RAS, Physical Series. 2003;**67**(7):1072 (in Russian)

[29] Abdel-Latif IA. Study on the effect of particle size of strontium - ytterbium manganites on some physical properties. AIP Conference Proceedings. 2011;**1370**:108-115

[30] Abdel-Latif IA, Al-Hajary A, Hashem H, Ghoza MH, El-Sherbini T. The nano particle size effect on some physical properties of neodymium coblate-manganites for hydrogen storage. AIP Conference Proceedings. 2011;**1370**:158-164

[31] Khan SB, Faisal M, Rahman MM, Abdel-Latif IA, Ismail AA, Akhtar K, Al-Hajry A, Asiri AM, Alamry Kh. A. Highly sensitive and stable phenyl-hydrazine chemical sensors based on CuO flower shape and hollow sphere nanosheets. New Journal of Chemistry. 2013;**37**:1098

[32] Abdel-Latif IA. Rare earth manganites and their applications. Journal of Physics. 2012;**1**(2):50-53

[33] Ghozza MH, Abdel-Latif IA, Allam SH. Properties of 3d-4f Oxides Nanoparticles. Germany: Scholars' Press; 2013

[34] Abdel-Latif IA, Ismail A, Bouzaid H, Al-Hajry H. Synthesis of novel perovskite crystal structure phase of strontium doped rare earth manganites using sol gel method. Journal of Magnetism and Magnetic Materials. 2015;**293**:233

[35] Abdel-Latif IA. Advances in Rare Earth Transition Metal Oxides Semiconductor Materials. USA: Science Publishing Group; 2015

[36] Abdel-Latif IA, Rahman MM, Khan SB. Neodymium cobalt oxide as a chemical sensor. Results in Physics. 2018;**8**:578-583

[37] Faisal M, Ismail AA, Ibrahim AA, Bouzid H, Al-Sayari SA. Highly efficient photocatalyst based on Ce doped ZnO nanorods: Controllable synthesis and enhanced photocatalytic activity. Chemical Engineering Journal. 2013;**229**:225-233

[38] Faisal M, Ismail AA, Harraz FA, Bouzid H, Al-Sayari SA, Al-Hajry A. Mesoporous TiO_2 based optical sensor for highly sensitive and selective detection and preconcentration of Bi(III) ions. Chemical Engineering Journal. 2014;**243**:509-516

[39] Marchelek M, Bajorowicz B, Mazierski P, Cybula A, Klimczuk T, Winiarski M, Fijałkowska N, Zaleska A. $KTaO_3$-based nanocomposites for air treatment. Catalysis Today. 2014;**252**:47-53

[40] Liu X, Lv J, Wang S, Li X, Lang J, Su Y, Chai Z, Wang X. A novel contractive effect of $KTaO_3$ nanocrystals via La^{3+} doping and an enhanced photocatalytic performance. Journal of Alloys and Compounds. 2015;**622**:894-901

[41] Townsend TK, Browning ND, Osterloh FE. Overall photocatalytic water splitting with NiO_x–$SrTiO_3$ – a revised mechanism. Energy & Environmental Science. 2012;**5**: 9543-9550

[42] Chen H-C, Huang C-W, Wu JC, Lin S-T. Theoretical investigation of the metal-doped $SrTiO_3$ photocatalysts for water splitting. Journal of Physical Chemistry C. 2012;**116**:7897-7903

[43] Kato H, Sasaki Y, Shirakura N, Kudo A. Synthesis of highly active rhodium-doped $SrTiO_3$ powders in Z-scheme systems for visible-light-driven photocatalytic overall water splitting. Journal of Materials Chemistry A. 2013;**1**:12327-12333

[44] Jia Y, Shen S, Wang D, Wang X, Shi J, Zhang F, Han H, Li C. Composite $Sr_2TiO_4/SrTiO_3$(La,Cr) heterojunction based photocatalyst for hydrogen production under visible light irradiation. Journal of Materials Chemistry A. 2013;**1**:7905-7912

[45] Maeda K. Rhodium-doped barium titanate perovskite as a stable p-type semiconductor photocatalyst for hydrogen evolution under visible light. ACS Applied Materials & Interfaces. 2014;**6**:2167-2173

[46] Zhang H, Chen G, Li Y, Teng Y. Electronic structure and photocatalytic properties of copper-doped $CaTiO_3$. International Journal of Hydrogen Energy. 2010;**35**: 2713-2716

[47] Qu Y, Zhou W, Ren Z, Du S, Meng X, Tian G, Pan K, Wang G, Fu H. Electronic structure and photocatalytic properties of copper-doped $CaTiO_3$. Journal of Materials Chemistry. 2012;**22**:16471-16476

[48] Li L, Zhang Y, Schultz AM, Liu X, Salvador PA, Rohrer GS. Visible light photochemical activity of heterostructured $PbTiO_3$–TiO_2 core–shell particles. Catalysis Science & Technology. 2012;**2**:1945-1952

[49] Feng Y-N, Wang H-C, Luo Y-D, Shen Y, Lin Y-H. Magnetic and photocatalytic behaviors of Ca Mn co-doped $BiFeO_3$ nanofibres. Journal of Applied Physics. 2013;**113**:146101

[50] Shi H, Li X, Iwai H, Zou Z, Ye J. 2-propanol photodegradation over nitrogen-doped $NaNbO_3$ powders under visible-light irradiation. Journal of Physics and Chemistry of Solids. 2009;**70**:931-935

[51] Ding Q-P, Yuan Y-P, Xiong X, Li R-P, Huang H-B, Li Z-S, Yu T, Zou Z-G, Yang S-G. Enhanced photocatalytic water splitting properties of $KNbO_3$ nanowires synthesized through hydrothermal method. Journal of Physical Chemistry C. 2008;**112**:18846-18848

[52] Li G, Kako T, Wang D, Zou Z, Ye J. Enhanced photocatalytic activity of La-doped $AgNbO_3$ under visible light irradiation. Dalton Transactions. 2009:2423-2427

[53] Sang Y, Kuai L, Chen C, Fang Z, Geng B. Fabrication of a visible-light-driven plasmonic photocatalyst of $AgVO_3$@AgBr@Ag nanobelt heterostructures. ACS Applied Materials & Interfaces. 2014;**6**:5061-5068

[54] Barrocas B, Sério S, Rovisco A, Nunes Y, Melo Jorge ME. Removal of rhodamine 6G dye contaminant by visible light driven immobilized $Ca_{1-x}Ln_xMnO_3$ (Ln = Sm, Ho; 0.1 - x - 0.4) photocatalysts. Applied Surface Science. 2016;**360**:798-806

[55] Li et al. One-dimensional perovskite manganite oxide nanostructures: Recent developments in synthesis, characterization, transport properties, and applications. Nanoscale Research Letters. 2016;**11**:121

[56] Grabowska E. Selected perovskite oxides: Characterization, preparation and photocatalytic properties—A review. Applied Catalysis B: Environmental. 2016;**186**:97-126

[57] Liang et al. Research progress on electronic phase separation in low-dimensional perovskite manganite nanostructures. Nanoscale Research Letters. 2014;**9**:325

[58] Thirumalairajan S, Girija K, Mastelaro VR, Ponpandian N. Photocatalytic degradation of organic dyes under visible light irradiation by floral-like $LaFeO_3$ nanostructures comprised of nanosheet petals. New Journal of Chemistry. 2014;**38**:5480-5490

[59] Pena MA, Fierro JLG. Chemical structures and performance of perovskite oxides. Chemical Reviews. 2001;**101**:1981-2018

[60] Ismail D, Bahnemann W, Robben L, Yarovyi V, Wark M. Palladium doped porous titania photocatalysts: Impact of mesoporous order and crystallinity. Chemistry of Materials. 2010;**22**:108-116

[61] Ismail D, Bahnemann W, Bannat I, Wark M. Gold nanoparticles on mesoporous interparticle networks of titanium dioxide nanocrystals for enhanced photonic efficiencies. Journal of Physical Chemistry C. 2009;**113**:7429-7435

[62] Shui M, Yue LH, Xu ZD. Effect of lanthanum doping on the photocatalytic activity of titanium dioxide. Acta Physico-Chimica Sinica. 2000;**16**:459-464

[63] Li X, Zang JL. Facile hydrothermal synthesis of sodium tantalate ($NaTaO_3$) nanocubes and high photocatalytic properties. Journal of Physical Chemistry C. 2009;**113**:19411-19418

[64] Hu C, Tsai C, Teng H. Structure characterization and tuning of perovskite-like $NaTaO_3$ for applications in photoluminescence and photocatalysis. Journal of the American Ceramic Society. 2009;**92**:460-466

[65] Mizoguchi H, Eng HW, Woodward PM. Probing the electronic structures of ternary perovskite and pyrochlore oxides containing Sn^{4+} or Sb^{5+}. Inorganic Chemistry. 2004;**43**:1667-1680

[66] Abdel-Latif IA et al. Impact of the annealing temperature on perovskite strontium doped neodymium manganites nanocomposites and their photocatalytic performances. Journal of the Taiwan Institute of Chemical Engineers. 2017;**75**:174-182

[67] Demont A, Abanades S. High redox activity of Sr-substituted lanthanum manganite perovskites for two-step thermochemical dissociation of CO_2. RSC Advances. 2014; **4**:54885-54891

[68] Rossetti I, Allieta M, Biffi C, Scavini M. Oxygen transport in nanostructured lanthanum manganites. Physical Chemistry Chemical Physics. 2013;**15**:16779-16787

[69] Voorhoeve RJH, Remeika JP, Freeland PE, Matthias BT. Rare-earth oxides of manganese and cobalt rival platinum for the treatment of carbon monoxide in auto exhaust. Science. 28, 1972;**177**(4046):353-354

[70] Gupta P, Poddar P. Using raman and dielectric spectroscopy to elucidate the spin phonon and magnetoelectric coupling in $DyCrO_3$ nanoplatelets. RSC Advances. 2015; **5**:10094-10101

[71] Keav S, Matam SK, Ferri D, Weidenkaff A. Structured perovskite-based catalysts and their application as three-way catalytic converters—A review. Catalysts. 2014;**4**(3):226-255

[72] Mierwaldt D, Mildner S, Arrigo R, Knop-Gericke A, Franke E, Blumenstein A, Hoffmann J, Jooss C. In: Situ XANES/XPS investigation of doped manganese perovskite catalysts. Catalysts. 2014;**4**(2):129-145

[73] Madhavan B, Ashok A. Review on nanoperovskites: Materials, synthesis, and applications for proton and oxide ion conductivity. Ionics. 2015;**21**(3):601-610

Chapter 8

Thermoreversible Polymeric Nanocomposites

Ranjita K. Bose, Francesco Picchioni and
Henky Muljana

Additional information is available at the end of the chapter

http://dx.doi.org/10.5772/intechopen.80218

Abstract

Polymeric nanocomposites are widely used in applications such as structural materials, electronics, energy, and biomedical as they synergistically combine the desired properties of the filler and the polymer. The emergent properties can be designed and tuned based not only on the choice of filler and polymer but also on the type of bond and interface created between the two components. When the bond between the two is covalent, the nanocomposites have superior mechanical characteristics. When this covalent bond is reversible, a combination of high impact resistance and high tensile strength is achieved. A well-known approach to achieve these reversible covalent bonds is via the Diels-Alder reaction between a diene and a dienophile. At elevated temperatures, the retro Diels-Alder reaction is dominant resulting in bond cleavage. This chapter reviews the different strategies involving Diels-Alder reactions at the polymer-filler interface. Various fillers have been researched including silica, carbon nanotubes, and graphene, which impart different mechanical and conductive properties to the nanocomposite. A variety of polymer matrices have been reported by various researchers and are summarized here. The choice of diene and dienophile influences the rate of reversible reaction and thus the final properties as will be discussed.

Keywords: nanocomposites, thermally reversible interactions, Diels-Alder, graphene, carbon nanotubes

1. Introduction

Polymeric composites are all around us. The addition of nanofillers to polymers has opened pathways for designing materials with improved functionalities. The synergistic effects of each component can result in better mechanical properties, thermal or electrical conductivity, and enhanced optical properties. The wide range of applications, spanning diverse fields such as civil engineering (building and constructions), electronics, biomedical materials, etc.,

renders this kind of materials essential for our daily life. The simplest structure of a composite is the one consisting of a polymeric matrix in which a solid filler is dispersed. The logic behind this combination is the ability to manipulate the composite properties as function of those of the individual components and the interfacial bonding [1]. However, even at this very simple level, the system can be considered as quite complex. In particular, the geometrical shape of the filler as fibers, platelets, and particles (respectively approached as 1-, 2-, and 3-dimensional objects) is pivotal in determining the final properties. Many studies have been dedicated in the past to understand these features and to develop physical models that are able to predict the properties as a function of the structure [2–8].

One of the challenges in nanocomposites is the nanoscale dispersion and distribution of the filler, which can be achieved by chemical modification of the filler surface. During the last three decades, many works have been focusing on a relatively novel concept, i.e., on the use of a covalent, yet thermally reversible, linkage between the filler and the matrix. On the one hand, this fits the general idea that (thermally) reversible linkages between the components could significantly improve some mechanical characteristics, such as impact properties. This can be achieved also by using relatively weaker interaction forces, such as hydrogen bonding. On the other hand, the use of covalent, and yet reversible bonds, might significantly help in achieving the same goal while avoiding any significant compromise on the strength of the final material [9, 10]. Indeed, among all possible thermoreversible interactions, only covalent bonds can be defined as relatively strong (more than a few kcal/mol) and metal free (**Figure 1**).

Hydrogen bonding [11–14] and ionic interactions [9] have been often used as thermally reversible interactions for composites of different kinds. One of the main driving forces behind the use of such a strategy is the presence of special end properties. For example, the dynamic nature of thermally reversible interactions (as a function of temperature) endows composites with self-healing behavior [11, 13, 15–17] and shape-memory characteristics [18, 19].

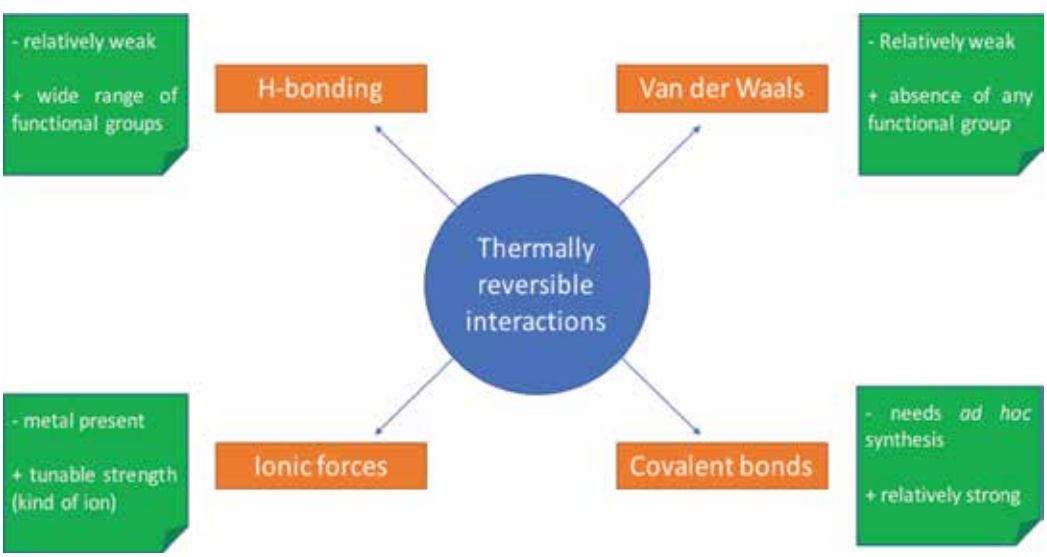

Figure 1. Schematic representation of different kinds of thermally reversible interactions.

Furthermore, the same kind of reversible chemistry can be also applied in solution [20–22] where the crosslinking yields gels of different nature finding applications in very popular fields such as biomedical products. It must also be stressed that very recently particular attention has been paid to a new research field, still in its infancy, dealing with the use of supramolecular polymer in composites [23, 24]. The overall concept, stemming from the use of reversible interaction for the polymer backbone, nicely fits in the thermally reversible context although with even more remarkable loss of properties at relatively high temperatures. In the present chapter, we focus on the use of the Diels-Alder (DA) reaction as a modification toolbox for nanocomposites. While presenting a general overview of the recent literature, we aim to highlight the strategic chemical modification routes and, whenever possible, the added value of such strategy for the properties of the final composite. Other kinds of "click" reactions are also possible, the reader being referred to recent works in the field [25].

2. Chemical strategies for the insertion of DA groups in nanocomposites

The use of Diels-Alder chemistry as a modification tool for composite materials stems from the peculiar characteristics of this reaction. The choice to proceed with or without catalyst at relatively mild temperatures as well as the intimate connection between the forward (DA) and reverse, i.e., retro Diels-Alder (rDA) reactions and the structure of the diene and dienophile render this reaction ideal in terms of being able to control its decrosslinking as a function of temperature. As a consequence, many efforts have been reported in the use of DA to decorate various types of fillers including carbon nanotubes (CNT) [20, 26] and silica [27, 28]. In particular, CNT represent a popular choice (**Figure 2**) in view of their increasing availability and the kaleidoscopic variety of properties they potentially endow the composite with (electrical conductivity, strength, and shape memory).

Functionalization of CNT improves their dispersion in polymer matrices and also improves the processability of the nanocomposites. The DA reaction has a clear effect on the debundling of CNT [29] and also on their dispersion in polymeric matrixes [33]. The mechanical property enhancement is due to two mechanisms: the fillers act as (additional) crosslink points while also serving as stress-transfer points, distributing the stress to the polymer matrix uniformly. In both cases, the key feature is the improved adhesion at the interface between filler and matrix [34]. It is also noteworthy how CNT can act as both diene and dienophile in the DA reaction, respectively, with maleimide and furan groups [30]. As these reactions are mainly aimed at introducing functional groups on the CNT surface, this testifies the versatility of the approach even if in some cases side reactions might be present [19] and there is no mention of the reversibility or its use [31]. Some of the reported approaches towards incorporation of CNT via DA clearly indicate relatively easy synthetic routes [35] (**Figure 3**).

In the present case, functionalized CNT and furfuryl amine are simply mixed with di-glycidyl-bisphenol A, yielding in one step, a multifunctional monomer that can be subsequently crosslinked via addition of a bis-maleimide. In this case, the self-healing behavior can be induced by near-infrared (NIR) irradiation (**Figure 4**). Scratch healing was demonstrated in the vicinity of the

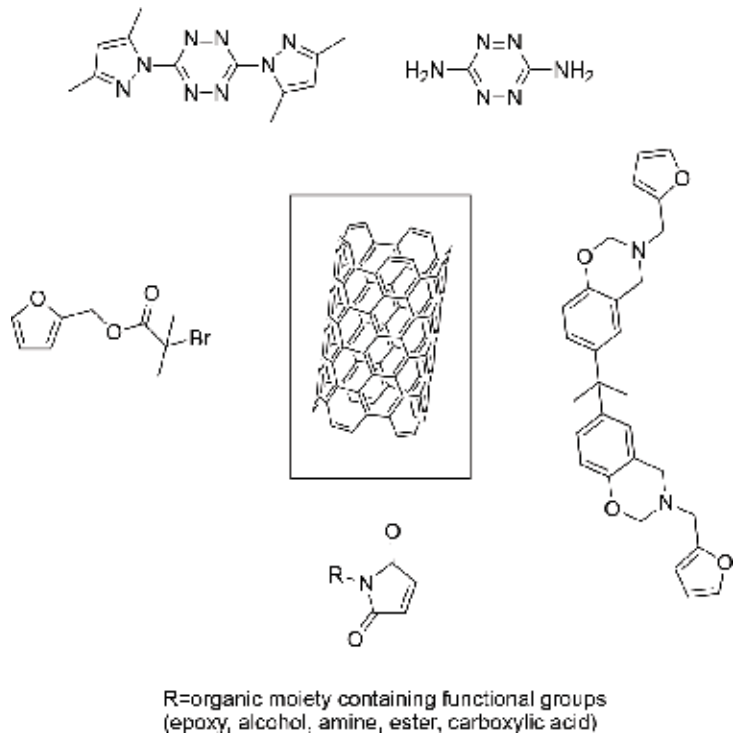

Figure 2. Schematic overview of CNT decoration via the DA reaction. Adapted and redrawn based on [29–32].

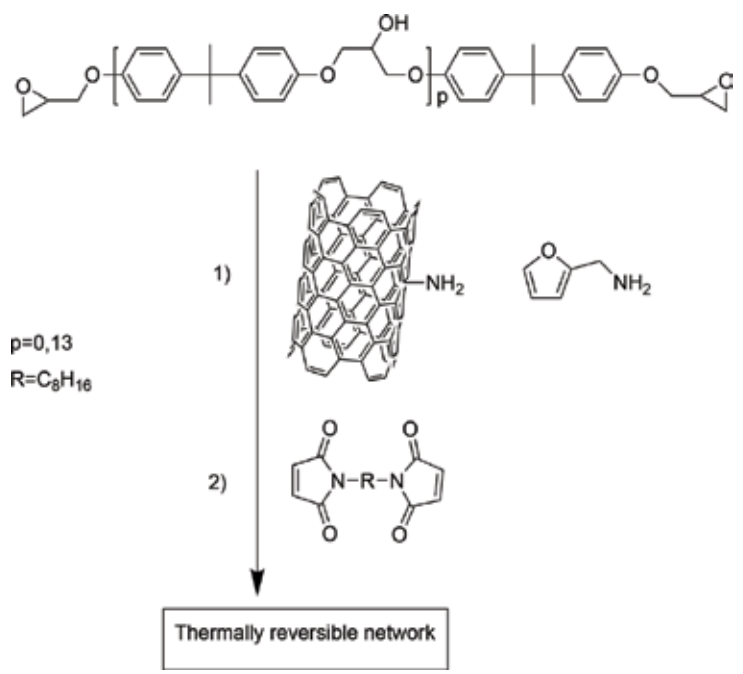

Figure 3. Simple incorporation of CNT into epoxy-like resin [35].

http://dx.doi.org/10.5772/intechopen.80218

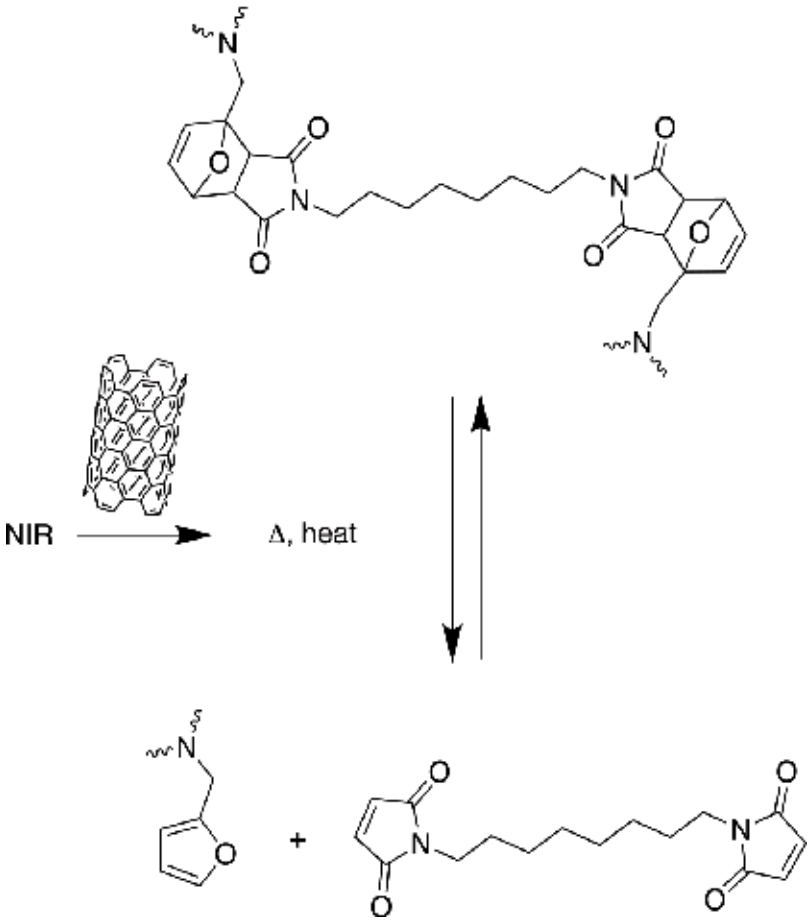

Figure 4. NIR induced self-healing process of epoxy resins [35].

damage using optical microscopy by optimizing the location and power of the laser source. The presence of the CNT ensured the overall robustness and integrity of the nanocomposite samples while also increasing the photothermal conversion efficiency, which enhanced self-healing.

CNT-polymer nanocomposites were demonstrated as reversibly bendable actuators in solvent detection sensors [34]. The incorporation of CNT was crucial in this work as they contributed toward the thermal and electrical conductivity necessary for this particular application. The reversible DA linkages comprising of furan and maleimide moieties ensured good adhesion between the dissimilar layers in the bilayer sensors. This concept of anisotropic expansion in different environments could be extended to multiresponsive materials with applications in soft robotics or self-deployable actuators in different stimuli such as moisture, solvents, pH, and/or temperature. Moreover, the incorporation at the same time of CNT with magnetic nanoparticles (**Figure 5**) is also possible via the DA approach [36].

In this case, the functionalization of Fe_3O_4 nanoparticles with maleimide groups is followed (route A) by DA reaction with CNT and finally by mixing with the polymeric matrix. In another approach [37] (route B), the functionalized nanoparticles can be directly embedded

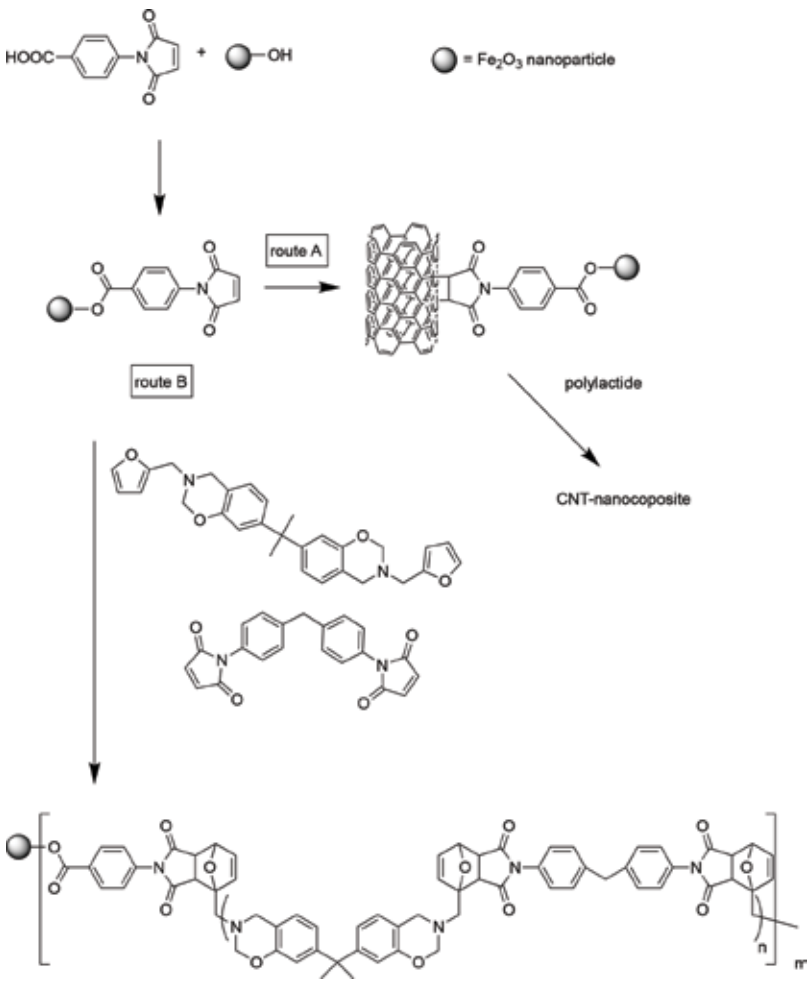

Figure 5. Preparation of composites based on CNT and magnetic particles [36, 37].

in a telechelic polymer via the DA reaction, thus yielding composites without CNT but with magnetic particles. The simplicity of these approaches is in stark contrast with the complex behavior, particularly the response to heat, electricity, and magnetic field. It is worth also noticing, for electrospun fibers produced in this way, the relevant toughening behavior, which might indeed be related to the thermally reversible interaction at the interface.

The extreme precision of the DA reaction, almost devoid of any side reaction, renders it particularly suitable also for simple decoration of different fillers. A recent example [38] is constituted by the synthesis of nanocomposites, forming gold particles and poly-*p*-phenylene ethynylene (**Figure 6**).

As expected, the good adhesion at the interface has a clear influence on the self-assembly behavior of the Au-nanoparticles, and peculiarly in this case, this improves the electronic communication between the conducting backbone and the nanoparticles. Other kinds of nanoparticles, with tailor-made structure and properties, have also been reported, particularly aiming

http://dx.doi.org/10.5772/intechopen.80218

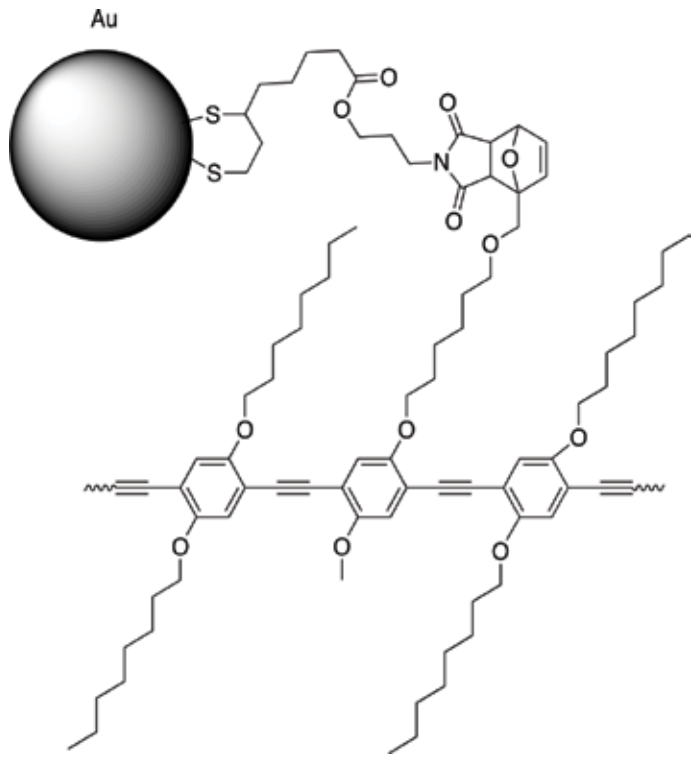

Figure 6. Maleimide functionalized gold (MA-Au)-nanoparticles-based composite [38].

at producing high-k nanocomposites for applications as motion sensors [39]. In this case, the dielectrical permittivity of the material is tunable as a function of the filler intake and can be systematically recovered upon self-healing of the corresponding films. The hybrid polymer-ceramic materials had an improved dielectric property and improved retention of capacitance due to the recoverable DA bonds. The specific capacitance was shown to restore up to 82% even after 10 cycles of cutting and healing. Thus, in addition to improved interfacial properties, the DA reaction also enables the lifetime extension of such materials during application. Functionalized nanoparticles (with DA groups) might have an important role as additives as they have been also employed as dynamic crosslinker in gels [40].

The same approach has been used for POSS-based composites [41] and polyesters (**Figure 7**). The partially crosslinked network was insoluble to common organic solvents while showing thermoreversibility at 120°C. The occurrence of the DA reaction between furan and maleimide functional groups was induced by melt mixing as opposed to casting. The resultant nanocomposites had significantly higher flexural and tensile moduli as well as glass transition temperature as compared to the polymer matrix. This mechanical behavior clearly highlights the dynamic nature of the bonds, while at the same time suggesting a synergy in terms of strength and impact properties.

Besides CNT and nanoparticles, graphene has also attracted much attention. This is not surprising when making allowances for the similar structure and reactivity of these two fillers. In one report, self-healing was achieved by catalyst containing microcapsules and graphene

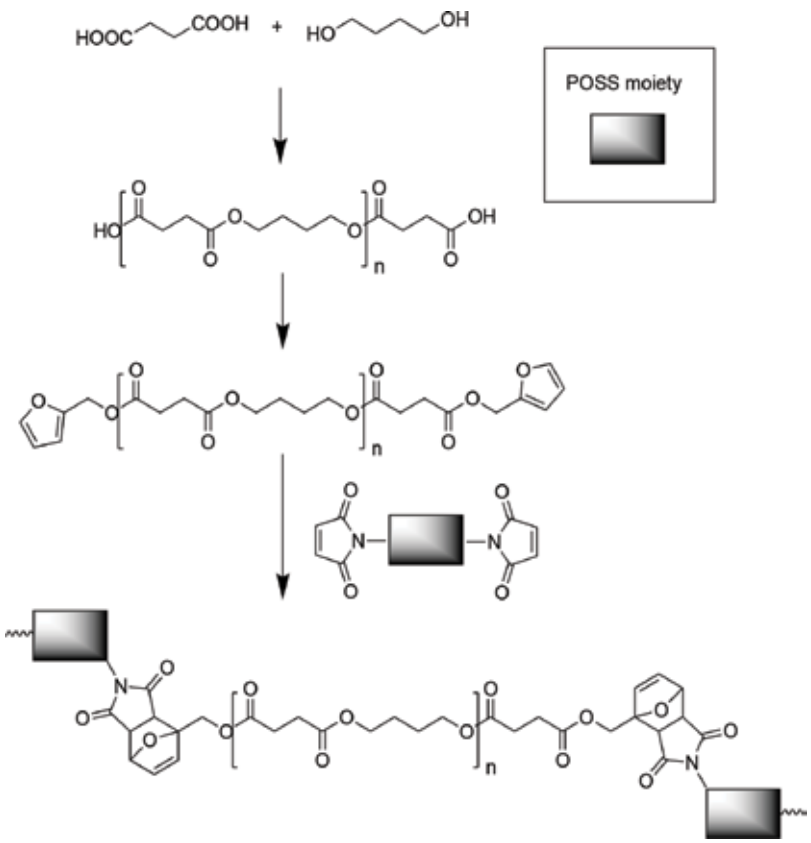

Figure 7. POSS-based composites [41].

was added to offset the reduction in tensile strength due to the addition of the weaker microcapsules [42]. Graphene-based nanocomposites have been reported for possible application as supercapacitors [43]. In this case, a conductive polymer polypyrrole was chosen due to its stability upon exposure to oxygen, cheap cost, and easy synthesis. Tetrazine derivatives were reacted onto reduced graphene sheets via the inverse electron demand Diels-Alder reaction. The nanocomposites showed good electrochemical properties and a small resistance due to easy ion accessibility and thus are promising as potential electrode materials for supercapacitors. Graphene-based nanocomposites have also been demonstrated as strain sensors for flexible electronics [44]. Here, furfuryl containing polyurethane was crosslinked with a bismaleimide onto reduced functionalized graphene oxide sheets. The nanocomposites showed good flexibility, and thermal and electrical conductivity was required for the aforementioned application. Healing via rDA reaction was achieved by microwave heating in <5 min. A particularly simple approach (**Figure 8**) allows easy fabrication of composites based on graphene and a multifunctional DA crosslinker [45].

The mechanical behavior of the final product clearly reflects the pivotal role of the graphene intake (**Figure 9**). As expected, tensile strength and Young's modulus increase with the graphene intake while the elongation at break decreases.

http://dx.doi.org/10.5772/intechopen.80218

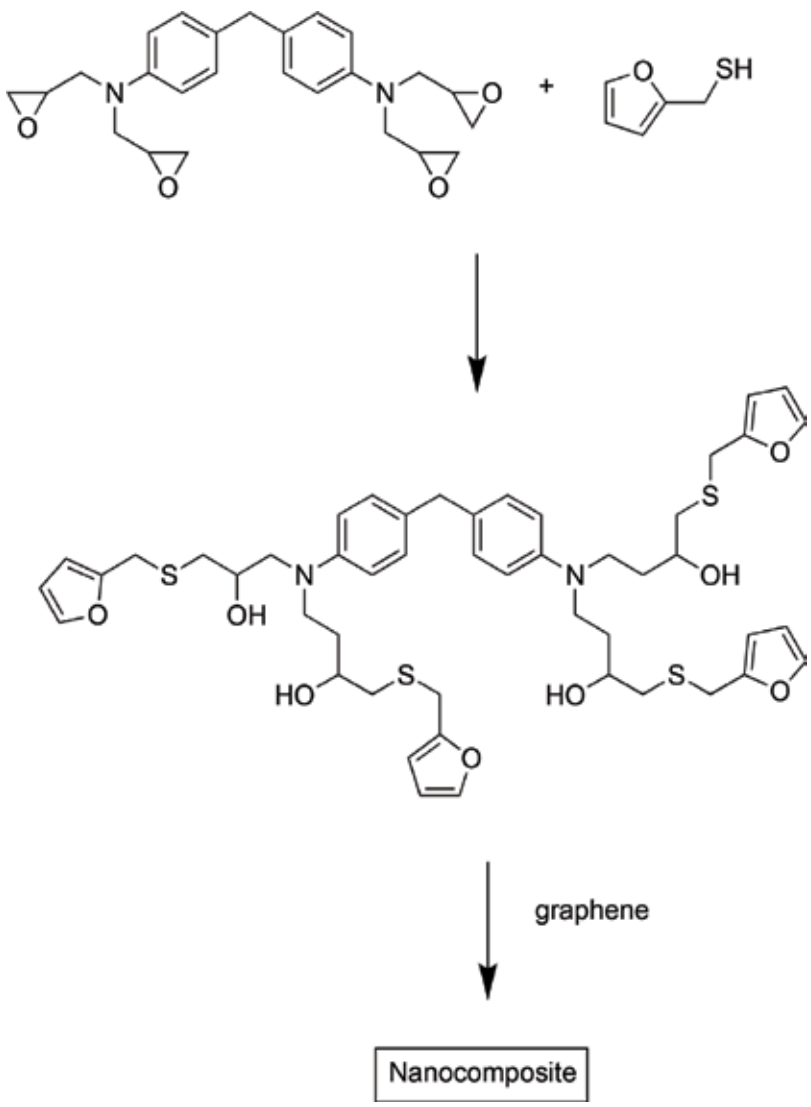

Figure 8. Nanocomposite fabrication via DA reaction between graphene and a multifunctional crosslinker.

Although in a different work [46], a significant improvement of the impact properties has also been reported and preliminarily attributed to the wave propagation through the graphene platelets. Also in the case of graphene, as for CNT, reactivity as diene or dienophile, can be exploited [47]. The occurrence of the reaction between graphene and the maleimide crosslinker is once more testified by the excellent dispersion of the graphene sheets within the matrix. These sheets act as a local thermal collector by converting adsorbed infrared or microwave energy into heat, thus triggering the reversible bond behavior. This renders the final composite responsive to multiple stimuli (heat, electricity, infrared, microwave) for self-healing and shape memory. These effects are then on top of the change in mechanical properties as, for example, highlighted above. Such improvement of mechanical behavior can also

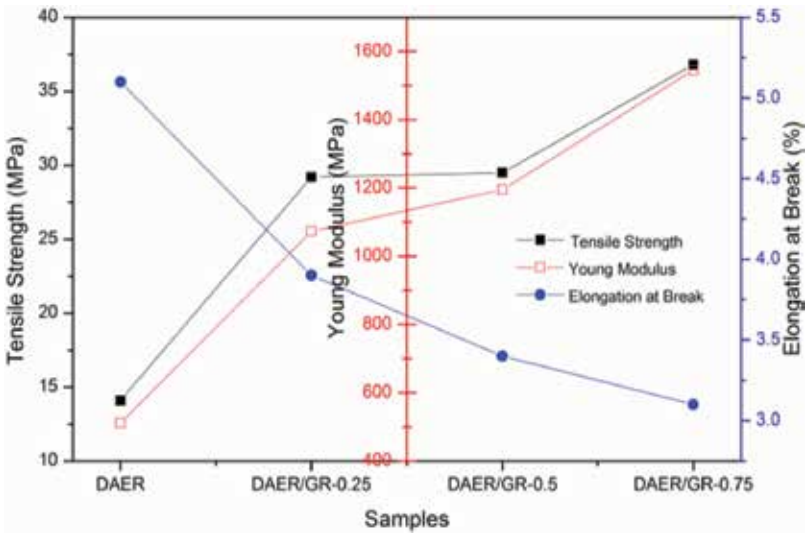

Figure 9. Mechanical properties of nanocomposites as function of the graphene intake [45].

be "dramatic" as reported in the case of styrene-butadiene rubber (SBR) functionalized with furan groups, mixed with furan-functionalized CNT and crosslinked by addition of a bis-maleimide [48]. In this case, a relevant increase (over 200%) in modulus values and toughness could be booked. This highlights once more the synergy in the combination of nanofillers and their thermally reversible adhesion to the matrix. The concept of "local" self-healing, for which nanoparticles play a crucial role, is actually broader than merely graphene and DA. The fact that heat can be generated locally renders the crosslinking kinetics faster [49] also in the case of ionic interactions and magnetic nanoparticles.

In addition to relatively novel nanofillers, composites with thermally reversible interactions have also been prepared based on more "classical" ones, such as silica [50] again with the general aim of inducing self-healing behavior. The general preparation strategy is similar to the ones presented above and entails the functionalization of the polymer and the filler with furan groups, followed by crosslinking with bis-maleimides [50]. However, in the special case of silica, also different approaches are possible in view of the possibility to obtain silica as result of sol-gel reactions (**Figure 10**).

Furan and maleimide groups are the most commonly used diene and dienophile in self-healing reversible systems. This is due to their high reactivity and low activation energy of the rDA reaction, which enables the rDA reaction to proceed around 100 to 140°C. In the majority of the examples illustrated so far, attention has been paid to the occurrence of the DA reaction while aiming at relatively low rDA temperature (typically 120°C) in view of self-healing properties at relatively mild experimental conditions. In some cases, a catalyst has also been used to achieve self-healing at even lower temperatures [51]. On the other hand, for some specific applications in extreme environments (e.g., in automotive or aerospace), thermal stability up to 200°C is a *conditio sine qua non*. This can be achieved by changing the chemical structure of the DA groups. A recent example involves the use of anthracene and maleimide groups [52] (**Figure 11**).

http://dx.doi.org/10.5772/intechopen.80218

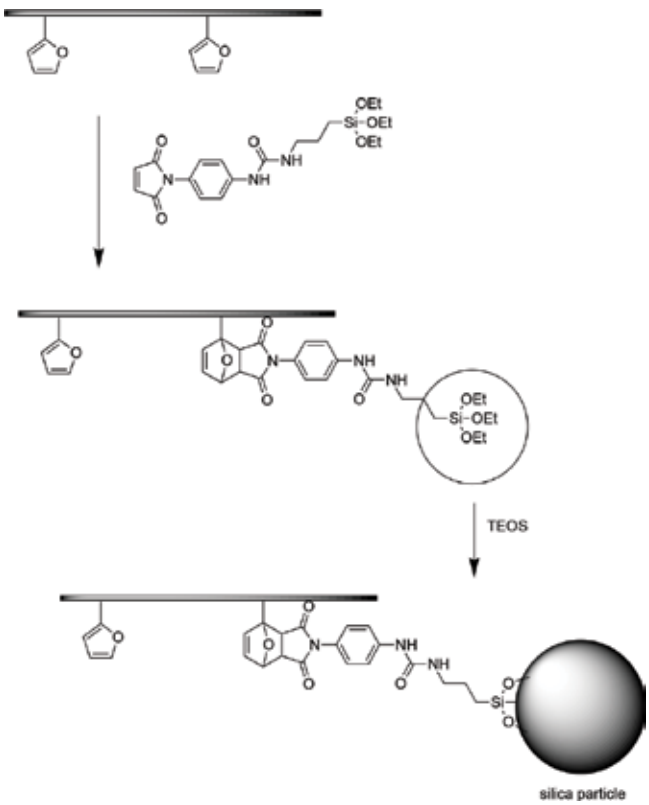

Figure 10. Sol-gel approach toward the synthesis of silica-based thermally reversible composites [50].

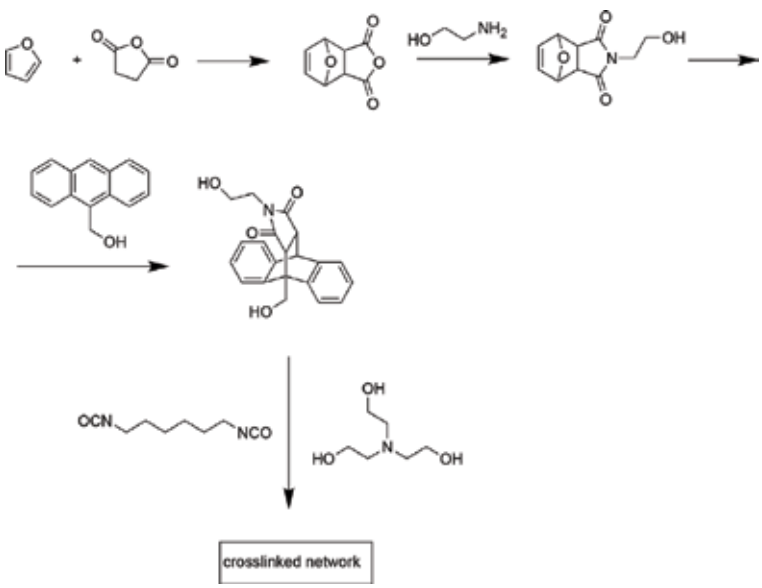

Figure 11. Anthracene-based composites [52].

The resulting polyurethanes (PU) show self-healing behavior by pure DA reaction for mechanically cleaved adducts. The use of continuous fibers also helped with mechanical robustness comparable to those of engineering polymers and structural composites. These materials were exceptionally thermally stable and showed high strength, stiffness, and toughness.

3. Future outlook

Thermal reversibility allows adding another tool for the design of smart composites. Properties such as self-healing and shape memory, besides the "classical effects" on thermal and mechanical ones, are easily added to the composite behavior. The sensitivity to multiple external stimuli such as electricity, irradiation, and heat [11, 18, 53, 54], represents a focal point for the design of smart materials. An added value in this case is the possibility (via irradiation) of remote-induced self-healing as well as of ultrafast kinetics [55]. In this context, it is conceivable that many research efforts will be spent in achieving a systematic control over this multifunctionality and responsiveness. In turn, this will require even more precise control over the kind of functional groups present and the chemical structure in more general terms. Further studies are then envisioned in the general field of structure-property relationships, for example, by a systematic investigation on the influence of spacers [56] on the DA decrosslinking. Other factors influencing the structure of the composite and thus its properties, such as the nature of the filler and the backbone, continue to represent points of attention. The possibility to extend the concept to inorganic polymers [57], the use of fullerene derivatives [58] as well the general trend toward the use of green fillers [59] have been recently reported, but deserve further study in order to explore all possible application fields. Finally, the combination of the properties highlighted above and their synergy with additional ones, such as color change upon thermally reversible behavior [60], constitute attractive characteristics of these materials.

Conflict of interest

The authors declare no conflict of interests,

Author details

Ranjita K. Bose[1], Francesco Picchioni[1]* and Henky Muljana[1,2]

*Address all correspondence to: f.picchioni@rug.nl

1 Department of Chemical Engineering, ENTEG, University of Groningen, Groningen, The Netherlands

2 Department of Chemical Engineering, Parahyangan Catholic University, Bandung, West Java, Indonesia

References

[1] Lin H, Liu Y. Reactive hybrid of polyhedral oligomeric silsesquioxane (POSS) and sulfur as a building block for self-healing materials. Macromolecular Rapid Communications. 2017;**38**(10):1700051. DOI: 10.1002/marc.201700051

[2] Bostanabad R, Zhang Y, Li X, Kearney T, Brinson LC, Apley DW, et al. Computational microstructure characterization and reconstruction: Review of the state-of-the-art techniques. Progress in Materials Science. 2018;**95**:1-41. DOI: 10.1016/j.pmatsci.2018.01.005

[3] Myshkin N, Kovalev A. Adhesion and surface forces in polymer tribology-a review. Friction. 2018;**6**(2):143-155. DOI: 10.1007/s40544-018-0203-0

[4] Xiong X, Shen SZ, Hua L, Liu JZ, Li X, Wan X, et al. Finite element models of natural fibers and their composites: A review. Journal of Reinforced Plastics and Composites. 2018;**37**(9):617-635. DOI: 10.1177/0731684418755552

[5] Boris D, Xavier L, Damien S. The tensile behaviour of biaxial and triaxial braided fabrics. Journal of Industrial Textiles. 2018;**47**(8):2184-2204. DOI: 10.1177/1528083716654469

[6] Bogenfeld R, Kreikemeier J, Wille T. Review and benchmark study on the analysis of low-velocity impact on composite laminates. Engineering Failure Analysis. 2018;**86**: 72-99. DOI: 10.1016/j.engfailanal.2017.12.019

[7] Hunter A, Leu B, Beyerlein IJ. A review of slip transfer: Applications of mesoscale techniques. Journal of Materials Science. 2018;**53**(8):5584-5603. DOI: 10.1007/s10853-017-1844-5

[8] Li N, Liu X. Review: Mechanical behavior of metal/ceramic interfaces in nanolayered composites-experiments and modeling. Journal of Materials Science. 2018;**53**(8):5562-5583. DOI: 10.1007/s10853-017-1767-1

[9] Potier F, Guinault A, Delalande S, Sanchez C, Ribot F, Rozes L. Nano-building block based-hybrid organic-inorganic copolymers with self-healing properties. Polymer Chemistry. 2014;**5**(15):4474-4479. DOI: 10.1039/c4py00172a

[10] Amaral AJR, Emamzadeh M, Pasparakis G. Transiently malleable multi-healable hydrogel nanocomposites based on responsive boronic acid copolymers. Polymer Chemistry. 2018;**9**(4):525-537. DOI: 10.1039/c7py01202k

[11] Zhu B, Noack M, Merindol R, Barner-Kowollik C, Walther A. Light-adaptive supramolecular nacre-mimetic nanocomposites. Nano Letters. 2016;**16**(8):5176-5182. DOI: 10.1021/acs.nanolett.6b02127

[12] Xing L, Li Q, Zhang G, Zhang X, Liu F, Liu L, et al. Self-healable polymer nanocomposites capable of simultaneously recovering multiple functionalities. Advanced Functional Materials. 2016;**26**(20):3524-3531. DOI: 10.1002/adfm.201505305

[13] Noack M, Merindol R, Zhu B, Benitez A, Hackelbusch S, Beckert F, et al. Light-fueled, spatiotemporal modulation of mechanical properties and rapid self-healing of graphene-doped supramolecular elastomers. Advanced Functional Materials. 2017;**27**(25):1700767. DOI: 10.1002/adfm.201700767

[14] Yari H, Mohseni M, Messori M. A scratch resistant yet healable automotive clearcoat containing hyperbranched polymer and POSS nanostructures. RSC Advances. 2016; **6**(79):76028-76041. DOI: 10.1039/c6ra07824a

[15] Duarah R, Karak N. High performing smart hyperbranched polyurethane nanocomposites with efficient self-healing, self-cleaning and photocatalytic attributes. New Journal of Chemistry. 2018;**42**(3):2167-2179. DOI: 10.1039/c7nj03889e

[16] Li Y, Gao F, Xue Z, Luan Y, Yan X, Guo Z, et al. Synergistic effect of different graphene-CNT heterostructures on mechanical and self-healing properties of thermoplastic polyurethane composites. Materials and Design. 2018;**137**:438-445. DOI: 10.1016/j.matdes.2017.10.018

[17] Moazzen K, Zohuriaan-Mehr MJ, Jahanmardi R, Kabiri K. Toward poly(furfuryl alcohol) applications diversification: Novel self-healing network and toughening epoxy-novolac resin. Journal of Applied Polymer Science. 2018;**135**(12):45921. DOI: 10.1002/app.45921

[18] Bai J, Shi Z. Dynamically cross-linked elastomer hybrids with light-induced rapid and efficient self-healing ability and reprogrammable shape memory behavior. ACS Applied Materials & Interfaces. 2017;**9**(32):27213-27222. DOI: 10.1021/acsami.7b06407

[19] Chuo T, Liu Y. Preparation of self-healing organic-inorganic nanocomposites with the reactions between methacrylated polyhedral oligomeric silsesquioxanes and furfurylamine. Composites Science and Technology. 2015;**118**:236-243. DOI: 10.1016/j.compscitech.2015.09.005

[20] Garcia-Garcia JM, Mar Bernal M, Verdejo R, Lopez-Manchado MA, Doncel-Perez E, Garrido L, et al. Semiconductive bionanocomposites of poly(3-hydroxybutyrate-co-3-hydroxyhexanoate) and MWCNTs for neural growth applications. Journal of Polymer Science Part B-Polymer Physics. 2014;**52**(5):349-360. DOI: 10.1002/polb.23417

[21] Garcia-Astrain C, Ahmed I, Kendziora D, Guaresti O, Eceiza A, Fruk L, et al. Effect of maleimide-functionalized gold nanoparticles on hybrid biohydrogels properties. RSC Advances. 2015;**5**(62):50268-50277. DOI: 10.1039/c5ra06806a

[22] Garcia-Astrain C, Miljevic M, Ahmed I, Martin L, Eceiza A, Fruk L, et al. Designing hydrogel nanocomposites using TiO_2 as clickable cross-linkers. Journal of Materials Science. 2016;**51**(11):5073-5081. DOI: 10.1007/s10853-016-9810-1

[23] de Espinosa LM, Fiore GL, Weder C, Foster EJ, Simon YC. Healable supramolecular polymer solids. Progress in Polymer Science. 2015;49-50:60-78. DOI: 10.1016/j.progpolymsci.2015.04.003

[24] Zhu B, Merindol R, Benitez AJ, Wang B, Walther A. Supramolecular engineering of hierarchically self-assembled, bioinspired, cholesteric nanocomposites formed by cellulose nanocrystals and polymers. ACS Applied Materials & Interfaces. 2016;**8**(17):11031-11040. DOI: 10.1021/acsami.6b00410

[25] Arslan M, Tasdelen MA. Polymer nanocomposites via click chemistry reactions. Polymer. 2017;**9**(10):499. DOI: 10.3390/polym9100499

[26] Kaur A, Singh I, Kumar J, Bhatnagar C, Dixit SK, Bhatnagar PK, et al. Enhancement in the performance of multi-walled carbon nanotube: Poly(methylmethacrylate) composite thin film ethanol sensors through appropriate nanotube functionalization. Materials Science in Semiconductor Processing. 2015;**31**:166-174. DOI: 10.1016/j.mssp.2014.11.030

[27] Ursache O, Gaina V, Gaina C. Poly(vinyl alcohol)-inorganic hybrid materials with Thermocleavable groups. Polymer - Plastics Technology and Engineering. 2013;**52**(6): 546-552. DOI: 10.1080/03602559.2012.762377

[28] Engel T, Kickelbick G. Thermoreversible reactions on inorganic nanoparticle surfaces: Diels-Alder reactions on sterically crowded surfaces. Chemistry of Materials. 2013;**25**(2):149-157. DOI: 10.1021/cm303049k

[29] Hayden H, Gun'ko YK, Perova T, Grudinkin S, Moore A, Obraztsova ED. Investigation of tetrazine functionalised single walled carbon nanotubes. Plastics, Rubber and Composites. 2009;**38**(6):253-256. DOI: 10.1179/174328909X435384

[30] Munirasu S, Albuerne J, Boschetti-de-Fierro A, Abetz V. Functionalization of carbon materials using the Diels-Alder reaction. Macromolecular Rapid Communications. 2010;**31**(6):574-579. DOI: 10.1002/marc.200900751

[31] Zhang W, Zhou Z, Li Q, Chen G. Controlled dielectric properties of polymer composites from coating multiwalled carbon nanotubes with octa-acrylate silsesquioxane through Diels-Alder cycloaddition and atom transfer radical polymerization. Industrial and Engineering Chemistry Research. 2014;**53**(16):6699-6707. DOI: 10.1021/ie404204g

[32] Wang Y, Chang C, Liu Y. Benzoxazine-functionalized multi-walled carbon nanotubes for preparation of electrically-conductive polybenzoxazines. Polymer. 2012;**53**(1):106-112. DOI: 10.1016/j.polymer.2011.11.040

[33] Lin C, Sheng D, Liu X, Xu S, Ji F, Dong L, et al. Polymer. 2017;**127**:241-250. DOI: 10.1016/j.polymer.2017.09.001

[34] Toncheva A, Willocq B, Khelifa F, Douheret O, Lambert P, Dubois P, et al. Bilayer solvent and vapor-triggered actuators made of cross-linked polymer architectures via Diels-Alder pathways. Journal of Materials Chemistry B. 2017;**5**(28):5556-5563. DOI: 10.1039/c7tb01661a

[35] Li Q, Jiang M, Wu G, Chen L, Chen S, Cao Y, et al. Photothermal conversion triggered precisely targeted healing of epoxy resin based on thermoreversible Diels-Alder network

and amino-functionalized carbon nanotubes. ACS Applied Materials & Interfaces. 2017;**9**(24):20797-20807. DOI: 10.1021/acsami.7b01954

[36] Li H, Chang C, Hsu K, Liu Y. Poly(lactide)-functionalized and Fe_3O_4 nanoparticle-decorated multiwalled carbon nanotubes for preparation of electrically-conductive and magnetic poly(lactide) films and electrospun nanofibers. Journal of Materials Chemistry. 2012;**22**(11):4855-4860. DOI: 10.1039/c2jm14689d

[37] Wu C, Kao T, Li H, Liu Y. Preparation of polybenzoxazine-functionalized Fe_3O_4 nanoparticles through in situ Diels-Alder polymerization for high performance magnetic polybenzoxazine/Fe_3O_4 nanocomposites. Composites Science and Technology. 2012;**72**(13):1562-1567. DOI: 10.1016/j.compscitech.2012.06.018

[38] Liu X, Zhu M, Chen S, Yuan M, Guo Y, Song Y, et al. Organic-inorganic nanohybrids via directly grafting gold nanoparticles onto conjugated copolymers through the Diels-Alder reaction. Langmuir. 2008;**24**(20):11967-11974. DOI: 10.1021/la8020639

[39] Yang Y, Zhu B, Yin D, Wei J, Wang Z, Xiong R, et al. Flexible self-healing nanocomposites for recoverable motion sensor. Nano Energy. 2015;**17**:1-9. DOI: 10.1016/j.nanoen.2015.07.023

[40] Garcia-Astrain C, Hernandez R, Guaresti O, Fruk L, Mijangos C, Eceiza A, et al. Click crosslinked chitosan/gold nanocomposite hydrogels. Macromolecular Materials and Engineering. 2016;**301**(11):1295-1300. DOI: 10.1002/mame.201600247

[41] Shibata M, Teramoto N, Akiba T, Ogihara M. High-performance hybrid materials prepared by the thermo-reversible Diels-Alder polymerization of furfuryl ester-terminated butylene succinate oligomers and maleimide compounds. Polymer Journal. 2011;**43**(5):455-463. DOI: 10.1038/pj.2011.14

[42] Rana S, Doehler D, Nia AS, Nasir M, Beiner M, Binder WH. "Click"-triggered self-healing graphene nanocomposites. Macromolecular Rapid Communications. 2016;**37**(21):1715-1722. DOI: 10.1002/marc.201700610

[43] Li Y, Louarn G, Aubert P, Alain-Rizzo V, Galmiche L, Audebert P, et al. Polypyrrole-modified graphene sheet nanocomposites as new efficient materials for supercapacitors. Carbon. 2016;**105**:510-520. DOI: 10.1016/j.carbon.2016.04.067

[44] Li J, Zhang G, Sun R, Wong C. A covalently cross-linked reduced functionalized graphene oxide/polyurethane composite based on Diels-Alder chemistry and its potential application in healable flexible electronics. Journal of Materials Chemistry C. 2017;**5**(1):220-228. DOI: 10.1039/c6tc04715g

[45] Cai C, Zhang Y, Zou X, Zhang R, Wang X, Wu Q, et al. Rapid self-healing and recycling of multiple-responsive mechanically enhanced epoxy resin/graphene nanocomposites. RSC Advances. 2017;**7**(73):46336-46343. DOI: 10.1039/c7ra09258j

[46] Zabihi O, Ahmadi M, Abdollahi T, Nikafshar S, Naebe M. Collision-induced activation: Towards industrially scalable approach to graphite nanoplatelets functionalization

for superior polymer nanocomposites. Scientific Reports. 2017;**7**:3560. DOI: 10.1038/s41598-017-03890-8

[47] Cai C, Zhang Y, Li M, Chen Y, Zhang R, Wang X, et al. Multiple-responsive shape memory polyacrylonitrile/graphene nanocomposites with rapid self-healing and recycling properties. RSC Advances. 2018;**8**(3):1225-1231. DOI: 10.1039/c7ra11484b

[48] Kuang X, Liu G, Dong X, Wang D. Enhancement of mechanical and self-healing performance in multiwall carbon nanotube/rubber composites via Diels-Alder bonding. Macromolecular Materials and Engineering. 2016;**301**(5):535-541. DOI: 10.1002/mame.201500425

[49] Hohlbein N, Shaaban A, Schmidt AM, et al. Polymer. 2015;**69**:301-309. DOI: 10.1016/j.polymer.2015.04.024

[50] Engel T, Kickelbick G. Self-healing nanocomposites from silica - polymer core - shell nanoparticles. Polymer International. 2014;**63**(5):915-923. DOI: 10.1002/pi.4642

[51] Doehler D, Michael P, Binder WH. CuAAC-based click chemistry in self-healing polymers. Accounts of Chemical Research. 2017;**50**(10):2610-2620. DOI: 10.1021/acs.accounts.7b00371

[52] Heo Y, Malakooti MH, Sodano HA. Self-healing polymers and composites for extreme environments. Journal of Materials Chemistry A. 2016;**4**(44):17403-17411. DOI: 10.1039/c6ta06213j

[53] Willocq B, Bose RK, Khelifa F, Garcia SJ, Dubois P, Raquez J. Healing by the joule effect of electrically conductive poly(ester-urethane)/carbon nanotube nanocomposites. Journal of Materials Chemistry A. 2016;**4**(11):4089-4097. DOI: 10.1039/c5ta09793b

[54] Polgar LM, van Essen FCM, Hermosilla RA, Migliore N, Lenti M, Raffa P, et al. Thermoreversibly cross-linked EPM rubber Nanocomposites with carbon nanotubes Nanomaterials. Nanomaterials. 2018;**8**(2):58. DOI: 10.3390/nano8020058

[55] Wu S, Li J, Zhang G, Yao Y, Li G, Sun R, et al. Ultrafast self-healing nanocomposites via infrared laser and their application in flexible electronics. ACS Applied Materials & Interfaces. 2017;**9**(3):3040-3049. DOI: 10.1021/acsami.6b15476

[56] Schaefer S, Kickelbick G. Self-healing polymer nanocomposites based on Diels-Alder-reactions with silica nanoparticles: The role of the polymer matrix. Polymer. 2015;**69**:357-368. DOI: 10.1016/j.polymer.2015.03.017

[57] Jo YY, Lee AS, Baek K, Lee H, Hwang SS. Thermally reversible self-healing polysilsesquioxane structure-property relationships based on Diels-Alder chemistry. Polymer. 2017;**108**:58-65. DOI: 10.1016/j.polymer.2016.11.040

[58] Bai J, He Q, Shi Z, Tian M, Xu H, Ma X, et al. Self-assembled elastomer nanocomposites utilizing C-60 and poly(styrene-b-butadiene-b-styrene) via thermally reversible Diels-Alder reaction with self-healing and remolding abilities. Polymer. 2017;**116**:268-277. DOI: 10.1016/j.polymer.2017.03.080

[59] Shahabadi SIS, Kong JH, Lu XH. Aqueous-only, green route to self-healable, UV-resistant, and electrically conductive polyurethane/graphene/lignin nanocomposite coatings. ACS Sustainable Chemistry & Engineering. 2017;**5**(4):3148-3157. DOI: 10.1021/acssuschemeng.6b02941

[60] Imato K, Natterodt JC, Sapkota J, Goseki R, Weder C, Takahara A, et al. Dynamic covalent diarylbibenzofuranone-modified nanocellulose: Mechanochromic behaviour and application in self-healing polymer composites. Polymer Chemistry. 2017;**8**(13):2115-2122. DOI: 10.1039/c7py00074j

Chapter 9

Ultrasound-Assisted Melt Extrusion of Polymer Nanocomposites

Carlos A. Ávila-Orta, Pablo González-Morones, Diana Agüero-Valdez, Alain González-Sánchez, Juan G. Martínez-Colunga, José M. Mata-Padilla and Víctor J. Cruz-Delgado

Additional information is available at the end of the chapter

http://dx.doi.org/10.5772/intechopen.80216

Abstract

A review of the latest developments in ultrasound-assisted melt extrusion of polymer nanocomposites is presented. In general, the application of ultrasound waves during melt extrusion of polymer in the presence of nanoparticles results in a more homogeneous dispersion of the nanoparticles in the polymer matrix. In spite of this, a lack of understanding in the field has hindered the development of this processing technique. Based on the analysis of literature on the field, key aspects are identified for a better understanding of the physical and chemical effects of ultrasound waves and the fabrication of polymer nanocomposites by means of melt extrusion.

Keywords: extrusion, ultrasound, melt, nanocomposites, cavitation

1. Introduction

The study of polymeric nanocomposites has grown during the last 10 years due to the remarkable properties that result from the combination of a continuous phase (polymer matrix) and a dispersed phase (nanoparticles), where at least one dimension of the dispersed phase is found in the scale of nanometric size (<100 nm). Such nanocomposites have attracted the attention of academic and industrial researchers due to their extraordinary electrical, thermal, chemical, and biological properties and potential applications in various sectors of the industry such as in the health sector, automotive industry, energy, construction, and food industry among

others [1, 2]. One of the most popular methods used to prepare such materials is melt extrusion, since it is a flexible and versatile process, which does not require the use of solvents and can be scaled up at industrial level.

However, even with all these advantages, the lack of homogeneous dispersion of nanoparticles in the polymer matrix is still a problem with melt extrusion. An alternative to improve the dispersion is the application of ultrasound waves during the polymer processing in the molten state, named ultrasound-assisted extrusion. The first report of the use of ultrasound coupled in extrusion was made by Isayev et al. for processing vulcanized elastomers devulcanization [3]. These authors reported that the ultrasound waves have the ability to cause an incision in the C-S and S-S bonds of the crosslinked rubber, causing the breaking of the reticulated network and thereby achieving the devulcanization of the rubber. Later, it was applied to the study of polymer mixtures in the molten state [4], and in the last decade, this technology has been used for the preparation of polymer nanocomposites. Although it has been proven that this technology improves the dispersion of nanoparticles and that it has a great potential for application, the fundamentals for applying this technology in melt extrusion process are still not well understood. For example, the effects observed by the application of ultrasound have been explained on the basis of acoustic cavitation, treating the molten polymer as a Newtonian system; however, polymer cannot be considered as Newtonian fluids. For this reason, a general overview of the basic principles of ultrasound, the development and use of this technology in the preparation of polymeric nanocomposites in the molten state, and the mechanisms that have been proposed so far for the understanding of the phenomenon that generates the dispersion of the nanoparticles in the polymer is described below.

2. Extrusion applied in the manufacture of polymeric nanocomposites

2.1. Polymers and nanoparticles

Thermoplastic polymers and nanoparticles are the main materials used to produce polymer nanocomposites by melt extrusion. Thermoplastic polymers include polyolefins, polyesters, and polyamides among other polymer families. On the other hand, the nanoparticles can be classified according to the number of dimensions in the nanometer range. Zero-dimensional (0D): it is defined as a particle that is measured within a nanoscale range, that is, less than 100 nm, among them are all the nanoparticles, for example ZnO, TiO_2, etc. One-dimensional (1D) has two dimensions in this scale, such as nanotubes and nanofiber. Finally, two-dimensional (2D) is referred to nanoparticles, where one dimension is in the nanometer scale, for example graphene and nanodisks [5].

2.2. Modification of nanoparticles

Unlike particles of micro size, in the nanoparticles, the interparticle forces such as Van der Waals and electrostatic forces, as well as the magnetic attraction, become stronger, which results in the nanoparticles forming agglomerates, which are difficult to disperse individually

and uniformly in the polymeric matrix; this implies obtaining compounds similar to conventional composites [6]. For this reason, various techniques in the modification of nanoparticles have been explored.

The modification of the surface, in general, decreases the surface energy of the nanoparticles, improving the affinity between the polymer matrix and the nanoparticles. Natural clays have a stratified structure bonded by strong covalent bonds [7], thus hindering its homogeneous dispersion in many polymers. Therefore, a surface modification is needed, and in this case, it is carried out through a cation exchange process, in which the sodium and calcium cations present in the inter-clay galleries are replaced by alkylammonium species, usually quaternary ammonium containing alkyl, phenyl, benzyl, and pyridyl groups [8]. In metal nanoparticles such as nanoparticles of silicon dioxide, titanium dioxide and aluminum oxide are surface modified with organosilane coupling agents [9], while in carbon-based nanoparticles, surface modification is carried out by covalent functionalization or not covalent. In CNT for example, functionalization of the covalent bond of functional entities can be performed at the ends of the tubes or on their side walls. This process can be carried out by reaction with some molecules with high chemical reactivity, such as fluorine [10]. A noncovalent functionalization is the π-π interactions with aromatic molecules, such as pyrene, widely used to modify graphene [11].

Another approach to modify the surfaces of nanoparticles is based on grafting synthetic polymers on the surface of the substrate, which improves the chemical functionality and alters the topology of the surface of the materials [12]. The graft can be done in two ways: (1) by means of obtaining a polymer with a reactive terminal group and subsequently it is grafted to the surface of the nanomaterial, and (2) the graft is made from the growth of the polymer from an initiator [13].

In spite of all the available modifications for nanoparticles, sometimes they are not usually enough and it is necessary to look for alternative or previous methods to the extrusion process that helps us to de-agglomerate the nanoparticles and to reduce the size of these. One of these methods is mechanical milling by high-energy ball mill. The alteration of the solids by mechanical grinding gives rise not only to the fragmentation of the particles but also to structural changes, polymorphic transformations, variation of the properties of the surface, generation of defects, increases of reactivity, induction of chemical reactions, etc. [14]. Mechanical grinding has been applied in phyllosilicates, for example some studies have been carried out on kaolinite, pyrophyllite and some smectites, finding that grinding originates first a disordered phase of the mineral and later a more amorphous phase giving a structural destruction of the same, resulting in an exfoliation of the clay layers [15, 16]. It has also been successfully applied to carbon materials either to modify the morphology of carbon nanotubes or to introduce functional groups, which allow an improvement in dispersion and compatibility with the polymer matrix.

Another way is to carry out a premixing of the nanoparticles with the polymer using by calendaring. This method has been used in the exfoliation and dispersion of montmorillonite in a DEGBA epoxy resin [17], as well as in dispersion of multiple-wall carbon nanotubes in an epoxy resin [18]. In both cases, a better dispersion of the nanoparticles in the polymer matrix was observed.

Mechanical agitation is a common technique for the dispersion of nanoparticles in liquid systems; however, after a while, the nanoparticles tend to agglomerate. To improve the efficiency of dispersion and exfoliation, the ultrasound waves have been applied to stir particles, taking as the separation of individualized nanoparticles results. Ultrasonication is an effective method to disperse CNT in liquids that have a low viscosity, such as water, acetone, and ethanol. In this stage of application of ultrasound, some power factors must be taken care of, for example, because in the case of nanotubes, it has been seen that ultrasound waves can induce defects such as the formation of amorphous carbon in the CNT [19]; recommendations have been made as a sonication of the low power bath to preserve the length and structure of the CNT [20].

After applying these methods to modify the nanoparticles aiming to improve their dispersion in the polymer, it is necessary to consider the conditions of the extrusion process where these nanoparticles are incorporated, since it can be in different modalities or extrusion conditions in order to avoid reagglomerations or degradations of the polymer.

2.3. Manufacture of nanocomposites

In general, the most used mixing methods for the preparation of nanocomposites are in-situ polymerization, solution, and melt mixing. In the in-situ polymerization method, the nanoparticles are first dispersed in the liquid monomer (or a monomer solution), and from there, they are mixed to carry out the polymerization, which can be initiated by heat or by the diffusion of an initiator. In the solution method, the polymer is dissolved in a solvent, and the filler is dispersed in the same solution. The intercalated nanocomposite is obtained by removing the solvent by vaporization or precipitation [21]. Because both processes use a solvent, it is not practical at the industrial level. The melt mixing method takes advantage of the melt temperature of the polymer matrix, and in this way, it achieves the mixing with the nanoparticles. Within this method, one of the most striking is the melt extrusion process [22].

Melt extrusion is a continuous process that consists of passing a material in the molten state through a profile or given geometry. The preparation of a large variety of polymeric nanocomposites has been reported through this process from varying the polymer matrix to modifying the geometry and size of the nanoparticles to be used. It has been observed that the size and dispersion of the nanoparticles in the polymer are related to the improvement in the properties of the final nanocomposite. A great challenge in the preparation of polymeric nanocomposites is to achieve the homogeneous dispersion of the nanoparticles in the polymer matrix, knowing that a complete dispersion of the nanoparticles allows a greater matrix-nanoparticle interaction responsible for the improved properties in the final material [23].

2.3.1. Melt extrusion

In a broad definition, the extrusion process refers to any transformation operation in which a molten material is forced to traverse a nozzle to produce an article of constant cross section and in principle of indefinite length [24]. From the point of view of plastics, melt extrusion is clearly one of the most important processes of transformation, where the polymer is fed

http://dx.doi.org/10.5772/intechopen.80216

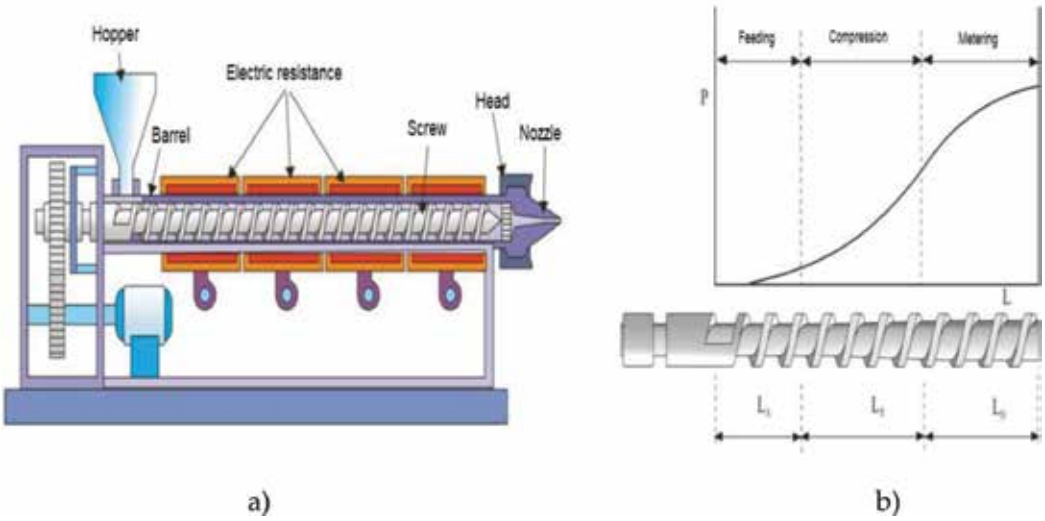

Figure 1. (a) Basic diagram of an extruder, (b) evolution of the pressure along an extruder [25].

in solid form; it is heated until reaching the molten state and leaves the extruder in the latest state. In this case, the extruder acts as a pump, providing the necessary pressure to pass the polymer through the nozzle.

An extruder must have a system for feeding the material, a system for melting-plasticizing it, a pumping and pressurizing system (which usually generates a mixing effect), and finally, a device for forming the molten material. **Figure 1a** shows a basic scheme of an extruder [25]. Depending on the pressure that is exerted along the barrel or extrusion barrel, three main zones can be identified as indicated in **Figure 1b**. The feeding zone is the closest to the feeding of the material, where it is gradually compacted at a certain speed. The transition zone is a zone of intermediate compression of the material where the fusion takes place, in addition to which the air that could be trapped in the same escapes by means of the feed hopper. Finally, there is the dosing zone, in which the molten material is homogenized and pressurized to exit the extruder by means of the forming nozzle [26].

2.3.2. Screw configuration

One of the most important parts in this process is the screw and the barrel, since they contribute to carry out the functions of transporting, heating, melting, and mixing the material. For this reason, the stability of the process and the quality of the final product depend to a great extent on the screw design. The screw consists of a long cylinder surrounded by a helical fillet (**Figure 2**). The most important parameters to design it are: the length (L), diameter (D), the angle of the propeller (θ), and the thread pitch (w). When only one screw is used, the machine is called single-screw extruder, while when two screws are used, the term double-screw or twin-screw extruder is used. The mixing is highly dependent on the number of screws and its configuration. In the case of twin-screw extruders, the screws can co-rotate or counter-rotate

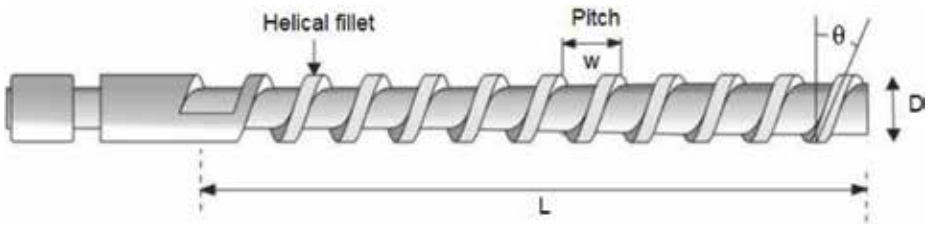

Figure 2. Screw of an extruder [25].

and have different degrees of interpenetration. In **Figure 3**, some possible variants are shown. The advantages of its use include a good mixing and degassing capacity, as well as good control of the residence time and its distribution. Some disadvantages of these extruders are their price superior to that of the single screw and the fact that their performance is difficult to predict.

It is important to mention that the selection of a twin-screw extruder to a single-screw extruder depends mainly on the efficient transport as a function of the friction of the material with the barrel and the extrusion screw. In a single screw-extruder, a high level of friction material/barrel and a low level in the screw provide a high carry per revolution. On the other hand, a poor carry per revolution will result in a low level of friction in the barrel and a high level in the screw. In addition, the amount of friction between the metal of the barrel or the screw and the performance of the extruder can change caused by a decrease in temperature. These troubles are minimized in a twin-screw extruder, where the interlock between the screws forms very close chambers, carrying the material forward [27].

2.3.3. Screw configuration modification

One aspect of great relevance is the definitive choice of the number and geometric design of the areas of the screw; this decision depends not only on the design of the nozzle and the expected flow rates but also on the melting characteristics of the polymer, its rheological behavior, and the speed of the screw. A simple screw, of three zones, is usually defined according to the number of turns of the propeller in the areas of feeding, compression, and dosing. An example of different screw configurations is shown in **Figure 4**.

2.3.4. Mixing lines

Most plastics need a previous stage of mixing before processing. Sometimes, it requires only extensive mixing, where the components of the formulation are mixed superficially and is made in fast mixers, and in other, intensive mixing of the different components of the formulation is necessary and is usually carried out in extruders. In some cases, both are necessary, extensive mixing prior to intensive. The use of twine-screw extruders is common in mixing lines. The configuration of the line is determined, among other things, by the type of additives to be combined in the extrusion. These lines usually have pelletizers at the extruder exit to obtain the material in pellet form. When additives or abrasive fillers have to be mixed with

http://dx.doi.org/10.5772/intechopen.80216

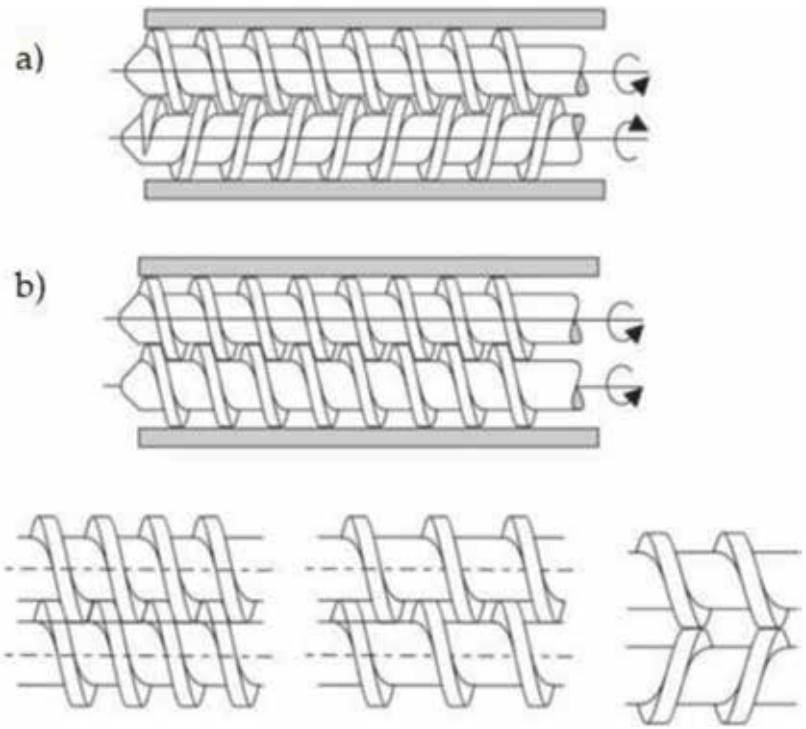

Figure 3. Possible arrangement of the spindles in the twin screw extruders; (a) rotation against rotary and (b) rotary rotation; different degrees of interpenetration of the screws [25].

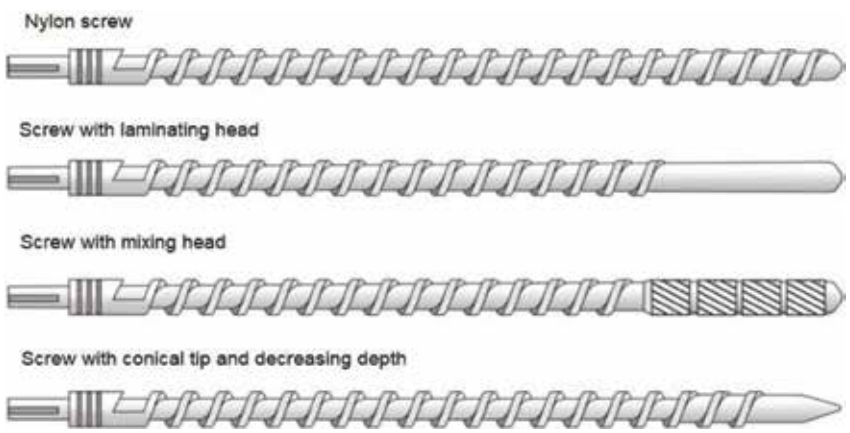

Figure 4. Examples of different types of screw [25].

the polymer, the polymer is usually added in the first feed hopper, and the filler is added once the plastic has melted, thereby reducing wear of the extruder caused by the filling. With large amounts of filler, the melt often has a large amount of air, steam, or gases, and so the extruder must have a vent zone (**Figure 5**).

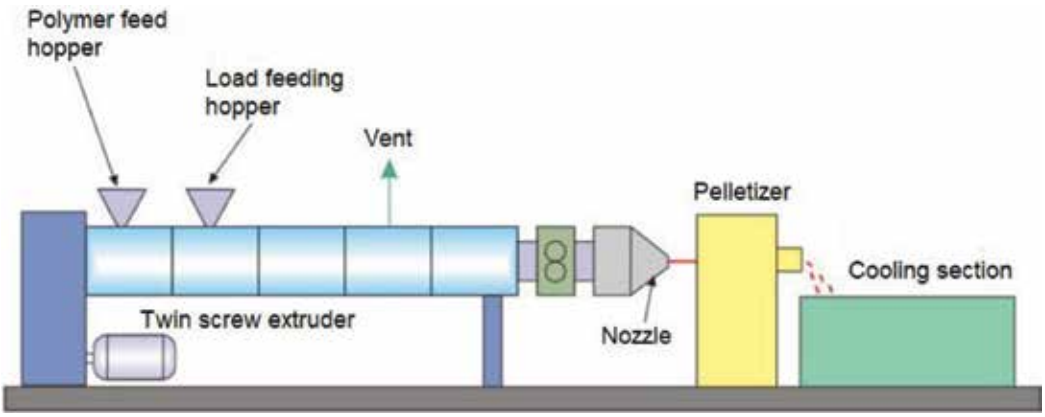

Figure 5. Typical mixing line [25].

The characteristics of the melt extrusion process both in the selection and configuration of the screw type, as well as the feeding of the materials, affect the pre-dispersion of the nanoparticles, since a homogeneous predispersion will improve the dispersion efficiency when using ultrasound.

3. Ultrasound-assisted extrusion applied to the manufacture of polymeric nanocomposites

In the last decade, the application of ultrasound waves for the preparation of polymer nanocomposites by melt extrusion has shown a growing interest. It seems that the scientific interest is ten times larger than the industrial interest, since only 3 patents have been registered in comparison to 36 published articles, as can be seen in **Figure 6**. This gives us a perspective of the relevance that this technology has had in recent years. Several studies report the preparation of polymer nanocomposites by means of ultrasound-assisted extrusion, resulting in the break nanoparticle agglomerates as nanoclays, as well as improvements in the dispersion of nanoparticles in a polyamide 6 [28]. Another study reported an improvement in both rheological and mechanical properties after the ultrasonic treatment, where it is also shown that this change in properties is attributed to the decrease in the size of the clay agglomerates in HDPE [29].

Other authors argue that the application of ultrasound to extrusion has to be carried out in stages to favor the dispersion of the nanoparticles, as in the case of carbon nanotubes (CNT), where it has been found that the dispersion of CNT can be favored when using two stages of processing. The first is the preparation of a masterbach (concentrate method), which is then diluted in the polymer to increase the dispersion of CNT. It is generally accepted that the dispersion is improved due to the high voltage of cutting that acts on the agglomerates during the second stage [30]. The combination of the masterbach technique with assisted ultrasound has been an important improvement for the dispersion of nanoparticles in polymeric matrices, mainly tested in polymer-CNT systems [31]; in turn, it has also been shown that ultrasound can favor the hybridization of polymer chains on the nanoparticles [32].

http://dx.doi.org/10.5772/intechopen.80216

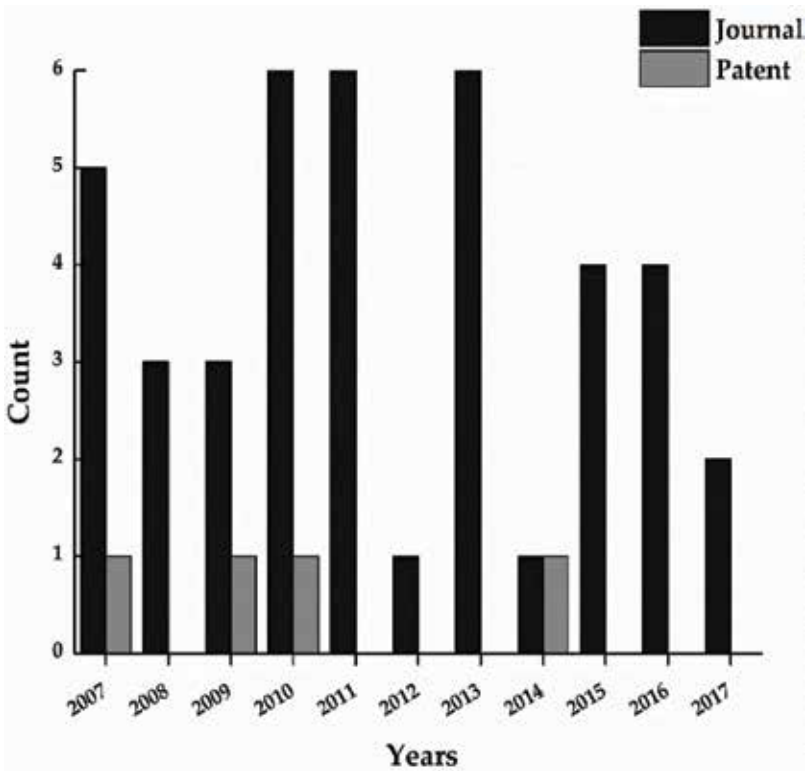

Figure 6. Production of articles and patents on ultrasound-assisted extrusion for the preparation of polymeric nanocomposites (last 10 years).

3.1. Fundamentals of ultrasound applied to the manufacture of nanocomposites

Before delving into the subject, it is necessary to mention that sound is a mechanical wave that needs a medium for its propagation. This medium can be liquid, solid, or gas. The propagation of the sound according to the medium can be transverse and longitudinal, and this will depend on the direction in which the energy travels. The frequency of audible sound for humans is between 20 Hz and 20 kHz. That inaudible sound with values of frequencies above 20 kHz is known as ultrasound. The ultrasound of low power or high frequency corresponds to the sound of low amplitude (higher frequency) and is related to the physical effect of the medium on the wave and is in a range of 2–10 MHz; these frequencies are widely used in the medical area for obtaining images and chemical analysis. On the other hand, ultrasound of high power (low frequency), between 20 and 100 kHz, is used for cleaning, plastic welding, as well as for the area of sonochemistry, which with the development of high-performance equipment power, can reach frequencies up to 2 MHz [33].

Chemical and physical effects of ultrasound in liquid systems are typically explained in terms of acoustic cavitation. The definition of cavitation is complicated. In some cases, acoustic cavitation is defined as an isothermal transition of the liquid-vapor phase limit in a fluid due to a decrease in pressure, as a response to the change below of the vapor pressure of the liquid, or when the temperature has risen above the boiling point [34]. In both cases, acoustic cavitation

is presented as a response to the decrease in pressure due to the propagation of an acoustic wave. In other words, during the expansion and compression characteristic of ultrasound waves, there is a formation, growth, and the implosive collapse of bubbles. But how is this bubble formed? The nucleus theory states that any liquid contains intrinsically tiny spaces (cavitation nuclei) full of gases, which undergo a change of pressure to quickly grow to cavities and then to bubbles. However, this principle has evolved, and it is accepted that a nucleus is needed that originates cavitation. The formation of this core can occur in two ways: for pure homogeneous liquid that does not contain impurities or gas, cavities will form due to the effect that the acoustic pressure will have on the liquid called homogeneous nucleation. In real systems or practical experiments, it is thought that a heterogeneous nucleation occurs, in which the neighboring liquid molecules are broken because the liquid contains "weak sites," in the limits of the liquid and a solid or in the liquid-solid-gas interfaces, where cavitation can start more easily [35]. These cavitation cores generate bubbles that expand during the phase of rarefaction and collapse during the compression phase; stable and transient bubbles are formed [36]. Stable bubbles can remain oscillating during many cycles of acoustic pressure. On the other hand, transients generally exist for less than one cycle; during this cycle, they expand at least twice their original size and then collapse violently. It is said that the pressure and temperature inside the bubble increase to more than 1000 atm and 5000 K [37] during cavitation (**Figure 7**). The collapse of the bubble is a violent process which generates localized shock waves, which results in an effect on the liquid or solid.

3.2. Preparation of nanocomposites by means of ultrasound-assisted extrusion

The incorporation of ultrasound in melt processing methods requires, in its simplest form of a processing system or equipment, a sonotrode, and an ultrasonic wave generator. At present,

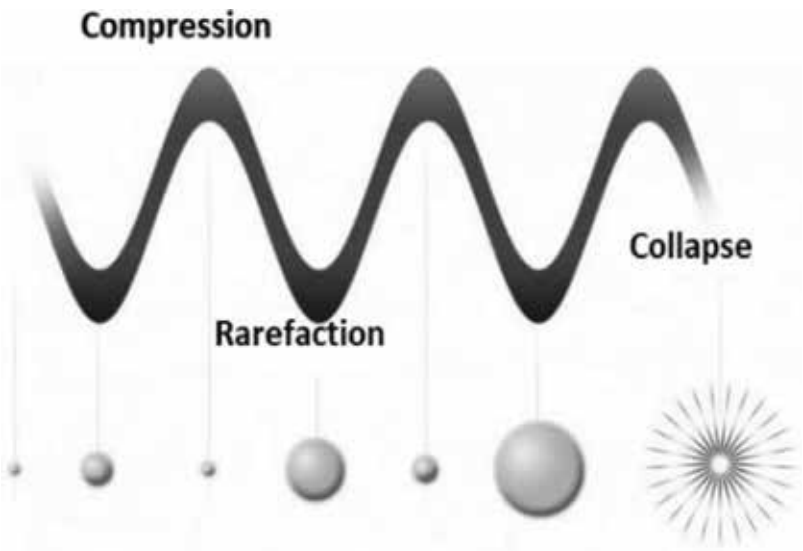

Figure 7. Acoustic cavitation phenomenon in Newtonian fluid.

double or single screw extruders with different arrangements in their mixing zones are used, at speeds ranging from 50 to 100 rpm, in order to improve the efficiency in the dispersion of nanoparticles, while temperature profiles vary according to the polymer-nanoparticle system. As for the treatment with ultrasound, a specially designed camera to contain a sonotrode is attached to the extruder, which in general according to the literature is usually made of titanium. This chamber has a controlled temperature and a nozzle to extract the molten nanocomposite. The sonotrode is connected to an ultrasonic generator, which operates at frequency intervals that can range from 10 to 100 kHz and with powers that can reach 1000 W. The data obtained are usually collected by means of an oscilloscope. **Figure 8** shows a system developed by Ávila-Orta et al. [38].

3.2.1. Technical characteristics of the design of the process of ultrasound-assisted extrusion

Ultrasound has been applied to molten polymers as a very efficient way to reduce the resistance of the shaping channels by decreasing the viscosity of the polymers. The results showed that the application of ultrasound disturbs the convergent flow of molten polymer in the entrance zone and changes the flow patterns, which leads to lower elastic stresses, increasing the movement of the molecular chains, so that the elastic recovery is faster. Guo et al. [39] demonstrated significant changes in the properties of polymeric materials by applying ultrasound during the extrusion process and applying ultrasonic oscillations in the direction parallel to the polymer melt flow (**Figure 9**). Scientists at the University of Akron have applied longitudinal vibrations in the direction perpendicular to the direction of flow using two sonotrodes symmetrically in the nozzle during the extrusion double screw of polymer nanocomposites containing carbon nanotubes and polypropylene clays (Isayev et al. [30]; **Figure 10**). In addition to dispersing nanocomposites, the application of ultrasound to the polymer has resulted in an increase in crystallinity, the reduction of structural defects, and the improvement of mechanical properties.

Ultrasound in the extrusion process has been used to improve the compatibility and dispersion of additives. The effects of ultrasound on polymers can be both physical and chemical.

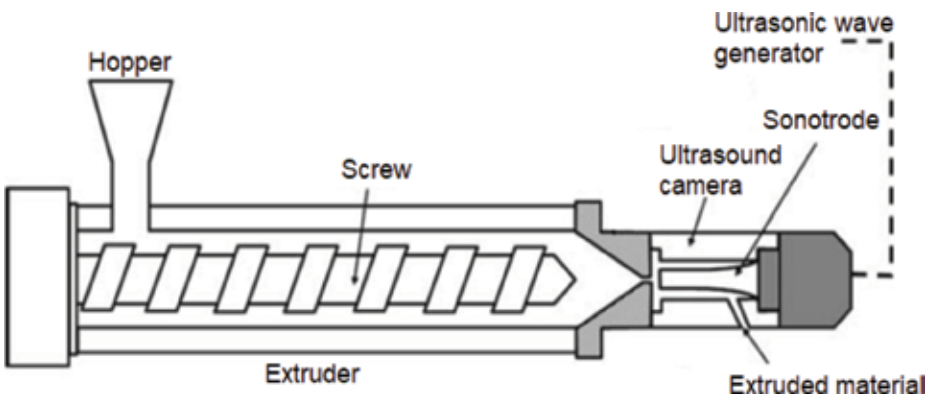

Figure 8. Typical configuration of an extruder coupled with an ultrasound device.

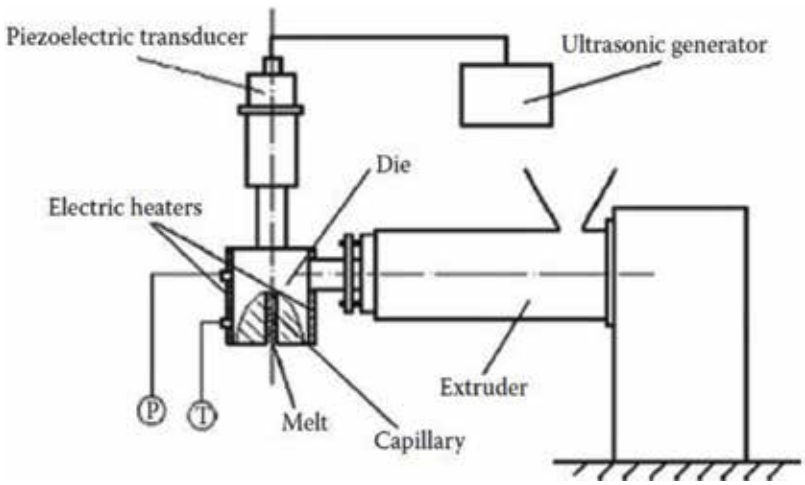

Figure 9. Schematic diagram of the ultrasonic irradiation extrusion system used by Guo et al. [39].

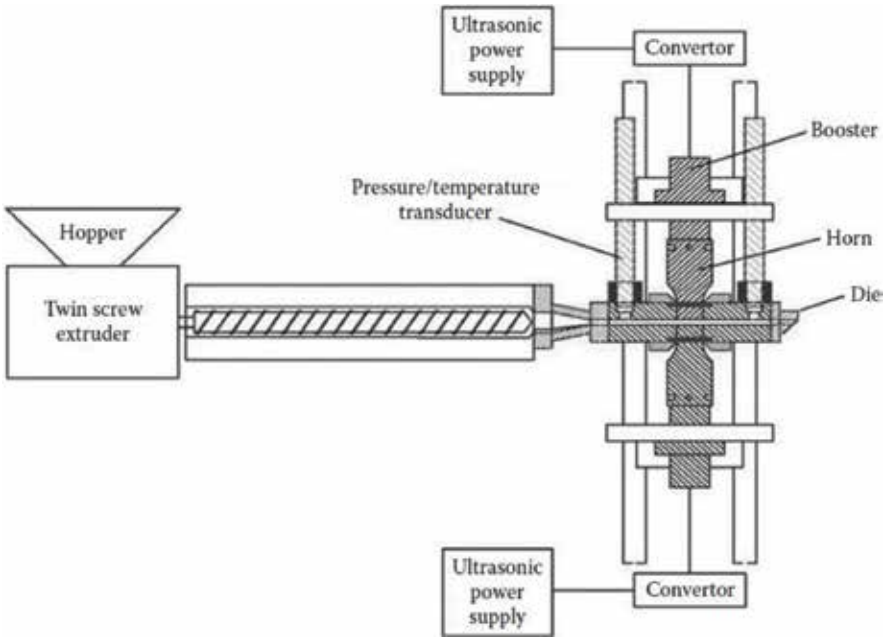

Figure 10. Schematic diagram of the ultrasonic irradiation extrusion system used by scientists at the University of Akron, Isayev et al. [30].

Some physical changes induced by ultrasound in polymer systems are the dispersion of loads and other base components. Several systems have been developed, where good results of nanoparticle dispersion are obtained. Different ways of feeding and positions of the ultrasound along the zones of the extruder have been tested, aiming to find out the behavior of the nanoparticles in the matrix depending on the type of configuration. Some configurations of ultrasound-assisted extrusion of equipment that have been patented are

http://dx.doi.org/10.5772/intechopen.80216

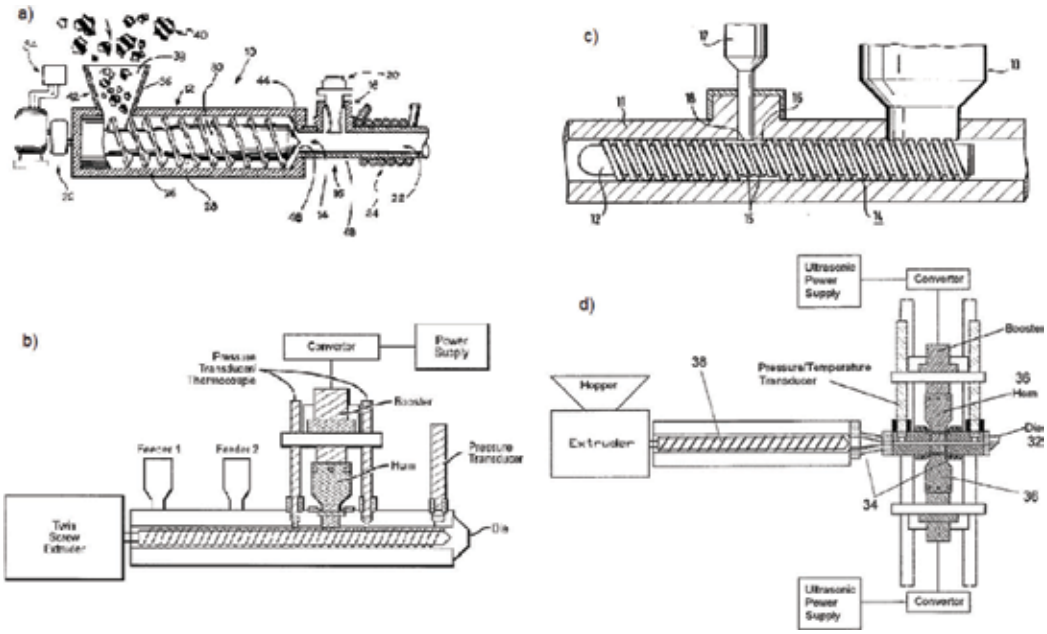

Figure 11. Some configurations of the process of extrusion assisted by ultrasound in molten polymers. (a) [40], (d) [41] ultrasound equipment placed at the exit of the extruder. (b) [42], (c) [43] ultrasound chamber along the extrusion equipment.

shown in **Figure 11**. It is important to mention that within the aspects that modify the dispersion of the nanoparticles is the intensity of the applied ultrasound, where it has been demonstrated that the power of the ultrasound is a function of the reduction in the size of the agglomerates of nanoparticles, which favors the dispersion. It has also been found that a good exfoliation and dispersion are improved at low extrusion rates in order to increase the time of the ultrasonic treatment [44]. However, high exposure times to ultrasonic vibrations produce a degradation of the polymeric material, that is, there is a breakdown of the polymer chains, as demonstrated by means of rheological studies.

3.2.2. Characteristics and final properties of NCPs produced by ultrasound-assisted extrusion

In the last two decades, the effect of ultrasound in the preparation of nanocomposites has been studied. In 2003, Isayev and Hong employed for the first time the ultrasonic vibration to prepare nanocomposites. This study reported that the application of ultrasound improves the dispersion and reduced size of silica agglomerate (0.3 μm). The viscosity of the ultrasonically treated mixtures was found to be higher than that of the silane-treated mixtures.

Table 1 summarizes information from publications involving the use of the ultrasonic treatment technology for the preparation of polymer nanocomposites. The information shows the polymer matrix studied, the nanoparticles, the focus of the study, and improved properties. It is evident that the most studied structures using ultrasound are clays and those based on carbon such as graphene and nanotubes.

Polymer nanocomposite		Focus of the study	Property improvement(s)	Reference
Carbon nanoparticles	MWCNT	Effect of ultrasound on thermal, electrical, mechanical and rheological properties.	Improvement electrical and thermal conductivity, Young's modulus. Storage modulus and complex viscosity generally increased.	[30, 45–54]
	CNF	Effects of the variation of the ultrasonic amplitude and concentration on CNFs (morphology), rheology, electrical resistivity, abrasion and mechanical properties.	Improved dispersion, elongation at break, Young's modulus and tensile strength. The abrasion resistance was improved at certain amplitudes at low CNT loadings only.	[55, 56]
	GNP	Effects of the ultrasound vibration on exfoliation, and dispersion of GNP's in the polymer matrix.	Increased the exfoliation and dispersion of GNPs on the polymer. Thermal and conductivity properties were increased.	[47]
Ceramic nanoparticles	Cloisite 20A	Effects of ultrasound on clay dispersion, morphology, mechanical and rheological properties.	Improved clay dispersion compared with non-treated ones, intercalated-exfoliated structures was found. Young's modulus enhanced and increase viscosity in most studies.	[57–60]
	Sepiolite	Effect of ultrasound on dispersion and mechanical properties of polymer matrix	Improves nanoclay dispersion, which results in an enhancement of the reinforcement of the fillers and decreases the viscosity of the composites during the process.	[61]
	Nanosilica	Effects of ultrasound on the morphology, as well as the rheological and mechanical properties of the composites	Improve strength and elongation of the composites at break, ultrasound-induced homogeneous dispersion of nanoparticles in the polymeric matrix	[62]
Other nanoparticles	Flash aluminum flake pigments (FAFP)	Effects of the ultrasound intensity, experimental temperature, filler content, and particle size on the composite viscosity	Composite viscosity decreased as the ultrasound intensity and the filler content decreased.	[63]

Table 1. Summary of the experimental results of some reviewed publications involving the application of extrusion assisted by ultrasound for preparation of polymer nanocomposites, last 10 years.

Regarding the use of ultrasound in the preparation of nanocomposites with clay, improvements in degree of clay dispersion have been found. Kim and co-workers made use of the ultrasonic-assisted continuous extrusion process to the preparation of polypropylene (PP) and polystyrene (PS) nanocomposites with 3% loading of organophilic montmorillonite clay.

They found that the waves of ultrasound improve the compatibility between PP and PS and breakup of the clay agglomerates and as a result exfoliated the clay layers in the PP/PS matrix [64]. Similar observations were made for PP/clay nanocomposites. Two methods for the fabrication of polypropylene/clay nanocomposites are compared. In the first approach, a two-stage process was implemented. First, the nanocomposites were prepared using a co-rotating twin-screw extruder followed by a single-screw extruder, in which the ultrasound was implemented. In the second method, a single-stage process was used. In addition, two regimens of feeding were used in the process. In both processes, it was observed that the ultrasound generates a degradation of the polymer matrix and intercalation/exfoliation of clay; however, the single-stage process led to a minor polymer degradation [65]. Li et al. [28] prepared polyamide 6/montmorillonite nanocomposites by using a conventional and an ultrasonic extrusion technology. The results showed that the elongation at break and impact strength of the ultrasonicated nanocomposites increase due to the improved dispersion of montmorillonite and decreased size of spherulites [28]. Other works have focused on the preparation of clay nanocomposites with different polymer matrix as a HDPE and LLDPE. For example, Niknezhad and Isayev [59] applied ultrasound continuous method for the production of films polymer/clay nanocomposites. In this process, compounding, ultrasonic treatment, and film casting were combined in a single-step process. It has been found that the effect of the dispersion of the clay depends on the amplitude of ultrasound used, affecting the crystallinity and the mechanical properties of the material, as well as the permeability to gases [59]. On the other hand, the application of ultrasound irradiation and maleic anhydride (MA) addition, during the preparation of PP/Clay nanocomposites in a twin screw extruder, showed to have a very significant effect on the simultaneous grafting of MA onto the PP chains and in the exfoliation/dispersion of the clay. The tensile modulus increased with ultrasound intensity, and an opposite effect occurs with elongation, which decreases with the applied ultrasound [58].

As for carbon-based nanocomposites, polyetherimide (PEI) systems with 20% carbon nanofibers (CNF) have been studied. It was established that ultrasound with high power is effective in obtaining relatively more homogeneous dispersion with improved electrical and thermal conductivity in the CNF/PEI nanocomposites in comparison with extruded untreated ones. An increase in Young's modulus was observed while retaining tensile strength up to 15% of CNF [54]. In another study, it was mentioned that the effect of ultrasound on the rheological, electrical, morphological, and mechanical properties of the Polyetherimide (PEI) matrix with multiple-wall carbon nanotubes (MWCNT) has been carried out from 1 to 10% by weight. In ultrasound-treated nanocomposites, an increase in viscosity and storage module was observed. As for the mechanical properties, the authors conclude that there is a relationship between the content of MWCNT and the application of ultrasound because the Young module and the resistance showed an increase by using 5 and 10% load. The authors also notice that working amplitudes are important factor to improve the dispersion. Rheological and electrical percolations were found between 1 and 2% in load weight of MWCNT. The observed effect is attributed to the fact that the ultrasound breaks the agglomerates of MWCNT improving its dispersion, which affects to a greater degree the rheology of the material than to the electrical conductivity [30]. Blanco et al. [53] mention that ultrasonic vibration has a significant effect on the conductivity of PA/MWCNT systems; in these nanocomposites, the percolation rate is reduced from 7 to 3 wt% when ultrasound is applied. This is attributed to a better

dispersion of nanotubes in the matrix, resulting in an increase of three orders of magnitude in the electrical resistivity for the system PA6/MWCNT at 7 wt%. These authors concluded that the application of ultrasound improves the processability of the material and that it is possible to reduce the percentage of nanotubes in the preparation of nanocomposites with conductive properties without affecting thermal properties [53]. Ávila-Orta et al. [51] used polypropylenes with different flow rates (MFI) and 10% multiwall carbon nanotubes for the preparation of nanocomposites. Four different fabrication methods based on melt extrusion were used. In the first method, melt extrusion fabrication without ultrasound assistance was used. In the second and third methods, an ultrasound probe attached to a hot chamber located at the exit of the die was used to subject the sample to fixed frequency and variable frequency, respectively. In the fourth method, the carbon nanotubes were treated in a fluidized air-bed with an ultrasound probe before being used in the fabrication of nanocomposites. It was found that the MFI decreases regardless of the method used in processing, the same is not the case with the other properties. For example, as to the size of agglomerates, the smallest value was found using PP of MFI = 2.5 using variable ultrasound frequency in processing; in this sample, it was found a lower surface/agglomerate ratio and a higher value of electrical charge (1040 V) [51]. A similar study showed that the electrical properties in nanocomposites of PP/MWCNT with different values of MFI of the polymer matrix depend on the methods used in the ultrasound-assisted extrusion because the ultrasound waves decrease the agglomerates of nanotubes producing conductive materials and static dissipators with a negative dielectric constant [66].

In summary, the application of ultrasound in the preparation of nanocomposites by extrusion generates an increase in some properties of great importance. However, the mechanisms by which ultrasound helps in the dispersion of nanoparticles is not known with precision, which is a significant aspect and would help to improve and create innovative methodologies aimed at the implementation of more specific nanocomposites.

3.3. Models of the mechanism of dispersion of NPs in ultrasound-assisted extrusion

The effect of ultrasound on fluids and Newtonian systems has been explained in terms of acoustic cavitation. This process, as mentioned above, involves at least three stages: nucleation, bubble growth, and the implosive collapse of the same, propitiating stable and transient acoustic cavitation events that are the cause of the effect of ultrasound. However, these physical or chemical effects will not be presented if ultrasound-led energy is less than the cavitation threshold [67]. In non-Newtonian fluids, the bubble in polymer solution implodes less violently compared to a Newtonian fluid such as water (**Figure 12**), which makes the impact of the liquid jet on the limit very small or even null. In particular, the dynamics of the collapse of bubbles near a solid boundary appears to be a critical problem in the dispersion of nanostructures in liquid systems, since the impact of the liquid jet on the surface of the agglomerates is considered mechanism dominant for the reduction of agglomerate size during acoustic cavitation [68].

If a solid is within the sample, the cavitation is given in a different way, due to the liquid–solid interface. An accepted explanation is that the cavitation that takes place near the solid

http://dx.doi.org/10.5772/intechopen.80216

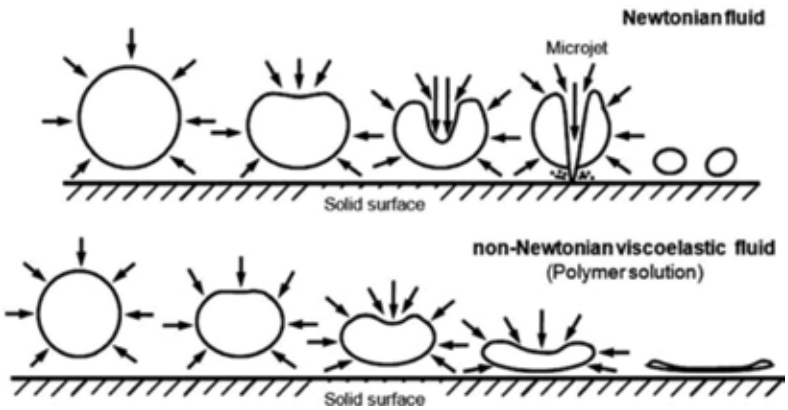

Figure 12. Comparison between the dynamics of the induced ultrasound of a Newtonian fluid and a non-Newtonian.

surface will generate microjets of fluid of high velocity, directed toward the solid surface. The impact of microjets of fluid on the solid surface causes localized erosion. In addition to this effect, we have the formation of shock waves, inducing effects such as breaking aggregates of particles [69].

Researchers have tried to explain the phenomenon of the dispersion of nanoparticles in polymeric matrices when using ultrasound in molten state. In this context, Zhong et al. argue that the propagation of the ultrasonic wave in a material generates waves of oscillatory pressure and induces the expansion and contraction of bubbles in the polymeric matrix that leads to a possible rupture of the agglomerates of nanoparticles, which would give place to a better dispersion. A small amount of bubbles usually dissolves or is trapped in the polymer that melts during extrusion [70]. In polymeric compounds, the particles are easily present in the form of porous agglomerates that introduce more gaps in the system. The existence of bubbles in the nanocomposites decreases the speed of the ultrasound and therefore the energy consumption. Based on experimental observation, a possible cavitation mechanism is suggested, depicted in **Figure 13**. The cavitation of bubbles in compounds can occur by internal and external cavitation mechanisms. The cavitation of the outer bubble could remove the particles from the primary agglomerates (**Figure 13a**), while the cavitation of the inner bubble would break the agglomerates from the inside (**Figure 13b**). One or both of these mechanisms would lead to better dispersion seen after ultrasonic treatment [71].

Espinoza-González proposed [72] a mechanism based on mechanochemistry to explain the physical and chemical effects of ultrasound in polymer matrices, as well as for the dispersion mechanism of nanostructures. This mechanochemical mechanism is mainly based on the deformation or stress experienced by the chemical bonds during the vibration movement. The generated vibration movement causes the appearance of different fatigue points along the polymer chain called nodes, in which the greatest deformation occurs between the links of the chain, reducing the energy of link dissociation leading to the activation of multiple reaction mechanisms, degradation, or chain extension.

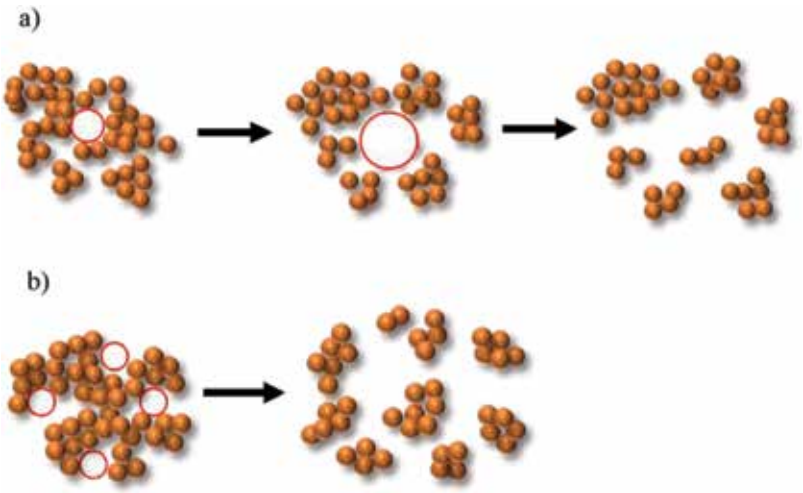

Figure 13. Phenomenon of internal acoustic cavitation (a) and external (b) in polymeric nanocomposites according to Zhong et al. [71].

3.4. Relevant aspects to consider in the dispersion mechanisms of NPs by ultrasound-assisted extrusion

Ultrasound-assisted extrusion process turns out to be a very promising technology and that in the last 10 years has shown great advances in its application to the elaboration of polymeric nanocomposites. However, the mechanism to achieve the deagglomeration of nanoparticles and their dispersion in the polymer remains unknown. The phenomenon of acoustic cavitation is mainly proposed for the explanation of bubble dynamics, but it is possible to find in the literature and as mentioned above that the strict notion of cavitation is an isothermal transition of the liquid–vapor phase limit in a fluid of a single component, due to a decrease in pressure [34, 35, 73]. In other words, the cohesion between the fluid particles is overcomed by an externally applied stress, which causes the homogeneous nucleation of the vapor. Based on this argument and answering the initial question of the text on the phenomenon by which the dispersion of nanoparticles in polymeric systems results, the phenomenon of acoustic cavitation is questionable, since it is not enough to be able to explain the dispersion of nanoparticles during the ultrasound-assisted extrusion process to produce nanocomposites, since there is no phase change and also due to the viscoelastic characteristics of the polymer matrices that imply higher cutting efforts, which would hinder the formation of bubbles. However, it has been proven that in polymeric solutions, there is poor bubble formation due to cavitation effects [74]. On the other hand, there is also the idea that ultrasound causes vibrational effects on the polymer related to relaxation times at the chain level [75], which could help explain that the effects of friction in the polymer are the main causes of the dispersion of nanoparticles in the formation of nanocomposites.

A number of researches are still necessary to understand the effects of the different parameters (power, amplitude, and working frequencies) of the ultrasound waves in the preparation of nanocomposites, as well as the mechanism of action. To understand the nature of a

system as robust as ultrasound-assisted extrusion, it is necessary to simplify the system, so that the dispersion phenomenon can be analyzed from the simplest possible perspective. For example, studies can be carried out in batch systems of polymer melts and nanoparticles.

4. Conclusions

In the last decade, the use of the ultrasonic assisted extrusion process has been used in the preparation of polymeric nanocomposites. This process has shown improvements in the dispersion of nanoparticles in the polymer matrix, which has led academics to make improvements in the design to achieve a greater effect on the properties of the final compound. Although the technique of ultrasound is known, it has not been possible to clearly explain the mechanisms of its action in polymer-nanoparticle systems, where despite the efforts made to achieve an adequate understanding of how the dispersion of nanoparticles occurs, it is still insufficient for the polymer nanocomposite theory to explain this phenomenon, and this limits the application of ultrasound in the manufacture of nanocomposites with specific properties. However, the large number of satisfactory results obtained in scientific articles on the novel properties and innovations that are made in patents on equipment and processing of nanocomposites provides a broad perspective of the evolution of this technology and its potential applications.

Acknowledgements

The authors acknowledge the financial support of CIQA through grant 6438 (2018), and of CONACyT through grants 294030 (LANIAUTO) and 296395 is greatly appreciated.

Conflict of interest

The authors declare no conflict of interest.

Author details

Carlos A. Ávila-Orta[1]*, Pablo González-Morones[1], Diana Agüero-Valdez[1], Alain González-Sánchez[1], Juan G. Martínez-Colunga[1], José M. Mata-Padilla[1] and Víctor J. Cruz-Delgado[2]

*Address all correspondence to: carlos.avila@ciqa.edu.mx

1 Centro de Investigación en Química Aplicada (CIQA), Saltillo, Coahuila, México

2 CONACYT—Unidad de Materiales, Centro de Investigación Científica de Yucatán (CICY), Mérida, Yucatán, México

References

[1] Battisti A, Skordos AA, Partridge IK. Percolation threshold of carbon nanotubes filled unsaturated polyesters. Composites Science and Technology. 2010;**70**(4):633-637

[2] Müller MT, Pötschke P, Voit B. Dispersion of carbon nanotubes into polyethylene by an additive assisted one-step melt mixing approach. Polymer. 2015;**66**:210-221

[3] Isayev A. US patent 5258413. 1993

[4] Isayev A. US patent 2003/124211 A1

[5] Vengatesan MR, Mittal V. Surface modification of nanomaterials for application in polymer nanocomposites: An overview. In: Surface Modification of Nanoparticle and Natural Fiber Fillers. Wiley-VCH Verlag GmbH & Co. KGaA; 2015. pp. 1-27

[6] Chandra A, Turng LS, Gopalan P, Rowell RM, Gong S. Study of utilizing thin polymer surface coating on the nanoparticles for melt compounding of polycarbonate/alumina nanocomposites and their optical properties. Composites Science and Technology. 2008; **68**(3-4):768-776

[7] Zhou CH, Keeling J. Fundamental and applied research on clay minerals: From climate and environment to nanotechnology. Applied Clay Science. 2013;**74**:3-9

[8] Olad A. Polymer/clay nanocomposites. In: Boreddy Reddy Dr, editor. Advances in Diverse Industrial Applications of Nanocomposites. InTech; 2011. ISBN: 978-953-307-202-9

[9] Caseri W. Nanocomposites of polymers and inorganic particles. In: Hybrid Materials: Synthesis, Characterization, and Applications. John Wiley and Sons; 2007. pp. 49-86

[10] Ma PC, Siddiqui NA, Marom G, Kim JK. Dispersion and functionalization of carbon nanotubes for polymer-based nanocomposites: A review. Composites Part A: Applied Science and Manufacturing. 2010;**41**(10):1345-1367. Available from: http://dx.doi.org/10.1016/j.compositesa.2010.07.003

[11] Ji L, Wu Y, Ma L, Yang X. Noncovalent functionalization of graphene with pyrene-terminated liquid crystalline polymer. Composites. Part A, Applied Science and Manufacturing. 2015;**72**:32-39

[12] Kango S, Kalia S, Celli A, Njuguna J, Habibi Y, Kumar R. Surface modification of inorganic nanoparticles for development of organic-inorganic nanocomposites—A review. Progress in Polymer Science. 2013;**38**:1232-1261

[13] Rozenberg BA, Tenne R. Polymer-assisted fabrication of nanoparticles and nanocomposites. Progress in Polymer Science. 2008;**33**:40-112

[14] Suryanarayana C, Ivanov E, Boldyrev VV. The science and technology of mechanical alloying. Materials Science and Engineering A. 2001;**304-306**(1-2):151-158

[15] Jiang X, Trunov MA, Schoenitz M, Dave RN, Dreizin EL. Mechanical alloying and reactive milling in a high energy planetary mill. Journal of Alloys and Compounds. 2009; **478**(1-2):246-251

[16] Palaniandy S, Azizi Mohd Azizli K, Hussin H, Fuad Saiyid Hashim S. Mechanochemistry of silica on jet milling. Journal of Materials Processing Technology. 2008;**205**(1-3):119-127

[17] Yasmin A, Abot JL, Daniel IM. Processing of clay/epoxy nanocomposites by shear mixing. Scripta Materialia. 2003;**49**(1 SPEC):81-86

[18] Thostenson ET, Chou TW. Processing-structure-multi-functional property relationship in carbon nanotube/epoxy composites. Carbon. 2006;**44**(14):3022-3029

[19] Korayem AH, Tourani N, Zakertabrizi M, Sabziparvar AM, Duan WH. A review of dispersion of nanoparticles in cementitious matrices: Nanoparticle geometry perspective. Construction and Building Materials. 2017;**153**:346-357. Available from: http://www.sciencedirect.com/science/article/pii/S0950061817313053

[20] Islam MF, Rojas E, Bergey DM, Johnson AT, Yodh AG. High weight fraction surfactant solubilization of single-wall carbon nanotubes in water. Nano Letters. 2003;**3**(2):269-273

[21] Kotal M, Bhowmick AK. Polymer nanocomposites from modified clays: Recent advances and challenges. Progress in Polymer Science. 2015;**51**:127-187

[22] Rauwendaal C. Polymer Extrusion: Fifth Edition. 2014. 1-934 p

[23] Peponi L, Puglia D, Torre L, Valentini L, Kenny JM. Processing of nanostructured polymers and advanced polymeric based nanocomposites. Materials Science & Engineering R: Reports. 2014;**85**:1-46

[24] Klein I, McKevley JM, King T. Plastics Extrusion Technology Handbook. 1989. p. 388

[25] Beltrán M, Marcilla A. In: Alicante U, San Vicente del Raspeig, Primera, editors. Tecnología de Polímeros. 2012. pp. 102-167. http://iq.ua.es/TPO/Tema4.pdf

[26] Wagner JR, Mount EM, Giles HF. Extrusion. Elsevier; 2014. 3-11 p. http://www.sciencedirect.com/science/article/pii/B9781437734812000016

[27] Lafleur PG, Vergnes B. Polymer Extrusion. Wiley Blackwell; 2014. 1-337 p. ISBN: 9781848216501

[28] Li J, Zhao L, Guo S. Ultrasound assisted development of structure and properties of polyamide 6/montmorillonite nanocomposites. Journal of Macromolecular Science, Part B Physics. 2007;**46**(3):423-439

[29] Swain SK, Isayev AI. Effect of ultrasound on HDPE/clay nanocomposites: Rheology, structure and properties. Polymer. 2007;**48**(1):281-289

[30] Isayev AI, Kumar R, Lewis TM. Ultrasound assisted twin screw extrusion of polymer-nanocomposites containing carbon nanotubes. Polymer. 2009;**50**(1):250-260. Available from: http://dx.doi.org/10.1016/j.polymer.2008.10.052

[31] Zhong J, Isayev AI, Huang K. Influence of ultrasonic treatment in PP/CNT composites using masterbatch dilution method. Polymer. 2014;**55**(7):1745-1755

[32] Ledezma Rodriguez R, Avila-Orta CA, González Morones P, España Sánchez BL, Rodriguez González JA, Hernandez Hernandez E, et al. MX/a/2013/015220. 2013

[33] Mason TJ, Lorimer JP. Applied Sonochemistry: The Uses of Power Ultrasound in Chemistry and Processing. 2002; 314 p

[34] Ashokkumar M, Cavalieri F, Chemat F, Okitsu K, Sambandam A, Yasui K, et al. Handbook of Ultrasonics and Sonochemistry. Singapore: Springer; 2016. 1-1487 p

[35] Brennen CE. Cavitation and Bubble Dynamics 2013. https://doi.org/10.1017/CBO9781107338760

[36] Neppiras EA. Acoustic cavitation. Physics Reports. 1980;**61**(3):159-251

[37] Pokhrel N, Vabbina PK, Pala N. Sonochemistry: Science and engineering. Ultrasonics Sonochemistry. 2016;**29**:104-128

[38] Ávila-Orta CA, Martinez-Colunga G, Bueno Baquéz D, Raudry López CE, Cruz-Delgado VJ, González-Morones P, et al. US patent 2012/98163 A1

[39] Guo S, Li Y, Chen G, Li H. Ultrasonic improvement of rheological and processing behaviour of LLDPE during extrusion. Polymer International. 2003;**52**(1):68-73

[40] Dinzburg B, Berdichevsky A. US patent 5955035. 1999

[41] Isayev A. US patent 2009/275689

[42] Hanan JC, Bandla S. US patent 2017/81482

[43] Wessling BM, Volk HK. US patent 4935164. 1990

[44] He S, Zhang J, Xiao X, Xinmi H. Effects of ultrasound vibration on the structure and properties of polypropylene/graphene nanoplatelets composites. Polymer Engineering & Science. 2017;**58**:377-386

[45] Mata-Padilla JM, Ávila-Orta CA, Medellín-Rodríguez FJ, Hernández-Hernández E, Jiménez-Barrera RM, Crúz-Delgado VJ, et al. Structural and morphological studies on the deformation behavior of polypropylene/multi-walled carbon nanotubes nanocomposites prepared through ultrasound-assisted melt extrusion process. Journal of Polymer Science Part B: Polymer Physics. 2015;**53**(7):475-491. https://doi.org/10.1002/polb.23655

[46] Quiñones-Jurado Z, Waldo-Mendoza M, Mata-Padilla J, González-Morones P, Martínez-Colunga J, Soriano-Corral F, et al. Transparent low electrostatic charge films based on carbon nanotubes and polypropylene. Homopolymer cast films. Polymers. 2018;**10**(1):55. Available from: http://www.mdpi.com/2073-4360/10/1/55

[47] He S, Zhang J, Xiao X, Hong X. Effects of ultrasound vibration on the structure and properties of polypropylene/graphene nanoplatelets composites. Polymer Engineering and Science. 2018;**58**(3):377-386

[48] Gao X, Isayev AI, Zhang X, Zhong J. Influence of processing parameters during ultrasound assisted extrusion on the properties of polycarbonate/carbon nanotubes composites. Composites Science and Technology. 2017;**144**:125-138

[49] Zhong J, Isayev AI. Ultrasonically assisted compounding of CNT with polypropylenes of different molecular weights. Polymer. 2016;**107**:130-146

[50] Espinoza-Gonzalez C, Avila-Orta C, Martinez-Colunga G, Lionetto F, Maffezzoli A. A measure of CNTs dispersion in polymers with branched molecular architectures by UDMA. IEEE Transactions on Nanotechnology. 2016;**15**(5):731-737

[51] Ávila-Orta CA, Quiñones-Jurado ZV, Waldo-Mendoza MA, Rivera-Paz EA, Cruz-Delgado VJ, Mata-Padilla JM, et al. Ultrasound-assist extrusion methods for the fabrication of polymer nanocomposites based on polypropylene/multi-wall carbon nanotubes. Materials. 2015;**8**(11):7900-7912

[52] Zhong J, Isayev AI. Properties of polyetherimide/graphite composites prepared using ultrasonic twin-screw extrusion. Journal of Applied Polymer Science. 2015;**132**(5). DOI: 10.1002/app.41397

[53] Blanco M, Sarasua JA, López M, Gonzalo O, Marcaide A, Muniesa M, et al. Ultrasound assisted extrusion of polyamide 6 nanocomposites based on carbon banotubes. In: Macromolecular Symposia. 2012. pp. 80-83

[54] Isayev AI, Jung C, Gunes K, Kumar R. Ultrasound assisted single screw extrusion process for dispersion of carbon nanofibers in polymers. International Polymer Processing. 2008; **23**(4):395-405

[55] Kumar R, Isayev AI. Thermotropic LCP/CNF nanocomposites prepared with aid of ultrasonic waves. Polymer. 2010;**51**(15):3503-3511

[56] Choi J, Isayev AI. Ultrasonic aided extrusion of CNT- and CNF-filled SBR compounds and properties of their vulcanizates. Rubber Chemistry and Technology. 2012;**85**(1):14-37

[57] Martínez-Colunga JG, Sánchez-Valdes S, Blanco-Cardenas A, Ramírez-Vargas E, Ramos-de Valle LF, Benavides-Cantu R, et al. Dispersion and exfoliation of nanoclays in itaconic acid funcionalized LDPE by ultrasound treatment. Journal of Applied Polymer Science. 2018;**135**(20). DOI: 10.1002/app.46260

[58] Martínez-Colunga JG, Sánchez-Valdés S, Ramos-Devalle LF, Muñoz-Jiménez L, Ramírez-Vargas E, Ibarra-Alonso MC, et al. Simultaneous polypropylene functionalization and nanoclay dispersion in PP/clay nanocomposites using ultrasound. Journal of Applied Polymer Science. 2014;**131**(16). DOI: 10.1002/app.40631

[59] Niknezhad S, Isayev AI. Online ultrasonic film casting of LLDPE and LLDPE/clay nanocomposites. Journal of Applied Polymer Science. 2013;**129**(1):263-275

[60] Lapshin S, Swain SK, Isayev AI. Ultrasound aided extrusion process for preparation of polyolefin-clay nanocomposites. Polymer Engineering and Science. 2008;**48**(8):1584-1591

[61] García L, Castell P, Peinado V, Muniesa M, Fernández Á. Improvement of mechanical properties of poly(lactic acid) by integration of sepiolite nanoclays: Effect of ultrasonication on clay dispersion. Materials Research Innovations. 2014;**18**(Sup 2):S2-85-S2-89

[62] Peng B, Wu H, Bao W, Guo S, Chen Y, Huang H, et al. Effects of ultrasound on the morphology and properties of propylene-based plastomer/nanosilica composites. Polymer Journal. 2011;**43**(1):91-96

[63] Hong X, Xiao X, Zhang Z, Zhang JJ. Effects of ultrasonic vibration on the rheological behavior of high-density polyethylene composites filled with flash aluminum flake pigments. Journal of Applied Polymer Science. 2017;**134**(23). DOI: 10.1002/app.44906

[64] Kim KY, Ju DU, Nam GJ, Lee JW. Ultrasonic effects on PP/PS/clay nanocomposites during continuous melt compounding process. In: Macromolecular Symposia. 2007. pp. 283-288

[65] Lapshin S, Isayev AI. Ultrasound-aided extrusion process for preparation of polypropylene-clay nanocomposites. Journal of Vinyl & Additive Technology. 2007;**13**(1):40-45

[66] Pérez-Medina JC, Waldo-Mendoza MA, Cruz-Delgado VJ, Quiñones-Jurado ZV, González-Morones P, Ziolo RF, et al. Metamaterial behavior of polymer nanocomposites based on polypropylene/multi-walled carbon nanotubes fabricated by means of ultrasound-assisted extrusion. Materials. 2016;**9**(11). DOI: 10.3390/ma9110923

[67] Sivakumar M, Muthupandian A. Cavitation—A Novel Energy-Efficient Technique for the Generation of Nanomaterials. 2014. 445 p. https://doi.org/10.4032/9789814463133

[68] Ávila-Orta C, Espinoza-González C, Martínez-Colunga G, Bueno-Baqués D, Maffezzoli A, Lionetto F. An overview of progress and current challenges in ultrasonic treatment of polymer melts. Advances in Polymer Technology. 2013;**32**. DOI: 10.1002/adv.21303

[69] Crawford AE. A practical introduction to ultrasonic cleaning. Ultrasonics. 1963;**1**(2):65-69

[70] Kanser AI, Meinecke EA. Porosity in rubber, a review. Rubber Chemistry and Technology. 1996;**69**:424-443

[71] Zhong J, Isayev AI, Zhang X. Ultrasonic twin screw compounding of polypropylene with carbon nanotubes, graphene nanoplates and carbon black. European Polymer Journal. 2016;**80**:16-39. Available from: http://dx.doi.org/10.1016/j.eurpolymj.2016.04.028

[72] Espinoza-González C. Mecanismo para los efectos del ultrasonido en matrices de polímeros en estado fundido y dispersión de nanoestructuras. Sistema modelo: Nylon y nanotubos de carbono [Thesis]. Saltillo, Coahuila México: Centro de Investigación en Química Aplicada; 2012

[73] Trevena DH. Cavitation and the generation of tension in liquids. Journal of Physics D: Applied Physics. 1984;**17**:2139-2164

[74] Brujan EA, Ikeda T, Matsumoto Y. Dynamics of ultrasound-induced cavitation bubbles in non-Newtonian liquids and near a rigid boundary. Physics of Fluids. 2004; **16**(7):2402-2410

[75] Li J, Liang M, Guo S, Lin Y. Studies on chain scission and extension of polyamide 6 melt in the presence of ultrasonic irradiation. Polymer Degradation and Stability. 2004; **86**(2):323-329

Chapter 10

Electrodeposited Zinc-Nickel Nanocomposite Coatings

Heidi Conrad and Teresa D. Golden

Additional information is available at the end of the chapter

http://dx.doi.org/10.5772/intechopen.80219

Abstract

Composite coatings can demonstrate improved property performance as compared to metals and alloy materials. One category of composite coatings is composed of metal or metal alloys with a dispersed phase of nonmetallic nanoparticles. The addition of these nanoparticles has been found to improve corrosion, wear resistance, and hardness. Producing metal composite coatings using electrochemical techniques can be advantageous due to reduced production cost, lower working temperatures, and precise control of experimental parameters. Metal coatings such as zinc have been successfully co-deposited with TiO_2, SiO_2, CeO_2 and mica particles and nickel has been co-deposited with a number of materials including TiO_2, SiC, Al_2O_3, PTFE and silicates. Zinc-nickel alloys have long been studied for a number of properties, most notably corrosion resistance and recently their tribological properties. This chapter reviews the literature on electrodeposition of ZnNi nanocomposite coatings. Although there has been much work done on composite coatings, there is much less literature available on composite coatings with zinc-nickel alloys. So in this review, we look at the general trends for nanoparticle incorporation, deposition mechanisms, system stability, microstructures of the coatings and general corrosion trends.

Keywords: electrodeposition, alloys, nanocomposites, corrosion, Zn-Ni alloys, metal matrix composites

1. Introduction

Metal matrix composite (MMC) coatings are promising materials developed by inclusion of a dispersed reinforcing material into a metal matrix. MMC's can replace traditional materials through their ability to offer improved mechanical and physical properties such as increased hardness, wear resistance, low thermal expansion coefficients, lubrication properties, antibacterial properties and improved corrosion resistance [1–11]. Nanosized particle incorporation

in metal matrixes forms a nanocrystalline structure, leading to improved properties of the material due to modification of the growth of the deposit [7, 12]. The properties of the composite coating are dependent on concentration, size, distribution and type of nanoparticle incorporated, in addition to the method and parameters used during coating formation [13, 14]. Although there are a large number of successful metal/particle combinations, this review will focus on zinc-nickel nanoparticle coatings exclusively. Individually nickel has been successfully co-deposited with a number of materials including TiO_2, SiC, Al_2O_3, PTFE and layered silicates such as montmorillonite (Mt) [2, 7, 15–19] and zinc has been successfully co-deposited with TiO_2, CeO_2, ZrO_2, SiO_2, mica particles and polymeric nano-aggregates (PNAs) [20–25] but a review of current literature on ZnNi alloy nanocomposite coatings has not been compiled to our knowledge. An overview of the literature is shown in **Table 1**. The most commonly used reinforcement material for zinc-nickel coatings is Al_2O_3 constituting ~32% of the papers, followed by TiO_2 and SiO_2/SiC with ~20% each, carbon nanotubes and CeO_2 with ~8% each, and Al_2O_3/SiC, CeO_2/SiO_2 and Mt with ~4% each [11–13, 26–48].

Zinc-nickel coatings are well known in the field of corrosion resistance as a corrosion resistant material. Corrosion protective coatings are commonly used to extend the lifetime of materials such as stainless steel from corrosion onset as a substitute for more expensive, less available materials [49–53]. Coating zinc onto stainless steel, known as galvanization, is an industry standard to protect against corrosion. The zinc coating sacrificially corrodes, thereby protecting the stainless steel from corrosion [54–56]. Options are now being explored to withstand harsher conditions, longer lifetimes, reduced thickness and better overall strength of the protective coating layer. Although a large focus has been on the development of generalized corrosion resistant coatings, when considering cost, environmental impact and performance,

Reference and application	Plating bath	Incorporated particle and deposition parameters	Dispersion method
Blejan et al. [17] Corrosion	106 g/L ZINCATE 75 (75 g/L Zn and 400 g/L NaOH), 12 mL PERFORMA 285 Ni-CPL, 100 mL PERFORMA Additive K. 82.6 g/L NaOH, pH = 13	Al_2O_3 60 nm powder, S.A. 74 m^2/g 5, 10, 15 g/L 2 A/dm^2, 23 ± 2°C	Ultrasonication and solution stirring during deposition.
Ghaziof et al. [33, 34] Corrosion, microhardness	35 g/L $ZnSO_4 7H_2O$, 35 g/L $NiSO_4 6H_2O$, 80 g/L Na_2SO_4, pH = 4	Alumina Sol 6 mL/L $i_{DC} = i_{avg.} = 80$ mA/cm^2 $i_{peak} = 160$ mA/cm^2 Frequency (HZ) = 100 ($t_{on} = T_{off} = 5$ ms), 500 ($t_{on} = t_{off} = 1$ ms) 40°C	Bath agitated 10 min prior to deposition.
Ataie et al. [35] Tribological properties	150 g/L $ZnCl_2$, 250 g/L $NiCl_2 6H_2O$, 45 g/L H_3BO_3, 100 g/L KCl, 100 g/L NH_4Cl, 0.1 g/L SDS, pH = 4	α-Al_2O_3 ~30 nm 15 g/L 18 a/dm^2, 30°C	Magnetic stirring 24 h prior to deposition, 500 rpm. Sonicated 2 h (500 W) (15 min on, 15 min off for 2 h). Magnetic stirring during deposition, 250 rpm simultaneously with sonication.

Reference and application	Plating bath	Incorporated particle and deposition parameters	Dispersion method
Shourgeshty et al. [36, 37] Corrosion, wear properties	250 g/L $ZnCl_2$, 150 g/L $NiCl_2{\cdot}6H_2O$, 45 g/L H_3BO_3, 100 g/L KCl, 100 g/L NH_4Cl, 0.5 g/L, pH = 4 ± 0.5	α-Al_2O_3 ~20 ± 5 nm 15 g/L 4 A/dm^2, 30 ± 2°C	Magnetic stirring 12 h prior to deposition, 300 rpm, followed by 1 h ultrasonication (250 W, 20 KHz). During deposition mechanical stirring, 150 rpm and ultrasonic waves (50 W, 20 KHz).
Zheng et al. [38, 39]	60 g/L $ZnCl_2$, 120 g/L $NiCl_2{\cdot}6H_2O$, 120 g/L KCl, 100 g/L NH_4Cl, 30 g/L $NaCH_3COO$, pH = 5.0	α-Al_2O_3, particle diameter ~100 nm 50 g/L 4 A/dm^2, 35 ± 1°C	Magnetic stirring 24 h, 2000 rpm prior to deposition. Ultrasound generator and mechanical stirring (200 rpm) during deposition.
Momeni et al. [14] Hardness, antibacterial properties	57.5 g/L $ZnSO_4{\cdot}7H_2O$, 52.5 g/L $NiSO_4{\cdot}6H_2O$, 9.3 g/L H_3BO_3, 56.8 Na_2SO_4, 0.53 H_2SO_4, pH = 2.5	TiO_2 0.0–3.0 g/L 1 A/dm^2, 35°C	Stirring during deposition, 500 rpm.
Gomes et al. [40, 41]	0.10 M $ZnSO_4{\cdot}7H_2O$, 0.30 M $NiSO_4{\cdot}6H_2O$, 0.20 M $MgSO_4$, 0.15 M H_3BO_3, pH = 4	TiO_2, particle size ~25 nm 10 g/L –3.2 A/dm^2, Room Temp	Ultrasonic agitation 30 min prior to deposition. Stirring during deposition, 400 rpm.
Katamipour et al. [42] Corrosion, mechanical	60 $ZnCl_2$, 120 g/L $NiCl_2{\cdot}6H_2O$, 120 KCl, 100 NH_4Cl, 30 $NaCH_3COO$, pH = 4.6	TiO_2, ~25 nm 3 g/L 3.5 A/dm^2, 35 ± 1°C	Magnetic stirring, 1500 rpm 24 h prior to deposition. Ultrasound generator and stirring during deposition, 600 rpm.
Praveen et al. [43] Corrosion	160 g/L $ZnSo_4{\cdot}7H_2O$, 16 g/L $NiSO_4{\cdot}6H_2O$, 12 g/L H_3BO_3, 40 g/L Na_2SO_4, 1.5 g/L cetyl trimethyl ammounium bromide, pH = 4	TiO_2, ~100–200 nm 3 g/L 2 A/dm^2, 27°C	Magnetic stirring 10 h prior to deposition.
Tuaweri et al. [30, 44] Corrosion	57.5 g/L $ZnSO_4{\cdot}7H_2O$, 131 g/L $NiSO_4{\cdot}6H_2O$, 162 $Na_2SO_4{\cdot}10H_2O$, pH = 2.0–2.5	SiO_2 13–52 g/L 1–10 A/dm^2	Agitation through use of vibro-agitation with vibromixer prior to deposition.
Ullal et al. [45] Corrosion	100 g/L $ZnSO_4{\cdot}7H_2O$, 100 g/L $NiSO_4{\cdot}6H_2O$, 75 g/L $NaCH_3COO{\cdot}3H_2O$, 2 g/L citric acid, 0.5 g/L thiamine hydrochloride, pH = 3.0 ± 0.05	SiO_2 nanopowder 5 g/L Deposition current and temp—not specified	Magnetic stirring 24 h prior to deposition. Agitation of solution with circulation pump during deposition.
Takahashi et al. [46]	1 M $ZnSO_4{\cdot}7H_2O$, 0–0.7 M $NiSO_4{\cdot}6H_2O$, pH = 2.0	SiO_2 colloid (Cataloid SN) 0–300 g/L 100 A/dm^2, 50°C	Not specified
Poliak et al. [47] Mechanical properties	125 g/L $ZnSO_4{\cdot}7H_2O$, 75 g/L $NiSO_4{\cdot}6H_2O$, 25 g/L H_3BO_3, pH = 4	SiO_2 powder, ~10 nm 1 g/L 2A/dm^2	Not specified

Reference and application	Plating bath	Incorporated particle and deposition parameters	Dispersion method
Müller et al. [48]	0.16 M ZnO, 1.7×10^{-2} $NiSO_4 6H_2O$, 3.75 M NaOH, 3.4×10^{-2} M diethylenetriamine, pH = alkaline	α-SiC powder, ~7.0 μm 20–120 g/L 25°C	Stirring 24 h prior to deposition, substrate rotated during deposition.
Creus et al. [49, 50] Corrosion	63 g/L $ZnCl_2$, 100 g/L $NiSO_4 6H_2O$, 215 g/L KCl, 20 g/L H_3BO_3, pH = 5.3.	CeO_2, ~80 nm 5 g/L Cathodic pulse, i_p = 5.0 A/dm² with t_{on} = 4 ms, t_{off} = 16 ms. Anodic pulse, J_a = 1.0 A/dm² with t_{on} = 4. Average current density ~0.67 A/dm². ms, 25°C	Stirred 24 h prior to deposition, continued stirring during deposition, 200 rpm.
Tseluikin et al. [18, 51]	10 g/L ZnO, 50 g/L $NiCl_2 6H_2O$, 220 g/L NH_4Cl, 20 g/L $NaCH_3COO$	Carbon nanotubes 0.05 g/L Reversing mode, i_c = 6 A/dm², i_a = 1.5 A/dm².	Not specified
Tulio et al. [52]	0.25 M $ZnSO_4 7H_2O$, 0.2 M $NiSO_4 6H_2O$, 0.4 M H_3BO_3, 0.1 M sodium citrate, pH = 4.9.	α-SiC ~9.5 μm, α-Al_2O_3 ~3.4 μm Not specified 25°C	Stirred 12 h prior to deposition. Substrate rotated during deposition.
Xiang et al. [53] Corrosion	Not specified	CeO_2 modified SiO_2, 400–500 nm Not specified Deposition current and temp—not specified	Not specified
Conrad et al. [54] Corrosion	0.2 M $ZnSO_4 H_2O$, 0.1 M $Ni(NH_4)_2(SO_4)_2 6H_2O$ 0.1 M $Na_2B_4O_7 10H_2O$ pH = 9.5	Montmorillonite (Mt) 1, 5 g/L E_1 = −1.45 V, T_1 = 10 sec. E_2 = −0.9 V, T_2 = 2 sec, Room Temperature	Sonicated 1 h prior to deposition, N_2 gas bubbled through solution during deposition.

Table 1. Survey of literature.

zinc alloys have become an attractive option. An alloy modifies the composition of a material resulting in different corrosion properties then the original element which can significantly improve the stability of the protective coating [2–5, 52, 57, 58], therefore, by picking the correct combination of alloys, one can greatly increase the corrosion resistance of the material [49, 52]. Alloy formation can result in various phases, dependent upon the experimental conditions at the time of formation. For zinc-nickel, there are 5 known alloy phases: α- and β- (30% Ni, nickel rich), γ- (Ni_5Zn_{21}), δ- (Ni_3Zn_{22}) and η- (1% Ni) (zinc rich), all dependent upon the Zn/Ni ratio and experimental parameters used to form the alloy [50, 55, 59–61]. The γ-phase and δ-phase are predominantly formed through electrochemical methods, with γ-phase showing the strongest protection against corrosion [57, 60, 62–65]. Zinc nickel γ-phase alloys with approximately 8–18% have been found to be optimal for maximum corrosion protection [48, 57, 62, 65].

http://dx.doi.org/10.5772/intechopen.80219

Although several methods are available for the development of nanocomposite coatings, electrodeposition remains a favorable choice due to relative ease of use, low cost, convenience, ability to work at low temperatures and overall control of experimental parameters [39, 48, 58, 65]. A general survey of the literature concerning zinc-nickel nanocomposite coatings found electrochemical deposition to be the main preparation method, so general trends and properties of the coatings formed through electrochemical methods will be the focus of this chapter.

2. Electrodeposition of zinc-nickel nanocomposite coatings

2.1. Dispersion of particles

A variety of particles, including Al_2O_3, TiO_2, SiO_2, SiC, ceria, carbon nanotubes and montmorillonite (Mt) have been successfully incorporated into zinc-nickel coatings. For optimal effect, the nanoparticles need to be dispersed throughout the metallic coating. To accomplish this, the particles first need to be suspended in the electrolytic solution and agglomeration of the particles needs to be kept to a minimum to prevent issues in coating formation. Particle agglomeration is an issue seemingly independent of particle concentration as it occurs under low to high concentrations, though smaller particle size does increase tendency to form agglomerations, leading to less incorporation in the final coating. To prevent agglomeration, various methods can be used such as organic additives, agitation of the solution, current density, etc. Treatment of the nanoparticles prior to deposition is varied throughout the field but the most common methods used for particle suspension are magnetic stirring, sonication or a combination of stirring and sonication prior to and during deposition [11–13, 26–48]. In addition to treatment of the nanoparticles, concentration in the bath also affects the quality of the coatings. As expected, as the concentration of nanoparticles in the bath increases, the concentration of nanoparticles in the resulting coating tends to increase. The small sized particles are easily incorporated into irregularities on the metal surface and positively charged particles are attracted to the cathode, so more easily incorporated into the coating [13]. In the case of oxide nanoparticles, the oxides compete with the metallic ions for adsorption onto the active sites, creating more nucleation sites and perturbing metallic grain growth. Other particles are trapped during deposition, filing holes or gaps within the naturally forming coating [22, 40].

Concentration of nanoparticles in the bath varies from 0.05–300 g/L with most work using around 5–15 g/L. Müller et al., who relied on mechanical stirring to disperse the nanoparticles, found optimal concentration of SiC particles to be 60 g/L, beyond which the particles began to agglomerate. Beyond this concentration, stirring was not sufficient to keep the particles suspended in solution and a decreasing trend of SiC in the coatings was observed [42].

Katamipour et al. studied the effects of ultrasonic conditions to promote uniform dispersion of the coating particles, and to determine if improvement occurred in the corrosion and mechanical properties of the coatings. They found that increasing the ultrasonic power density lead to a decrease in particle size, an increase in nanoparticle incorporation in the coating, and initially, an improvement in corrosion and mechanical properties. The agglomeration often observed with nanoparticles also dissipated with the use of sonication [36]. Nano-alumina

particles were found to be uniformly imbedded in the ZnNi-Al_2O_3 coating after treatment of ultrasonic vibration [32, 33]. Without sonication, ceria nanoparticles were seen organized in long string-shape agglomerates. These agglomerates became trapped inside voids and pores during coating growth [44]. Though sonication or mechanical disruption of the nanoparticles is needed to distribute them throughout the metal matrix, care must be taken as excessive agitation can lead to a lower quality of particles in the deposit [7].

Na-smectites, a type of clay mineral, specifically montmorillonite (Mt) were also examined, for incorporation into metal matrixes. Within aqueous solutions, Na-montmorillonite can be completely exfoliated and incorporated into other materials, forming continuous, crack free films, which is beneficial in corrosion resistant coatings [5, 8–9, 52, 66]. Exfoliation causes the short range order of the clay particles to be disrupted, causing individual clay platelets to exist, unassociated from one another. The resulting clay platelets range 1–2 nm in width with 100–1000 nm in length [66]. These platelets are easily incorporated into the coating during deposition, increasing the overall thermal stability and mechanical strength of the coating, which leads to increased corrosion resistance [2, 8]. As the alloy coating is forming, the exfoliated clay in solution is freely dispersed throughout the electrolytic bath. Mt is a cationic clay with a negatively charged surface which attracts metal ions, increasing incorporation of the platelets into the metal composite during deposition. The clay platelets settle onto the substrate surface as the coating is being formed, allowing them to be incorporated into the coating. Exfoliated Mt, which has a plate-like structure, increases the surface area of the material when imbedded in the coating and leads to a more tortuous mean free path of the corrosion cells upon onset [5]. This technique has previously been successful with the incorporation of montmorillonite platelets into pure nickel, nickel-molybdenum and nickel-copper coatings [2, 5, 8, 9, 52, 58, 66]. However, many traditional particles used in composite coatings are spherical in shape. For example SiO_2 nanoparticles coated with a layer of cerium oxide have been introduced into ZnNi coatings to improve corrosion resistant properties [47].

2.2. Influence of nanoparticle addition on deposition mechanism

Though many researchers use electrochemical deposition as a tool to form a coating of interest, there is little published work on the electrochemical system used for the deposition of zinc-nickel nanocomposite coatings. A better understanding can lead to an improved deposition system, and an overall superior coating. Work continues to be done in acidic and alkaline conditions with a goal of further improving the materials, longer material lifetimes and a better understanding of the mechanisms involved in various alloy formations [49, 50, 55, 57, 59, 60, 65, 67–71] but little work has been done to examine systems with nanoparticle incorporation.

Zinc-nickel alloy formation follows an anomalous deposition mechanism which occurs when the electrochemically less noble metal deposits preferentially to the more noble metal. This is verified through examination of the voltammetry patterns of the zinc-nickel system as the individual zinc and nickel reduction peaks are shifted based on the presence of the other metal species in solution [48, 59, 62, 70, 72–74]. During deposition, a thin layer of nickel is initially deposited onto the substrate. As the deposition continues, zinc is intercalated into the nickel, leading to formation of the alloy [57, 61, 67]. In acidic systems under low current density, a transition from anomalous to normal codeposition has been noted. Normal codeposition is dominant when the

applied potential is more similar to the free corrosion potential of zinc and zinc-nickel alloys. These systems also present with lower current efficiencies [57, 61, 73–77]. Normal deposition leads to alternate ZnNi phases, which are not preferred for maximized corrosion protection, so the goal is to remain under an anomalous deposition route, to further aid in the deposition of γ-phase ZnNi alloy. Within the research presented on the deposition mechanism with nanoparticle presence, the effect of SiO_2, SiC, Al_2O_3, Mt and carbon nanotubes on the deposition mechanism has been explored and is discussed under their individual sections.

Hydrogen evolution at cathodic potentials is a concern in electrochemical deposition as it can lead to the formation of cracks and defects in the overall coating structure, both during deposition and later during use of the material. Hydrogen evolution competes with metal electrodeposition in this system and can play a major role in determining the composition of ZnNi coatings [35, 46]. In ZnNi deposition systems under alkaline conditions, boric acid was found to suppress hydrogen evolution. Hydrogen evolution is a larger concern for nickel deposition than zinc deposition as a larger overpotential is required for nickel deposition since the deposition is under kinetic control while zinc deposition is thermodynamically controlled [57]. Our previous study examined the change in hydrogen evolution onset with varying borate concentrations in alkaline solutions, and found as the borate concentration is increased, hydrogen evolution is pushed to more cathodic values [48]. A maximum borate concentration of 100 mM was used due to conductivity of borate in the system [57]. In addition to borate, nanoparticles can have an overall effect on hydrogen evolution in the system as well. The hydrogen evolution onset was compared for solutions with and without the presence of Mt in **Figure 1**. For nickel, a large cathodic shift was observed when Mt was added to the system. For zinc and zinc-nickel, small cathodic shifts were observed with Mt. The Mt can help further shift the onset of hydrogen evolution within this system, in addition to borate [48, 57]. Alloy formation typically occurs at or near the onset of hydrogen evolution for this system. By shifting the onset in a cathodic direction, less hydrogen will be produced during alloy formation, leading to less entrapped hydrogen in the overall coating. Hydrogen evolution can hinder adsorption of nanoparticles on the surface of the coating material and lead to embrittlement [7].

The addition of Al_2O_3 and SiC was also found to cause a surface blockage preventing hydrogen evolution to occur. This effect is found to be dependent on the concentration of SiC in solution, but for addition of Al_2O_3 no dependency is observed. It is believed that SiC and Al_2O_3 are adsorbed onto the electrode surface, reducing the active surface area. At lower pH, H^+ has a higher tendency to adsorb onto the SiC particles, leading to a reduction in hydrogen evolution [46].

2.3. Deposition methods

Electrodeposition techniques include potentiostatic and galvanostatic deposition, and further into both methods, applied vs. pulsed deposition parameters in the literature for zinc-nickel nanocomposite coatings [44]. The particles co-deposit with the zinc-nickel coating which has advantages over other methods such as better control of coating thickness, deposition speed, working under controlled temperatures, and it is a single-step method. The nanoparticles are incorporated as the metal species are reduced onto the electrode surface, forming the nanoparticle coating. Applied methods include direct current or direct potential, where a constant current or potential is applied to the electrode. Pulsed methods include pulse current

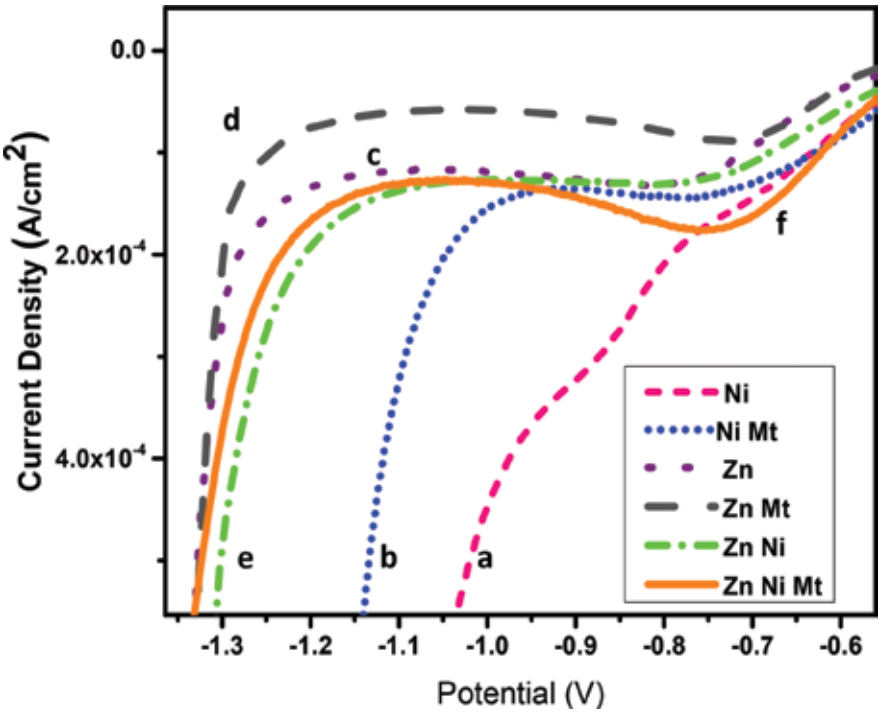

Figure 1. The onset of hydrogen evolution in solutions containing metal salts (specified), Mt (specified) 0.1 M borate and pH = 9.4 with NH_4OH (a) Ni^{2+} (pink short dash); (b) Ni^{2+} Mt (blue dot); (c) Zn^{2+} (purple square dot); (d) Zn^{2+} Mt (black long dash); (e) Zn^{2+}, Ni^{2+} (green dash dot); (f) Zn^{2+}, Ni^{2+} Mt (orange solid) [54].

(PC), pulse reversed current (PRC), pulse potential (PP) and pulse reversed potential (PRP). PC and PP involve alternatively applying two or more cathodic direct current or potentials during the deposition, with off times, when no current or potential is being applied. PRC and PRP are similar to PC and PP as a cathodic pulse is applied but during the off times, an anodic pulse is applied to the electrode. Previous studies show an increase in incorporation of particles through a pulse deposition method with better overall coverage of the underlying material compared to a constant applied potential technique [7, 45, 48, 57, 62, 68, 78–80]. The nanoparticles are incorporated in a higher percentage because of the partial dissolution of the metal deposit during the anodic pulse. Pulse plating was found to improve overall quality of deposits and reduce grain size which inherently increases the corrosion protection of the coating [48, 57–58, 79, 81]. Pulse deposition includes the following attributes: (1) better inclusion of nanoparticles in the metal matrix, (2) lower concentration of nanoparticles needed in the electrolytic solution, (3) selective entrapment based on size of nanoparticles, (4) release of trapped hydrogen prior to coating use which leads to longer coating lifetime and (5) a more opened grain structure which allows hydrogen to escape from the deposit without forming holes or pits in the coatings which could otherwise be used as corrosion cell development sites [7, 48, 57, 80]. Pulsed deposits help embed higher concentrations of nanoparticles because it helps eliminate a fraction of the electrodeposited metal during the off time [7]. Pulse durations affect the shape and size of crystallite formation [21, 81, 82]. During off time,

adsorbed metallic adatoms are able to reorganize and minimize surface energy. The grain growth continues during this time due to desorption of impurities leading to changes in grain morphology and size while chemical composition remains relatively constant [20].

2.4. pH studies

Coating composition and quality is dependent on the pH of the system at the time of formation. Although extensive work has been done on zinc-nickel coatings in both acidic and alkaline conditions, less work has been done on zinc-nickel coatings with nanoparticle incorporation. A review of the literature shows most studies being performed under acidic conditions [32–37, 39–40, 44, 46] with little work in alkaline conditions [12, 42, 48]. ZnNi-Al_2O_3 coatings were predominantly deposited under acidic conditions (pH = 4, 4.9 and 5.0) with one group examining deposition at pH = 13 [12, 27–33]. The literature for the deposition of ZnNi-TiO_2 coatings was done under acidic conditions with pH = 2.5, 4 and 4.6 from a variety of groups [11, 34–37]. The deposition of ZnNi-SiO_2 particles was performed at pH = 2, 3 and 4 while the deposition of ZnNi-SiC was done under an unspecified alkaline pH [26, 38, 39–42]. The deposition of ZnNi-ceria particles was undertaken with a pH = 5.3 [43, 44]. ZnNi-carbon nanotubes, though not specified are believed to have been deposited under alkaline conditions due to specified bath components [13, 45] and the deposition of ZnNi-Mt coatings was done at pH = 9.4 [48]. Though the bulk of the work has been done under acidic conditions, focus of the research may benefit from pushing into the realm of alkaline deposition as throughout literature, optimal coating formation is realized under alkaline conditions. Although zinc-nickel coatings deposited under acidic conditions tend to have a higher current efficiency, alkaline processes tend to lead to better substrate coverage [12, 57, 62, 79]. A drawback of alkaline conditions is stabilizing agents are needed to keep the metal species from precipitating as metal hydroxides from the solution.

3. Characterization of the zinc-nickel nanocomposite coatings

3.1. Coating composition

Zinc and nickel content and nanoparticle incorporation were examined with various techniques including atomic absorption spectroscopy (AAS), inductively coupled plasma-mass spectrometry (ICP-MS), energy dispersive spectroscopy (EDS) energy dispersive x-ray (EDX) and EDX mapping. Uptake of the nanoparticles is of interest as varying concentrations of nanoparticles are found, dependent upon the character of the particle being added to the solution. ZnNi coatings with Al_2O_3 incorporation were found to contain anywhere from trace Al_2O_3 up to 8.9 wt % throughout the literature [12, 27–33]. Zinc-nickel coatings with TiO_2 incorporation were found to contain on average 80–85% Zn, 12–17% Ni and 1.25–2.5% Ti [35–37]. ZnNi-SiC coatings contained 11% SiC [42]. ZnNi coatings with ceria incorporation contained 10–11% Ni, with 2–3% ceria content [43, 44]. ZnNi-Mt coatings contained 86–90% Zn, 10–14% Ni with trace amounts of Mg and Al from Mt nanoparticles confirmed in ICP-MS analysis [48]. Throughout the studies, the coatings maintain the Ni% needed (8–18%) for maximized corrosion protection [57, 59, 70, 83].

3.2. X-ray diffraction (XRD)

The phase of electrodeposited ZnNi alloy coatings is dependent upon the nickel content in the alloy and can be controlled by a number of factors including electrolytic bath conditions [12]. γNi_5Zn_{21} is known to be the most corrosion resistant ZnNi alloy phase and appears to be preferentially deposited under alkaline conditions in ZnNi systems without nanoparticle incorporation. The γ ZnNi has a preferred orientation with the (330) reflection as main peak in the XRD pattern [42, 59, 65–67, 71, 72]. This preferred orientation continues with the incorporation of nanoparticles although an overall decrease in peak intensity and broadening of peak suggest smaller crystallite size formation [12, 35, 48]. The peak width of the diffraction peak at half maximum height (FWHM) is dependent on crystallite size and lattice strains due to lattice imperfections such as dislocations or atom vacancies with the values dependent most heavily on crystallite size [84, 85]. If we assume there is little strain in the system, we can assume the broadening at FWHM is due to a decrease in crystallite size of the metallic particles [35]. The average crystallite size of ZnNi coatings with TiO_2, SiC, and Al_2O_3 nanoparticles are presented in **Table 2**. The trends show an overall decrease in particle size with the increase in nanoparticle incorporation as compared to pure ZnNi coatings.

3.3. Microhardness

Hardness (HV) values are a measurement of the microhardness or resistance to penetration of a sample and can be used to compare quality of the coatings. All composite coatings studied demonstrate improved microhardness values as compared to the base alloy as presented in **Table 3**. As expected, addition of nanoparticles to the coatings improve the overall hardness values, as demonstrated with an increase of 305 HV to 524 HV for ZnNi coatings with CeO_2 treated SiO_2 particles, an increase of 35 HV with the addition of TiO_2 particles in Praveen's work, a 300% increase in hardness with an incorporation of 11.2 wt % Al_2O_3 particles in Zheng's work and noticeable increases in both Ataie's and Ghaziof's work with incorporation of Al_2O_3 particles as well [27, 29, 32, 37, 47]. The improved microhardness is believed to be due to dispersive strengthening as the ceramic like particles (TiO_2) form a barrier to deformation commonly observed in metal matrix systems. As the incorporation of nanoparticles increases, the microhardness also increases [36]. The higher hardness of the coating is due to the fine-grained structure. The dispersed particles in the matrix are able to obstruct easy movement of dislocations [37].

Nanoparticle	ZnNi (nm)	ZnNi nanocomposite (nm)
Al_2O_3 (5 g/L) [17]	40.93	26.4
Al_2O_3 (10 g/L) [17]	40.93	33.2
Al_2O_3 (15 g/L) [17]	40.93	20.68
TiO_2 [43]	—	30
TiO_2 [41]	—	19.7
TiO_2 [40]	15.5	11.7
SiC [48]	28.5	21.0–22.0

Table 2. Crystallite size of coatings listed in the literature.

Reference	Coating composition	Hardness values (HV)	Additional parameters
Xiang et al. [53]	Bare substrate	134	Direct deposition
	ZnNi coating	305	
	ZnNi coating with incorporated SiO_2 nanoparticles	535	
	ZnNi coating with incorporated CeO_2 treated, SiO_2 nanoparticles	524	
Ataie et al. [35]	ZnNi Coating with incorporated Al_2O_3 nanoparticles	340	Direct deposition
	ZnNi Coating with incorporated Al_2O_3 nanoparticles	640	30 W ultrasonic application during deposition
	ZnNi Coating with incorporated Al_2O_3 nanoparticles	750	45 W ultrasonic application during deposition
Zheng et al. [38]	ZnNi coating	215	Ultrasound generation and magnetic stirring during deposition
	ZnNi coating with incorporated 11.2 wt % Al_2O_3 nanoparticles	640	
Praveen et al. [43]	Zinc-nickel coating	135	Direct deposition
	ZnNi with incorporated TiO_2 particles	170	
Ghaziof et al. [33]	ZnNi coating with incorporated Al_2O_3 nanoparticles	235	Direct deposition
	ZnNi coating with incorporated Al_2O_3 nanoparticles	310	Pulsed current deposition, 100 Hz
	ZnNi coating with incorporated Al_2O_3 nanoparticles	323	Pulsed current deposition, 500 Hz

Table 3. Microhardness values of coatings throughout the literature.

3.4. Corrosion studies

An advantage to developing metal matrix composite coatings is for increased corrosion resistance as compared to pure metal coatings. Properties that may contribute to this added protection include a finer coating structure with refined grains, incorporation of electrochemically inert particles dispersed throughout the metallic coating, and filling of crevices, gaps, and micron sized holes on the coatings surface. These could otherwise lead to localized defects which are vulnerable to corrosion. Improvement of self-passivation of the coating is offered through improved barrier protection due to the incorporated particles in the naturally formed defects of the coatings. Common methods to examine the corrosion resistance of a material include open circuit potential (OCP) studies, linear polarization resistance (LPR), potentiodynamic polarization, and electrochemical impedance spectroscopy (EIS).

The open circuit potential (OCP) is the potential of the working electrode relative to the reference electrode when no external potential or current is being applied to the system. OCP is dependent on the composition of the working electrode, treatment of the electrode prior

to the study, and the electrolytic bath in which the electrode resides. Linear polarization resistance is the measurement of current in relation to the electrode potential. This can be used to predict the corrosion rate of the coatings within a specific environment. The film is polarized by applying an external potential forcing the system away from equilibrium and monitoring the resulting potential and current. The deviation from an equilibrium potential is called polarization. The polarization resistance (R_p) is experimentally observed between the electrochemical current density and applied potential for the corroding electrode within a few millivolts of the polarization from the open circuit potential (E_{ocp}). Potentiodynamic polarization pushes the potential even further from the equilibrium potential for the anodic and cathodic sweeps. From this data the anodic slope (β_a) and cathodic slope (β_c) are obtained from the curves. The E_{corr} is determined from the intercepts of the curves. The i_{corr} value is obtained by substituting the β_a, β_c and R_p values into a simplified rearranged Stern and Geary equation [86, 87].

The anticorrosive ability of ZnNi-nanocomposite coatings can be further investigated with EIS. Nyquist plots show a semicircle shape in the investigated frequency range with an increased axial radius, which is indicative of better corrosion resistance. Equivalent circuit models are used to simulate the metal-solution interface to better understand the system. A few studies have done corrosion work for these ZnNi nanocomposite coatings and shown improvement with addition of the nanoparticles. **Table 4** lists some results which are discussed in sections below.

Coating [ref]	E_{corr} (V)/SCE	i_{corr} (A)	R_p (Ω cm²)
Zn [54]	−1.17	2.09×10^{-4}	1333
Ni	−0.45	2.75×10^{-5}	6790
ZnNi γ phase	−0.74	1.06×10^{-5}	30,485
ZnNi-Mt γ phase	−0.73	3.72×10^{-6}	34,900
ZnNi [50]	−0.92	6.20×10^{-5}	—
ZnNi-CeO_2	−0.77	3.30×10^{-5}	—
ZnNi-CeO_2 (sonicated)	−0.78	2.80×10^{-5}	—
ZnNi-TiO_2 [41]	−1.09*	9.90×10^{-5}	122.2
ZnNi	−1.05*	4.30×10^{-5}	352.0
ZnNi-TiO_2 (24 h immersion)	−1.11*	1.25×10^{-5}	97.3
ZnNi (24 h immersion)	−1.03*	—	94.1
ZnNi [17]	−0.62	2.51×10^{-6}	1167.6
ZnNi-Al_2O_3 5 g/L	−0.52	1.23×10^{-6}	4024.9
ZnNi-Al_2O_3 10 g/L	−0.63	2.37×10^{-6}	2038.3
ZnNi-Al_2O_3 15 g/L	−0.70	2.57×10^{-6}	1190.0

*Corrected to SCE.

Table 4. Corrosion potential (E_{corr}), corrosion current (i_{corr}) and polarization resistance (R_p) of ZnNi and ZnNi-Mt coatings.

4. Zinc-nickel nanocomposites

4.1. ZnNi-Al_2O_3 and Al_2O_3/SiC

Most work to date has examined ZnNi-Al_2O_3 coatings (~32% of papers) with 4% examining the effects of Al_2O_2/SiC combined in the nanocomposite. Though the deposition mechanism of ZnNi-Al_2O_3 coatings was not explicitly discussed, Tulio et al. examined the effects of SiC and Al_2O_3 in slightly acidic pH with rotating disc. They first examined the effect of SiC and Al_2O_3 on nickel and zinc, without the other metal ion present in solution and found the addition of SiC and Al_2O_3 encouraged deposition of both Ni and Zn individually. For nickel, a marked increase in current densities was observed. In the Zn system when the solution was scanned cathodically without the presence of nanoparticles, the deposit exhibited many discontinuities, or areas without a deposit present. When the SiC and Al_2O_3 particles were added to the solution, there was a noticeable increase of coating coverage so much that the discontinuities almost disappeared entirely, suggesting encouragement of Zn deposition. SiC and Al_2O_3 do not affect the initial nucleation and growth in the ZnNi system when the metal species are combined, though at higher concentrations of nanoparticles, surface blockage has been observed. Larger current densities are observed for systems with SiC and Al_2O_3 as compared to systems free of nanoparticle presence and a positive shift in potential was noted at the onset of secondary nucleation. This is due to an increase in the mass-transport of the particles to the electrode surface during the rotation. During the scans the quantity of particles reaching the electrode increased, leading to an increase in current density. The ZnNi deposition did remain anomalous under all conditions examined [46]. Blejan and Muresan examined the XRD patterns of deposited ZnNi-Al_2O_3 films (using a Cr x-ray tube), which only exhibited γ-phase ZnNi alloys, showing small growth of the (330) plane with addition of Al_2O_3 particles with deposition giving a preferred (600) orientation [12]. Improvement of nanoparticle incorporation was noted through the use of ultrasonication [29, 32, 33].

Zhang and An found an increase of hardness with the addition of Al_2O_3 [32]. Ataie et al. examined the effect of sonication during the deposition. Without sonication, the hardness was 340 HV, with 30 W sonication it was 640 HV and with 45 W sonication it was 750, a 220% increase over the coating with no sonication [29]. The hardness of ZnNi and ZnNi-Al_2O_3 coatings under direct current and pulse current deposition conditions was examined. ZnNi under applied current was 235 HV while pulsed ZnNi was 310–323 HV, a 40% increase and ZnNi-Al_2O_3 was 338 HV, a slight increase over pulsed ZnNi coatings [27]. Shourgeshty et al. examined multilayer coatings of ZnNi and ZnNi-Al_2O_3 deposits. As expected, an increase in the number of layers improved the hardness values of the coatings but addition of Al_2O_3 also had a positive effect [30, 31].

ZnNi-Al_2O_3 coatings were studied in Na_2SO_4 solution. ZnNi-Al_2O_3 coatings (**Table 4**) present corrosion potentials of the composite coatings at more positive potential with initial Al_2O_3 incorporation as compared to ZnNi alloys which is attributed to the chemical inertia of the incorporated particles [12]. The corrosion current decreases from 1.83×10^{-5} to 0.92×10^{-5} as the Al_2O_3 content is doubled from 4.5 to 8.9 wt% [32]. EIS of ZnNi-Al_2O_3 with varying incorporation

of Al_2O_3 and varying immersion (0, 24, 48 and 120 h) is presented in **Figure 2**. The coatings were studied in 0.2 g/L Na_2SO_4 (pH 5) using a potentiostat PARStat 2273 (Princeton Applied Research). The frequency domain was 10 kHz to 100 mHz and temperature was maintained at 23 ± 2°C. The plots were fit with ZSimpWin 3.21 software. The impedance modulus of the nanocomposite is higher than pure ZnNi films. The charge transfer resistance for the composite coating is higher than ZnNi films, yet the double layer capacitance is smaller. Initially the measurement decreases at a systematic rate, suggesting a rapid degradation of the coating due to corrosion but after 50 h the rate of degradation decreases, likely due to the formation of corrosion products on the surface of the coating [12]. Incorporation of Al_2O_3 particles results in γ-phase zinc-nickel alloys with nanoparticle incorporation. ZnNi-Al_2O_3/SiC coatings still follow an anomalous deposition route. Improved hardness and corrosion properties are observed with incorporation of Al_2O_3 [12, 27, 29, 32, 46].

4.2. ZnNi-TiO_2

ZnNi-TiO_2 coatings comprise ~20% of the papers on ZnNi-nanocomposite coatings. As demonstrated with the Al_2O_3 composite coatings, improved corrosion and mechanical properties of the ZnNi coatings occur with the incorporation of TiO_2 particles into the metal matrix. In a study by Praveen et al. they varied the TiO_2 concentration in the bath from 0.5 to 5.0 g/L. Lower current densities were observed at 3 g/L and above this concentration the corrosion current increased so it was chosen as the optimal concentration [37].

The deposition with TiO_2 gave coatings with preferential γ-phase alloy, though small amounts of a pure zinc phase are seen in ZnNi coatings without TiO_2 incorporation. Textural modifications due to the presence of TiO_2 nanoparticles are suggested due to slight changes in peak intensity in the XRD patterns as compared to ZnNi coatings without TiO_2 incorporation. The metallic grain size also decreases with the incorporation of TiO_2, due to changes to nucleation and growth due to disruption of the metallic growth by incorporation of semiconducting particles during coating formation [35]. TiO_2 incorporation can also cause a considerable decrease in grain size for the metallic phase, with rough and irregular deposits as demonstrated by SEM and AFM (**Figure 3**) [34, 35]. The ZnNi coating without TiO_2 exhibited multiple defects, cracks, gaps, crevices and microholes. The TiO_2 nanoparticles fill these gaps, leading to an overall decrease in the corrosion rate. The crystal size of the composite coating also appears smaller as compared to the ZnNi coating [37]. The compact size is preferred as it also better protects from corrosion onset. The effects of soniciaton on morphology were also examined. Ultrasonic vibration during deposition was found to result in increased nanoaparticle incorporation and a more homogeneous coating, suggesting the vibration promotes uniform distribution of the particles and decreased agglomeration of the particles. Improvement of nanoparticle incorporation due to ultrasonicaiton was also noted [36].

TiO_2 particles restrained the growth of the ZnNi alloy grains leading to a significantly higher microhardness in the presence of TiO_2 [37]. As expected, with increasing nanoparticle incorporation, the hardness increases, which is believed to be due to the dispersion of the ceramic like TiO_2 particles throughout the metal matrix [36]. As observed with Al_2O_3 addition, sonication of the electrolytic bath lead to increased microparticle incorporation, with hardness

http://dx.doi.org/10.5772/intechopen.80219

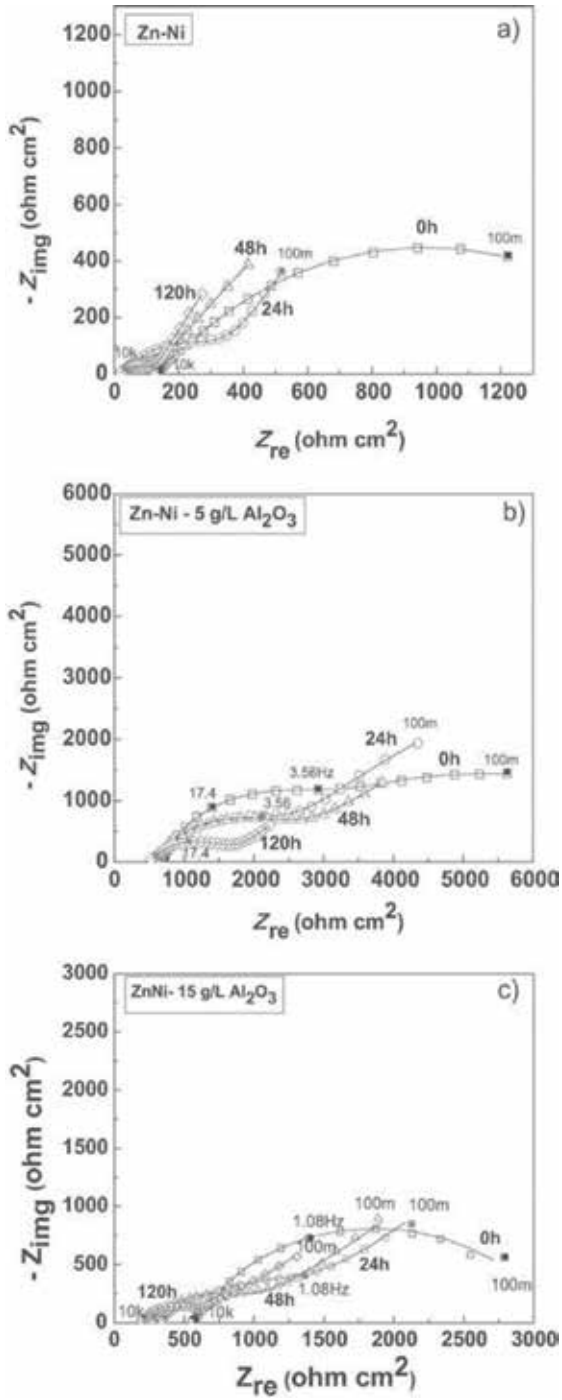

Figure 2. Impedance spectra of electrodeposited ZnNi and ZnNi-Al_2O_3 coatings, a) ZnNi, b) ZnNi-5 g/L Al_2O_3 and c) ZnNi-15 g/L Al_2O_3, recorded at 0, 24, 48 and 120 h immersion in 0.2 g/L Na_2SO_4 solution. "Reprinted with permission from [17]. Copyright 2013, John Wiley and Sons."

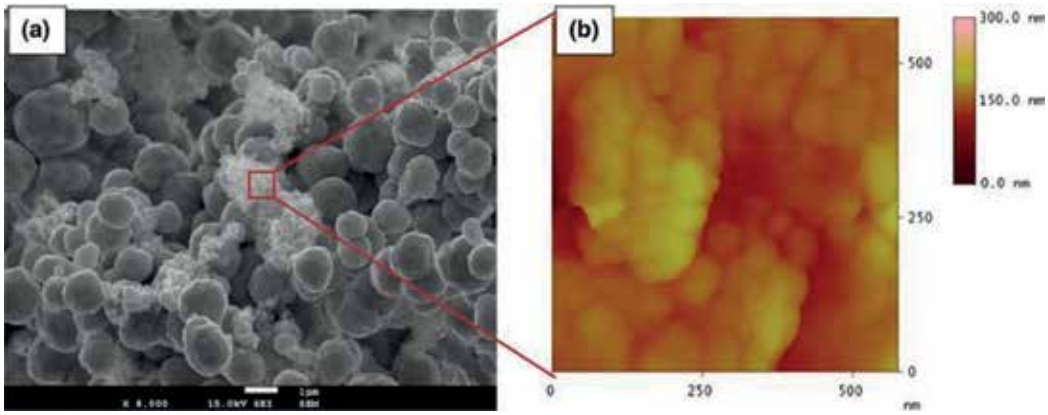

Figure 3. Morphology of ZnNi-TiO_2 coatings (a) SEM and (b) AFM. "Reprinted with permission from [41]. Copyright 2012, Springer Nature."

increasing from 253 HV for ZnNi coatings, and 464 for ZnNi-TiO_2 coatings without sonication, to 754 HV for ZnNi TiO_2 with sonication during deposition, a 60% increase in hardness with sonication and a 200% increase in hardness as compared to coating with the addition of Al_2O_3 particles incorporated under sonication. TiO_2 particles hinder the dislocation of movement, leading to an increased hardness of the material though a reverse trend which was observed at higher concentrations of TiO_2 in the deposition bath and believed to be due to agglomeration of the nanoparticles in solution [37].

The OCP was monitored over time for ZnNi and ZnNi-TiO_2 coatings in 3.5% NaCl and near-neutral 0.05 M Na_2SO_4 solutions, respectively [35]. The initial OCP values show that OCP of ZnNi and ZnNi-TiO_2 coatings appear at more noble values due to the presence of nickel (a more noble metal as compared to zinc) in the coating. Initially, the OCP values were − 1.49, −1.51, −1.43 and − 1.23 V (vs. Hg/Hg_2SO_4) for Zn, Zn-TiO_2, ZnNi and ZnNi-TiO_2, respectfully. After 24 h submersion, these values changed to −1.47, −1.49, −1.18 and −1.10 V for Zn, Zn-TiO_2, ZnNi and ZnNi-TiO_2, respectfully. The ZnNi coating undergoes the most drastic change in OCP in the 24 h time frame. The ZnNi-TiO_2 appears to reach a steady state at a faster rate than ZnNi, possibly due to the smaller grain size of the particles due to nanoparticle incorporation [35]. There is a small positive shift in all coatings, due to dissolution of zinc on the surface of the coating, as zinc undergoes a sacrificial protection method.

The polarization of ZnNi and ZnNi-TiO_2 coatings were found to have a larger corrosion current after 24 h of submersion in 0.05 M Na_2SO_4 solution than the as deposited coatings but the ZnNi-TiO_2 coating still maintained a smaller corrosion current value than the ZnNi coating even after immersion (**Table 4**). The microstructure of as deposited and submerged coatings was examined to determine any structural design which could affect the corrosion current of each coating. The incorporation of TiO_2 nanoparticles decreased the grain size of the metallic phase and the coatings appear more rough and irregular in surface morphology [35]. The initial increase in corrosion current observed by ZnNi-TiO_2 coatings prior to submersion are attributed to the smaller grain size and more porous structure observed in the coatings. The higher porosity of the coatings could be the cause of the increased corrosion resistance [34, 35]. Polarization curves and kinetic data show ZnNi-TiO_2 and ZnNi deposits initially have a high

corrosion density (0.4–0.6 mA/cm^2) and low polarization resistance. At 24 h immersion in the Na_2SO_4 solution, the i_{corr} of the ZnNi-TiO_2 coating has decreased by a factor of 5 and the R_p had increased by a factor of 3. The ZnNi-TiO_2 coating presented the highest corrosion protection after 24 h immersion [35]. ZnNi-TiO_2 coatings were examined in 3.5% NaCl solution and a decrease in corrosion current density was observed as TiO_2 was incorporated into the coating, with a decreasing trend following increased sonication of the particles prior to deposition [36]. Coatings throughout literature demonstrate a wide array of corrosion potentials, varying from E = −0.5 to −1.2 V, which follow values found for ZnNi coatings [12, 28, 30–32, 34–37, 39, 43, 44]. The value of the corrosion potential, which can show corrosion tendencies, is indicative of the components of the coatings. The optimal corrosion potential will lie between that of a pure zinc coating and a pure nickel coating, as it will have character of each metal and with that, corrosion behavior of each metal. The corrosion current, which is proportional to the corrosion rate, does decrease with the incorporation of nanoparticles as demonstrated in **Table 4**. The addition of nanoparticles, even in small amounts shows an overall improvement on the corrosion potential, corrosion current and resistivity of the systems.

Momeni et al. studied ZnNi-TiO_2 coatings on copper substrates as a possible coating for antibacterial inhibition, specifically the antibacterial resistance toward Gram positive (*Staphylococcus aureus* PTCC1431) and Gram negative (*E. coli* PTCC1394) bacteria through an inhibition zone method (**Figure 4**). The bacterial strains were transferred into flasks containing nutrient broth and bacteria which had been cultured at 37°C under aerated conditions. An agar diffusion test was used to study antibacterial activity. Inoculums of *E. coli* and *S. aureus* were spread over the surface of the nutrient agar, and the ZnNi-TiO_2 sample was placed

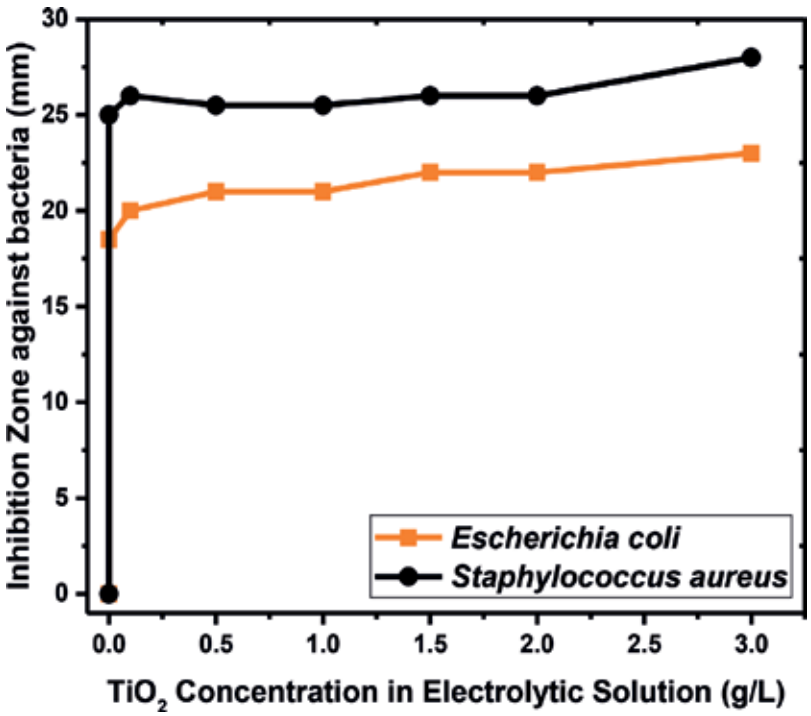

Figure 4. Inhibition capability of ZnNi-TiO_2 coatings with increase of TiO_2 in the electrolytic bath [14].

onto this sample and incubated for 24 h at 37°C. The best coating was found to be ZnNi-TiO_2 prepared with 3 g/L TiO_2 in solution, which had an inhibition zone of 23 mm for *E. coli* and 28 mm for *S. aureus* [11].

4.3. ZnNi-SiO_2 and ZnNi-SiC

SiO_2 and SiC comprise ~20% of the literature on ZnNi-nanocomposite coatings. SiO_2 was examined by Tuaweri and Wilcox. They studied the change in current density as a function of % Ni in the deposit with and without bath agitation, and with varying SiO_2 particle size. SiO_2 is believed to deposit with the ZnNi coating under a codeposition mechanism. As expected, without SiO_2 presence in the bath, nickel appears to follow an anomalous deposition mechanism as the current density of the system is increased from 3 to 6 A/dm^2. When 26 g/L of 20 nm SiO_2 particles was added to the system, a transition from anomalous to normal deposition is noted at 4 A/dm^2 [38]. The SiO_2 colloids have been previously noted to increase deposition rate of Fe group metals [40]. SiO_2 colloids shift this deposition from an anomalous mechanism to a normal mechanism. A possible explanation is due to adsorption of the Fe group metals onto the SiO_2 nanoparticles in the electrolytic bath. During the deposition process, the pH of the electrolyte at the working electrode surface increases, or becomes more alkaline due to removal of hydrogen by the generation of hydrogen gas, also known as hydrogen evolution. The SiO_2 particles tend to agglomerate once a neutral pH is reached, so the agglomerated colloid can suppress $Zn(OH)_2$ formation causing a slowing in the diffusion of zinc ions from the solution, through the inner layer and to the cathode for reduction. As the SiO_2 particle size was increased from 20 nm to 2 μm, a slightly higher nickel wt. % was observed in the coatings. Addition of the SiO_2 nanoparticles resulted in increased Ni wt. % at all current densities, as compared to coatings without SiO_2. This suggests that the SiO_2 in the bath encourages the deposition of nickel in the coating. Throughout the studies SiO_2 appears to have an overall effect on the deposition mechanism of ZnNi coatings through emergence of a normal deposition route, while SiC continues to follow an anomalous deposition pattern. Further studies need to be completed in this area to determine if increased particle presence will encourage a transition from anomalous to normal deposition for other systems or if this is unique to the behavior of SiO_2 nanoparticles in the ZnNi electrolytic system.

Tuaweri et al. found the corrosion potentials of ZnNi and ZnNi-SiO_2 coatings were more anodic as compared to zinc. Under open circuit potential conditions, ZnNi and ZnNi-SiO_2 coatings behave in a similar manner, but once the applied potential is increased, the ZnNi-SiO_2 coatings shift toward more anodic potentials as compared to ZnNi coatings. This suggests the presence of SiO_2 promoted shifting of the dissolution potential to more anodic values as compared to ZnNi due to the inert nature of SiO_2 particles and possible changes in the deposition mechanism in the presence of SiO_2. SiO_2 appears to have an overall effect on properties such as deposit texture, morphology, microstructure due to the ability of the SiO_2 particles to provide barrier protection to the coating through packing of microholes, gaps and crevices in the coating [38]. The incorporation of SiC and SiO_2 nanoparticles shows no changes on phase composition, with γ-phase being the predominant phase in the XRD patterns. Some Zn_{101}, Zn_{102} and δ-phase XRD peaks were observed, but this was expected as these coatings were deposited under acidic conditions. Low intensity peaks corresponding to SiO_2 confirms incorporation of the nanoparticles into the coatings without leading to any structural phase changes [39, 42].

In other nanoparticle coatings, we find similar trends such as finely grained, uniform, clearly pronounced crystal structures with the incorporation of SiO_2 and SiC [26, 38, 40, 41]. Finer grains were common with even distribution of the nanoparticle in the coatings [42]. SiO_2 coatings were examined for hardness changes, and showed an increase in hardness with an increase in current density during deposition of the coatings. Coatings were deposited from 2.0–5.0 A/dm^2 in increments of 1, and hardness values increased correspondingly from 155 to 210 HV. The improved hardness of the coating was attributed to the incorporation of SiO_2 particles which add mechanical strength due to embedded SiO_2 particles [39].

4.4. ZnNi-CeO_2 and SiO_2/CeO_2

ZnNi-CeO_2 coatings comprise ~8% of the literature, while ZnNi-SiO_2/CeO_2 comprises ~4%. Nanoparticle incorporation was found to be improved through pulsed deposition methods [43, 44]. Exbrayat et al. examined ZnNi coatings with ceria incorporation and confirmed the presence of single phase γ Ni_5Zn_{21} with preference to the (330) plane as previously observed in other deposition systems. The intensity of the (600) reflection increases with the addition of ceria particles, which could be attributed to the preferential incorporation of ceria nanoparticles at the grain boundaries which affects the overall growth of the crystals [44]. The incorporation of CeO_2 nanoparticles is shown in **Figure 5** for the SEM micrographs. Ceria nanoparticles were first added to the electrolytic bath without prior sonication (**Figure 5a**), and the nanoparticles agglomerated into long string-shape structures. Due to the agglomeration tendancies of the nanoparticles, sonication of the nanoparticles prior to depositon was examined. The coatings obtained from the sample post sonication (**Figure 5b**) take on a pyramidal growth pattern and appear more coarse. EDX was used to determine placement of the nanoparticles in the coating and the CeO_2 particles appear to be primarily adsorbed onto the electrode surface. The agglomerated nanoparticles appear uniformly trapped inside the metal matrix. Ultrasonic agitation was done at 20°C with an amplitude value of 35 (power of 41 W/cm^2, output frequency of 20 kHz) for 20 min prior to deposition. As the samples were sonicated prior to deposition, the agglomerated particles dispersed and were able to better fill the voids and pores naturally formed in the matrix, leading to better overall corrosion protection [43, 44]. Improvement of nanoparticle incorporation through the use of ultrasonication, previously noted for other systems including TiO_2 and Al_2O_3 was also noted for CeO_2 [32, 33, 36, 43, 44].

The OCP of ZnNi-CeO_2 coatings was measured in 3.5% NaCl and near-neutral 0.05 M Na_2SO_4 solutions, respectively and monitored over time [44]. Exbrayat et al. studied two differing ZnNi-CeO_2 samples, ZnNi-CeO_2 which was determined to contain 84% Zn, 14% Ni and 2% CeO_2 and ZnNi-Ce_2 (sonicated) which was found to contain 85% Zn, 12.8% Ni and 2.2% CeO_2. When first submerged in the Na_2SO_4 solution, the OCP values changed drastically for ZnNi, ZnNi-CeO_2 and ZnNi-CeO_2 (sonicated). For ZnNi, a significant ennoblement was observed moving from an OCP value more cathodic than E = −0.95 V to E = −0.55 V after ~20 h of submersion. The OCP then begins to decrease steadily before stabilizing at ~E = −0.65 V after 96 h of immersion. ZnNi-CeO_2 (sonicated) follows a similar pattern to ZnNi, with a shift in OCP from ~E = −0.85 V initially to ~−0.57 V after 30 h of submersion, while ZnNi-CeO_2 which was not sonicated prior to deposition, stayed relatively stable throughout the 4 day submersion test, decreasing in OCP from ~E = −0.82 V to ~E = −0.75 V. Zinc coatings often settle

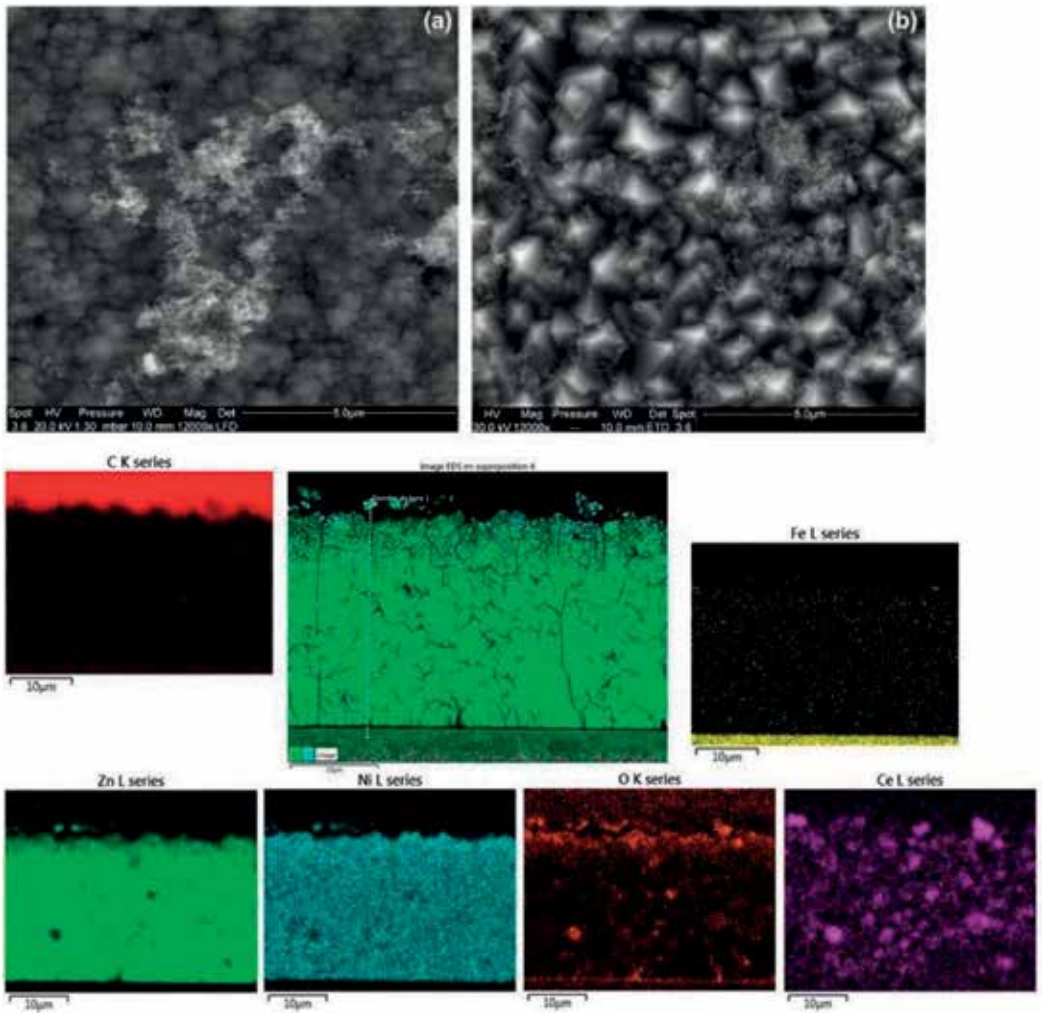

Figure 5. SEM micrographs of electrodeposited ZnNi-CeO_2 nanoparticle coatings without prior sonication (a) and with prior sonication (b), and X-ray maps of the main elements in the coating. "Reprinted with permission from [50]. Copyright [2017], John Wiley and Sons."

over the initial submersion due to the formation of corrosion products, which then begin to protect the coating [43, 44]. EIS of ZnNi-CeO_2 coatings were examined using a PGP 301 Autolab potentiostat after 24, 48, 96 h immersion in 35 g/L saline solution at 25°C with a frequency range of 64 kHz to 1 mHz, AC voltage amplitude of ±10 mV. Analysis was completed with Zview software. The Nyquist diagrams exhibit two capacitive loops at middle and low frequencies, with similar time constants. The loop diameter of the ZnNi coating remains relatively constant, suggesting stability in the corrosion rate. In the nanocomposite coatings, the loop diameter increased with immersion time. The incorporation of ceria enhances the corrosion resistance by ennoblement of the surface through reduction of galvanic corrosion of the steel [44].

4.5. ZnNi-carbon nanotubes

ZnNi-carbon nanotubes comprise ~8% of the literature to date. The dispersion, linear sweep voltammetry, surface morphology and friction properties of ZnNi coatings with nanotube incorporation was discussed. When carbon nanotubes were introduced into a ZnNi electrolytic solution, a positive shift (~0.1 V) in the polarization curves were observed and the deposition current of the system increased. The transport of the carbon nanotubes to the cathode surface and their incorporation into the coating is believed to be due to adsorption of Zn^{2+} and Ni^{2+} ions onto the nanotubes which are then reduced onto the coating, thereby entrapping the nanotubes in the coating. Initially the nanoparticles are weakly adsorbed onto the cathode, but once the particles lose their ionic and solvation shells, they become securely attached to the surface of the deposit. The adsorbed metal ions on the surface of the dispersed phase discharge at this point permanently attaching the nanotube to the coating [13, 45]. The actual deposition mechanism is not discussed in this work, so it is unclear if the nanotubes have an overall effect on the deposition mechanism or if anomalous deposition is still followed for this system.

In the case of carbon nanotubes, they are believed to act as nuclei for crystallization, further promoting even distribution of the nanotubes throughout the cathode surface. Microcracks are often observed in ZnNi coatings, but once carbon nanotubes have been added to the electrolytic mixture, the surface appears uniform and dense.

Another property examined for ZnNi-carbon nanotube nanocomposites was the sliding friction coefficient of the coatings as compared to ZnNi coatings. The ZnNi-carbon nanotube coatings were found to have a sliding friction coefficient 1.3–1.5 times smaller than ZnNi coatings without nanotube disbursement both in direct current and reverse current deposition modes. ZnNi coatings showed a decrease in friction coefficient values from 0.30 to 0.24 for current densities changing from 1.0 to 2.5 (A/dm^2) while the corresponding ZnNi-carbon nanotube coatings decreased from 0.23 to 0.17 for the same current density values. Under a reverse current mode, ZnNi coatings had friction coefficients starting at 0.31 and decreasing to 0.23 as the ratio between cathodic and anodic periods was increased from 10:1 to 16:1 while for ZnNi-carbon nanotube coatings under the same conditions, the friction coefficients decreased from 0.24 to 0.15 [13, 45].

4.6. ZnNi-Mt

The effect of montmorillonite (Mt) addition to the ZnNi bath was examined through anodic linear sweep voltammetry (ALSV) as presented in **Figure 6**. Montmorillonite is a smectite mineral and has a 2:1 layered structure, with two layers of silicon tetrahedral sandwiching one layer of aluminum octahedral. The layers can be stacked together, but when the van der Waals forces holding the individual clay layers together are overwhelmed, the individual layers become exfoliated (also known as delaminated). For this work, mechanical agitation and/or sonication was used to exfoliate the layered silicate and produce individual nanoplatelets. Individual montmorillonite nanoplatelets exist as coordinated layers, measuring 1–2 nm thick. Mt is a hydrous aluminum silicate with approximate formula (Na,Ca) $(Al, Mg)_6(Si_4O_{10})_3$-$(OH)_6.nH_2O$. The Al^{3+} and Si^{4+} locations can be replaced by lower valent cations, causing the montmorillonite structure to have an excess of electrons. The negative

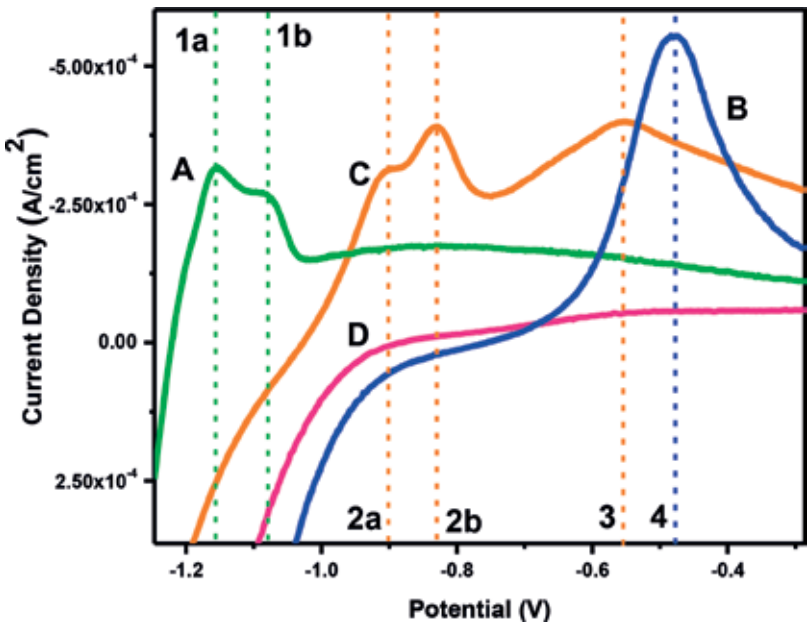

Figure 6. Anodic linear sweep voltammetry (ALSV) data of 1:1 molar ratio equivalent of $ZnSO_4H_2O$: $Ni(NH_4)_2(SO_4)_26H_2O$ all solutions prepared in 0.1 g/100 mL Mt in 0.1 M borate solution, pH = 9.40 with NH_4OH, sweep rate of 50 mV/S. (A) Zn^{2+}; (B) Ni^{2+}; (C) Zn^{2+} and Ni^{2+}; (D) no Zn^{2+} or Ni^{2+} present; (1a, 1b) anodic stripping potentials of Zn^{2+}; (2a, 2b) anodic stripping potentials of Zn^{2+} in presence of Ni^{2+}; (3) anodic stripping potential Ni^{2+} in presence of Zn^{2+}; (4) Ni^{2+} anodic stripping potential [54].

charge is compensated through loosely held cations from the associated water. Sodium montmorillonite, the clay mineral in which the loosely held cation is the Na^+ ion, was the clay source used throughout the work. ALSV was used to obtain initial dissolution data of Zn^{2+} and Ni^{2+} ions in solution, as well as any electrochemical effect of the Mt nanoparticles on the metal dissolution peaks and the electrochemical behavior of Mt. The potential was scanned from OCP to E = −1.5 V (vs. SCE) at a sweep rate of 50 mV/s, held briefly and scanned back to OCP. During the anodic scan, the metals of interest were stripped back into the electrolytic solution. As previously observed for zinc-nickel systems under anomalous deposition control [57, 62, 69, 79], the anodic stripping peaks of the metals in solution are shifted based on other metal species in solution. According to the linear sweep voltammetry (LSV) data, zinc in the electrolytic solution had two anodic dissolution peaks present at potentials of E = −1.12 V and E = −1.08 V. During the cathodic scan, a small $Zn(OH)_2$ layer deposits on the steel surface, slowing down dissolution kinetics. The dissolution of this species caused the second peak in the LSV [48, 57, 88]. Nickel had an anodic dissolution peak present at a potential of E = −0.48 V. When combined in solution, the zinc anodic dissolution peaks were shifted to potentials of E = −0.91 V, E = −0.83 V and the nickel anodic dissolution peak was shifted to a potential of E = −0.55 V. As previously stated, the zinc-nickel dissolution peaks of zinc and nickel are shifted in potential with respect to the individual metals in solution and this is indicative of an anomalous deposition system [51, 70, 76]. With the presence of Ni^{2+} in the system, Zn^{2+} is able to deposit at a more positive potential, and the nickel potential is shifted cathodically as previously observed in ZnNi systems [57, 62, 79, 82]. As

ZnNi is known to undergo anomalous deposition, the dependence of the metal dissolution peaks relative to one another was expected [48, 50, 65, 68]. The added Mt appeared electrochemically inactive itself and has no overall effect on the anomalous deposition previously observed for ZnNi coating deposition [48].

Though the effect of pH was not discussed in most works, it was studied with the addition of Mt nanoparticles by monitoring the pH of the baths with and without Mt addition over a period of days to determine overall stability of the system. More acidic plating conditions lead to nonuniform coatings, specifically areas of low to no corrosion protection on the underlying substrate [49]. In **Figure 7**, line A represents the system with zinc, nickel and ammonium hydroxide (starting pH = 9.40), line B represents the system with zinc, nickel, ammonium hydroxide and borate (starting pH = 9.40) and line C represents the line with zinc, nickel, ammonium hydroxide, borate and Mt (starting pH = 9.40). The horizontal dot-dash line represents pH 9.21, where the zinc equilibrium species exists (Zn^{2+} and $HZnO_2^-$) [57]. Since this work is based at a pH range near this equilibrium, careful control of the pH is needed throughout all studies. The systems were closed to air for 7 days, then opened to atmosphere and monitored for an additional 32 h. Upon exposure to atmosphere, there was a definite decrease in pH as compared to closed systems for the previously stable baths. Line C (containing Mt in the system) decreased in pH at a slower rate than line B (not containing Mt) suggesting the Mt has an additional effect on the stabilization of metal species in solution. The system without borate or Mt addition passed through pH 9.21 (zinc equilibrium) even as a closed system (Line A). After 7 days the pH of the system with Zn, Ni and NH_4OH had decreased from pH = 9.40 to 9.17, the system with Zn, Ni, borate and NH_4OH had decreased from pH = 9.40 to 9.37 and the system with Zn, Ni, borate, NH_4OH and Mt had decreased

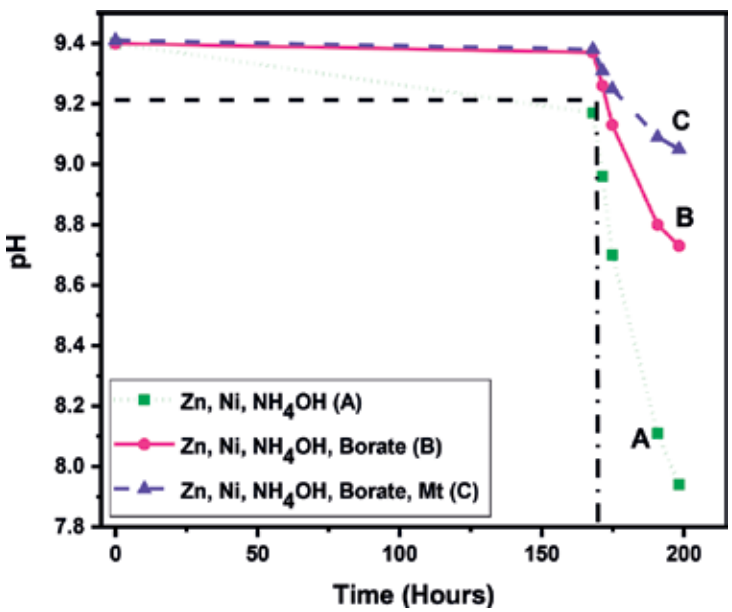

Figure 7. pH studies of electrochemical bath solutions in atmosphere and in a closed system over time. (A) Zn^{2+}, Ni^{2+}, and NH_4OH (dot); (B) Zn^{2+}, Ni^{2+}, 0.1 M borate and NH_4OH (solid); (C) Zn^{2+}, Ni^{2+}, Mt, borate and NH_4OH (dash) [54].

from pH = 9.40 to 9.38. Once opened to atmosphere, it took the borate system 4.5 h to reach a pH of 9.21 and a pH of 8.73 after 32 h, a total decrease of 0.64 pH units. The borate/Mt system reached pH 9.21 after 10 h of exposure to atmosphere and a pH of 9.05 after 32 h, a decrease of 0.33 pH units. The nonstabilized system (no borate or Mt) reached pH 7.94 after 32 h of exposure to atmosphere, a total decrease of 1.46 pH units. The decrease in pH in the closed system is due to formation of metal hydroxide species forming and precipitating out of solution. The large decrease in pH upon exposure to the atmosphere is due to absorption of carbon dioxide from the air [48, 57]. The system with borate demonstrates a clear stabilization of the system when in a closed system, and absorbs CO_2 at a slower rate as compared to the system without borate. The addition of exfoliated Mt nanoparticles further stabilized the system, as shown in the relatively slow pH decrease in this system when closed to air and when opened to atmosphere. The nanoparticles stabilize the pH of the bath improving the deposition of the nanocomposite coating [48].

In the case of ZnNi-Mt nanocomposites, **Figure 8**, XRD pattern had a strong (330) reflection present at 2θ = 42.9°, indicative of ZnNi γ-phase alloy formation with a (330) preferred orientation as previously observed in coatings without nanoparticle incorporation [57, 62, 79]. The coating of pattern B was formed under the same conditions as pattern A, but Mt nanoparticles were dispersed into the electrolyte solution and incorporated into the resulting coating. Since Mt nanoparticles do not give diffraction peaks upon exfoliation, no additional peaks were observed due to its presence [2, 8, 52, 58, 66, 89]. The coating with Mt

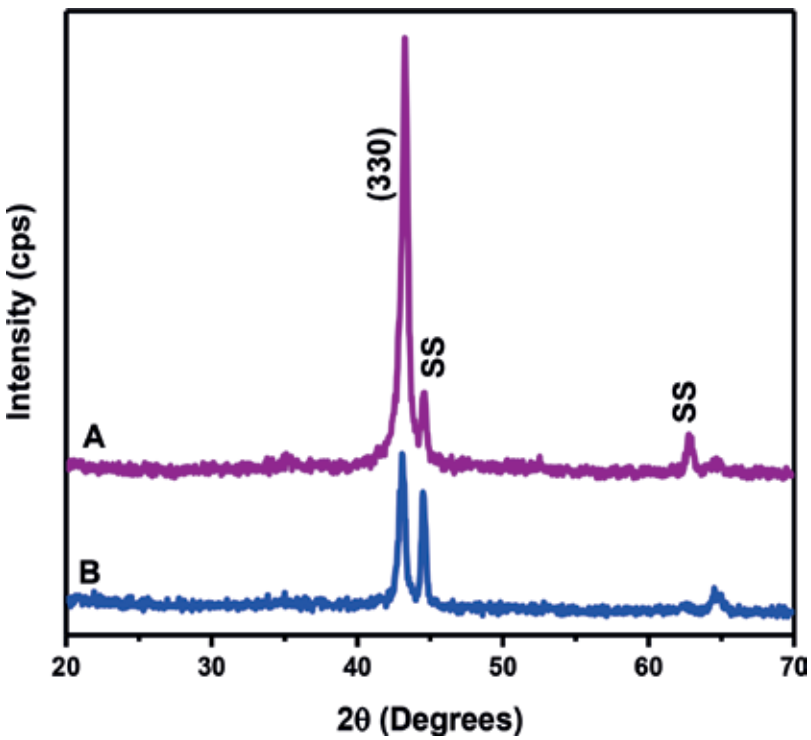

Figure 8. X-ray diffraction patterns of (A) ZnNi and (B) ZnNi Mt scanned from 20 to 70 2Θ at a step size of 0.05° and a dwell time of 1 second [54].

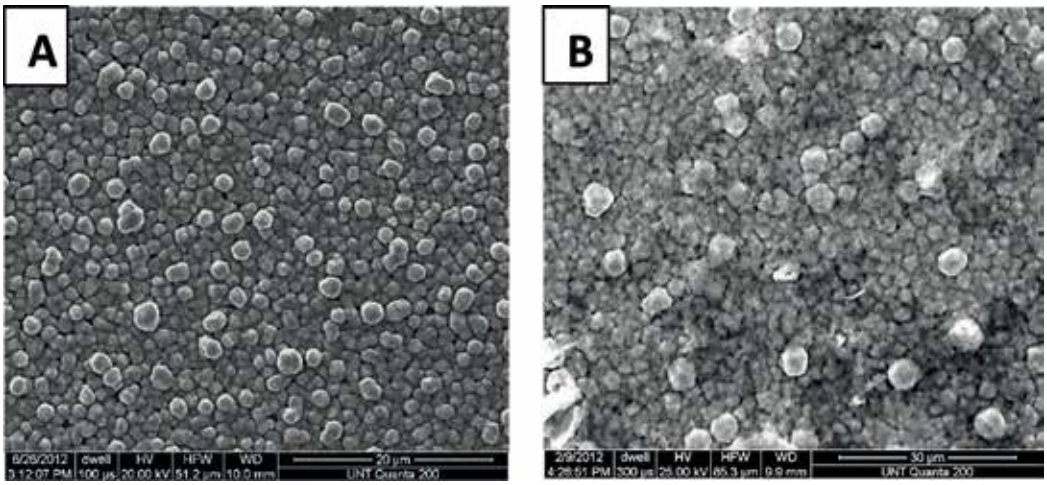

Figure 9. SEM micrographs of (A) ZnNi γ-phase alloy; (B) ZnNi Mt γ-phase nanocomposite alloy [54].

incorporation was thin as compared to the alloy coating without Mt but the γ-phase alloy was still formed even in the presence of Mt, confirming the Mt did not affect the deposition of the alloy phase of interest. The incorporation of Mt into the coating is shown in **Figure 9**. Films with Mt incorporation have strong adherence, small grain size and overall good coverage of the stainless steel substrate. Small spherical particles covered the surface and no voids appeared present in the coating. The structure was not affected by the incorporation of Mt under these conditions. A strong overall coverage of the substrate material was observed, and particles of exfoliated clay were observed, confirming clay presence within the coating.

The potentiodynamic polarization curves of the electrodeposited zinc-nickel and zinc-nickel-Mt nanocomposite alloys in 3.5% NaCl solution are illustrated in **Figure 10** and the corrosion current and potential are given in **Table 4**.

In previous studies ZnNi coatings with optimal corrosion resistance was found to have a corrosion potential (E_{corr}) more anodic as compared to pure zinc but more cathodic as compared to pure nickel. The optimal coatings had a corrosion potential around E = −0.74 V in that study [57]. In this study, the ZnNi-Mt nanocomposite coating had a corrosion potential of E = −0.73 V, which is in agreement with previous findings (**Table 4**). This value is slightly more cathodic (10 mV) than the coatings without Mt incorporation. The high zinc content (~90%) of the coating (confirmed with AAS and ICP-MS) but more cathodic corrosion potential are in the optimal range for improved protection. Corrosion current density is the primary parameter used for evaluating the kinetics of the corrosion reaction. The lower corrosion current density, the better corrosion protection. The corrosion current density for the zinc-nickel γ-phase alloy was 1.06×10^{-5} A/cm^2 and the corrosion current density for the ZnNi-Mt γ-phase nanocomposite alloy was 3.72×10^{-6} A/cm^2. The corrosion current density of the nanocomposite alloy was lower as compared to the alloy without Mt denoting an improved corrosion resistance. R_p of the coating with Mt was 34,900 Ω cm^2 as compared to 30,485 Ω cm^2 for the coating without Mt further confirming the results of improved protection with incorporation of Mt [48].

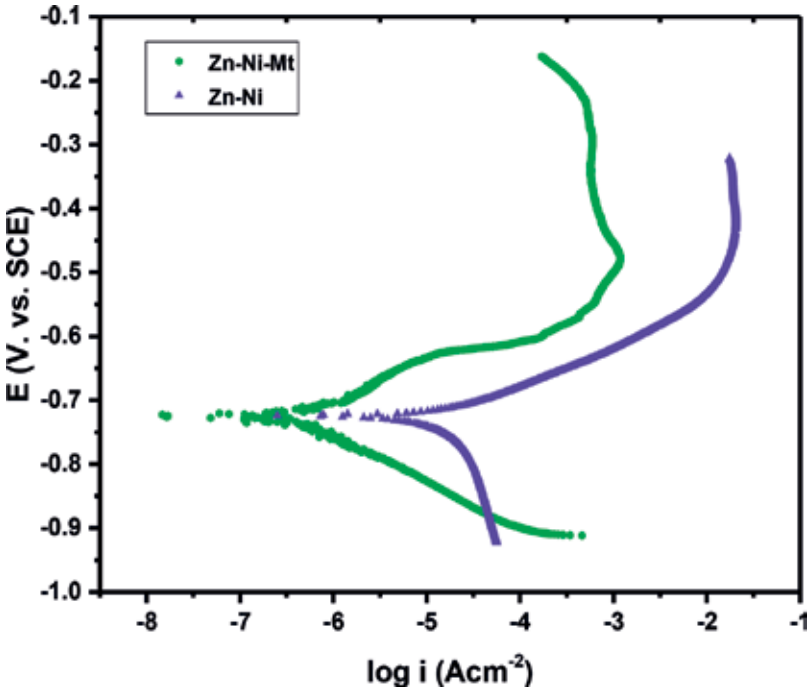

Figure 10. Potentiodynamic polarization curves of ZnNi and ZnNi-Mt nanocomposite coatings, electrolyte NaCl, 3.5 wt %, at scan rate 0.1667 mV/s [54].

5. Conclusions

ZnNi nanocomposites can be formed by incorporating nanoparticles into the coating during an electrochemical deposition. The nanoparticles under study do not appear to affect the electrochemical behavior or electrochemical deposition mechanism of zinc-nickel γ-phase alloy formation. Anomalous deposition of the zinc-nickel alloy was observed which is consistent with formation of the γ-phase alloy, but small anodic shifts were observed in the ALSV scans of the metal species in the ZnNi-Mt bath as compared to baths without Mt nanoparticles present. Al_2O_3 also noted no overall effect on the electrochemical behavior of the system. The addition of nanoparticles, including Mt, SiC and Al_2O_3 also affected the onset of hydrogen evolution, pushing the onset to more cathodic potentials, which can be an advantage in an aqueous plating system as it broadens the working window for the deposition. Zinc-nickel γ-phase deposition requires a high overpotential to overcome the kinetic limitations of nickel deposition, this added benefit of shifting the reduction of the metals anodically with the onset of hydrogen appearing more cathodically, leads to alloy formation with less entrapped hydrogen.

Particle dispersion in the electrolytic bath is an important factor when considering deposition. Optimal corrosion protection is acquired from systems with better dispersion of nanoparticles in the system. When nano-Al_2O_3 particles were dispersed uniformly throughout the coating, and incorporated in the matrix, they were able to protect the coating from corrosive medium, increasing the corrosion potential and retarding corrosion onset. Agglomerated nano-Al_2O_3

particles on the other hand, would combine loosely with the metal matrix, or fall off the coating entirely, leading to gaps and pores in the coating which were easily attacked by corrosion cells. All studies treated the nanoparticles prior to deposition to cause disruption and dispersion of the particles in the plating bath through stirring or sonication, but no studies have been found discussing the overall effect on the particles and any benefits or drawbacks of one method compared to another. It was noted that sonication during deposition leads to better incorporation and higher concentrations of nanoparticles in the final coatings. In addition to sonication, pulse current and pulse potential deposition tends to lead to better incorporation of the nanoparticles in the resulting coating. Up to 11% nanoparticle incorporation was noted throughout the studies, with confirmation of ZnNi-TiO_2, Al_2O_3, SiO_2, SiC, CeO_2, Al_2O_3/SiC, CeO_2/SiO_2, Mt and carbon nanotubes.

XRD results confirm formation of γ-phase ZnNi-nanocomposite coatings throughout the studies. Interestingly, in acidic conditions without nanoparticle incorporation, acidic electrolytic baths tended to give impure ZnNi coatings, with a mixture of γ and δ-phase ZnNi coatings. The studies with ZnNi nanoparticles show almost exclusive γ-phase ZnNi alloys, which previously was primarily observed under alkaline conditions. The crystallite size decreased with the increase of nanoparticle incorporation in the coatings. Mt nanoparticles have been successfully incorporated into the alloy coatings with no disruption in the crystal structure of the zinc-nickel γ-phase alloys, deposited with a preferred (330) orientation. The incorporation of TiO_2, Al_2O_3 and CeO_2 was also confirmed with XRD. The morphology of the coatings shows incorporation of the nanoparticles, with small, compact like structures and few cracks or holes. The hardness of the coatings increased as nanoparticle concentration in the coating was increased.

Corrosion studies all show nanoparticle incorporation into ZnNi coatings leads to lower corrosion currents, suggesting a lower corrosion rate for the coatings. The nanoparticles are believed to fill the crevices, gaps and holes within and on the surface of the coatings, leading to improved corrosion resistance. Overall the corrosion protection offered by the ZnNi-nanocomposite coatings was improved as compared to pure ZnNi coatings.

Author details

Heidi Conrad[1]* and Teresa D. Golden[2]

*Address all correspondence to: h.conrad@tcu.edu

1 Texas Christian University, Fort Worth, Texas, United States

2 University of North Texas, Denton, Texas, United States

References

[1] Musiani M. Electrodeposition of composites: An expanding subject in electrochemical materials science. Electrochimica Acta. 2000;**45**:3397-3402. DOI: 10.1016/S0013-4686(00)00438-2

[2] Tientong J, Ahmad YH, Nar M, D'Souza N, Mohamed AMA, Golden TD. Improved mechanical and corrosion properties of nickel composite coatings by incorporation of layered silicates. Materials Chemistry and Physics. 2014;**145**:44-50. DOI: 10.1016/j.matchemphys.2014.01.025

[3] Szcygiel B, Kolodziej M. Composite Ni/Al_2O_3 coatings and their corrosion resistance. Elecrochim. Acta. 2005;**50**:4188-4195. DOI: 10.1016/j.electacta.2005.01.040

[4] Ciubotariu AC, Benea L, Lakatos-Varsanyi M, Dragan V. Electrochemical impedance spectroscopy and corrosion behaviour of Al_2O_3-Ni nano composite coatings. Electrochimica Acta. 2008;**53**:4557-4563. DOI: 10.1016/j.electacta.2008.01.020

[5] Thurber CR, Ahmad YH, Sanders SF, Al-Shenawa A, D'Souza N, Mohamed AMA, et al. Electrodeposition of 70/30 Cu-Ni nanocomposite coatings for enhanced mechanical and corrosion properties. Current Applied Physics. 2016;**16**:387-396. DOI: 10.1016/j.cap.2015.12.022

[6] Abdulwahab M, Fayomi OSI, Popoola API, Dodo MR. In-situ hybrid study of thermal behaviour of Zn-Ni and Zn-Ni-Al_2O_3 nanocrystallite thin films induced TEA/MEA by electrodeposition. Results in Physics. 2017;**7**:213-215. DOI: 10.1016/j.rinp.2016.11.017

[7] Low CTJ, Wills RGA, Walsh FC. Electrodeposition of composite coatings containing nanoparticles in a metal deposit. Surface and Coating Technology. 2006;**201**:371-383. DOI: 10.1016/j.surfcoat.2005.11.123

[8] Ahmad YH, Tientong J, Nar M, D'Souza N, Mohamed AMA, Golden TD. Characterization and corrosion resistance of electrodeposited Ni-Mo-silicate platelet nanocomposite coatings. Surface and Coating Technology. 2014;**259**:517-525. DOI: 10.1016/j.surfcoat.2014.10.036

[9] Ahmad YH, Tientong J, D'Souza N, Golden TD, Mohamed AMA. Salt water corrosion resistance of electrodeposited Ni-layered silicate nanocomposite coatings from watts' type solution. Surface and Coating Technology. 2014;**242**:170-176. DOI: 10.1016/j.surfcoat.2014.01.040

[10] Roos JR, Celis JP, Fransaer J, Buelens C. The development of composite plating for advanced materials. Journal of Metals. 1990;**11**:60-63. DOI: 10.1007/BF03220440

[11] Momeni MM, Hashemizadeh S, Mirhosseini M, Kazempour A, Hosseinizadeh SA. Preparation, characterization, hardness and antibacterial properties of Zn-Ni-TiO_2 nanocomposite coatings. Surface Engineering. 2016;**32**(7):490-494. DOI: 10.1179/1743294415Y.0000000049

[12] Blejan D, Muresan LM. Corrosion behavior of Zn-Ni-Al_2O_3 nanocomposite coatings obtained by electrodeposition from alkaline electrolytes. Materials and Corrosion. 2013;**64**(5):433-438. DOI: 10.1002/maco.201206522

[13] Tseluikin VN, Koreshkova AA. Synthesis and properties of zinc-nickel-carbon Nanotube composite coatings. Russian Journal of Applied Chemistry. 2016;**89**(6):1027-1030. DOI: 10.1134/s1070427216060288

[14] Hovestad A, Janssen LJJ. Electrochemical codeposition of inert particles in a metal matrix. Journal of Applied Electrochemistry. 1995;**25**:519-527. DOI: 10.1007/BF00573209

[15] Yeh SH, Wan CC. Codeposition of SiC powders with nickel in a watts bath. Journal of Applied Electrochemistry. 1994;**24**:993-1000. DOI: 10.1007/BF00241190

[16] Mohajeri S, Dolati A, Ghorbani M. The photoinduced activity of Ni-TiO_2/TiO_2 multilayer Nanocomposites synthesized by pulse Electrodeposition technique. International Journal of Electrochemical Science. 2017;**12**:5121-5141. DOI: 10.20964/2017.06.50

[17] Li B, Zhang W, Huan Y, Dong J. Synthesis and characterization of Ni-B/Al_2O_3 nanocomposite coating by electrodeposition using trimethylamine borane as boron precursor. Surface and Coating Technology. 2018;**337**:186-197. DOI: 10.1016/j.surfcoat.2018.01.018

[18] Tam J, Jiao Z, Lau JCF, Erb U. Wear stability of superhydrophobic nano Ni-PTFE electrodeposits. Wear. 2017;**374-375**:1-4. DOI: 10.1016/j.wear.2016.12.023

[19] Tang A, Wang M, Huang W, Wang X. Composition design of Ni-nano-Al_2O_3-PTFE coatings and their tribological characteristics. Surface and Coating Technology. 2015;**282**: 121-128. DOI: 10.1016/j.surfcoat.2015.10.034

[20] Frade T, Gomes A, da S, Pereira MI, Alberts D, Pereiro R, et al. Studies on the stability of Zn and Zn-TiO_2 Nanocomposite coatings prepared by pulse reverse current. Journal of the Electrochemical Society. 2011;**158**(3):C63-C70. DOI: 10.1149/1.3531949

[21] Boshkov N, Koleva DA, Petrov P, Tsvetkova N. Corrosion resistant Nano-composite metallic coatings with embedded polymeric aggregates. In: Magagnin L, editor. Engineered Metal Matrix Composites: Forming Methods, Material Properties and Industrial Applications. 1st ed. Hauppauge, N.Y.: Nova Science Publishers; 2013. pp. 261-282. ISBN: 978-1-62081-719-3

[22] Azizi M, Schneider W, Plieth W. Electrolytic co-deposition of silicate and mica particles with zinc. Journal of Solid State Electrochemistry. 2005;**9**:429-437. DOI: 10.1007/s10008-004-0572-3

[23] Praveen BM, Venkatesha TV. Electrodeposition and properties of Zn-nanosized TiO_2 composite coatings. Applied Surface Science. 2008;**254**:2418-2424. DOI: 10.1016/j.apsusc.2007.09.047

[24] Ranganatha S, Venkatesha TV, Vathsala K, Punith kumar MK. Electrochemical studies on Zn/nano-CeO_2 electrodeposited composite coatings. Surface and Coating Technology. 2012;**208**:64-72. DOI: 10.1016/j.surfcoat.2012.08.004

[25] Vathsala K, Venkatesha TV. Zn-ZrO_2 nanocomposite coatings: Electrodeposition and evaluation of corrosion resistance. Applied Surface Science. 2011;**257**:8929-8936. DOI: 10.1016/j.apsusc.2011.05.067

[26] Tuaweri TJ, Wilcox GD. Influence of SiO_2 particles on zinc-nickel electrodeposition. Transactions of the IMF. 2007;**85**(5):245-253. DOI: 10.1179/174591907x229608

[27] Ghaziof S, Gao W. The effect of pulse electroplating on Zn-Ni alloy and Zn-Ni-Al_2O_3 composite coatings. Journal of Alloys and Compounds. 2015;**622**:918-924. DOI: 10.1016/j.jallcom.2014.11.025

[28] Ghaziof S, Gao W. Zn-Ni-Al_2O_3 nano-composite coatings prepared by sol-enhanced electroplating. Applied Surface Science. 2015;**351**:869-879. DOI: 10.1016/j.apsusc.2015.06.010

[29] Ataie SA, Zakeri A. Improving tribological properties of (Zn-Ni)/nano Al_2O_3 composite coatings produced by ultrasonic assisted pulse plating. Journal of Alloys and Compounds. 2016;**674**:315-322. DOI: 10.1016/j.jallcom.2016.02.111

[30] Shourgeshty M, Aliofkhazraei M, Karimzadeh A, Poursalehi R. Corrosion and wear properties of Zn-Ni and Zn-Ni-Al_2O_3 multilayer electrodeposited coatings. Materials Research Express. 2017;**4**:1-13. DOI: 10.1088/2053-1591/aa87d5

[31] Shourgeshty M, Aliofkhazraei M, Karimzadeh A. Study on functionally graded Zn-Ni-Al_2O_3 coatings fabricated by pulse-electrodeposition. Surface Engineering. **2018**:1-10. DOI: 10.1080/02670844.2018.1432172

[32] Zheng HY, An MZ. Electrodeposition of Zn-Ni-Al_2O_3 nanocomposite coatings under ultrasound conditions. Journal of Alloys and Compounds. 2008;**459**:548-552. DOI: 10.1016/j.jallcom.2007.05.043

[33] Zheng HY, An MZ, Lu JF. Surface characterization of the Zn-Ni-Al_2O_3 nanocomposite coating fabricated under ultrasound condition. Applied Surface Science. 2008;**254**:1644-1650. DOI: 10.1016/japsusc.2007.07.110

[34] Gomes A, Almeida I, Frade T, Taveres AC. Zn-TiO_2 and ZnNi-TiO_2 Nanocomposite Coatings: Corrosion Behaviour. Switzerland: Trans Tech Publications; 2010. DOI: 10.4028/www.scientific.net/MSF.636-637.1079

[35] Gomes A, Almeida I, Frade T, Tavares AC. Stability of Zn-Ni-TiO_2 and Zn-TiO_2 nanocomposite coatings in near-neutral sulphate solutions. Journal of Nanoparticle Research. 2012;**14**:692-704. DOI: 10.1007/s11051-011-0692-5

[36] Katamipour A, Farzam M, Danaee I. Effects of sonication on anticorrosive and mechanical properties of electrodeposited Ni-Zn-TiO_2 nanocomposite coatings. Surface and Coating Technology. 2014;**254**:358-363. DOI: 10.1016/jsurfcoat.2014.06.043

[37] Praveen BM, Venkatesha TV. Electrodeposition and corrosion resistance properties of Zn-Ni/TiO_2 Nano composite coatings. International Journal of Electrochemistry. 2001:1-4. DOI: 10.4061/2011/261407

[38] Tuaweri T, Jombo PP, Okpala AN. Corrosion resistance characteristics of Zn-Ni/SiO_2 composite coatings. International Journal of Advanced Science and Engineerin. 2014;**3**(2):1-12. DOI: 10.14810/ijamse.2014.3201

[39] Ullal Y, Hegde C. Corrosion protection of electrodeposited multilayer nanocomposite Zn-Ni-SiO_2 coatings. Surface Engineering and Applied Electrochemistry. 2013;**49**(2):161-167. DOI: 10.3103/S1068375513020142

[40] Takahashi A, Miyoshi Y, Hada T. Effect of SiO_2 colloid on the Electrodeposition of zinc-iron group metal alloy composites. Journal of the Electrochemical Society. 1994;**141**(4): 954-957. DOI: 10.1149/1.2054864

[41] Poliak NI, Anishchik VM, Valko NG, Karwat C, Kozak C, Opielak M. Mechanical properties of Zn-Ni-SiO_2 coating deposited under X-ray irradiation. Acta Physica Polonica, A. 2014;**125**(6):1415-1417

[42] Müller C, Sarret M, Benballa M. ZnNi/SiC composites obtained from an alkaline bath. Surface and Coating Technology. 2002;**162**:49-53. DOI: 10.1016/S0257-8972(02)00360-2

[43] Creus J, Rébéré C, Exbrayat L, Savall C, Fontaine J, Steyer P, et al. Corrosion behavior in saline solution of pulsed electrodeposited Nanocomposite Zn-Ni/CeO_2 coatings. In: Proceedings of the NACE International Conference on International Corrosion Series March 6-10, 2016, Vancouver Canada. December 2017. pp. 1-11

[44] Exbrayat L, Rébéré C, Eyame RN, Steyer P, Creus J. Corrosion behaviour in saline solution of pulsed-electrodeposited zinc-nickel-ceria nanocomposite coatings. Materials and Corrosion. 2017;**68**:1129-1142. DOI: 10.1002/maco.201709419

[45] Tseluikin VN, Koreshkova AA. Electrodeposition of zinc-nickel-carbon Nanotubes composite coatings in a reversing mode. Protection of Metals and Physical Chemistry of Surfaces. 2016;**52**(6):1040-1042. DOI: 10.1134/s2070205116060204

[46] Tulio PC, Rodrigues SEB, Carlos IA. The influence of SiC and Al_2O_3 micrometric particles on the electrodeposition of ZnNi films and the obtainment of ZnNi-SiC and ZnNi-Al_2O_3 electrocomposite coatings from slightly acidic solutions. Surface and Coating Technology. 2007;**202**:91-99. DOI: 10.1016/j.surfcoat.2007.04.084

[47] Xiang T, Zhang M, Li C, Dong C, Yang L, Chan W. CeO_2 modified SiO_2 acted as additive in electrodeposition of Zn-Ni alloy coating with enhanced corrosion resistance. Journal of Alloys and Compounds. 2018;**736**:62-70. DOI: 10.1016/j.jallcom.2017.11.031

[48] Conrad HA. Electrochemically deposited metal alloy-silicate nanocomposite corrosion resistant materials. Ph.D. Dissertation. Denton, TX: University of North Texas; 2013

[49] Rajendran S, Bharathi S, Vasudevan T. The electrodeposition of zinc-nickel alloy from a cyanide-free alkaline plating bath. Transactions of the IMF. 2000;**78**(3):129-133. DOI: 10.1080/00202967.2000.11871324

[50] Fedi B, Gigandet MP, Hihn JY, Mierzejewski S. Structure determination of electrodeposited zinc-nickel alloys: Thermal stability and quantification using XRD and potentiodynamic dissolution. Electrochimica Acta. 2016;**215**:652-666. DOI: 10.1016/j.electacta.2016.08.141

[51] Fratesi R, Roventi G. Electrodeposition of zinc-nickel alloy coatings from a chloride bath containing NH_4Cl. Journal of Applied Electrochemistry. 1992;**22**:657-662. DOI: 10.1007/BF1092615

[52] Lee L, Behera P, Sriraman KR, Chromik RR. The effect of contact stress on the sliding wear behavior of Zn-Ni electrodeposited coatings. Wear. 2018;**400-401**:82-92. DOI: 10.1016/j.wear.2017.12.018

[53] Dingwerth B, Eene van Schaik EG. Cost efficient and high performing: Zinc-alloy corrosion protection for threaded fasteners. Fastener + Fixing Technology, Technical Analysis. Fixing Magazines 2015. Ref. FFT161501/14

[54] El-Sayed AR, Mohran HS, El-Lateef HMA. Corrosion study of zinc, nickel, and zinc-nickel alloys in alkaline solutions by Tafel plot and impedance techniques. Metallurgical and Materials Transactions A: Physical Metallurgy and Materials Science. 2012;**43A**: 619-632. DOI: 10.1007/s11661-011-0908-4

[55] Khan R, Mehmood M, Rizwan R, Ahmad J, Hasan MU, Iqbal Z, et al. Corrosion behavior of zinc-nickel alloy coatings electrodeposited in additive free chloride baths. Corrosion Engineering, Science and Technology. 2001;**46**(7):755-761. DOI: 10.1179/147842210X12741768645794

[56] Gavrila M, Millet JP, Mazille H, Marchandise D, Cuntz JM. Corrosion behaviour of zinc-nickel coatings, electrodeposited on steel. Surface and Coating Technology. 2000;**123** (2-3):164-172. DOI: 10.1016/S0257-8972(99)00455-7

[57] Conrad HA, McGuire MR, Zhou T, Coskun MI, Golden TD. Improved corrosion resistant properties of electrochemically deposited zinc-nickel alloys utilizing a borate electrolytic alkaline solution. Surface and Coating Technology. 2015;**272**:50-57. DOI: 10.1016/j.surfcoat.2015.04.025

[58] Tientong J, Thurber CR, D'Souza N, Mohamed A, Golden TD. Influence of bath composition at acidic pH on electrodeposition of nickel-layered silicate nanocomposites for corrosion protection. International Journal of Electrochemistry. 2013;**853869**:1-8. DOI: 10.1155/2013/853869

[59] Feng Z, Li Q, Zhang J, Yang P, Song H, An M. Electrodeposition of nanocrystalline Zn-Ni coatings with single gamma phase from an alkaline bath. Surface and Coating Technology. 2015;**270**:47-56. DOI: 10.1016/j.surfcoat.2015.03.020

[60] Müller C, Sarret M, Benballa M. Some peculiarities in the codeposition of zinc-nickel alloys. Electrochimica Acta. 2001;**46**:2811-2817. DOI: 10.1016/S0013-4686(01)00493-5

[61] Lehmberg CE, Lewis DB, Marshall GW. Composition and structure of thin electrodeposited zinc-nickel coatings. Surface and Coating Technology. 2005;**192**:269-277. DOI: 10.1016/j.surfcoat.2004.07.109

[62] Conrad HA, Corbett JR, Golden RD. Electrochemical deposition of γ-phase zinc-nickel alloys from alkaline solution. ECS Transactions. 2011;**33**(30):85-95. DOI: 10.1149/1.3566091

[63] Rao VR, Bangera KV, Hegde AC. Magnetically induced electrodeposition of Zn-Ni alloy coatings and their corrosion behaviors. Journal of Magnetism and Magnetic Materials. 2013;**345**:48-54. DOI: 10.1016/j.jmmm.2013.06.014

[64] Tian W, Xie FQ, Wu XQ, Yang ZZ. Study on corrosion resistance of electroplating zinc-nickel alloy coatings. Surface and Interface Analysis. 2009;**41**:251-254. DOI: 10.1002/sia.3017

[65] Ghaziof S, Gao W. Electrodeposition of single gamma phased Zn-Ni alloy coatings from additive-free acidic bath. Applied Surface Science. 2014;**311**:635-642. DOI: 10.1016/j.apsusc.2014.05.127

[66] Horch RA, Golden TD, D'Souza NA, Riester L. Electrodeposition of nickel/montmorillonite layered silicate nanocomposite thin films. Chemistry of Materials. 2002;**14**: 3531-3538. DOI: 10.1021/cm010812+

[67] Kwon M, Jo DH, Cho SH, Kim HT, Park JT, Park JM. Characterization of the influence of Ni content on the corrosion resistance of electrodeposited Zn-Ni alloy coatings. Surface and Coating Technology. 2016;**288**:163-170. DOI: 10.1016/j.surfcoat.2016.01.027

[68] Bajat JB, Maksimović MD, Radović GR. Electrochemical deposition and characterization of zinc-nickel alloys deposited by direct and pulse current. Journal of the Serbian Chemical Society. 2002;**67**(8-9):625-634. DOI: 10.2298/JSC0209625B

[69] Pfiz R, Strub G. A new development for the electrolytic deposition of zinc-nickel alloy with 12-15% nickel from an alkaline bath. Transactions of the IMF. 1996;**74**(5):158-160. DOI: 10.1080/00202967.1996.11871117

[70] Petrauskas A, Grincevičienė L, Česūnienė A, Matulionis E. Stripping of Zn-Ni alloys deposited in acetate-chloride electrolyte under potentiodynamic and galvanostatic conditions. Surface and Coatings Technology. 2005;**192**:299-304. DOI: 10.1016/j.surfcoat.2004.08.191

[71] Wykpis K, Popczyk M, Budniok A. Electrolytic deposition and corrosion resistance of Zn-Ni coatings obtained from sulphate-chloride bath. Bulletin of Materials Science. 2011; **34**(4):997-1001. DOI: 10.1007/s12034-011-0228-8

[72] Magagnin L, Nobili L, Cavallotti PL. Metastable zinc-nickel alloys deposited from an alkaline electrolyte. Journal of Alloys and Compounds. 2014;**615**:S663-S666. DOI: 10.1016/j.jallcom.2014.01.240

[73] Lin YP, Selman R. Electrodeposition of corrosion-resistant Ni-Zn alloy I. Cyclic Voltammetric study. Journal of the Electrochemical Society. 1993;**140**(5):1299-1303. DOI: 10.1149/1.2220974

[74] Bobrikova IG, Kukoz FI, Selivanov VN, Kopin AV. On the zinc-nickel alloy Electrodeposition mechanism. Russian Journal of Electrochemistry. 2002;**38**(10):1148-1151. DOI: 10.1023/A:1020664022224

[75] Roventi G, Cecchini R, Fabrizi A, Bellezze T. Electrodeposition of nickel-zinc alloy coatings with high nickel content. Surface and Coating Technology. 2015;**276**:1-7. DOI: 10.1016/j.surfcoat.2015.06.043

[76] Roventi G, Fratesi R, Della Guardia RA, Barucca G. Normal and anomalous codeposition of Zn-Ni alloys from chloride bath. Journal of Applied Electrochemistry. 2000;**30**: 173-179. DOI: 10.1023/A:1003820423207

[77] Ashassi-Sorkhabi H, Hagrah A, Parvini-Ahmadi N, Manzoori J. Zinc-nickel alloy coatings electrodeposited from a chloride bath using direct and pulse current. Surface and Coating Technology. 2001;**140**:278-283. DOI: 10.1016/S0257-8972(01)01032-5

[78] Oswaldo Pagotto S Jr, Marina de Alverenga Freire C, Ballester M. Zn-Ni alloy deposits obtained by continuous and pulsed electrodeposition processes. Surface and Coating Technology. 1999;**122**:10-13. DOI: 10.1016/S0257-8972(99)00401-6

[79] Conrad H, Corbett J, Golden TD. Electrochemical deposition of γ-phase zinc-nickel alloys from alkaline solution. Journal of the Electrochemical Society. 2012;**159**(1):C29-C32. DOI: 10.1149/2.027201jes

[80] Chandrasekar MS, Pushpavanam M. Pulse and pulse reverse plating- conceptual, advantages and applications. Electrochimica Acta. 2008;**53**:3313-3322. DOI: 10.1016/j.electacta.2007.11.054

[81] Bajat JB, Petrović AB, Maksimović MD. Electrochemical deposition and characterization of zinc-nickel alloys deposited by direct and reverse current. Journal of the Serbian Chemical Society. 2005;**70**(12):1427-1439. DOI: 10.2298/JSC0512427B

[82] Ramanauskas R, Gudavičiūte L, Kaliničenko A, Juškėnas R. Pulse plating effect on micro structure and corrosion properties of Zn-Ni alloy coatings. Journal of Solid State Electrochemistry. 2005;**9**:900-908. DOI: 10.1007/s10008-005-0049-z

[83] Lee L, Behera P, Sriraman KR, Chromik RR. Effects of humidity on the sliding wear properties of Zn-Ni alloy coatings. RSC Advances. 2017;**7**:22662-22671. DOI: 10.1039/c6rs27352a

[84] Monshi A, Foroughi MR, Monshi MR. Modified Scherrer equation to estimate more accurately Nano-crystallite size using XRD. World Journal of Nano Science and Engineering. 2012;**2**:154-160. DOI: 10.4236/wjnse.2012.23020

[85] Langford JI, Wilson JC. Scherrer after sixty years: A survey of some new results in the determination of crystallite size. Journal of Applied Crystallography. 1978;**11**:102-113. DOI: 10.1107/S0021889878012844

[86] Bard AJ, Faulkner LR. Electrochemical Methods: Fundamentals and Applications. 2nd ed. New York: Wiley; 2001; 2000. p. 809. ISBN: 0-471-04372-9

[87] Zhang XL, Jiang ZH, Yao ZP, Song Y, Wu ZD. Effects of scan rate on the potentiodynamic polarization curve obtained to determine the Tafel slopes and corrosion current density. Corrosion Science. 2009;**51**:581-587. DOI: 10.1016/j/corsci.2008.12.005

[88] Armstrong RD, Bell FM. The electrochemical behaviour of zinc in alkaline solution. Electrochemistry. 1974;**4**:1-17

[89] Wang AQ, D'Souza N, Golden TD. Ceramic montmorillonite nanocomposites by electrochemical synthesis. Applied Clay Science. 2008;**42**:310-317. DOI: 10.1016/j.clay.2008.02.004

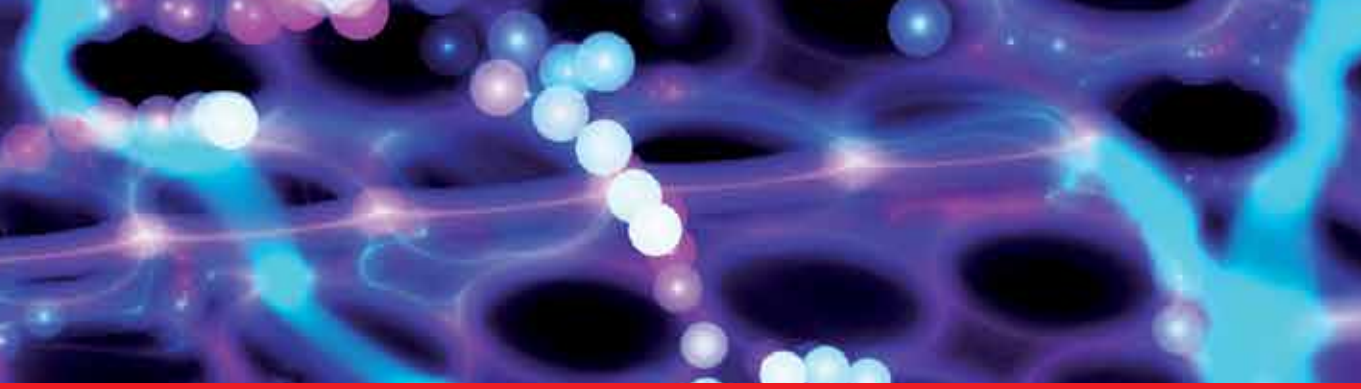

Edited by Subbarayan Sivasankaran

To have unimaginably outstanding useful properties (physical, mechanical, electrical, optical, chemical, and magnetic) in a single material design is a highly challenging task in the material science community, which can be achieved through nanocomposites. These nanocomposites can be produced from all conventional materials, which include polymers, metals/alloys, and ceramics, by modifying their internal structures. Due to modification of the structures of all kinds of conventional materials, at either the nano or ultra-fine level, the materials exhibit superior performance, which is a boon for all fields of science. In general, nanocomposite materials can be manufactured by solid-state processing techniques, liquid metallurgy, ex-situ and in-situ powder metallurgy, and other basic science synthesis routes. Furthermore, the possibility of making environmentally friendly materials is also possible with nanotechnology. Therefore, to investigate and demonstrate developments in the field of nanocomposites, this book is targeted at all the scientific personnel working in this field.

Published in London, UK

IntechOpen

ISBN 978-1-83881-737-4